

AD-R100 059

HIGH RESOLUTION PROTOTYPE REAL-TIME RADIOGRAPHY SYSTEM
(U) SCIENCE APPLICATIONS INTERNATIONAL CORP SAN DIEGO
CA R M POLICHRAR NOV 86 AFML-TR-86-4861

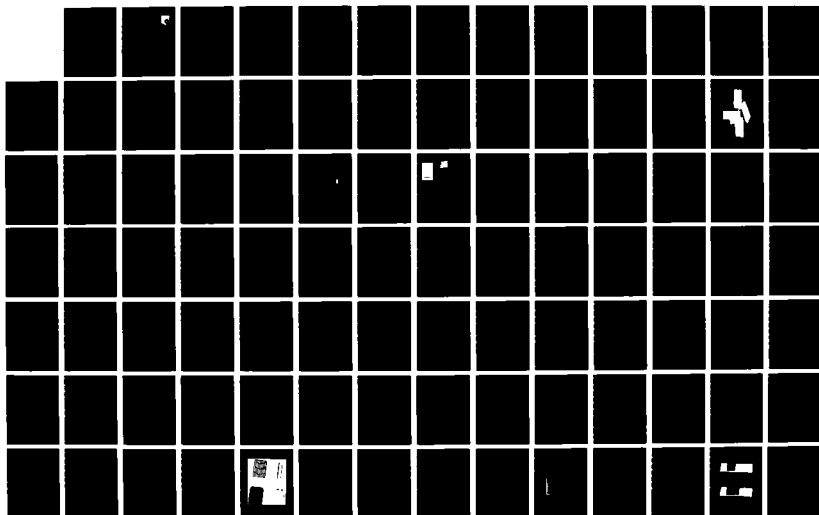
1/2

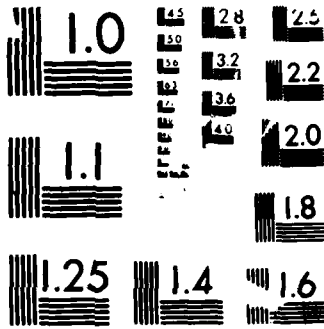
UNCLASSIFIED

F33615-83-C-5810

F/B 14/4

NL





MICROCOPY RESOLUTION TEST CHART
NBS 1963-A

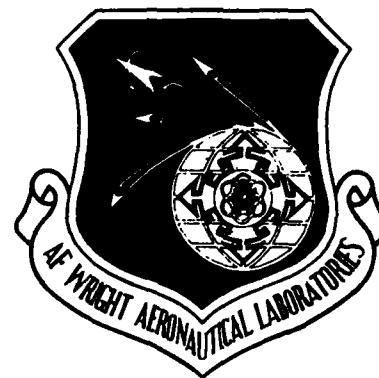
DWG FILE W/2

2

AFWAL-TR-86-4061

HIGH RESOLUTION PROTOTYPE

REAL-TIME RADIOGRAPHY SYSTEM



AD-A188 059

Raulf M. Polichar

SCIENCE APPLICATIONS INTERNATIONAL CORPORATION

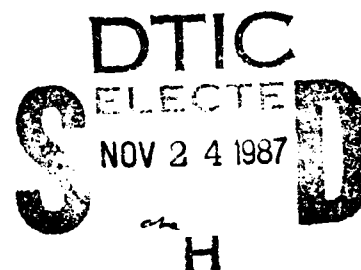
10401 Roselle Street

San Diego, CA 92121

NOVEMBER 1986

Final report for period August 1983 to April 1986

Approved for public release: distribution unlimited



MATERIALS LABORATORY

AIR FORCE WRIGHT AERONAUTICAL LABORATORIES

AIR FORCE SYSTEM COMMAND

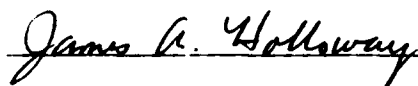
WRIGHT-PATTERSON AIR FORCE BASE, OHIO 45433-6533

NOTICE

When Government drawings, specifications, or other data are used for any purpose other than in connection with a definitely related Government procurement operation, the United States Government thereby incurs no responsibility nor any obligation whatsoever; and the fact that the government may have formulated, furnished, or in any way supplied the said drawings, specifications, or other data, is not to be regarded by implication or otherwise as in any manner licensing the holder or any other person or corporation, or conveying any rights or permission to manufacture, use, or sell any patented invention that may in any way be related thereto.

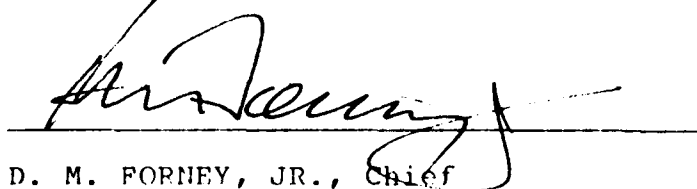
This report has been reviewed by the Office of Public Affairs (ASD/PA) and is releasable to the National Technical Information Service (NTIS). At NTIS, it will be available to the general public, including foreign nations.

This technical report has been reviewed and is approved for publication.



JAMES A. HOLLOWAY
Nondestructive Evaluation Branch
Metals and Ceramics Division

FOR THE COMMANDER



D. M. FORNEY, JR., Chief
Nondestructive Evaluation Branch
Metals and Ceramics Division

If your address has changed, if you wish to be removed from our mailing list, or if the addressee is no longer employed by your organization, please notify AFWAL/MLIP, W-PAFB OH 45433-6533 to help us maintain a current mailing list.

Copies of this report should not be returned unless return is required by security considerations, contractual obligations, or notice on a specific document.

UNCLASSIFIED

SECURITY CLASSIFICATION OF THIS PAGE

ADA188059

REPORT DOCUMENTATION PAGE

1a. REPORT SECURITY CLASSIFICATION UNCLASSIFIED		1b. RESTRICTIVE MARKINGS None	
2a. SECURITY CLASSIFICATION AUTHORITY		3. DISTRIBUTION/AVAILABILITY OF REPORT	
2b. DECLASSIFICATION/DOWNGRADING SCHEDULE N/A		Approved for public release; distribution is unlimited.	
4. PERFORMING ORGANIZATION REPORT NUMBER(S)		5. MONITORING ORGANIZATION REPORT NUMBER(S) AFWAL-TR-86-4061	
6a. NAME OF PERFORMING ORGANIZATION Science Applications International Corporation	6b. OFFICE SYMBOL (If applicable)	7a. NAME OF MONITORING ORGANIZATION Air Force Wright Aeronautical Laboratories Materials Laboratory (AFWAL/MLLP)	
6c. ADDRESS (City, State and ZIP Code) 10401 Roselle Street San Diego CA 92121		7b. ADDRESS (City, State and ZIP Code) Wright-Patterson AFB OH 45433-6533	
8a. NAME OF FUNDING/SPONSORING ORGANIZATION	8b. OFFICE SYMBOL (If applicable)	9. PROCUREMENT INSTRUMENT IDENTIFICATION NUMBER Contract F33615-83-C-5010	
8c. ADDRESS (City, State and ZIP Code)		10. SOURCE OF FUNDING NOS.	
		PROGRAM ELEMENT NO	PROJECT NO.
		TASK NO	WORK UNIT NO
11. TITLE (Include Security Classification) High Resolution Prototype Real-time Radiography System		62102F	2418
		02	26
12. PERSONAL AUTHOR(S) Polichar, Raulf M.			
13a. TYPE OF REPORT Final	13b. TIME COVERED FROM 7-20-83 TO 4-31-86	14. DATE OF REPORT (Yr., Mo., Day) November 1986	15. PAGE COUNT 177
16. SUPPLEMENTARY NOTATION			
17. COSATI CODES		18. SUBJECT TERMS (Continue on reverse if necessary and identify by block number)	
FIELD	GROUP	Real-time radiography	
14	02	X-ray Converters,	
		Screens	
19. ABSTRACT (Continue on reverse if necessary and identify by block number)			
<p>This report covers the evaluation of a number of advanced X-ray converter screens. It concentrates in particular on screen types that are compatible with direct fiber optic readout. The new converters included several types of scintillating fiber optic screens, intagliated phosphor screens and depositions of high efficiency screens directly on fiber optic couplers. The study covered the X-ray potentials between 20 KV and 320 KV. The report also describes the use of these screens with a solid-state line scan sensor and the advantages that such a sensor has in high resolution real-time radiography. Illustrations are provided on applications of this new technology to inspection of aerospace, electronic and ordnance samples. A design for an advanced solid-state line scanner is presented and its performance parameters predicted.</p>			
20. DISTRIBUTION/AVAILABILITY OF ABSTRACT UNCLASSIFIED/UNLIMITED <input type="checkbox"/> SAME AS RPT <input checked="" type="checkbox"/> DTIC USERS <input type="checkbox"/>		21. ABSTRACT SECURITY CLASSIFICATION	
22a. NAME OF RESPONSIBLE INDIVIDUAL JAMES A. HOLLOWAY		22b. TELEPHONE NUMBER (Include Area Code) (513) 255-9802	22c. OFFICE SYMBOL AFWAL/MLLP

ABSTRACT

This report covers the evaluation of a number of advanced X-ray converter screens. It concentrates in particular on screen types that are compatible with direct fiber optic readout. The new converters included several types of scintillating fiber optic screens, intagliated phosphor screens and depositions of high efficiency screens directly on fiber optic couplers. The study covered the X-ray potentials between 20 KV and 320 KV. The report also describes the use of these screens with a solid state line scan sensor and the advantages that such a sensor has in high resolution real-time radiography. Illustrations are provided on applications of this new technology to inspection of aerospace, electronic and ordnance samples. A design for an advanced solid state line scanner is presented and its performance parameters predicted.



Accession For	
NTIS GRA&I	<input checked="" type="checkbox"/>
DTIC TAB	<input type="checkbox"/>
Unannounced	<input type="checkbox"/>
Justification	
By	
Distribution/	
Availability Codes	
Avail and/or	
Special	

A-1

TABLE OF CONTENTS

<u>SECTION</u>		<u>PAGE</u>
1.0	INTRODUCTION AND PROGRAM OVERVIEW	1-1
	1.1 Program Definition	1-1
	1.2 Technical Overview	1-5
	1.3 Line Scan Technology	1-6
	1.4 X-ray To Light Converter Screens	1-7
	1.5 Line Scan Readout Systems	1-7
2.0	CHARACTERIZATION OF X-RAY TO LIGHT CONVERTER SCREENS	2-1
	2.1 Analysis of Critical Performance Factors	2-1
	2.2 Conversion Screens Evaluated in Program	2-5
	2.3 Direct Determination of X-Ray Conversion Screen Modulation Transfer Functions	2-12 2-9
	2.4 Spectral Output Distribution	2-29
	2.5 Measure of Screen Brightness and Absolute Radiance and Conversion Efficiency	2-41
	2.6 Quantitative Evaluation Methodology	2-64
	2.6.1 Introduction	2-64
	2.6.2 Determination of the Modulation Transfer Function	2-66
	2.6.3 Determination of the Noise Structure	2-72
	2.6.4 Definition of the Figure of Merit	2-78
	2-7 Development of a Practical Figure of Merit Ranking Conversion Screens	2-87 2-83
3.0	LINEAR SCANNER TECHNOLOGY	3-1
	3.1 Basic Principles of Operation	3-1
	3.2 Flux Requirements and Resolution	3-4
	3.3 Development of Breadboard Scanner	3-6
	3.4 Review of Breadboard System Performance	3-21
	3.5 Operational Experience with an 8-Inch Prototype Scanner	3-25
4.0	BREADBOARD SYSTEM RADIOGRAPHY OF TYPICAL AIRCRAFT PARTS	4-1
5.0	PROPOSED FULL SCALE DESIGN	5-1
	5.1 Proposed System Specifications	5-1
	5.2 Scanner Head Design	5-3
6.0	PROGRAM SUMMARY AND RECOMMENDATION FOR FURTHER STUDY	6-1

TABLE OF FIGURES

<u>FIGURE</u>		<u>PAGE</u>
2.2.1	Sample Test Screens Mounted on Special Line Scan Fixtures	2-6
2.2.2	Construction Details of Intagliated Screens	2-9
2.3.1	Direct measurement of X-Ray Conversion Screen Module Transfer Functions	2-13
2.3.2	Example Microdensitometer Plot	2-15
2.3.3	Comparison Between MTF and CTF	2-17
2.3.4	Modulation Transfer Function of KODAK OG-1 Film Exposed with X-Rays	2-18
2.3.5	Modulation Transfer Function of KODAK OG-1 Film Exposed with Light	2-19
2.3.6	2mm Thick Terbium Glass Fiber Optic Scintillator Modulation Transfer Function	2-22
2.3.7	5mm Thick Terbium Glass Fiber Optic Scintillator Modulation Transfer Function	2-23
2.3.8	10mm Thick Terbium Glass Fiber Optic Scintillator Modulation Transfer Function	2-24
2.3.9	TRIMAX 2 Screen in Contact With Fiber Optic Coupler Coupler Modulation Transfer Function	2-25
2.3.10	GOS Deposited on 5mm Terbium Fiber Optics Scintillator Modulator Transfer Function	2-22
2.3.11	0.012" Intagliated Screen Modulation Transfer Function	2-27
2.3.12	0.020" Intagliated Screen Modulation Transfer Function	2-28
2.4.1	Experimental Arrangement to Measure Output Spectrum Output of Conversion Screens	2-30
2.4.2	Calibration Response of perkin Elmer Monochrometer and and PMT Sensor	2-31
2.4.3	Response of Photometer PMT used to Measure Output Radiance of Conversion Screen	2-32
2.4.4	Spectral Output Function for Terbium Doped Glass	2-33
2.4.5	Spectral Shape of Cerium Doped Glass Fiber Optic (5mm) 60 kV X-Ray Excitation	2-34

2.4.6	Spectral Response for Gd_2O_2S on Non-Scintillating Fiber Optic	2-36
2.4.7	Spectral Response for intagliated Gd_2O_2S Screens	2-37
2.4.8	Spectral Response for Combined Terbium Glass	2-38
2.4.9	Spectral Shape of Bismuth Germinate (3mm Plate) 60 kV X-Ray Excitation	2-39
2.4.10	Typical Spectral Response for a Silicon Self-Scanned Array	2-40
2.5.1	Experimental Apparatus Used to Determine Radiance per Unit Dose Rate as a Function of X-Ray Spectra	2-42
2.5.2	Radiance/Dose Rate from the 2mm Thick Terbium Doped Glass Fiber Optic Converter Screen	2-48
2.5.3	Radiance/Dose Rate for 5mm Terbium Doped Fiber Optic Screen	2-49
2.5.4	Radiance/Dose Rate for 10mm Thick Terbium Doped Glass Fiber Optic Converter Screen	2-50
2.5.5	Radiance/Dose Rate for 5mm Thick Cerium Doped Fiber Optic Converter Screen	2-51
2.5.6	Radiance/Dose Rate for TRIMAX 2 Converter Screen	2-52
2.5.7	Radiance/Dose Rate for Gd_2O_2S Overcoated Terbium Fiber Optic Converter	2-53
2.5.8	Radiance/Dose Rate for .012" Deep Intagliated Gd_2O_2S Converter Screen	2-54
2.5.9	Radiance/Dose Rate for .020" Deep Intagliated Gd_2O_2S Converter Screen	2-55
2.5.10	Radiance/Dose Rate from a 3mm Thick Bismuth Germinate Single Crystal Converter Screen	2-56
2.5.11	Relative Comparison of Radiance/Dose Rate for All Screens Evaluated in Study	2-61 2-57
2.6.1	Comparison of Systems Based on Composite Figure of Merit	2-65
2.6.2	Alternative Approaches for Determination of MTF	2-67
2.6.3	Low Resolution Radiography of Grid Samples	2-68
2.6.4	Modulus of 2D Fourier Transform of Grid Image	2-71
2.6.5	Grid Images and Modulus of Their One-Dimensional Fourier Transforms	2-73

2.6.6	Modulation Transfer Function Derived from Data of Fig.2.4	2-74
2.6.7	Example of Two Independent Images for Analysis of the Noise Structure	2-76
2.6.8	Analysis of Single Pixel Variance Versus Intensity and Determination of Noise Equivalent	2-79
2.6.9	Definition of the Integral $S(D,MTF)$ used in Figure of Merit	2-80
2.6.10	Simulation of Image of Hole Observed with a System Characterized by MTF and S/N Ratio	2-84
2.6.11	Effect of Worsening of the MTF on the Figure 5.1 Test Case	2-85
2.6.12	Effect of Worsening of the S/N Ratio on the Figure 5.1 Test Case	2-86
2.7.1	Comparison Between $S(D,MTF)$ Integral Developed for FOM Model and the Corresponding MTF Curve	2-89
2.7.2	Figure of Merit for All Conversion Screens Based on Recognition of Circular Defect of Diameter, D. (mm)	2-90
3.3.1	Linear Scanner Detector Configuration	3-7
3.3.2	View of Breadboard X-Ray Linear Scanner	3-8
3.3.3	Mounting of Linear Diode Array and Preamplifier	3-10
3.3.4	MTF of Breadboard Linear Scanner	3-11
3.3.5	Block Diagram of Linear Scanner Data Processing System	3-13
3.3.6	Front Panel of Control Box for the Linear Diode Array	3-14
3.3.7	Fiber Optic Minifiers	3-16
3.3.8	Test Screen Mounted to Westinghouse 40- 25-mm Intensifier and Reticon Preamplifier	3-18
3.3.9	2 inch Field Breadboard Linear X-Ray Scanner	3-19
3.4.1	Funk Star Radiographs Recorded on the 2-Inch Breadboard Scanner	3-22
3.4.2	Compounded Modulation Transfer Function of Line Scan Inspection System Utilizing a Trimax 2 Screen in Contact with a Fiber Optic Coupler	3-24
3.5.1	Arrangement of Major Components in Linear Scanner	3-26
3.5.2	SAIC Linear X-Ray Scanner for High-Resolution Radiographic Inspection of Aircraft Composites	3-27

3.5.3	SAIC Prototype 8-inch Linear Scanner Shown with Scanning Table Assembly	3-28
3.5.4	Simplified Block Diagram of System Electronics	3-30
3.5.5	Leading Edge Section (Northrop) Image with 8-inch Prototype Scanner	3-31
3.5.6	Landing Gear Door (Northrop) Image Taken with 8-inch Prototype Linear Scanner	3-32
3.5.7	Landing Gear Door Honeycomb (Northrop) Image Using 8-inch Prototype	3-33
3.5.8	Radiograph of Tire Tread using 4-inch High Resolution Mode of Prototype Linear Scanner	3-34
3.5.9	Software Matched image of Honeycomb on 8-inch Prototype Scanner	3-36
4.1	Typical Aircraft Components Used to Show Performance of Breadboard Scanner	4-2
4.2	Simulated Cut Patch Inside General Dynamics Carbon Epoxy Bulkhead Test Piece	4-3
4.3	Real-Time Radiographic, Top through Bottom View of General Dynamics Hat Stiffener Test Piece	4-5
4.4a-b	Real Time X-ray Images of First Four Steps of McDonnell Douglas Graphite Test Wedge	4-7
4.4c	Conventional RTR Image of McDonnell Douglas Carbon Epoxy Test Wedge	4-8
4.5a-b	Aluminum Honeycomb Section Removed from Service Showing Evidence of Corrosion	4-9
4.5c-d	Aluminum Honeycomb Section Removed from Service Showing Evidence of Corrosion	4-10
4.6	Examples of Test Objects Used to Evaluate Breadboard System at Higher Energies	4-11
4.7	LSI 11/23 Microcomputer Chip	4-12
4.8	Printed Circuit Board Thumbwheel Switch	4-14
4.9	View of Aircraft Turbine Blade	4-15
4.10a-b	Real-Time Radiograph of Complex Turbine Blade	4-16
4.10c	Real-Time Radiograph of Complex Turbine Blade	4-17

4.11	Safe and Arming Mechanism within a Time Delay Fuse at 160kV	4-19
4.12	RTR Image of 81mm Mortar Aft Metal-Explosive Interface	4-20
5.2.1	Proposed Design of Fiber Optic Scanner Head for Prototype Scanner	5-4
5.3.1	Simplified Block Diagram of Proposed System Electronics	5-5
5.3.2	Block Diagram of Proposed Analog Electronics	5-7
5.3.3	High Resolution X-Ray System Unit Digital Data Processing and System Control	5-8
5.3.4	Detail of Dark Current Corrector	5-11
5.3.5	Detail of Gain Correction Circuits	5-12
6.1	X-Ray Linear Scanner Concept for a Field Portable System	6-5
6.2	SAIC 1024x1024 Pixel Solid State Imager	6-6

TABLES

<u>TABLE</u>		PAGE
1.0	Work Breakdown Structure	1-3
2.1	Conversion Screens Evaluated in High Resolution Radiography Program	2-10
2.5.1	Spectral Overlap, X_s for Converter Screens and RCA 4516 Photomultiplier	2-45
2.5.2	Relative Conversion Efficiency of Tested Screens at 160kV	2-63
2.6.1	Values of $S(D,MTF)$ for Typical MTF Curve	2-83

1.0 INTRODUCTION AND PROGRAM OVERVIEW

1.1 PROGRAM DEFINITION

The objective of this program has been the functional design of an all-electronic, high-resolution, prototype Real-Time Radiography System for the inspection of aerospace components. This system requires performance characteristics typical of film-based radiography both in performance parameters and available image size. Major portions of this program concentrated on the selection, evaluation, and optimization of commercially available X-ray-to-light/electron converter devices. We attempted to obtain a device which has, or shows promise of attaining, a resolution, dynamic range, and contrast sensitivity equivalent to industrial X-ray film (resolution > 10 lp/mm, dynamic range $> 10^3$ and a contrast sensitivity of better than 1%). The device also had to have promise of being expanded to a 10- to 12-inch field of view while maintaining these characteristics.

The remainder of the program concentrated on the construction of a breadboard RTR system which would allow the practical evaluation and optimization of the converter device and to the design concept for a practical RTR system based on the information and experimental results obtained during the program. The results of the program and the conceptual design were intended as a basis of a practical RTR system capable of replacing film radiography for energies of less than 300KV at manufacturing, remanufacturing, and depot maintenance facilities.

The program scope was divided into three principal tasks:

Task I included the testing and evaluation of the converter devices selected to represent the state of the art in this technology. Each of the converter devices evaluated (to a maximum of three) was to be conceptually different and not minor variations of each other. The results of the evaluations were to be carried over the range of energies from 20KV to 300KV. Concurrent with this evaluation then was to be the development of an objective figure of merit with which the devices could be compared and ranked.

Task II concentrated on the construction of a breadboard RTR system to demonstrate the performance of the converter device. This system included the associated X-ray source, electronics and data processing capability to measure total system performance. This system was to approximate as closely as possible film performance. A demonstration of the systems capability using test standards as well as typical aerospace parts will be held at the contractors facility to demonstrate the performance of the system.

At the time of contract award, there was a mutually agreed upon reduction in scope, limiting the studies of converter devices to those compatible with fiber optically coupled line scanner type sensors. The modified statement of work submitted at that time is included in Table 1.

TABLE 1

Work Breakdown Structure

1.0 TASK 1 TESTING & EVALUATION OF X-RAY CONVERTER DEVICES

- 1.1 Devise Figure of Merit
- 1.2 Obtain Appropriate Test Samples
- 1.3 Real Time Imager
 - 1.3.1 Study Competing Components for each approach
 - 1.3.2 Lab Test of Components
 - 1.3.2.1 Devise Objective Rating Criteria
 - 1.3.2.2 Devise Testing Procedure
 - 1.3.2.2.1 Fixturing (including X-ray facility)
 - 1.3.2.2.2 Electronics
 - 1.3.2.2.3 Testing (including sensitivity to external environment.)
 - 1.3.3 Assemble Linear Scanner Imagers
 - 1.3.3.1 Mechanical Fixturing
 - 1.3.3.2 Electronics
 - 1.3.4 Test Imager
 - 1.3.4.1 Testing Procedure
 - 1.3.4.2 Judge based on Figure of Merit (20 kVp to 300 kVp)
- 1.4 Select Imaging Device for Optimization based on F.O.M.
 - 1.4.1 Obtain PCO Concurrence on Selection

2.0 TASK 2 "BREADBOARD" RTR SYSTEM

- 2.1 Design and Fabricate a Simple Scanning Mechanism (for Test Samples)
- 2.2 Construct Optimization "Breadboard" RTR
 - 2.2.1 Construct Optimized Imager and Electronics
 - 2.2.2 Obtain Appropriate Display - Viewing Media
 - 2.2.3 Assemble Basic Image Processing Capability
- 2.3 Design and Fabricate penetrameters and test wedges (per ASTM E-142-77)
- 2.4 Test Samples
 - 2.4.1 PCO Approval
 - 2.4.2 Film Radiography
- 2.5 Demonstrate Capability of Breadboard RTR

3.0 TASK 3 RTR PROTOTYPE DESIGN

3.1 Provide Design, Sketches, Specifications, etc., of RTR Prototype System

3.1.1 Imager

3.1.2 Electronics

3.1.3 Image Processing Hardware and Software

3.1.4 RT Image Viewing System

3.1.5 Image Storage and Retrieval System

3.2 Recommended Areas of Improvement

1.2 TECHNICAL OVERVIEW

As was clearly indicated in the Air Force's original program objectives, the critical device limiting the performance of real time radiographic systems is the X-ray-to-light/electron image converter. We feel that this converter device should be treated with a systems approach and that this converter might well be composed of subsystems that carry the information from X-ray distribution to some type of electronic signal which can be processed and displayed. These elements may or may not require discrete components depending on the type of technology employed. We need to learn the characteristics of the individual parts of the subsystems and then integrate them into an optimized system. A typical system might contain an X-ray-to-light converter screen, some means of coupling (contact, or fiber optics) and an electronic light sensor. This system approach recognizes certain unavoidable yet critical performance limitations in each stage and tends to weight the other sub-systems performance in this area accordingly. Thus, if the light sensor is the limiting factor in the dynamic range of the system, one might not want to weigh a converter screen with 10,000:1 range much over the 1000:1 screen, especially since screens rarely are the limiting element in this performance factor. Similarly, one might select specific combinations of X-ray screens and receivers based on a good spectral match if other factors were about equal. The scope of this program was limited to those converter devices that might be integrated into a line scanner type imager. The measurements on the various subsystems were carried out both individually and where appropriate as a total system. The original measurement plan had called out the use of the imager readout system to evaluate input screen performance. For a number of practical reasons this was augmented by independent measures of the individual performance parameters. Where possible, several methods were employed to provide some test of consistency. During the course of developing the breadboard system, a number of technical difficulties were encountered which entailed "work around" tactics in order to complete the work. Some of these problems will be discussed where they are relevant to the measurements on performance of specific devices.

1.3 LINE SCAN TECHNOLOGY

Line-Scan Imagers represent a relatively new approach to industrial radiography. They represent the electronic image analog to moving slit film radiography. Until recently, the most common use of these line scanners has been in relatively low-resolution (1.0 lp/mm), wide-area scanning of airport baggage. The line-scan approach has several striking advantages over conventional area imagers. The use of a collimated line sensor and a matching fan beam dramatically reduces the effects of scatter in the image and increases the effective image contrast. The converter devices for a line scanner may have asymmetric resolution characteristics because only one dimension is electronically scanned. The resolution of the system in the direction perpendicular to the "line" is set by the mechanical spacing of a pair of collimating slits. Because an image is formed by successive scans, the image size can be effectively limitless along the motion axis as old data are rolled off the display while new data scrolls in from the other side. Because the sensors are "one-dimensional," several units can be stacked to form a wider scan. Because the resolution of each element remains constant and because the slit sets the perpendicular resolution, the system is easy to scale up to industrially useful sizes. Experience has shown that significant improvements in flaw detectability are obtained even if only one axis has the "ultra high" resolution, which can relax storage requirements for large-area systems.

All high-resolution sensors suffer from increased statistical noise as the picture elements of a system are reduced in size, because more X-ray flux is required to provide a given number of detected events per pixel. Moreover, high-resolution line scanner only looks at a given line once, with no subsequent integration possible. This sets a definite limit on scan speed and contrast sensitivity, which must be factored in the final performance. It also means that even though an image seems to move as it is scrolled across the display, the time between the first and last lines makes it difficult to follow motion. These same difficulties will also occur for area imager approaches that attempt to create a very high-resolution image by combining a mosaic of small area image files. The problem of obtaining enough fluence (flux x time) for each pixel is universal in any high-resolution system and will be dealt with in detail in this report.

The linear scanner explored in this study consists of an X-ray-to-light screen, fiber optically coupled to an optically intensified solid state linear photodiode array. The study has included measurement of MTF, spectral and intensity characteristics as well as measurements of X-ray imaging performance using the combined system. An objective figure of merit that defines relative performance of the system to the target defect size has been developed and with some adaptation been applied to both the X-ray screens as well as the total system. Other tangible performance parameters relevant to the systems practical use such as flux and interscene dynamic range are also discussed in detail. Finally, comparison between typical high-resolution line-scan images are compared with comparable images taken on a typical industrial imager.

1.4 X-RAY TO LIGHT CONVERTER SCREENS

The decision to concentrate on converter devices applicable to linear scanner technology has limited our study to those screens that are formed into fiber optic plates or that can be coupled by contact onto such plates. These screen types include several varieties of scintillating glass fiber plates, deposited films on conventional fiber optics and intagliated or filled fibers using salt screen materials deposited into etched, multi-fiber plates. The study has included examples of each type of screen as well as an example of a mixed mode screen. All screens have been characterized by conversion efficiency, spectral characteristics, and modulation transfer function. Other characteristics such as radiation resistance and stability have been observed but not quantified. All screens were tested both independently and with a breadboard linear scanner.

1.5 LINE SCAN READOUT SYSTEMS

As discussed in previous sections, the choices of converter screen are limited if a line scanner technology is employed. Early line scanners used for baggage inspection were typically fabricated out of discrete 1 to 2mm square detector elements. These detectors usually were fabricated from a thick scintillator directly bonded to a silicon photo diode. (Direct conversion in

silicon detectors using deep junction devices has been attempted but abandoned because of the problems caused by radiation damage. A 1mm-square detector corresponds to a spatial frequency cut off of approximately 1/2 lp/mm, and clearly does not even come close to the resolution limits required for this project. Attempts to simply reduce the size of the individual detector leads to insurmountable problems since at 10 lp/mm each detector is only 0.05 mm (0.002") on a side. The same flux that is easily measured by a simple scintillator photodiode at 1 mm² area is reduced by 400 for such a high resolution and far below useful levels. The physical detectors must be integrated into large contiguous arrays; problems occur at the boundaries of array elements. The readout electronics are also complicated using discrete arrays since many more amplifiers and digitizers are required.

The solutions to these problems appears to lie in more highly integrated and stackable modules of detectors to increase field of view, optical intensification to increase signals and sequential video processing using commercial self-scanned silicon arrays to simplify the readout. This is in fact the approach used by SAIC in the breadboard RTR imager concept. The procedure used was to couple the converter screen through a fiber optic light conduit to an electrostatic image amplifier and then on to one or more high resolution self-scanned silicon arrays through a second fiber optic link. We considered lens coupling as simpler and more flexible; however, we did not use it in the end because experiments indicated a light loss too great to be tolerated in this application. The design also included a 2:1 minifier which yielded a practical limit of 512 pixels/inch of detector to yield a limiting pixel resolution of 10 lp/mm. We concluded that this represented a good compromise between field of view per array and radiographic performance. We experimented with several versions of this breadboard during the course of the program. As part of an independent and separately funded program, SAIC has developed a line scanner which employed many of the concepts being studied in this work. The results of this practical implementation of these concepts plus the further research carried out in this program form the basis for our final proposed prototype design.

2.0 CHARACTERIZATION OF X-RAY-TO-LIGHT CONVERTER SCREENS

2.1 ANALYSIS OF CRITICAL PERFORMANCE FACTORS

The definition of an X-ray converter device is a somewhat ambiguous term. The critical performance characteristics that limit its performances depend on whether it is a passive converter or whether it contains a gain or subsequent internal electron converter mechanism as found in active devices. Our position in the analysis of the line scan converter, device is that, although it can be thought of as an active converter it can also be broken down into a series of elements that can be treated individually. In the designs studied in this program, the converter system can be broken into:

- An X-ray to light converter. (employing fiber optics)
- A light amplification and minification stage
- A light to charge converter
- An electronic-read out

Moreover, the restriction of technology to a line-scan device with all fiber optic coupling has added an additional perspective to the problem.

The original specification for this project called out a device whose properties included resolution approaching 10 lp/mm and a dynamic range of 10^3 . These are functional goals that must include the total converter system including all of its subsystems, their coupling and the readout device to be meaningful. Moreover, these performance goals must be defined by physical measurement on the converter system that predict performance for all types of radiographic subjects. Characteristics such as modulation transfer function and quantum detection efficiency represent physical properties that can be objectively measured and whose functional dependence determine overall system performance. The response of the system to changing incident X-ray energy and flux is also a significant factor since the goals of the project include performance from 20KV to 300KV. Moreover, since the system design is supposed to lead to a practical implementation, it is important that the flux required to produce a given signal-to-noise ratio be attainable with presently available X-ray sources.

We concluded that performance factors such as resolution and dynamic range result from combination of the properties of converter system elements, the characteristics of the required X-ray source and even the choice of image format technology (e.g., area vs line scan.). For this reason, we believe that an effective figure of merit that characterizes the usefulness of any system must be a function of its actual intended use. Typically, this would relate the system performance to the minimum size defect determined to be important. This type of analysis puts the systems performance in perspective and weighs the individual components in a more balanced way. This is generally the approach followed in our analysis and conclusions.

The choice of line-scan format and all fiber optic coupling was made at the beginning of the program. This set some constraints on the scope of the program but offered some significant potential advantages to total system performance. It had already been shown by Rudolf and Henry¹ and others that single crystal screens could reach limiting resolutions that approximated the 10 lp/mm program goal. These screens, and more recently their scintillating glass counterparts have resolution limited primarily by the spread in the X-ray interaction and to a more limited extent by the effects of scatter and internal reflections at the boundaries. Because they are clear plates of transparent material, they must be observed with a focused lens which adds an additional limitation due to the effects of depth of field, lens aberrations and poor optical capture efficiency. Nonetheless, such screens work well, especially at higher energies where their optical output is large. They tend to fail at the lower energies for just the reasons mentioned above and are typically replaced by conventional deposited salt screens for these applications.

The line-scan approach chosen gets around many of the above short-comings while potentially introducing a few new ones. The fact that both the X-ray beam and sensor are collimated into a fine line makes a dramatic improvement in image contrast over wide area imagers. This true increase in input signal contrast, even at the higher spatial frequencies, is the result of

¹Rudolf, R.G. and Henry, E.B., Jr., Real Time Radiographic Imaging for Submerged Arc Welded Pipe. ASTM STP 716, D.A. Garret and D.A. Bracher, Eds., American Society for Testing and Materials, 1980.

scatter suppression and produces crisper images on any screen type used. Its major limitation is that since only one line of the picture is illuminated at a time, one must scan more slowly to maintain a given X-ray fluence per pixel. (In an area imager, all pixels are illuminated simultaneously during a frame time making more efficient use of the output of the X-ray source.) This basic tradeoff between scatter reduction and flux limitations is one primary difference in the methods. Flux limitations can be recovered with a slower scan but loss of image contrast is never fully recoverable.

The use of fiber optic converters also represents a critical design choice. Fiber optics provide a much more efficient conduit of light and help make up for some of the effects of only looking at one line at a time. More importantly, they affect the shape of the modulation transfer function of both the X-ray screen as well as the overall system. In the important low to midrange of spatial frequencies, the use of fiber optics has been shown to improve image contrast. Many manufactures of X-ray image tubes have found as much as a 50% improvement in contrast ratios by using a fiber optic substrate for the output phosphor rather than a plain glass plate. This improvement is due to the reduction of internal reflections of the plain plate when viewed with a lens systems. The major disadvantage in the use of fiber optics is at the highest spatial frequencies since the finite fiber size causes some roll off in resolution. A typical 25-micron fiber screen will show a static limiting resolution of amount 20 lp/mm while a clear screen of the same glass may exhibit a limit of 30 lp/mm or greater when viewed with a lens. From the point of view of our functionally oriented figure of merit, we will evaluate the screens with the purpose of determining which choice produces the best overall reproduction at 10 lp/mm regardless of limiting resolution.

To make objective measurements on our converter system and optimize the individual components, a number of basic physical and optical properties were measured on the X-ray converter screens. These properties included.

- Modulation Transfer Function of Screens
- Brightness (both to the sensor and absolute)
- Optical Spectral Response
- Effective Conversion Efficiency (as a function of X-ray energy)

Other properties such as dynamic range and saturation effects are generally not important in passive screens but were checked by looking for linearity between flux and output.

We made measurements by using a variety of independent methods. The original plan for these measurements had envisioned using the light sensor and readout as a primary measurement tool. We felt that a more valid and useful measure of screen performance could be obtained if independent techniques were used. The final evaluation of system performance does however use the total system at limiting pixel resolution of 10 lp/mm. These results and the methods used to obtain them are discussed in the following sections.

2.2 CONVERSION SCREENS EVALUATED IN PROGRAM

The conversion screens evaluated in this study were all with one exception, either made of fiber optic scintillator or coupled intimately to a fiber optic image plate. Three basic types of screens were studied:

1. Scintillating glass (Terbium or Cerium doped) fiber plates
2. Salt screens (Gd_2O_2S) deposited on fiber plates
3. Intagliated screens (fiber holes filled with scintillator)

In addition, some combinations of the above types were fabricated to see what performance advantages might be obtained. A single crystal $BiGeO_4$ plate was also used as a reference point. A list of the screens studied is given in Table 2.1.

Each screen was mounted on an aluminum plate that permitted it to be handled or placed on the 2-inch linear scanner. Each screen was somewhat over 2 inches long and anywhere from 0.25 to 0.5" wide. The example of Cerium glass fiber was smaller than the others since it was a developmental sample. Figure 2.2.1 shows a group of screens mounted in their sample holders. All screens protruded about 0.020" beyond the back of the holder to ensure positive contact when fixed onto the scanner system. Similar shaped holders were used to standardize the location of screens for the brightness and MTF measurements.

The first four screens were fabricated by Synergistic Detector Design Inc., of Mountain View, CA, using a terbium doped glass. The plates were formed by fusion of 25-micron fibers with extra mural absorption (EMA) cladding. Three uncoated plates were produced in 2mm, 5mm, and 10mm thicknesses to determine the effect of thickness on self-absorption, resolution and sensitivity at higher energies. A fourth screen was fabricated using a 5mm plate of the same material but also overcoated with Gd_2O_2S phosphor (assumed to be approximately 150-200 microns). We expected this mixed phosphor to show a significant variation in performance, going from low to high energy due to the variation in response of the two phosphors as well as the change in spectrum of the combined light output.

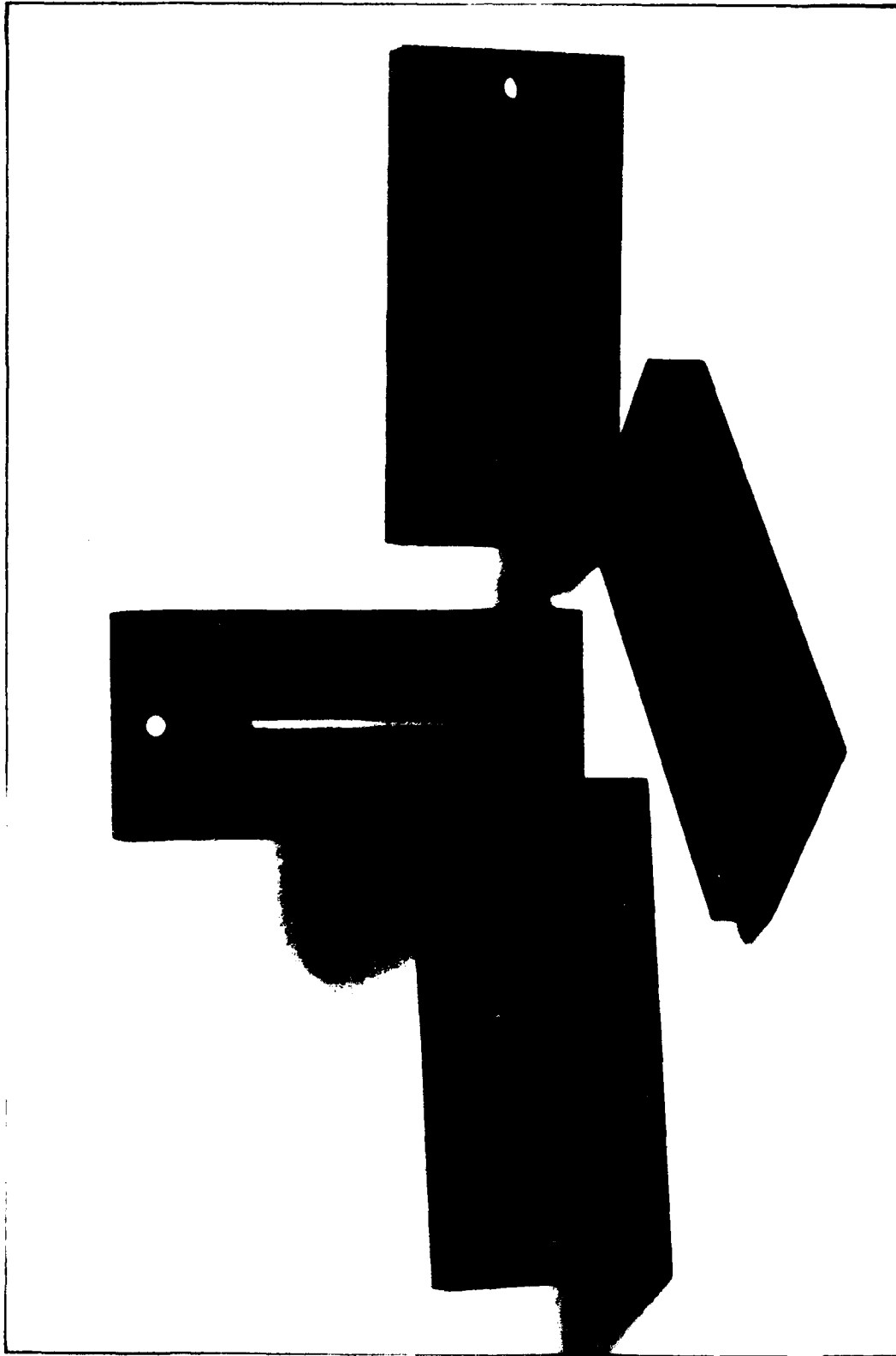


Figure 2.2.1 Sample Test Screens Mounted on Special Line Scan Fixtures.

During the course of the program, we became aware of work on a new type of scintillating glass using Cerium doping. This work was carried out by R. Ruchti² and his collaborators at Notre Dame University. A small sample of this material in the form of a fiber optic plate was graciously supplied to us by Mr. Richard Meade of Collimated Holes, Campbell, CA. This sample was measured for brightness and spectral characteristics, but it was too small to be actually mounted on the linear scanner for measurements.

To test the response of a "salt" screen deposited on fiber optics a piece of commercial Trimax 2 screen was bonded to a 1/4-inch-thick fiber plate. The screen was coupled using Dow Corning Silicon Oil and held with a positive pressure by two plates that permitted an approximate 1/8" x 2" clear field of view. The fiber optic was a numerical aperture (NA) = 1 plate with EMA manufactured by INCOM Inc. The screen was removable and could be replaced by other screens. TRIMAX 2, manufactured by 3M Corporation, is an approximately 50-micron-thick Gd_2O_2S screen and is similar to corresponding thickness Lanex-Fine fabricated by Kodak and Rarex-Be Fine by MCI Optronix. The use of silicon oil rather than microscope immersion oil, which is normally used to couple the fiber optic components, was required to keep from attacking the screen chemically and changing its properties.

We suggested the use of intagliated or filled-fiber-hole screens in our proposal. We feel such screens have numerous benefits over conventional settled screens since the light cannot spread in a lateral direction but is restricted to stay in one "hole". The light is restricted to the hole because of the internal reflections of the walls and in principal, these screens can be nearly as bright as a settled screen and yet maintain their resolution even for very thick layers. Our early attempts at fabricating such a screen were not successful. The screen was being deposited on etched fiber optic, plated with conventional 6-micron fibers. The problems of getting an even deposition or filling of 2-3 micron particles into a 6-micron hole are immense and the screens that were made were very nonuniform and thin.

²R. Ruchti, et al, IEEE Tran.Nuc. Sci. NS 30 #1, Feb. 83.

During the course of the program we became aware of a commercially available hollow glass-fiber material formed into plates. This material is similar to the structures used in microchannel plate intensifiers but much coarser. Samples were available with 45-50 micron ID glass fiber "holes" and with 60 micron center-to-center spacing.

It appeared that it would be much easier to fill holes 10 times larger than those we had tried initially to work with. The hole center spacing was, in fact, larger than ideal since it corresponded to a 7-8 lp/mm intrinsic limit but we decided to try to make a working intagliated screen. Since the holes penetrated all the way through this material, it had to be coupled to standard fiber optic plate for stability and light coupling. A diagram of the approach used is shown in Figure 2.2.2. The fiber hole plate was cut to an approximate thickness and polished on one surface. This surface was then resin bonded to a NA = 0.6 fiber optic plate as the backing. Spacers were cut to set the approximate desired thickness of screen and glued adjacent to the holes. The entire assembly was then polished until the holes were cut down to the size of the spacers. The structures fabricated in this way turned out to be 0.012" and 0.020" thick.

The screens were filled by settling Gd_2O_2S of about 2-3-micron mesh. No additional coating was put on the screens. The screens were mounted in aluminum fixtures similar to those used for the other screens and epoxied in. Because the scanner was not available when the screens were fabricated, they were only tested in a relative way. They were illuminated with X-rays and observed through a lead glass window. They appeared visually to be much brighter than the glass screens but did show some signs of unevenness especially near the edges. As time progressed, this nonuniformity seems to have grown on both screens and the light output diminished. This may be due to some degree of contamination of the uncoated screens and also to the holes separating from the fiber optic coupling plate. Nonetheless, the screens still perform with much more resolution than conventional deposited screens of corresponding thickness.

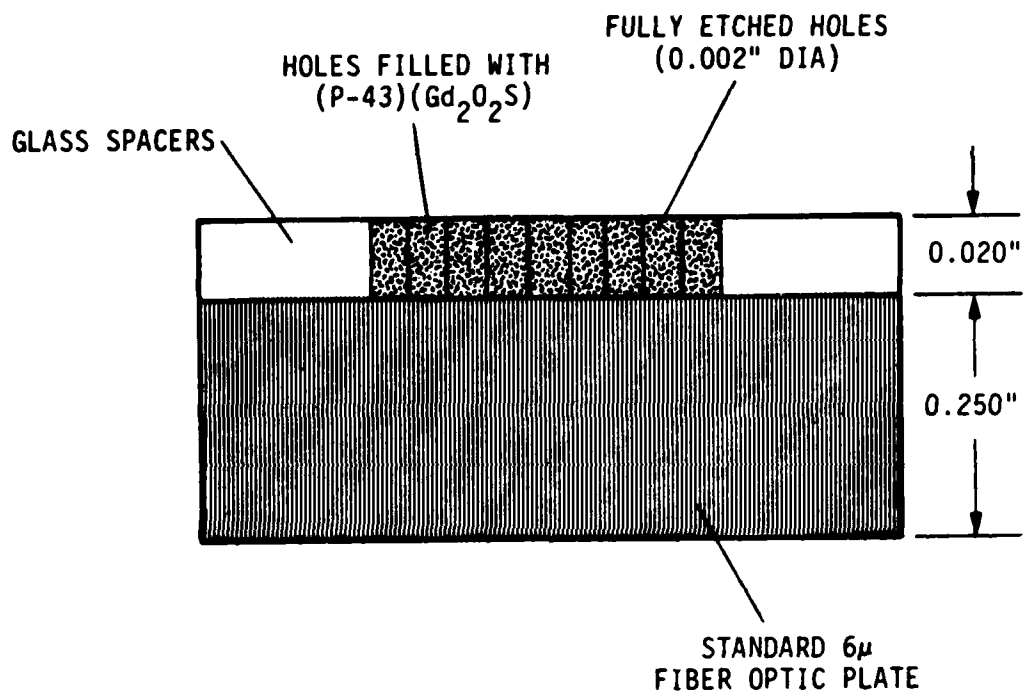


Figure 2.2.2 Construction Details of Intagliated Screens.

TABLE 2.1
CONVERSION SCREENS EVALUATED ON HIGH RESOLUTION RADIOGRAPHY PROGRAM

1. 2mm Terbium Doped Glass Fiber Optics
2. 5mm Terbium Doped Glass Fiber Optics
3. 10mm Terbium Doped Glass Fiber Optics
4. Gd_2O_2S (.005") on 5mm Terbium Doped Glass
5. 5mm Cerium Doped Glass Fiber Optic
6. Commercial High Resolution Medical Screen ($Gd_2O_2S + Y_2O_3$) 0.002" (TRIMAX 2)
7. 0.012" Intagliated Screen (60 Holes, Gd_2O_2S)
8. 0.020" Intagliated Screen (60 Holes, Gd_2O_2S)
9. $BiGeO_4$ Plate (2mm Thick Brightness Only)

A single crystal BiGeO_4 plate, 3 mm thick was also tested to provide a reference point and test the procedures. It could not be evaluated for MTF or used with the scanner because its thickness did not permit proximity focus coupling.

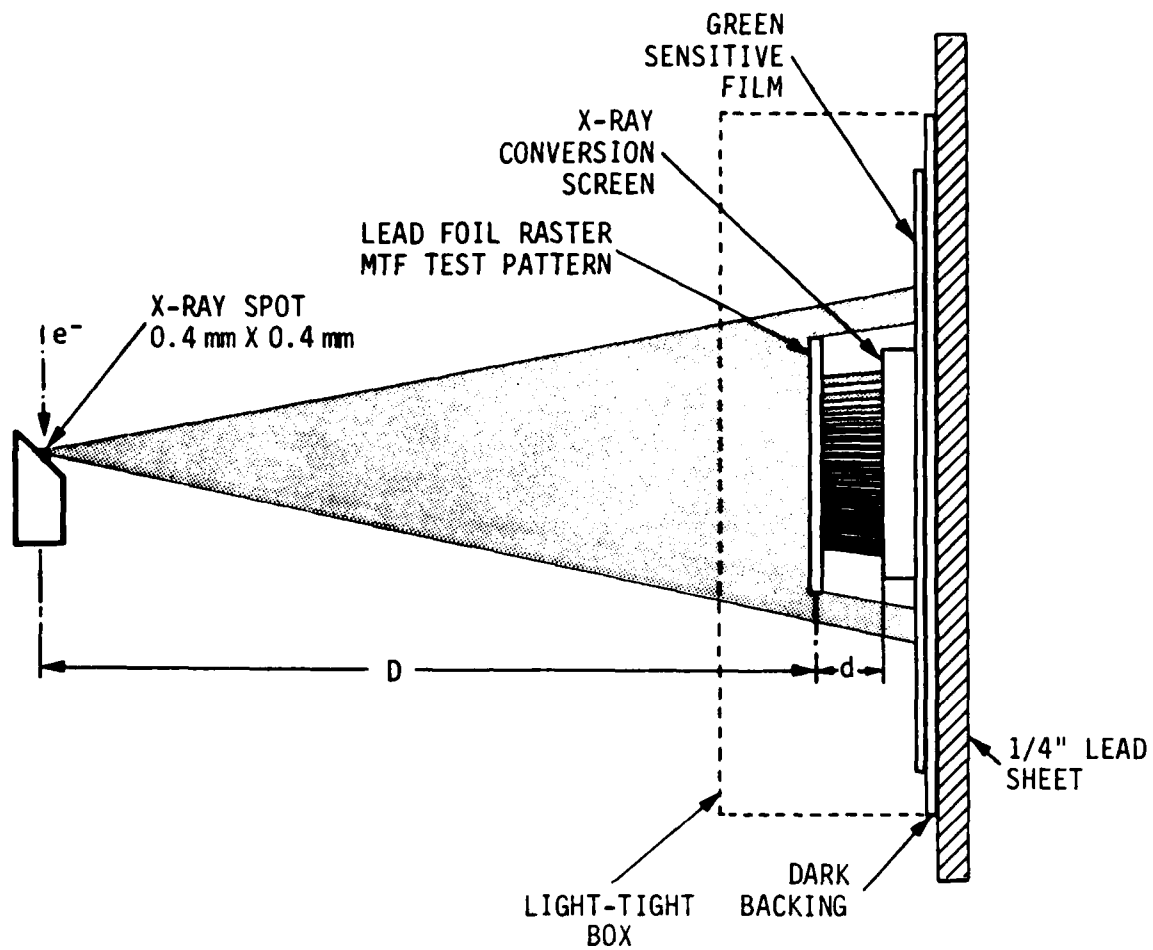
2.3 DIRECT DETERMINATION OF X-RAY CONVERSION SCREEN MODULATION TRANSFER FUNCTIONS

Modulation Transfer Functions (MTF's) of the X-ray to light conversion screens were determined independent of the rest of the line-scanner inspection system through the use of film and a microdensitometer. The characteristics of the film and microdensitometer were carefully divided out to give the MTF's of the conversion screens alone.

Green-light sensitive Kodak OG-1 X-ray film was exposed by the light generated from the screens under X-irradiation (see Figure 2.3.1). A lead foil raster burst test pattern was placed approximately 1/4" (the distance "d" in the figure) above the screens. The shadowgram, cast by the test pattern, was converted to light by the screens and recorded on the film in direct contact with the back of the fiber optic plates. The resolution test pattern used was a Nuclear Associates #07-553 constructed from a 0.05-mm lead foil raster sandwiched between plastic. The pattern was composed of sets of four line pairs each, varying from 0.5 to 10 line pairs per millimeter (lp/mm), and two line pairs at 0.25 lp/mm.

A Siefert Isovolt US-3 voltage generator with an AEG-Telefunken H-163 tube generated the X-ray flux. A constant potential of 55KV with a 1-mm Be filter was used for all of the screens. The tube head was kept normal to the surface at a distance D of 156cm from the test pattern and on a small spot size (0.4mm x 0.4mm) setting in order to ensure that geometric unsharpness was negligible. The current was 3mA and exposure times from 0.2 to 0.6 minutes. The exposure times were varied in accordance with the brightness of the particular screen so that a final film density in the same general range for all the screens would be produced.

During exposure and handling, the film and screens were contained in a light-tight card-board film box. The top of the box was essentially transparent to the incident X-rays. Lead pieces held the screens tightly against the film. A lead sheet was placed behind the box to help prevent back-scattered radiation from interfering with the measurements. The film was developed using standard techniques and 64⁰F developer.



SAIC-86RS-19

Figure 2.3.1 Direct Measurement of X-Ray Conversion Screen Modulation Transfer Functions.

A Joyce, Loebel, and Co. MKIII CS scanning microdensitometer was used to measure the film density variations. An example of the plots obtained and an X-ray of the test pattern can be seen in Figure 2.3.2. The microdensitometer is a chopped dual-beam instrument utilizing a calibrated optical grey wedge as the density reference. Neutral density filters are used to extend the range of the instrument. A slit whose effective width at the film was 18 microns was used in order to adequately sense the density fluctuations in the fine-line region of the plots. The length of the slit was set at 0.77 mm to help integrate out film grain noise and to pass enough light to keep the microdensitometer in a linear operating range. All plots were calibrated using a twenty-one step optical step-wedge. The darkest regions of the films reached an optical density of approximately 2.7.

Fog level for the Kodak OG-1 film was found to be negligible and would cancel out in any case. Therefore, a density-exposure relationship was assumed of the form:

$$D = \gamma \log E \quad 2.1$$

where D = optical density

E = exposure

Gamma of the film was measured for exposure to green light utilizing the optical step wedge and the definition of optical density. The measured gamma was 2.2 for the film type, density range, and developing procedure in question.

The peak to valley density variations of the plots were measured by hand. The line-pairs adjacent to groups of different spatial frequency and other obviously spurious data points were ignored. The MTF was taken to be the calculated exposure differences between the peaks and valley of the density plots at a particular spatial frequency divided by the difference at zero spatial frequency. Using equation 2.1, this difference ratio can be found to be:

$$MTF = \frac{\Delta 10^{\frac{D(f_s)}{\gamma}}}{\Delta 10^{\frac{D(f_0)}{\gamma}}} \quad 2.2$$

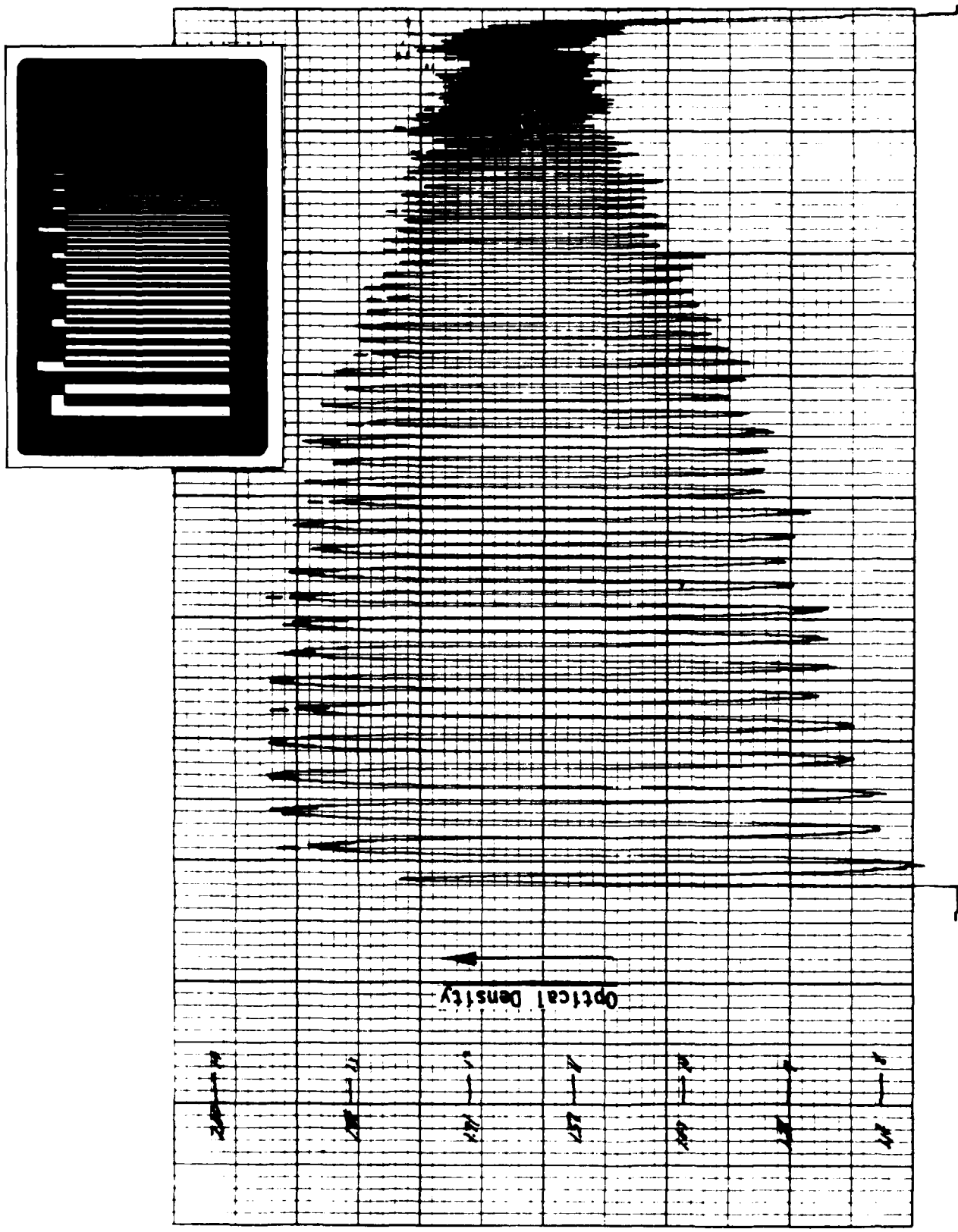


Figure 2.3.2 (a) Example Microdensitometer Plot (5 mm Terbium Glass Fiber Optic Scintillator, reduced scale).
 (b) X-Ray of Lead Foil Raster Test Pattern.

Technically, the square-wave response function above is called the Contrast Transfer Function (CTF). MTF is the sine-wave response function. It is extremely difficult to produce a sine-wave X-ray test pattern, so the CTF is usually measured instead. The mathematical relationships between the functions are:

$$MTF = \frac{\pi}{4} \left[CTF(f) + \frac{CTF(3f)}{3} - \frac{CTF(5f)}{5} + \frac{CTF(7f)}{7} \dots \right] \quad 2.3$$

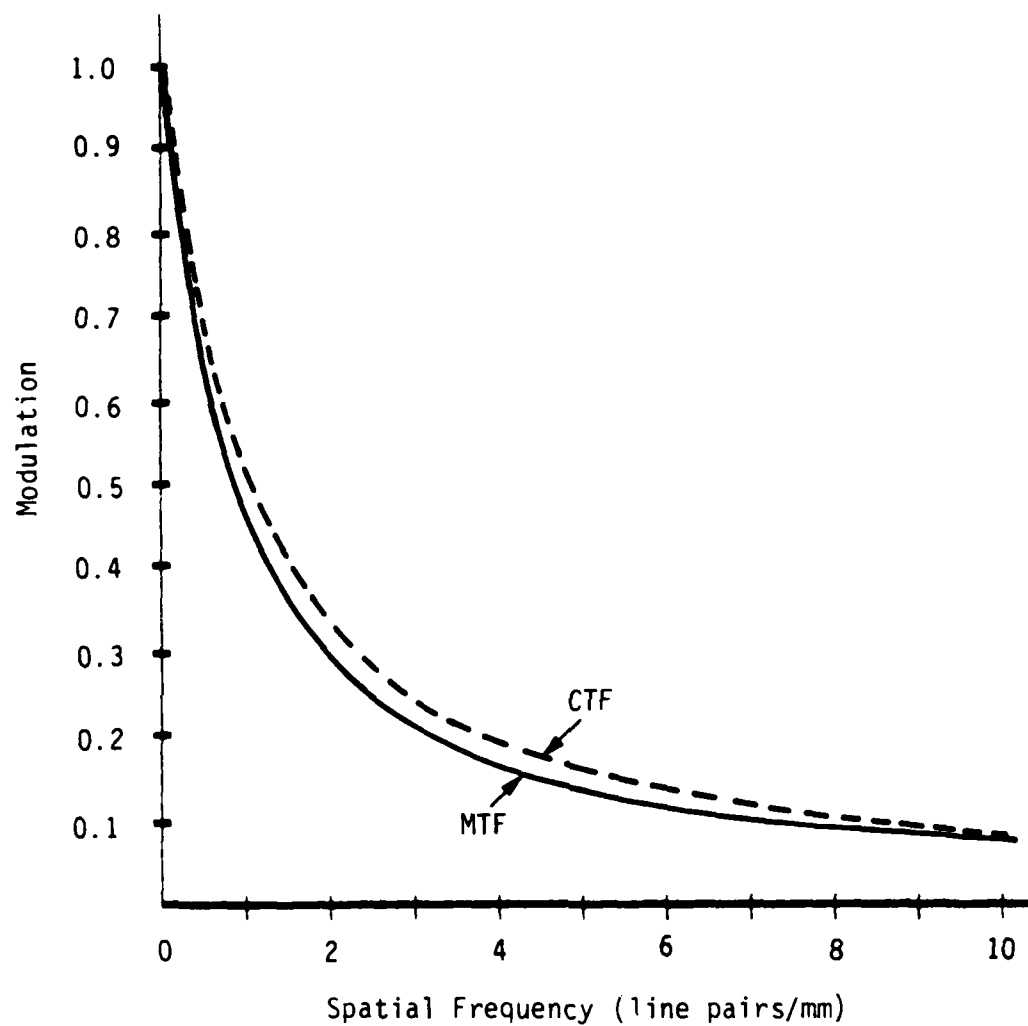
$$CTF = \frac{4}{\pi} \left[MTF(f) - \frac{MTF(3f)}{3} + \frac{MTF(5f)}{5} - \frac{MTF(7f)}{7} \dots \right] \quad 2.4$$

Figure 2.3.3 shows that MTF and CTF are very similar functions and can essentially be equated when experimental errors are taken into account (and if many MTF curves are not to be cascaded together).

The MTF's obtained from the plots using equation 2.2 are not the MTF's for the screens, but for the film-screen-microdensitometer combinations. Figure 2.3.4 shows the MTF for the film and test pattern alone exposed with X-rays. The geometry is the same as in the cases with conversion screens. The nearly flat response shows that the geometry and microdensitometer settings are not unduly affecting the measurement. But the response of the film to light was found to be a different matter. To obtain the response the test pattern was placed on an electroluminescent screen. Sources of stray light were shielded or masked off. The image of the back-lit test pattern was imaged 1 to 1 onto the back-plane of a bellows camera using a high resolution lens. A small lens aperture was used to obtain a large depth of field. A cut-film holder enabled this setup to expose the Kodak OG-1 film. A MTF plot for the film-microdensitometer combination is shown in Figure 2.3.5.

The MTF for the film was then fit to a function of the form:

$$MTF_{film} = A + (1-A)(1+bf^n)^{-1} \quad 2.5$$



SAIC-86RS-16

Figure 2.3.3 Comparison Between MTF and CTF for Function of the form $MTF = \left[1 + \left(\frac{f}{c} \right)^n \right]^{-1}$ $c = 0.8, n = 1.0$.

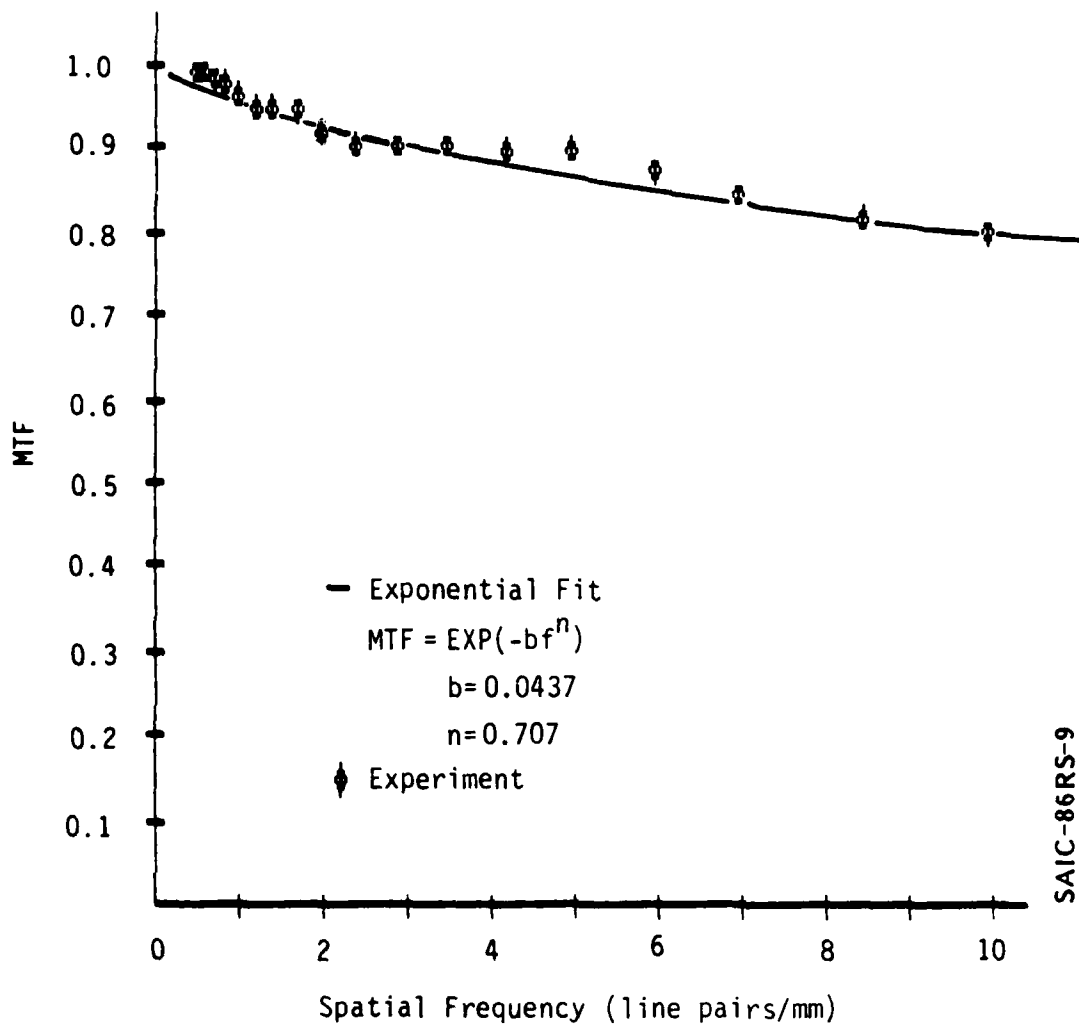
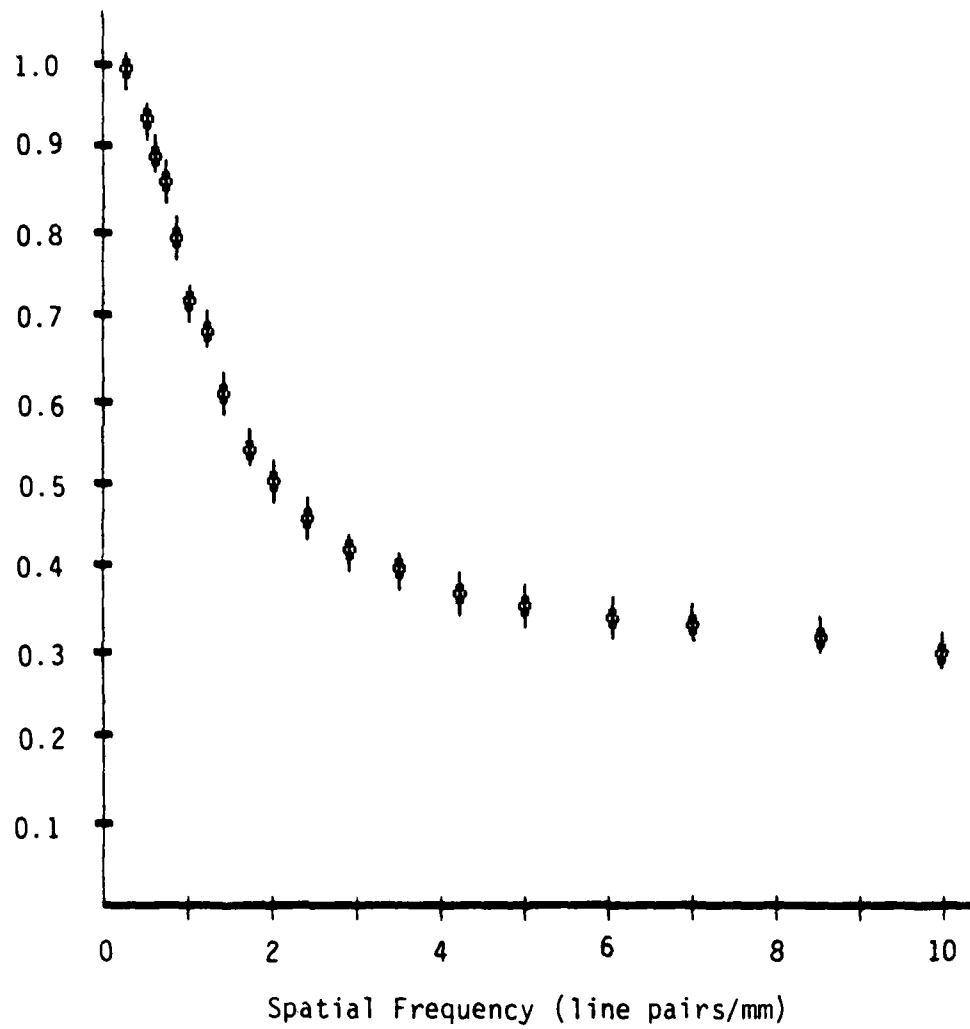


Figure 2.3.4 Modulation Transfer Function of Kodak 0G-1 Film Exposed with X-Rays.



SAIC-86RS-17

Figure 2.3.5 Modulation Transfer Function of Kodak OG-1 Film Exposed with Light.

The need for the additive term in the functional fit and the rapid fall of the MTF can be understood by realizing that the film has a front and back emulsion. The front emulsion in contact with the fiber optic plates would exhibit a relatively high MTF when compared to the back emulsion. The modulation for the entire film would be the separate modulations of the two emulsions added together.

The MTF's for the screens can be obtained by dividing the film-screen combination MTF's by the MTF for the film alone. The results are shown in Figures 2.3.6 through 2.3.12. The data are fit to either an exponential or a reciprocal power law function:

$$\text{exponential MTF} = \text{EXP} - \left(\frac{f}{f_c} \right)^n, \quad f_c = \frac{1}{e} \text{ point} \quad 2.6$$

$$\text{reciprocal power law MTF} = \left[1 + \left(\frac{f}{f_{1/2}} \right)^n \right]^{-1}, \quad f_{1/2} = 1/2 \text{ point} \quad 2.7$$

These similar functional fits have been reported in the literature as being useful for the type of processes at hand^{3,4}. Some of the plots do not fit either model well, though. This inability to fit the data is probably due to the multi-process nature of the true MTF's. One should not expect them all to follow a simple analytical model. In this case, the fits were developed only to be used for modeling in the spatial frequency range covered and not for extrapolation to very high spatial frequencies.

The MTF for higher frequencies for the 2 mm terbium glass fiber optic screen is anomalously low as compared to the 5- and 10-mm screens. We do not understand at this time if this lower response is due to incomplete self-absorption of large angle photons, improper fabrication, or some other reason.

³Engstrom, R.W., ed: RCA Electro-Optics Handbook, RCA Commercial Engineering, Harrison, NJ, 1974.

⁴Notea, A., NDT International. Vol 16., No. 5 October 1983

The GOS deposited on fiber optics and the intagliated screens also exhibit lower than expected MTF's. We believe that this discrepancy is due to non-optimal scintillator deposition processes used on these prototypes and/or possible unexpected damage due to humidity. These problems can be easily remedied.

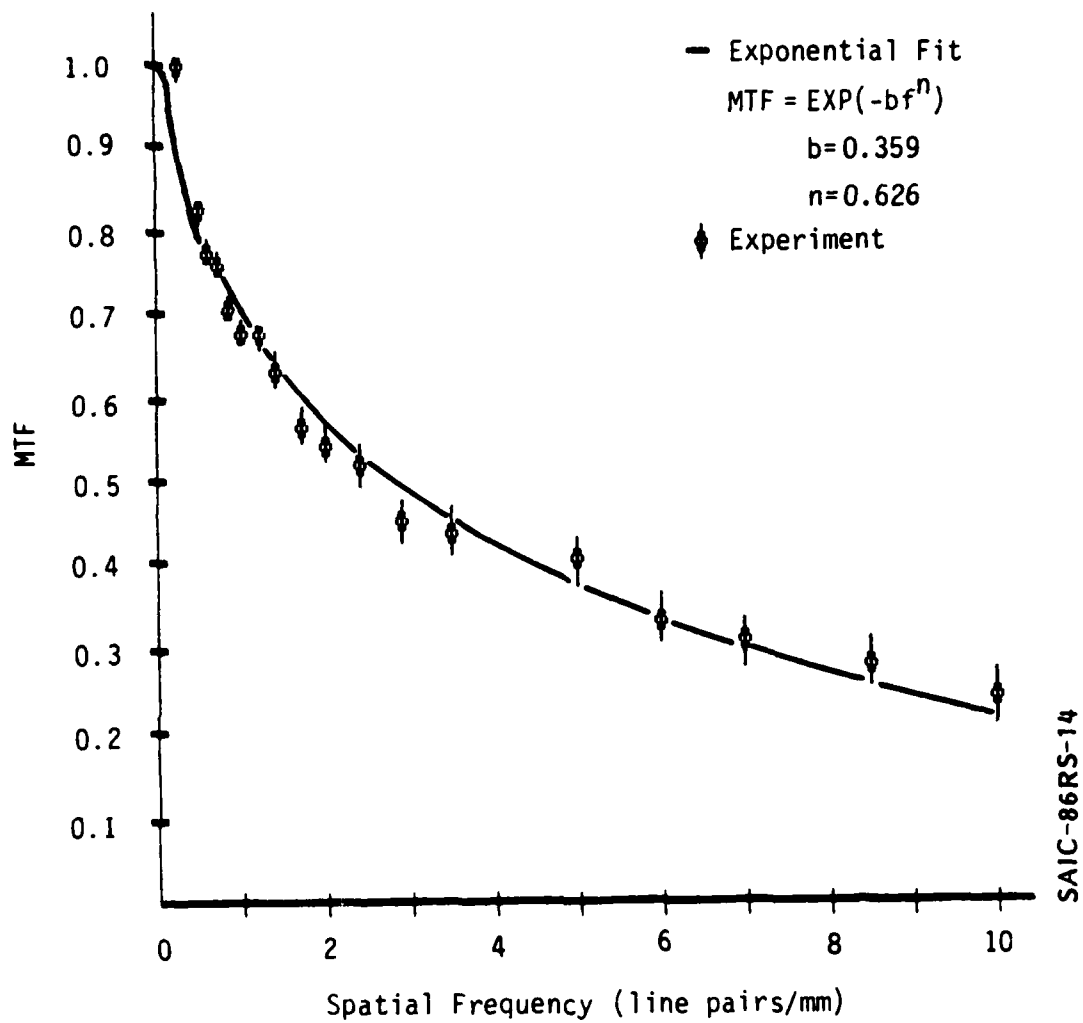
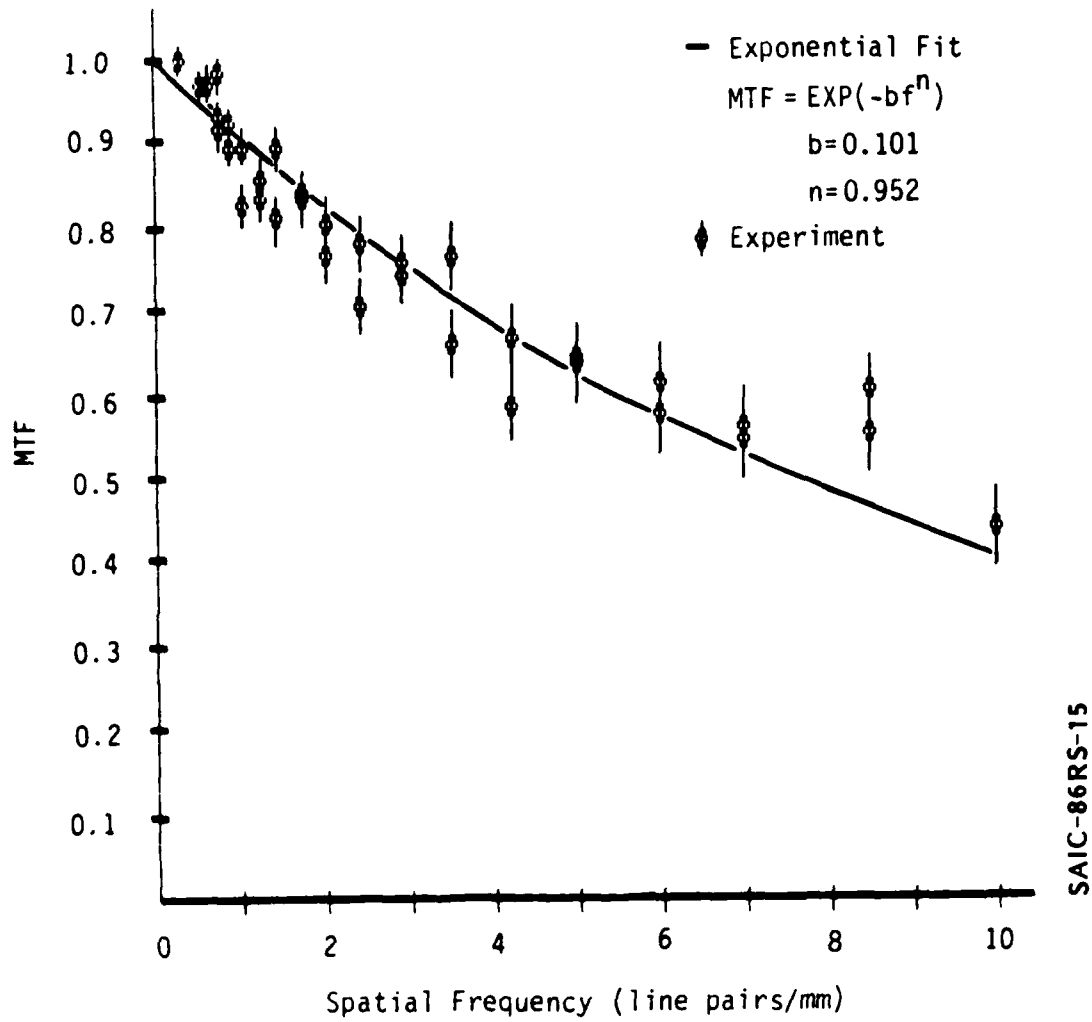
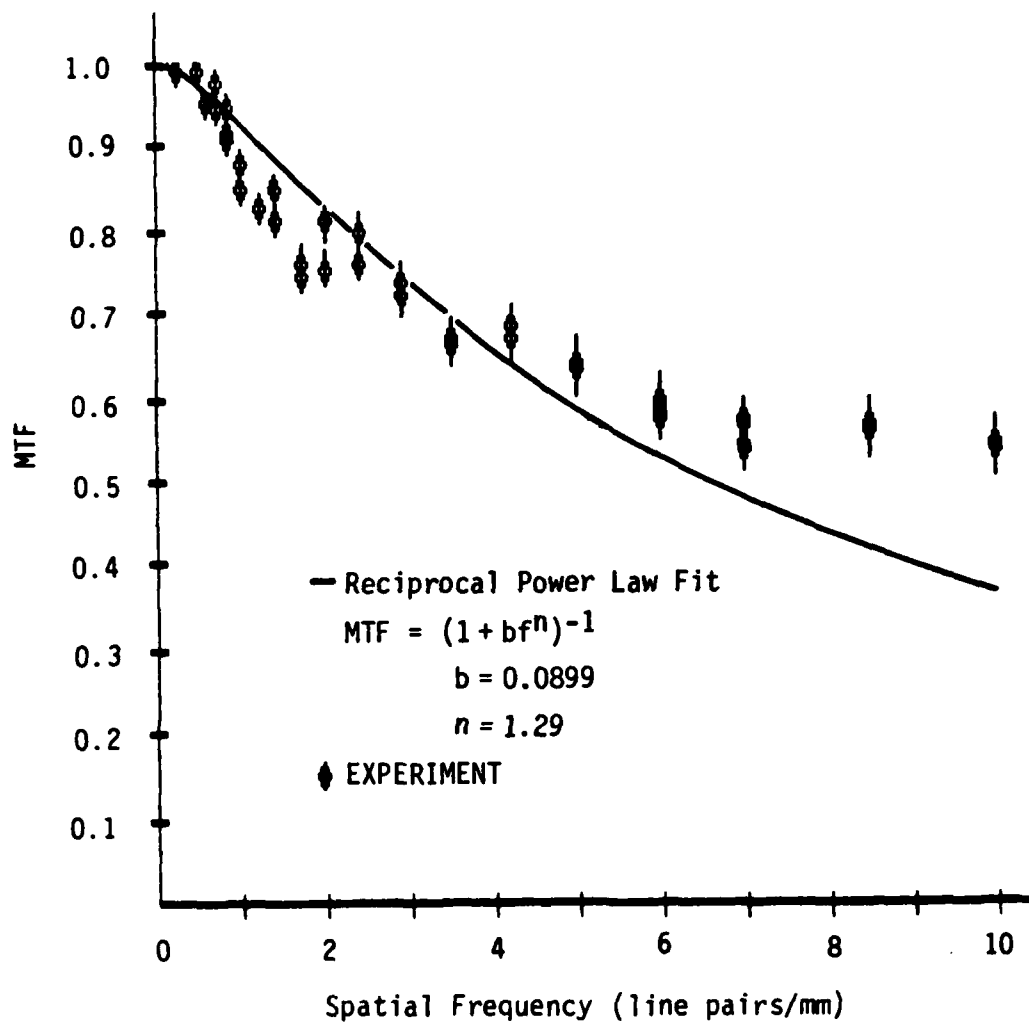


Figure 2.3.6 2mm Terbium Glass Fiber Optic Scintillator Modulation Transfer Function.



SAIC-86RS-15

Figure 2.3.7 5mm Terbium Glass Fiber Optic Scintillator Modulation Transfer Function.



SAIC-86RS-18

Figure 2.3.8 10mm Terbium Glass Fiber Optic Scintillator Modulation Transfer Function.

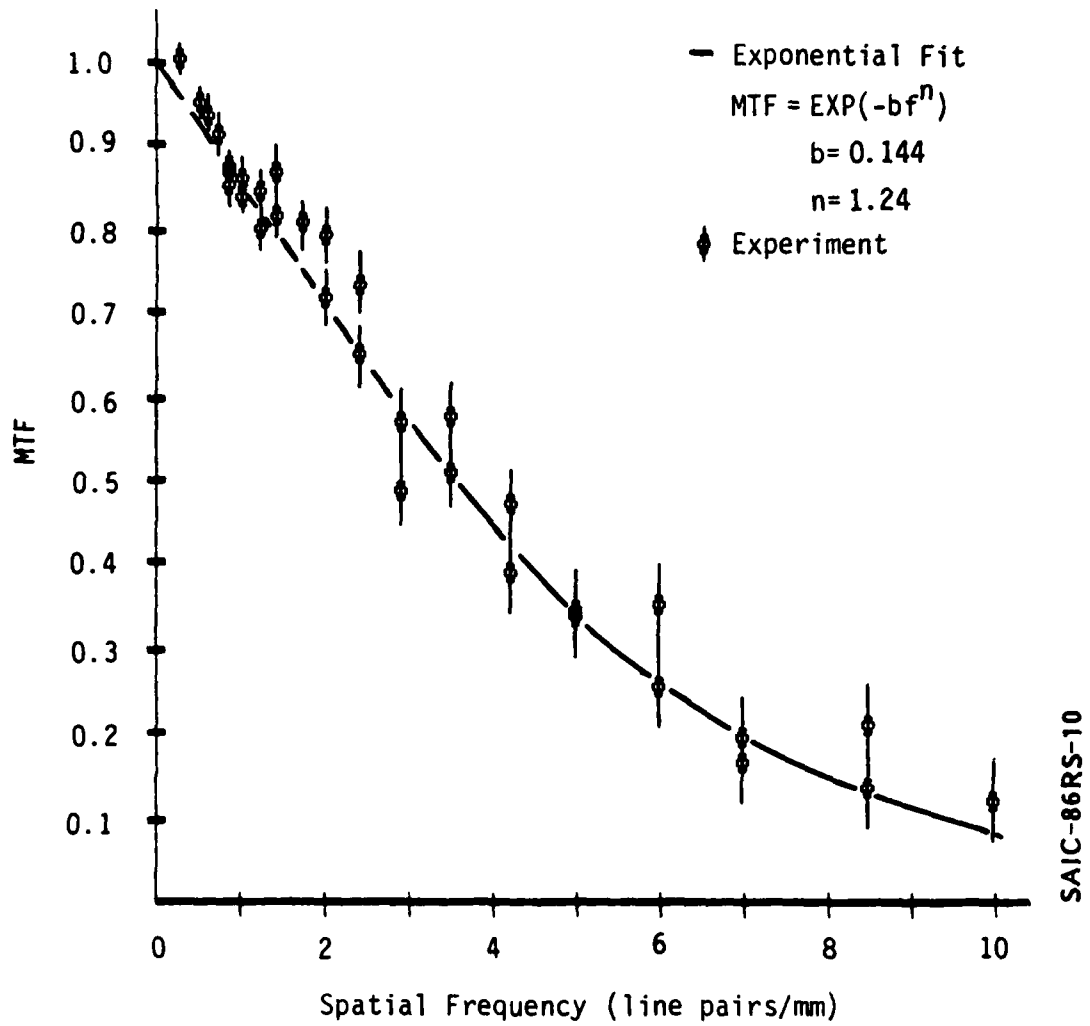
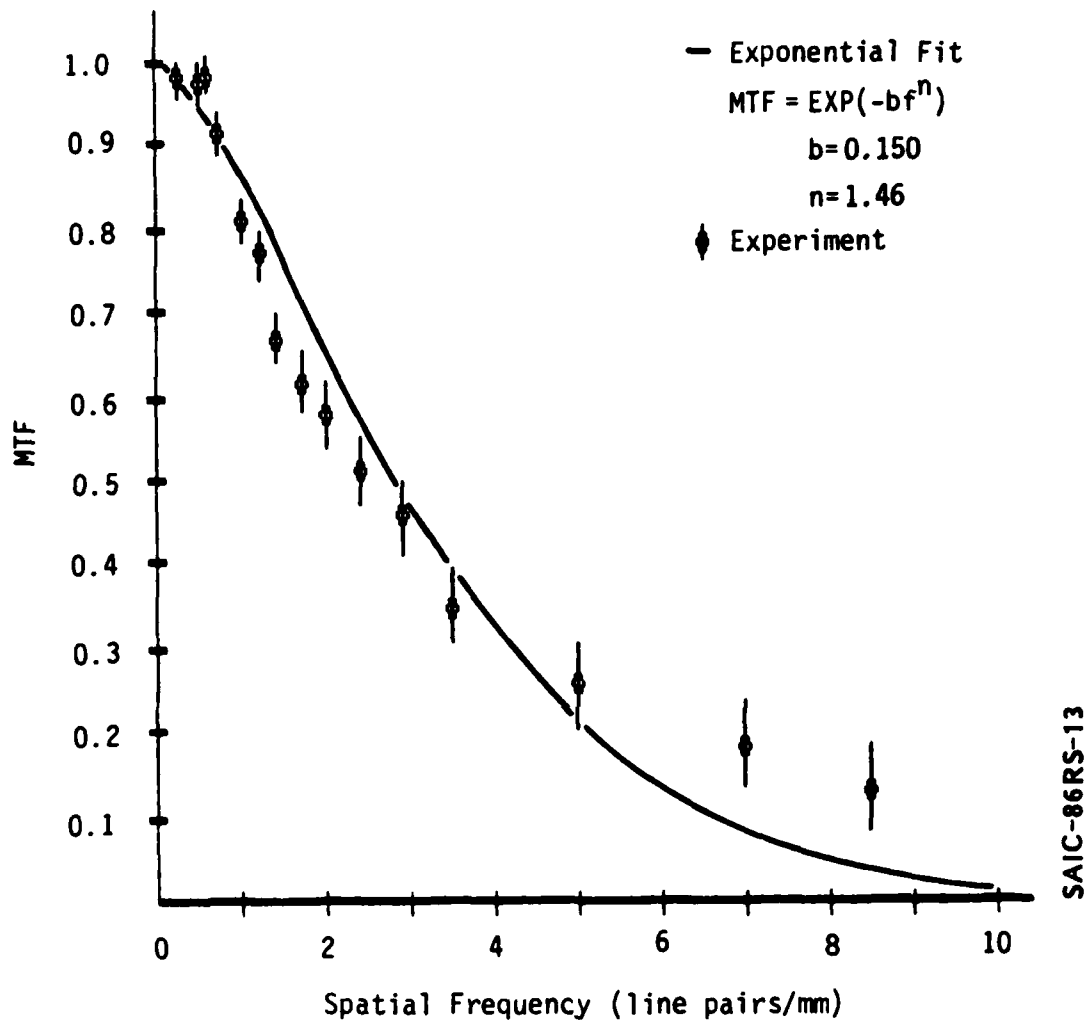


Figure 2.3.9 Trimax Screen in Contact with Fiber Optic Coupler Modulation Transfer Function.



SAIC-86RS-13

Figure 2.3.10 GOS Deposited on 5mm Fiber Optic Scintillator Modulator Transfer Function.

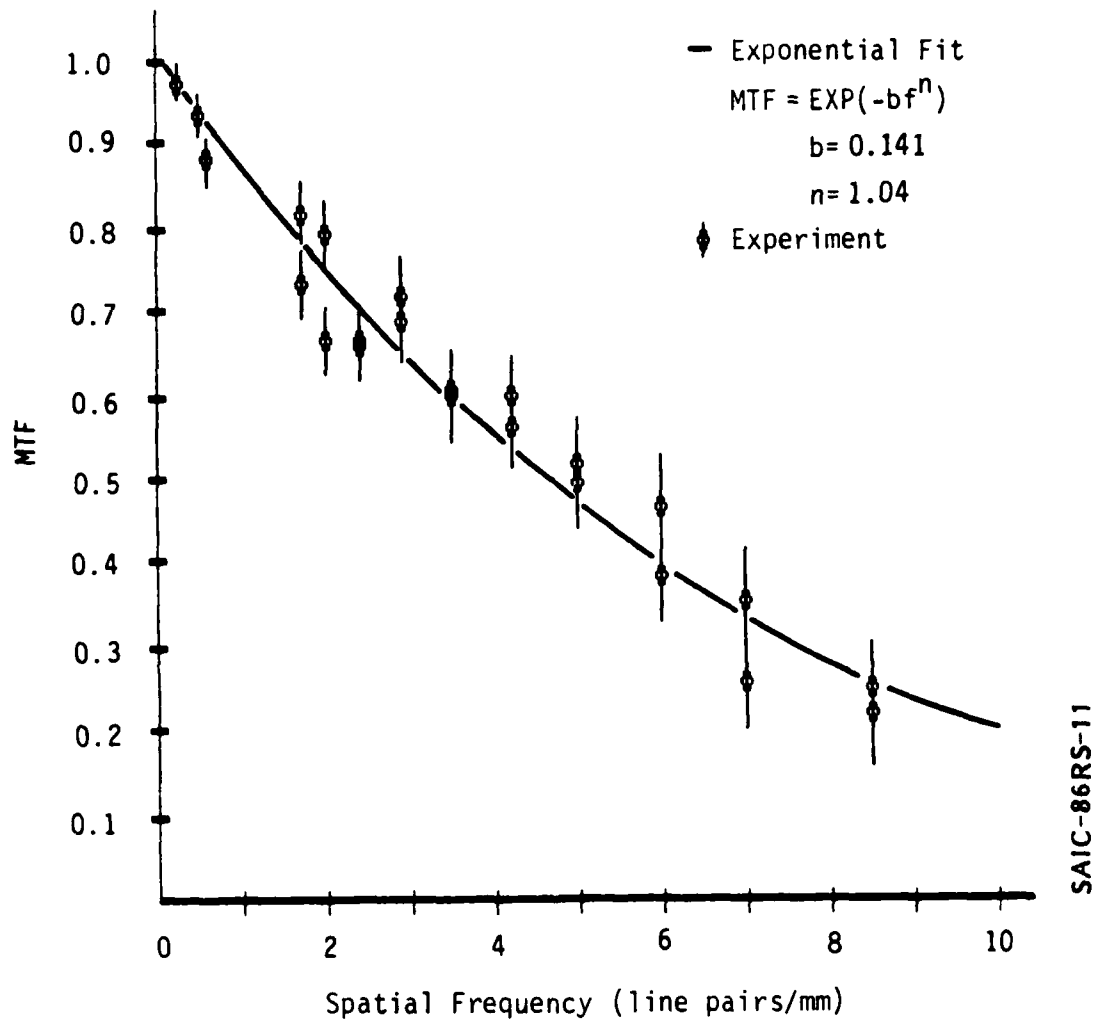


Figure 2.3.11 0.012" Intagliated Screen Modulation Transfer Function.

SAIC-86RS-11

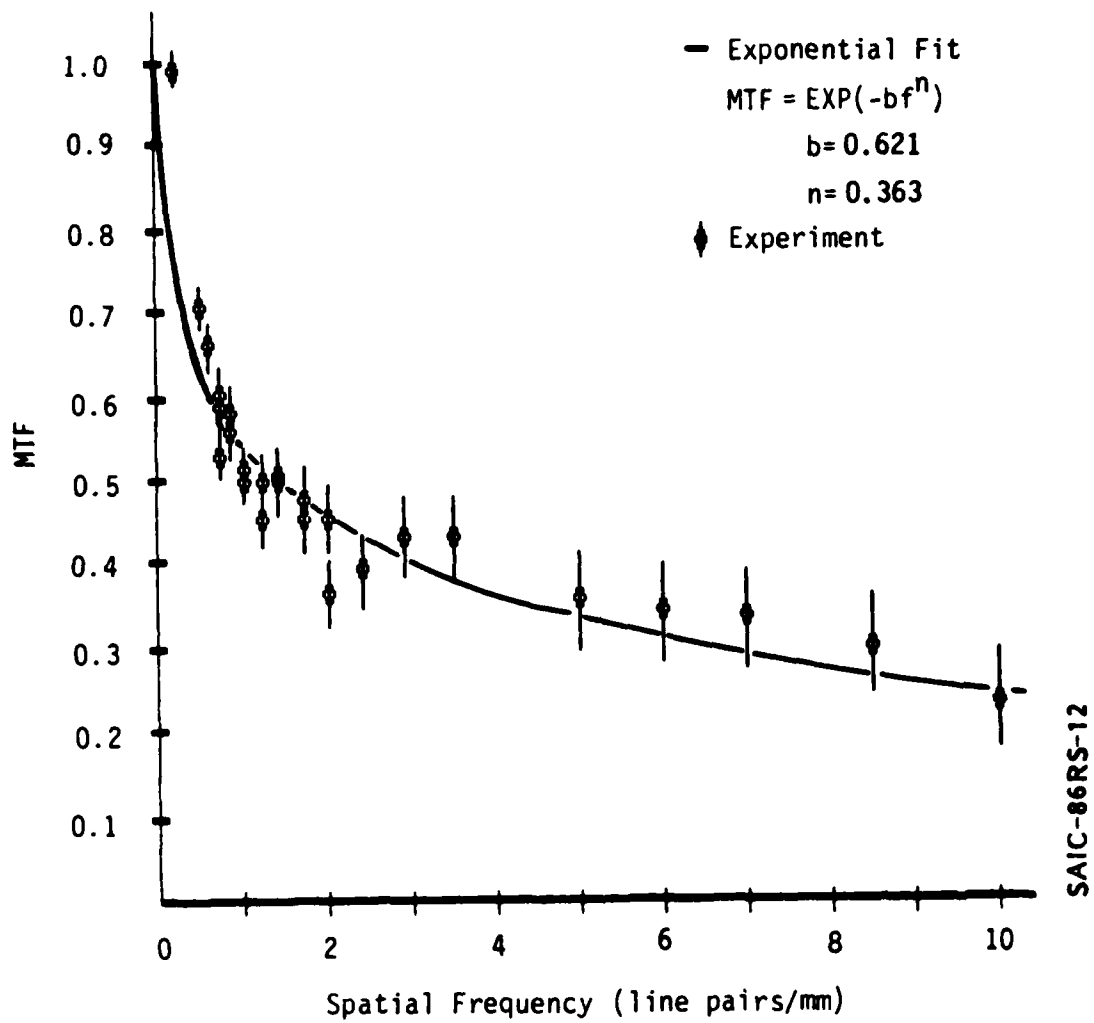


Figure 2.3.12 0.020" Intagliated Screen Modulation Transfer Function.

SAIC-86RS-12

2.4 SPECTRAL OUTPUT DISTRIBUTION

The spectral distribution of light from all screens was measured under direct X-ray excitation. The experimental apparatus is shown schematically in Figure 2.4.1. A Perkin Elmer 1/2m monochromator with a calibrated slit width was set up using an RCA 4516 PMT at the detector plane. The system was calibrated directing in watts per spectral interval using a stable light source and a previously calibrated monochromator as a source. The power at each point was compared to the response of an EMI photo diode whose calibration is NBS traceable.

A curve of the monochromators response is shown in Figure 2.4.2. A second 4516 photomultiplier was also calibrated for use in the relative brightness measurements. Its response is shown in Figure 2.4.3.

The monochromator was transported back to the radiation cell with the same 1 x 10mm slit in place. The fixturing around the slit was designed to support each test screen in close proximity to the slit. X-rays were allowed to strike the entire screen while the monochromator viewed the light from a 1 x 10mm area in the center. The output of the monochromator was then recorded on a chart recorder while the drum was remotely advanced. The resulting distribution for each curve was recorded as a function of drum position and this data fed into the computer. Each point was corrected for monochromator response and the results are plotted as relative power output vs wavelength. Because of the detectors diminished response for longer wavelengths results are only taken up to 620nm.

The spectral distribution results for the Terbium Doped Glass are shown in Figure 2.4.4. It shows a strong double peak near 550nm with lesser peaks on either side. The broad distribution near 620nm may be over emphasized due to the monochromator rapidly changing response. This spectra is in sharp distinction from that of the Cerium based glass shown in Figure 2.4.5 which is a single broad peak with a maximum near 400nm. This wavelength is almost ideally matched for most typical intensifier photocathodes and matches film very well. It's overlap with a typical semiconductor response is poorer and probably would not be a good match for direct coupling with a silicon diode.

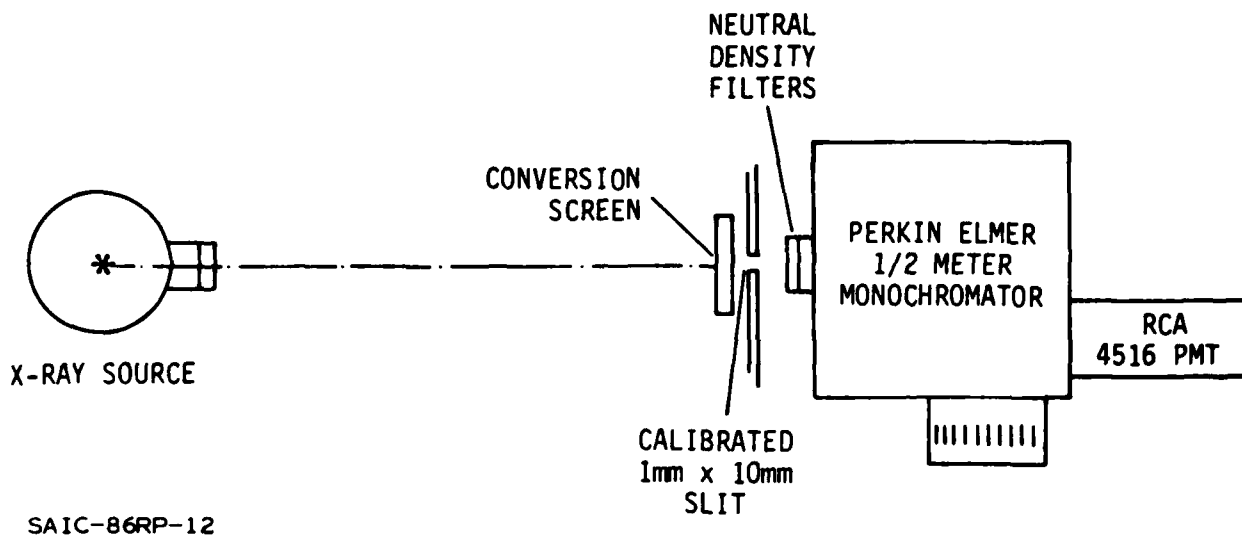


Figure 2.4.1 Experimental Arrangement to measure Optical Spectral Output of Conversion Screens.

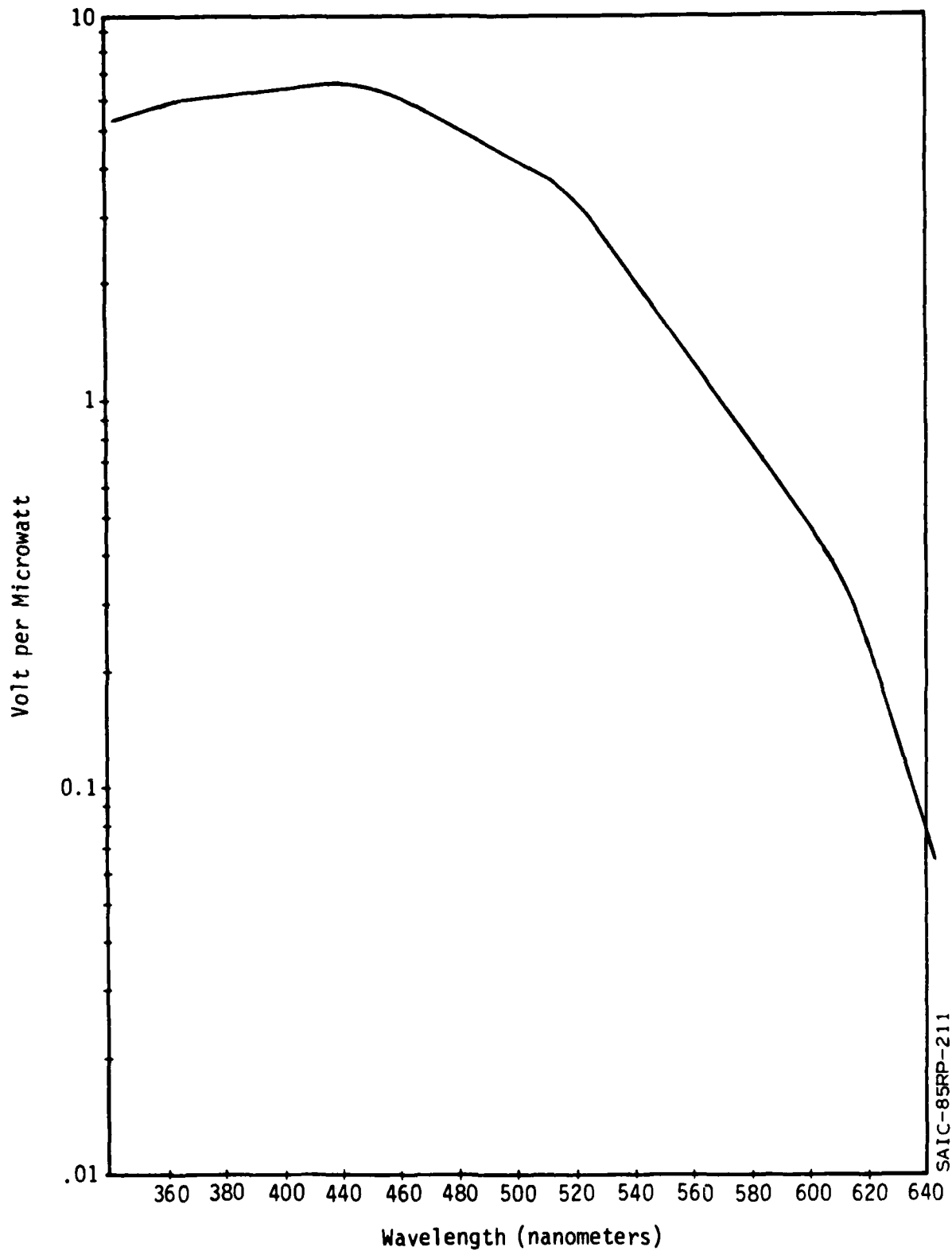


Figure 2.4.2 Calibration Response of Perkin Elmer Monochromator and PMT Sensor. Used to measure Spectral Characteristic of Conversion Screens.

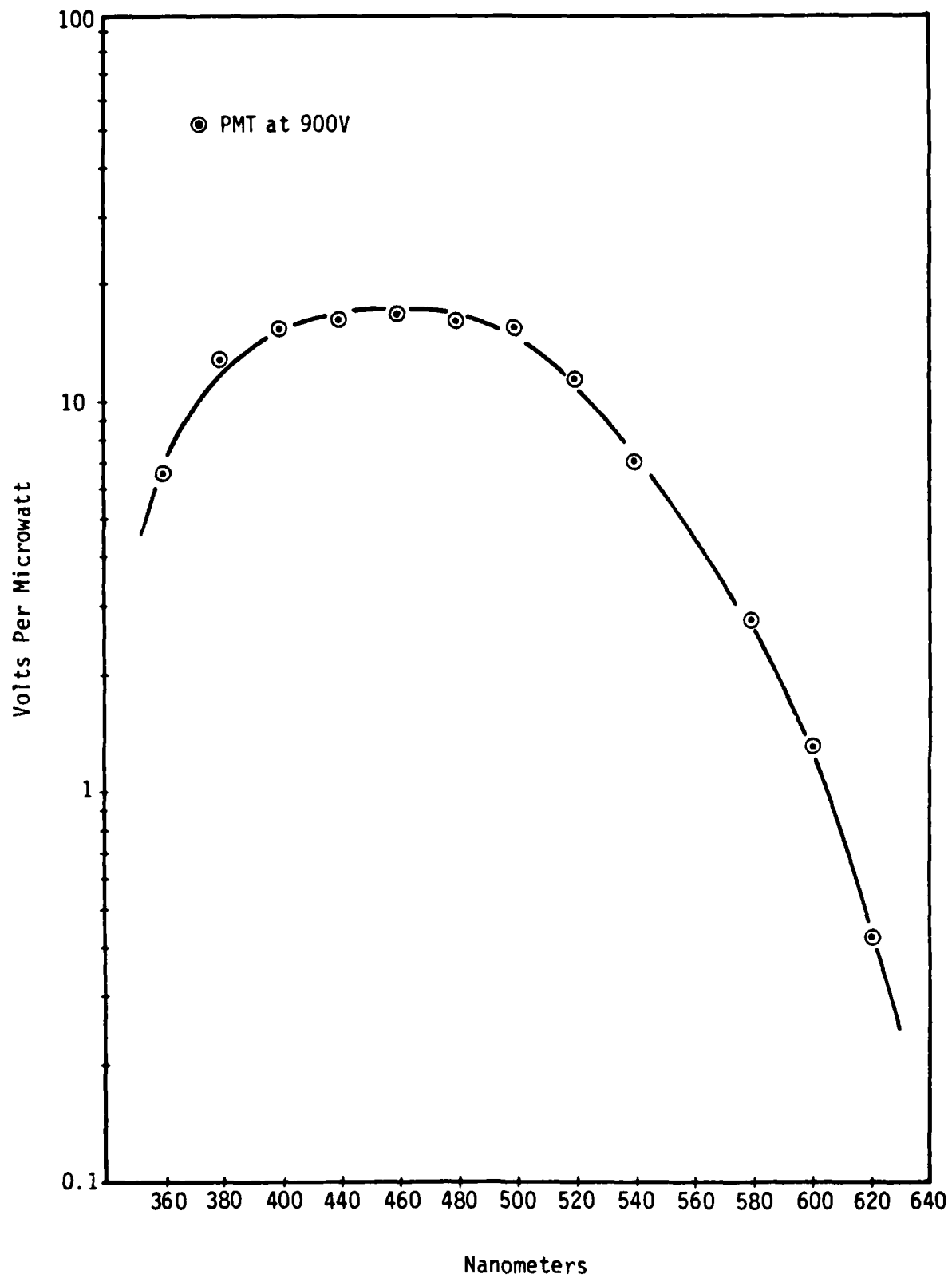


Figure 2.4.3 Response of Photometer PMT used to Measure Output Radiance of Conversion Screen.

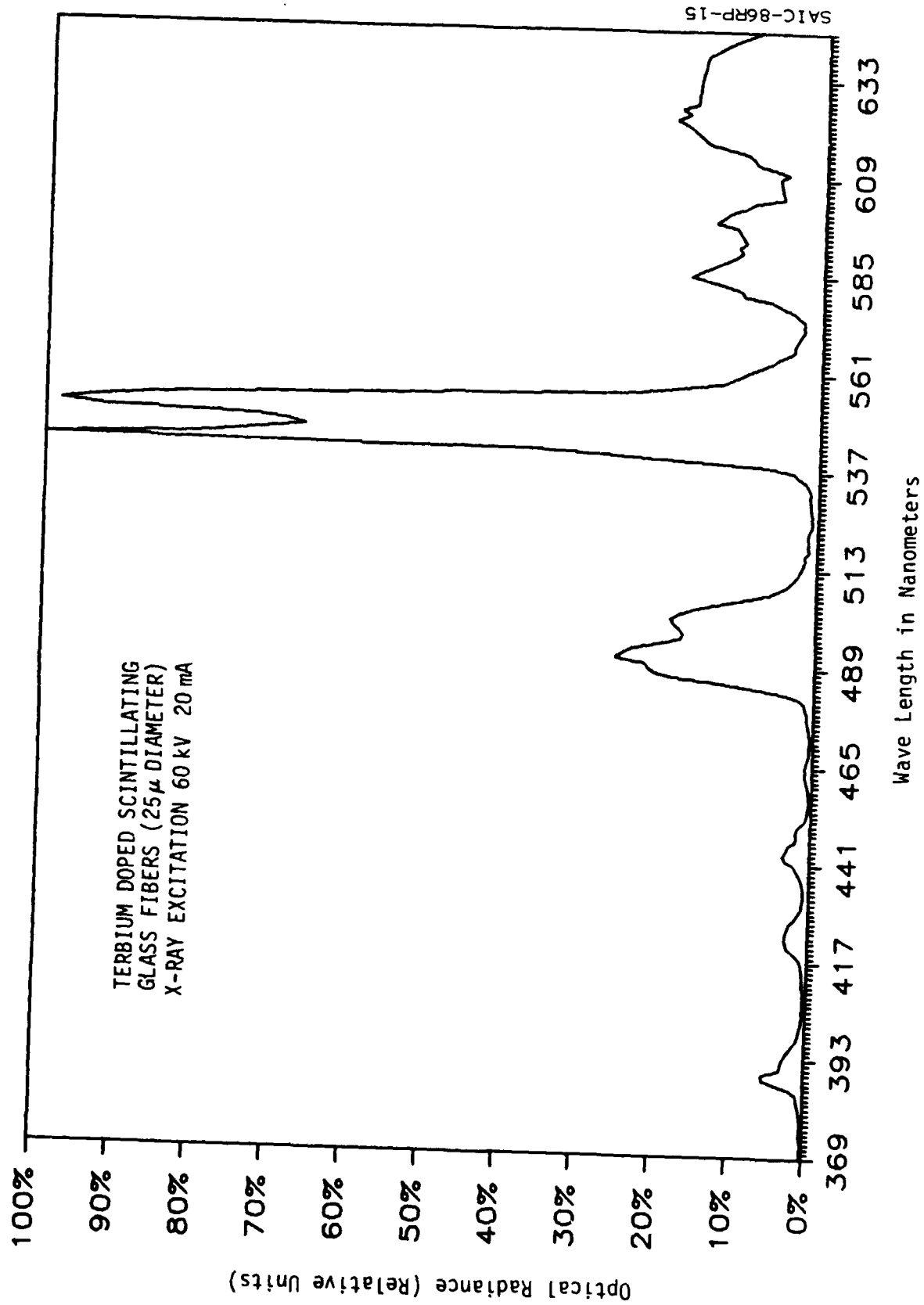
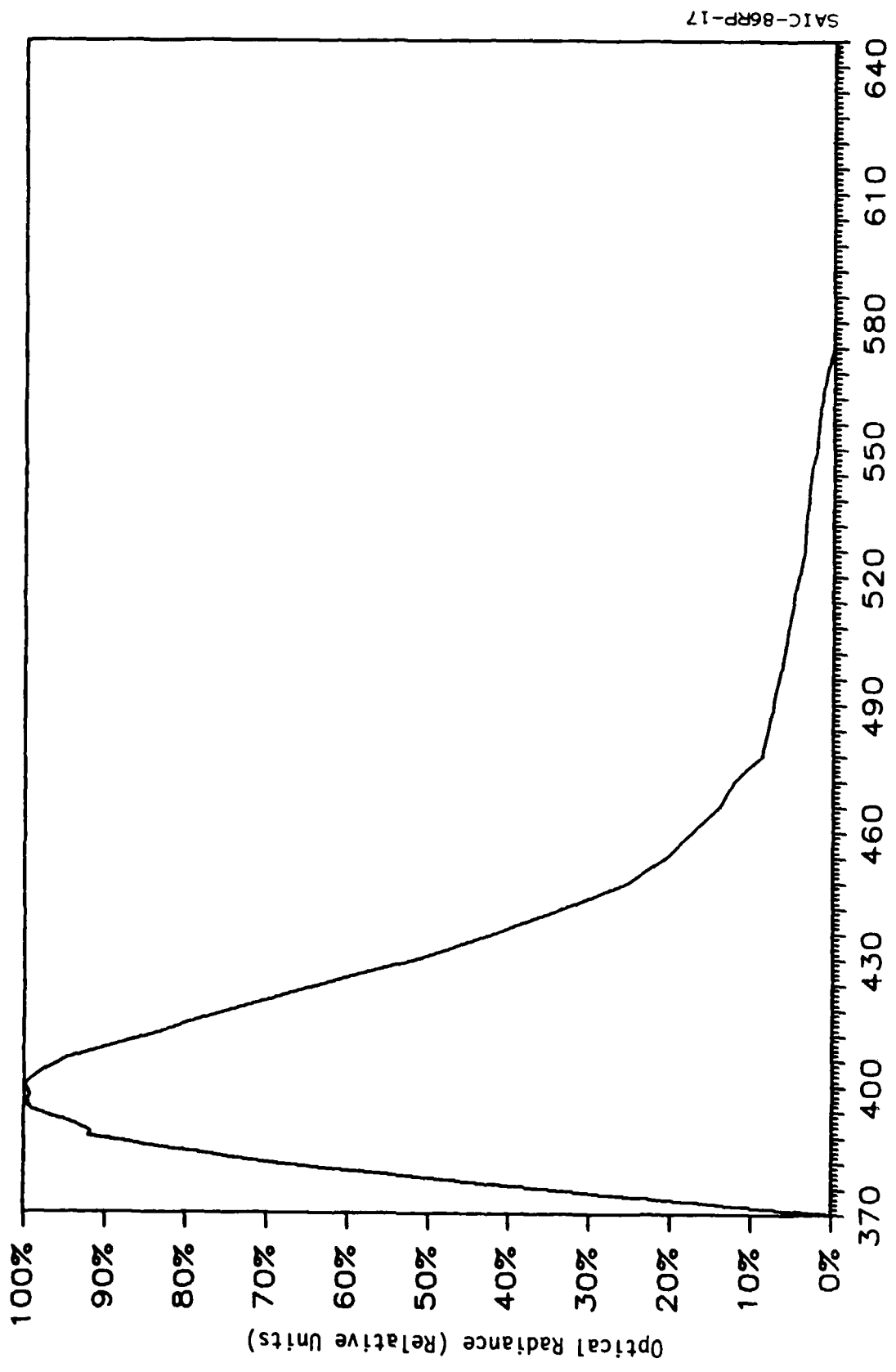


Figure 2.4.4 Spectral Response for Terbium Doped Glass.



SAIC-86RP-17

Wave Length in Nanometers
 Figure 2.4.5 Spectral Shape of Cerium Doped Glass Fiber
 Optic (5mm) 60 kV X-Ray Excitation.

The Trimax and intagliated screens were both thought to be pure Gd_2O_2S . From their spectra both seem to have Y_2O_2S mixed in to extend the blue response. The interesting thing is that the relative concentration seems to be lower in the Trimax 2 spectrum shown in Figure 2.4.6 than in Figure 2.4.7 which represents the intagliated output.

The terbium glass with overcoating shows a complex mixture of the two phosphors. At the 60 KV level the spectra in Figure 2.4.8 was taken, it appears dominated by the overcoat phosphor. A similar spectra taken at 300KV would show more influence of the terbium glass due to its greater efficiency at high energies.

The spectrum shown in Figure 2.4.9 is from $BiGeO_4$. This is a wide distribution typical of "intrinsic" scintillators. The data on this scintillator matches the published data for $BiGeO_4$.

Since all data are plotted as relative spectra, the figures can not quantitatively be compared with each other. This is done with a direct measurement discussed in the following section.

There has been increased interest in using these screens directly on solid state sensors. In order to estimate the degree of matching, one must calculate the product of the screen output spectrum with the spectral response of the detector. A typical curve for a self-scanned silicon array (Reticon Type S) is shown in Figure 2.4.10. This curve is broadly distributed with a peak near 800 nm. The use of fiber optics tends to reduce the absolute sensitivity and causes a sharp cutoff for wavelengths below 400 nm. This type of sensor is a good match for the GOS or Terbium doped glass and is less satisfactory with the blue scintillators such as $BiGeO_4$.

Generally at the smaller pixel sizes required for high resolution, direct coupling to a silicon detector produces too small a signal and some type of light amplification is required. For this reason, the typical cathode response shown in Figure 2.4-3 is more typical of the spectral sensitivity that must be matched by the converter screen. It is this type of cathode that has been used throughout the actual application shown in this report.

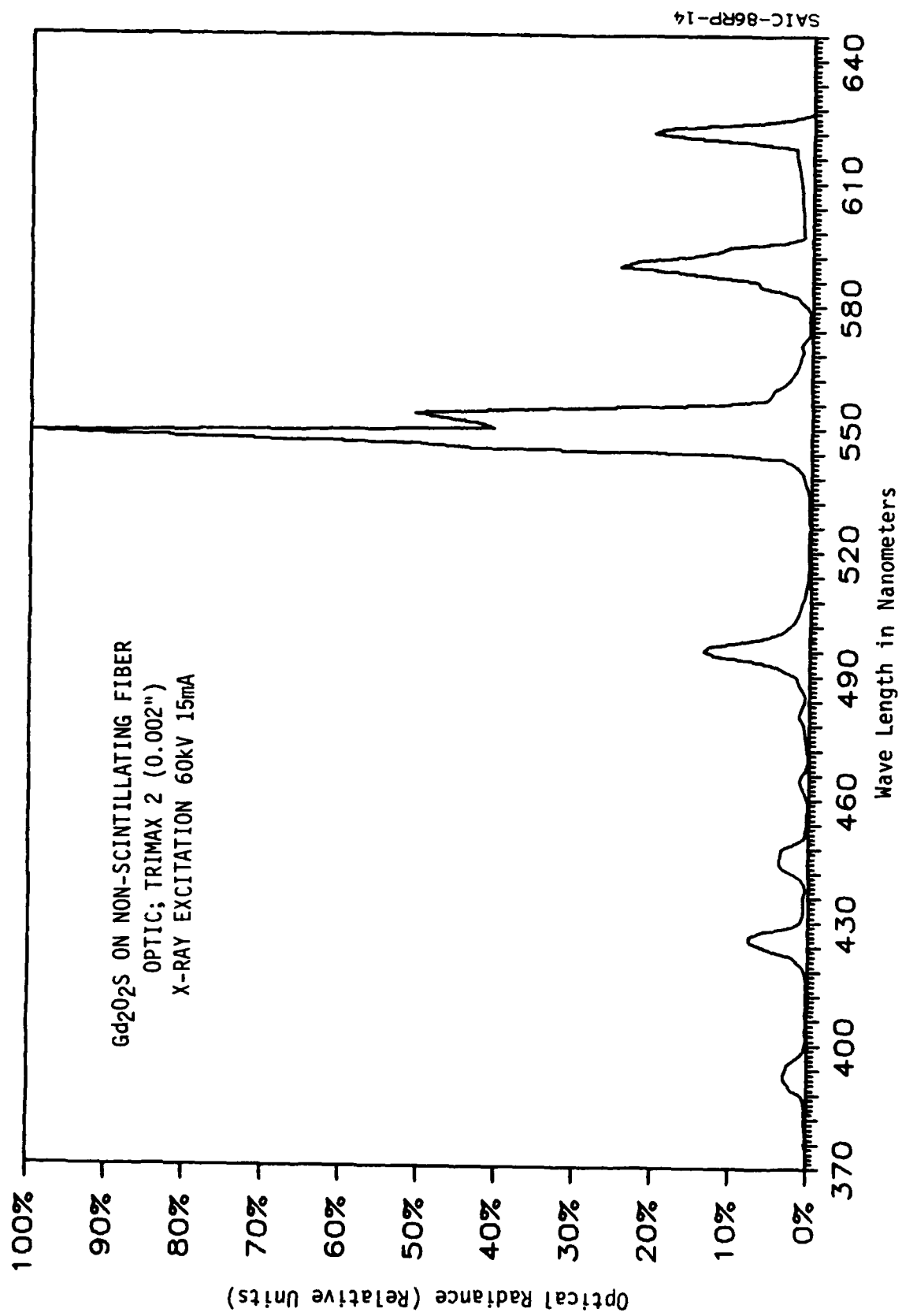


Figure 2.4.6 Spectral Response for Gd₂O₂S on Non-Scintillating Fiber Optics.

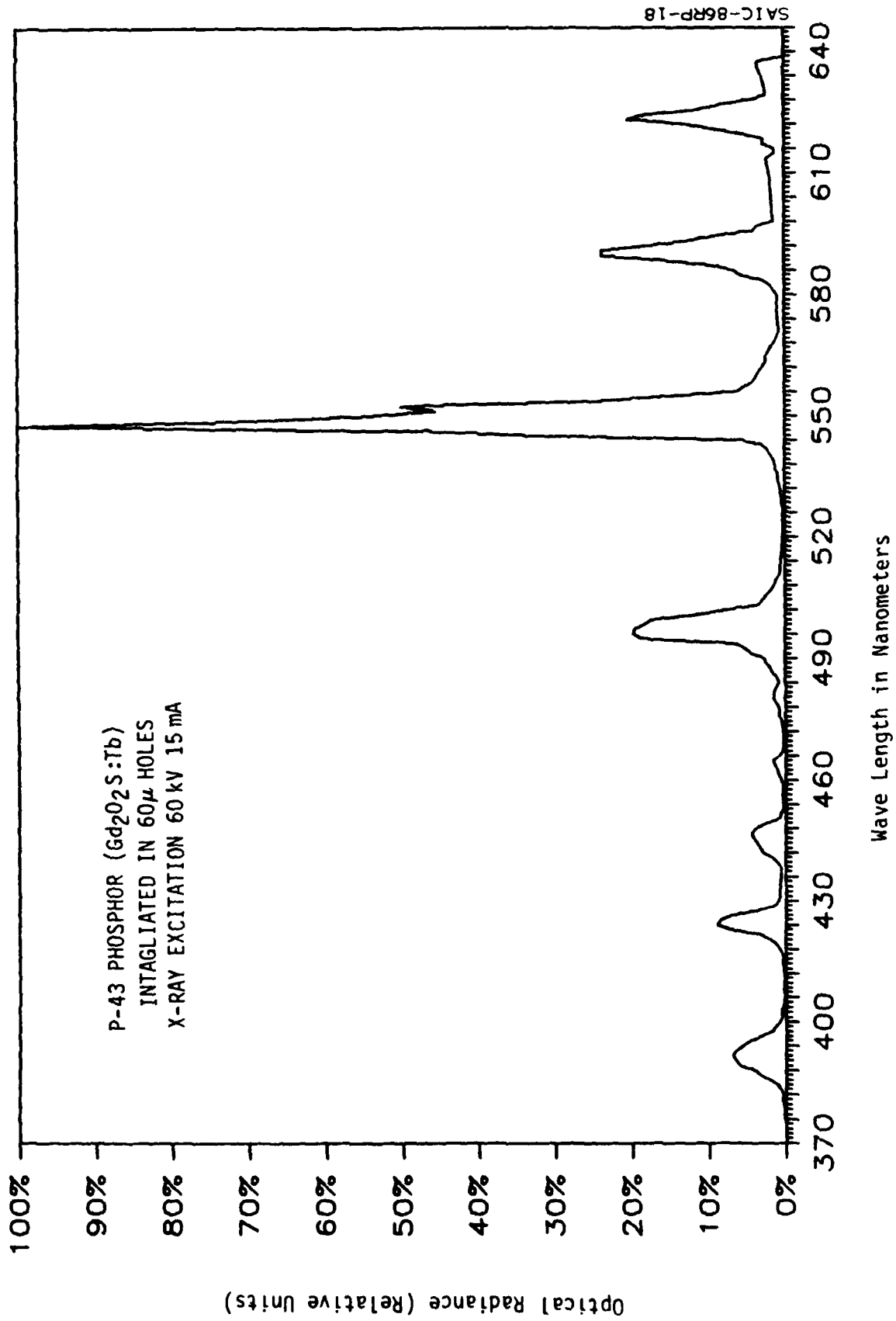


Figure 2.4.7 Spectral Response for Intagliated Gd_2O_2S Screens.

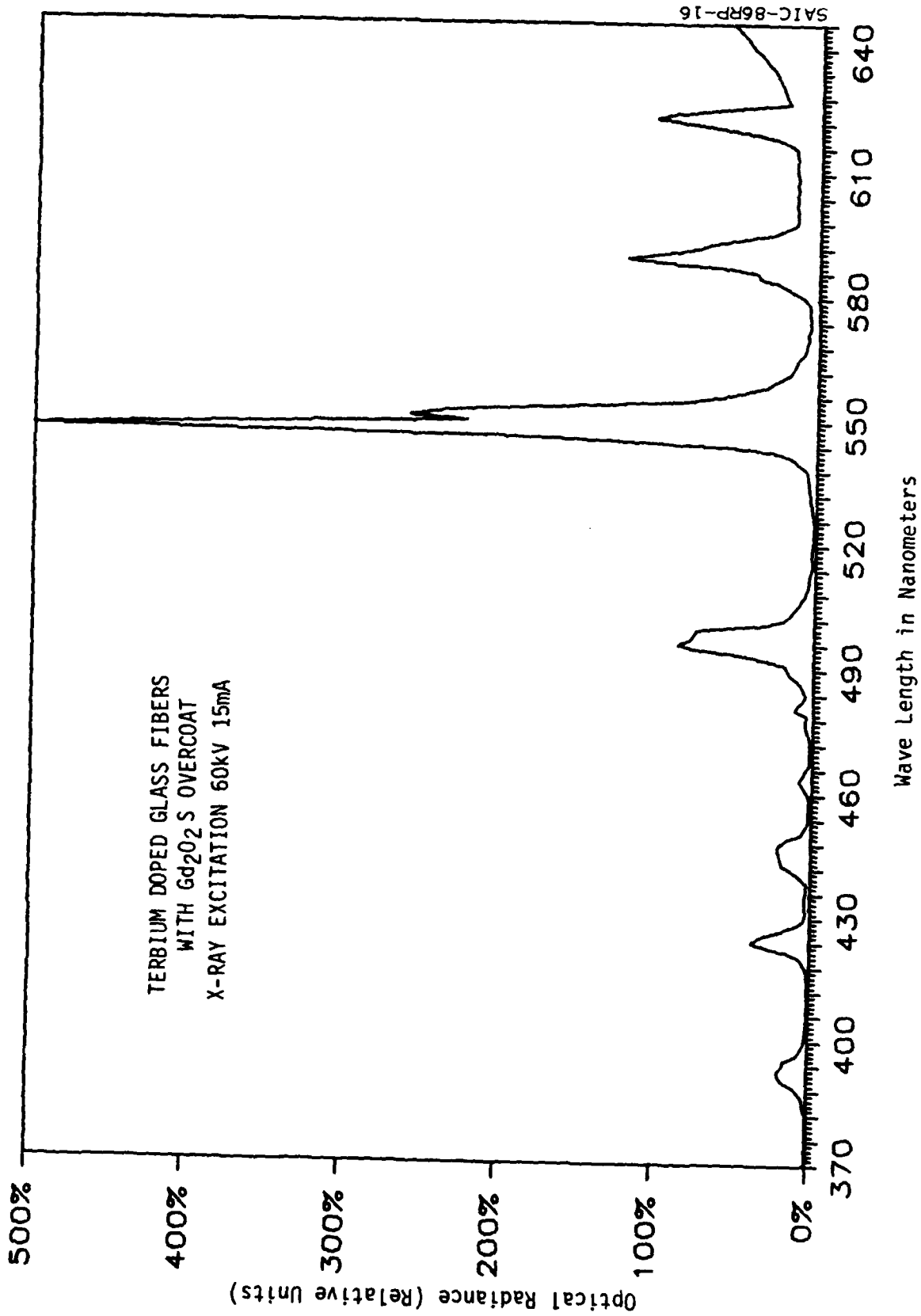


Figure 2.4.8 Spectral Response for Combined Terbium Glass - Gd₂O₃ Overcoat at low X-Ray Energies.

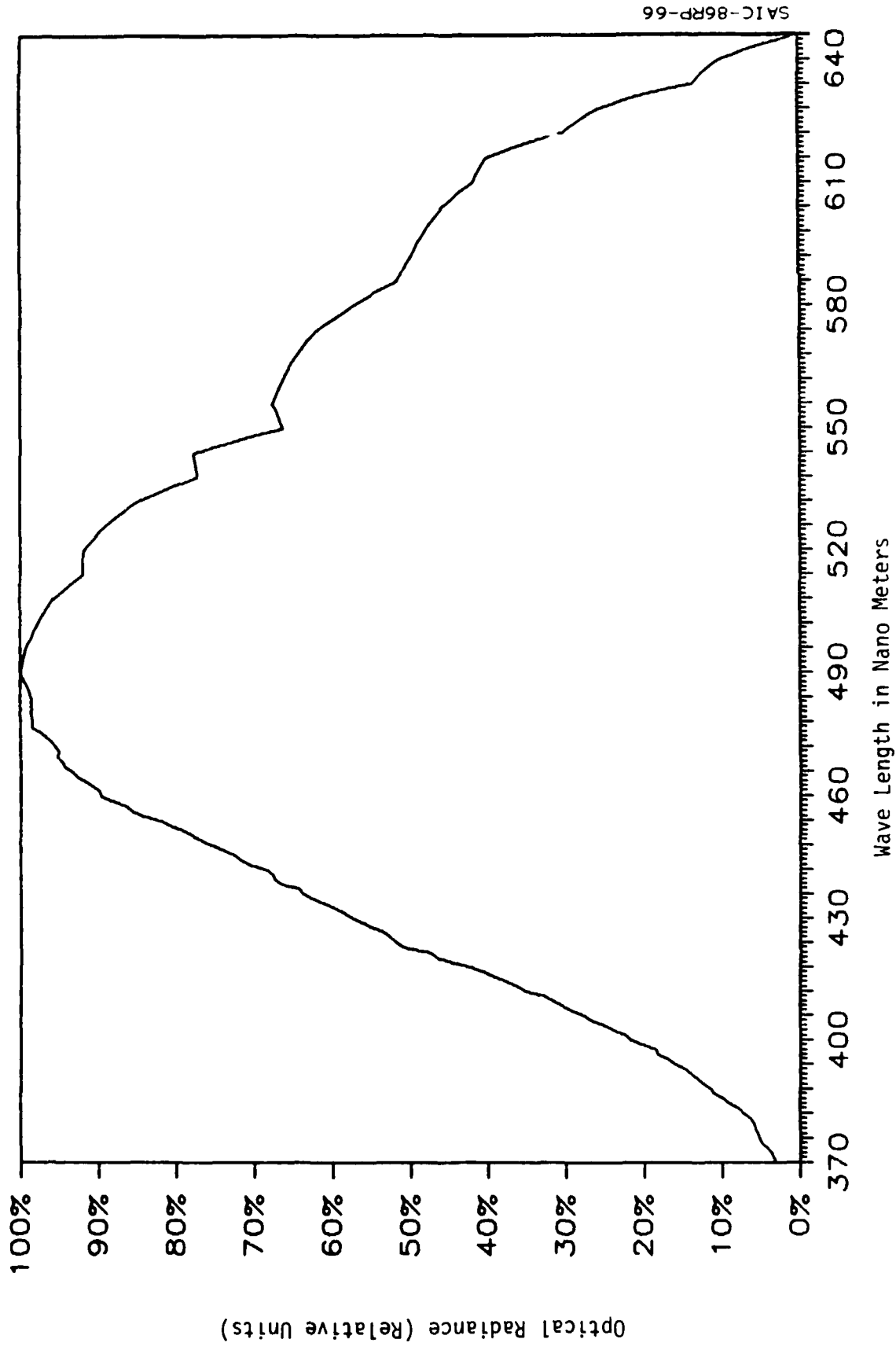


Figure 2.4.9 Spectral Shape of Bismuth Germanate
(3mm Plate) 60 kV X-Ray Excitation.

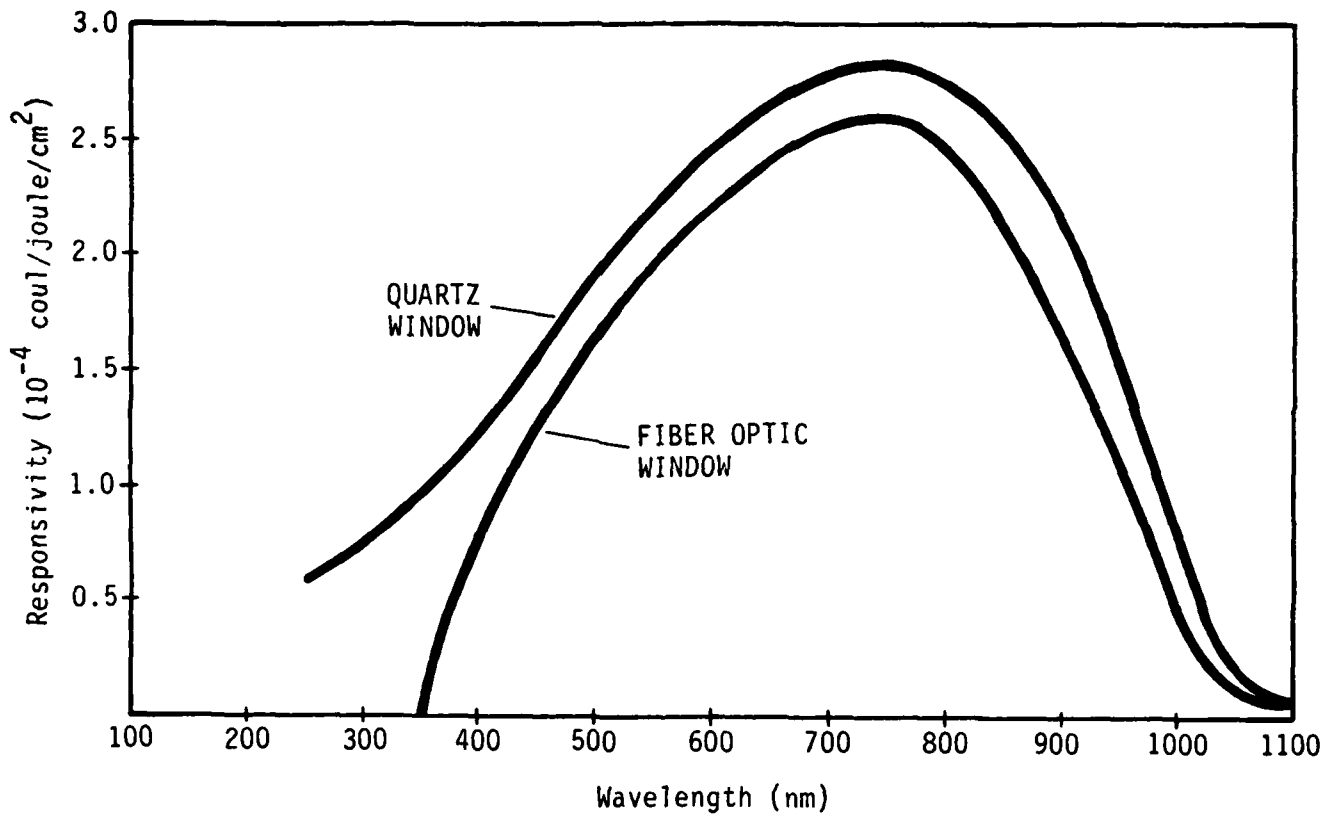


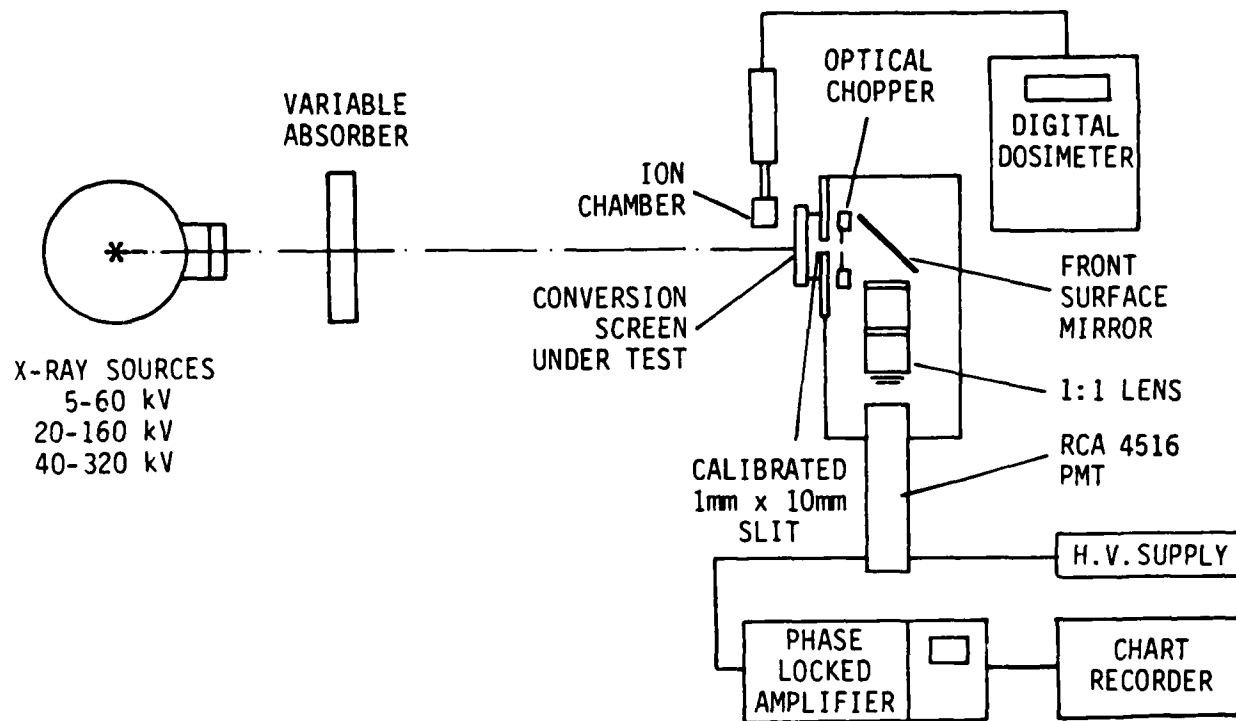
Figure 2.4.10 Typical Spectral Response for a Silicon Self Scanned Array (Reticon Type S).

2.5 MEASUREMENT OF SCREEN BRIGHTNESS AND ABSOLUTE RADIANCE AND CONVERSION EFFICIENCY

All screens evaluated in this study were measured for brightness as a function of incident X-ray flux. These measurements were made in absolute radiance units to make the results useful in further design calculations. The data was also recorded using several absorber thicknesses to provide a more realistic estimate of the effects on X-ray spectral distribution on screen performance.

The apparatus used to make this measurement is shown schematically in Figure 2.5.1. The screen area and illumination geometry were kept the same as that used in the spectral measurements. Conversion screens were placed in contact with a 1x10 mm entrance slit so that they could be illuminated by X-rays from the front side and optically measured from the rear side. A factory calibrated Victoreen model 660 digital dosimeter was used to measure X-ray flux. The small ion chamber probe was mounted in line with the beam and adjacent to the screens under test. Provision was included to put absorbers at the X-ray source to simulate the hardening of the beam by the sample. Two X-ray sources were used to represent a more realistic simulation of typical conditions. A Seifert Isovolt 160 unit with a 1 mm Be window was used to cover the range from 20 to 90 KV. A Seifert Isovolt 320 with an internal 7-mm Be window covered the range from 60 to 320 kV. Some effects of the slight difference in window attenuation are observed in the results. Both systems used the same regulator and control and therefore are relatively well matched in potential and current calibration.

The light from the scintillators was allowed to pass through an optical chopper whose dimensions did not restrict the slit. The use of chopper operated at a frequency other than at some multiple of the power lines and a phase locked amplifier reading out the voltage of a calibrated RCA 4516 phototube freed the system from the effects of d.c. drift and ambient room light. A 45° mirror put the PMT and coupling lens outside the radiation field reducing the effects of radiation induced noise signal. The lens system used was a 1:1 collimating pair with an effective aperture of $f/1.0$. This has the advantage of matching the radiating area to the detection area through an



SAIC-86RP-13

Figure 2.5.1 Experimental Apparatus used to determine Radiance per Unit Dose Rate as a Function of X-Ray Spectra.

exactly known solid angle. Using the geometry described, the calibration of the photomultiplier sensitivity and known spectral distribution of each screen, the results can be reduced to an absolute measure of optical radiance in units of nanowatts per mm^2 - steradian/for any given dose. These units are independent of the measuring system's response and can be matched to any specific spectral response by simply reversing the procedure described below. The data was recorded on an analog chart recorder with the value of X-ray potential and Rad Dose Rate being noted for each point. Several runs were made on identical samples to estimate the small errors present. The curves were all very reproducible and errors are estimated to be less than the size of the plot symbols in most cases. In some cases where an instrumental shift was suspected, data from one set of measurements were normalized to match the remainder of the energy range. In general this effect was less than 10%.

To translate the raw data to Radiance, the following procedure was used.

Data from the phase locked amplifier was recorded as $V(E)$ where E is the X-ray energy at some dose rate $D(E)$

The curve of photomultiplier response $\xi(\lambda)$ gave the calibration of voltage/microwatt at each wavelength, λ

A spectral correction factor X_s was calculated for each scintillator by doing a spectral integral weighted by $f(\lambda)$, the spectrum of the scintillator, thus for each scintillator

$$X_s = \frac{\int f(\lambda) / \xi(\lambda) d\lambda}{\int f(\lambda) d\lambda}$$

where the integral is carried from 370 to 620 nm.

The spectral correction factor is a measure of the relative overlap of the spectrum of the scintillator with that of the photomultiplier response. It may be thought of as a weighted response as here the weighting factor is the spectral shape. Generally the lower the value of X_s , the closer the converter

spectra matches the peak of the PMT. The absolute magnitude of the value of X_s are specific for the particular PMT and operating voltage but may also be taken to measure the amount of power required to yield a given level of signal (e.g. picowatts/volt). Thus the less power/volt required, the better matched the spectral distributions. Since the PMT used has a very similar shape to the S-20 photocathode response used in an image intensifier, this X_s represents also a good estimate for the linear scanners response. A summary of the X_s determined for the PMT used and the conversion screens is given in table 2.5.1. To determine the relative signal for any other sensor one would calculate the corresponding X for its match with the converter spectra. By then taking the absolute radiance and dividing by this new X_s , the relative brightness, measured by the new sensor would be determined from the absolute radiance curves determined here.

Now the total Radiance or power/area-solid angle is expressed at each energy is:

$$R(E) = \frac{P}{A\Omega} = \frac{V(E)X_s}{A\Omega}$$

Then dividing out the dose rate to put more usable terms, the Radiance per unit dose is expressed as

$$\frac{R(E)}{D(E)} = \frac{V(E)X_s}{D(E)A\Omega} \quad (\text{microwatt per mm}^2\text{-Str/Rad per min})$$

TABLE 2.5.1

Spectral Overlap X_s for Converter Screens and RCA 4516

Photomultiplier @900V (X-ray Excitation 60kV @15 ma for A11)

Converter Type	X_s (microwatts/volt)
Terbium Fiber Optic	.253
Cerium Fiber Optic	.088
Trimax 2	.269
Gd ₂ O ₂ S Intagliated	.232
Terbium F.O. + Gd ₂ O ₂ S	.253
Bismuth Germanate	.189

The Radiance/Unit Dose rate may be regarded as a composite Optical Conversion Efficiency (OCE). In reality it is the product of a number of terms each describing as intermediate step in the conversion of X-ray energy to light. Typically for any optically coupled system, the Optical Conversion Efficiency (OCE) is a product of at least 3 terms.

$$\text{O.C.E.} = \epsilon_{\gamma}(\bar{E}t) \epsilon_s(E) \epsilon_t$$

where: ϵ_{γ} is the interaction efficiency of the scintillator screen of thickness, t , to the incident X-ray spectra having some energy distribution E

ϵ_s is the specific light generating efficiency of the bulk scintillator material in converting X-ray of dose of average energy E into light

ϵ_t is the capture and transmission efficiency of the optical coupling to the sensor.

It is virtually impossible to fully separate these effects for fiber optic screens since in many cases, the conversion and transmission media are identical.

While we would like to separate those terms to better understand the conversion process and to optimize system performance, the choice of converter types require one to use the measurement of the Radiance/Unit Dose as the unit of Optical Conversion Efficiency. As we will point out later, the actual relative rankings did in fact not depend strongly on X_s for our imager. Since this might not be true in other cases, the use of total radiated energy units was used rather than the more spectrally dependent luminosity units.

The screens evaluated in the study fell into three general categories:

- Those in which the fiber optic glass also performed the conversion of X-ray energy to light,

- Those in which a scintillating salt such as Gadolinium Oxysulfide, Gd_2O_2S (or commonly referred to as GOS) is deposited on a fiber optic coupler,
- Combinations of the two above converters where either the GOS is formed into fiber like structures (intagliated) or where the screen technologies are simply combined (GOS deposited on scintillating fibers).

The results of the studies of these three basic screen types are shown in figures 2.5.2 through 2.5.10. These figures show Radiance per unit dose as a function of X-ray potential for each of the converter screens excited by X-ray beams from 30 to 320KV. The data were recorded for three different spectral shapes by using 1/2 inch, 1/4 inch and no aluminum absorber in front of the X-ray tube. The data all indicate significant hardening effects which show up both as general slope to the curves as well as pronounced fluctuations at low energies. Some of these effects have to do with the three factors discussed earlier involving the number of photons stopped from each energy group and the relative amount of light emitted for each group. The Victoreen 660 uses a simple $10\text{-cm}^2 \times 1\text{-cm-deep}$ air ionization chamber to convert charge to dose. The difference in air absorption and absorbed screen dose may contribute to some of the observed fluctuations at low energies. Without a detailed spectrum analysis of the incident X-ray beam, a separation of each contribution is virtually impossible. The decision to use known and reproducible absorbers to characterize each typical spectra should be just as effective. The lowest energy data in all cases was suspect and not included on the graphs. The fact that the two X-ray tubes have different intrinsic filtration (1-mm Be for 160KV, 7mm be for 320KV) also presents some matching problems. Data was collected with sufficient overlap to match results from both tubes in the 140 to 160KV region. Slight corrections were introduced to compensate for the differences in window characteristics.

Data were taken on two separate occasions nearly 4 months apart. Agreement was generally very good (less than 10% absolute). On some specific scintillators a general drop in sensitivity occurred. This was attributed to radiation damage or missalignment in the few cases where it occurred. The

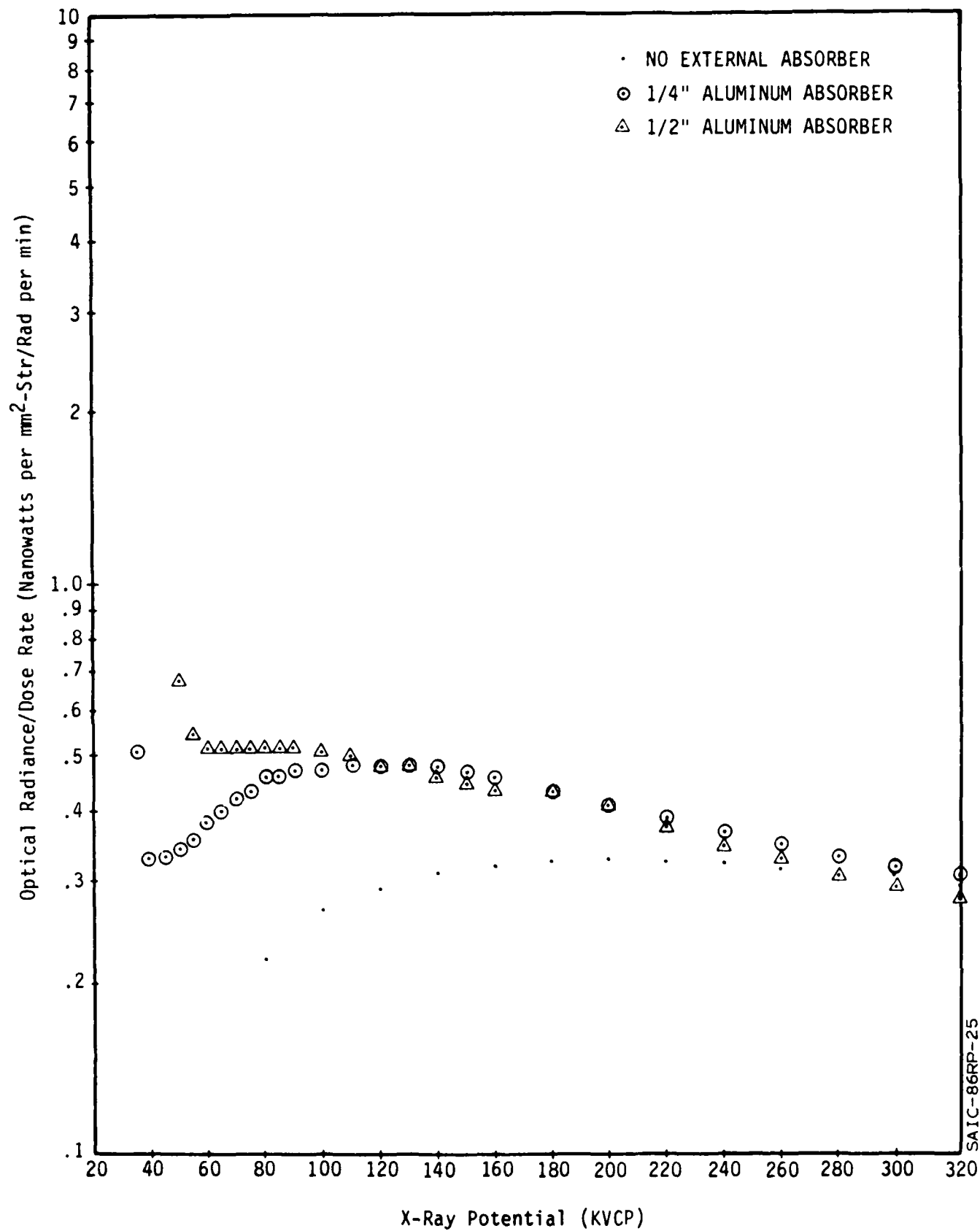


Figure 2.5.2 Radiance/Dose Rate from the 2mm Thick Terbium Doped Glass Fiber Optic Converter Screen.

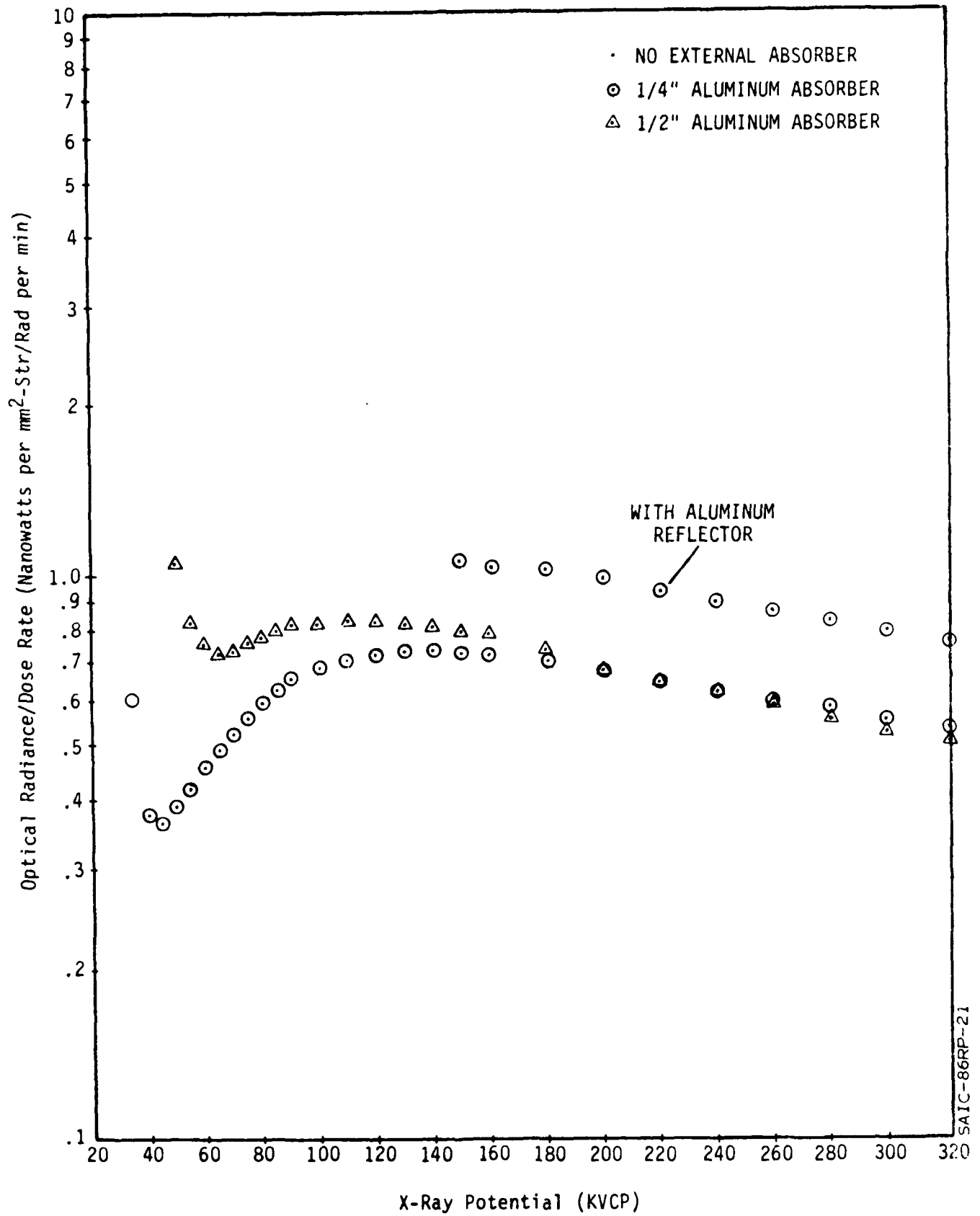


Figure 2.5.3 Radiance/Dose Rate from the 5mm Thick Terbium doped Glass Fiber Optic Converter Screen.

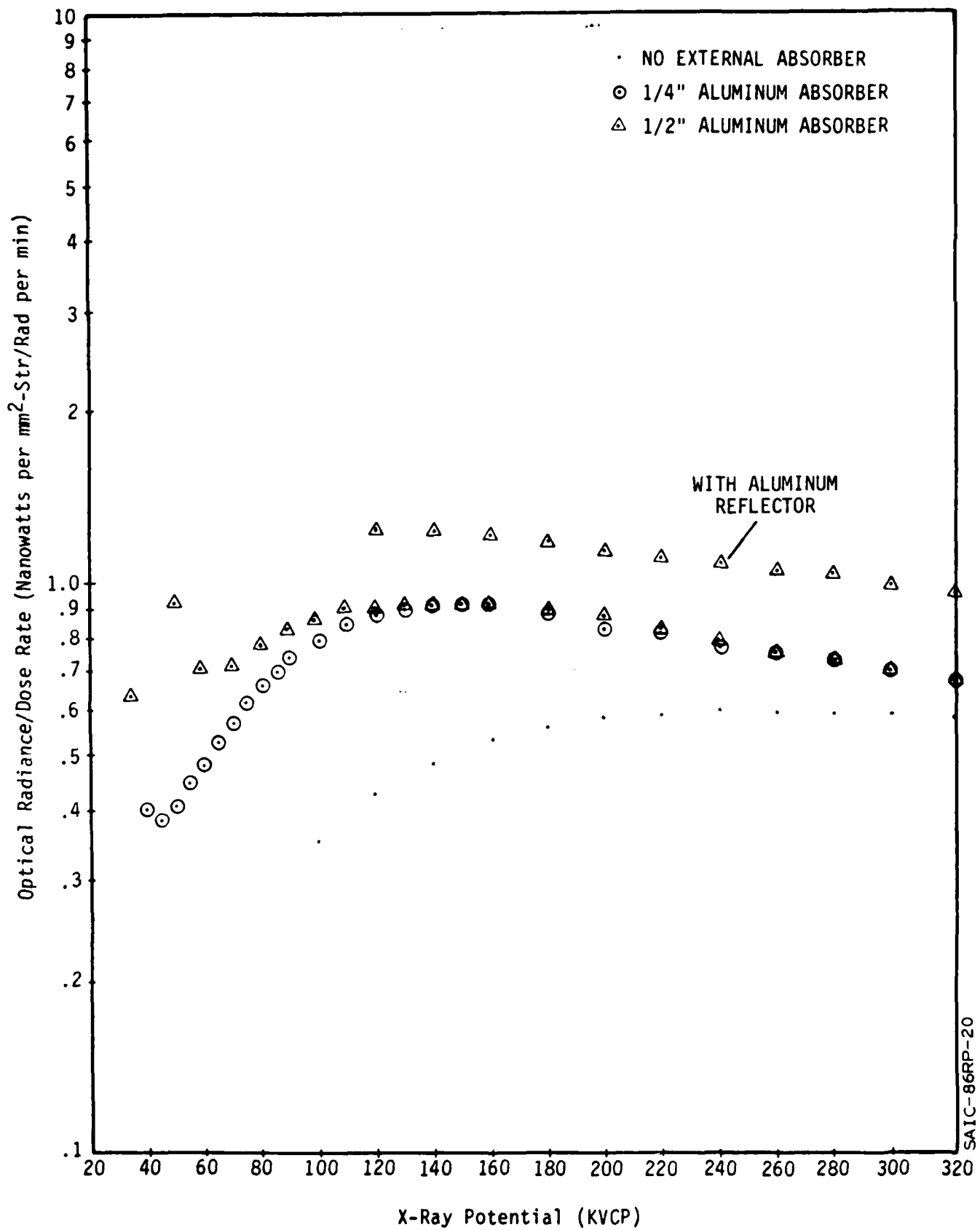


Figure 2.5.4 Radiance/Dose Rate from the 10mm Thick Terbium doped Glass Fiber Optic Converter Screen.

SAIC-86RP-20

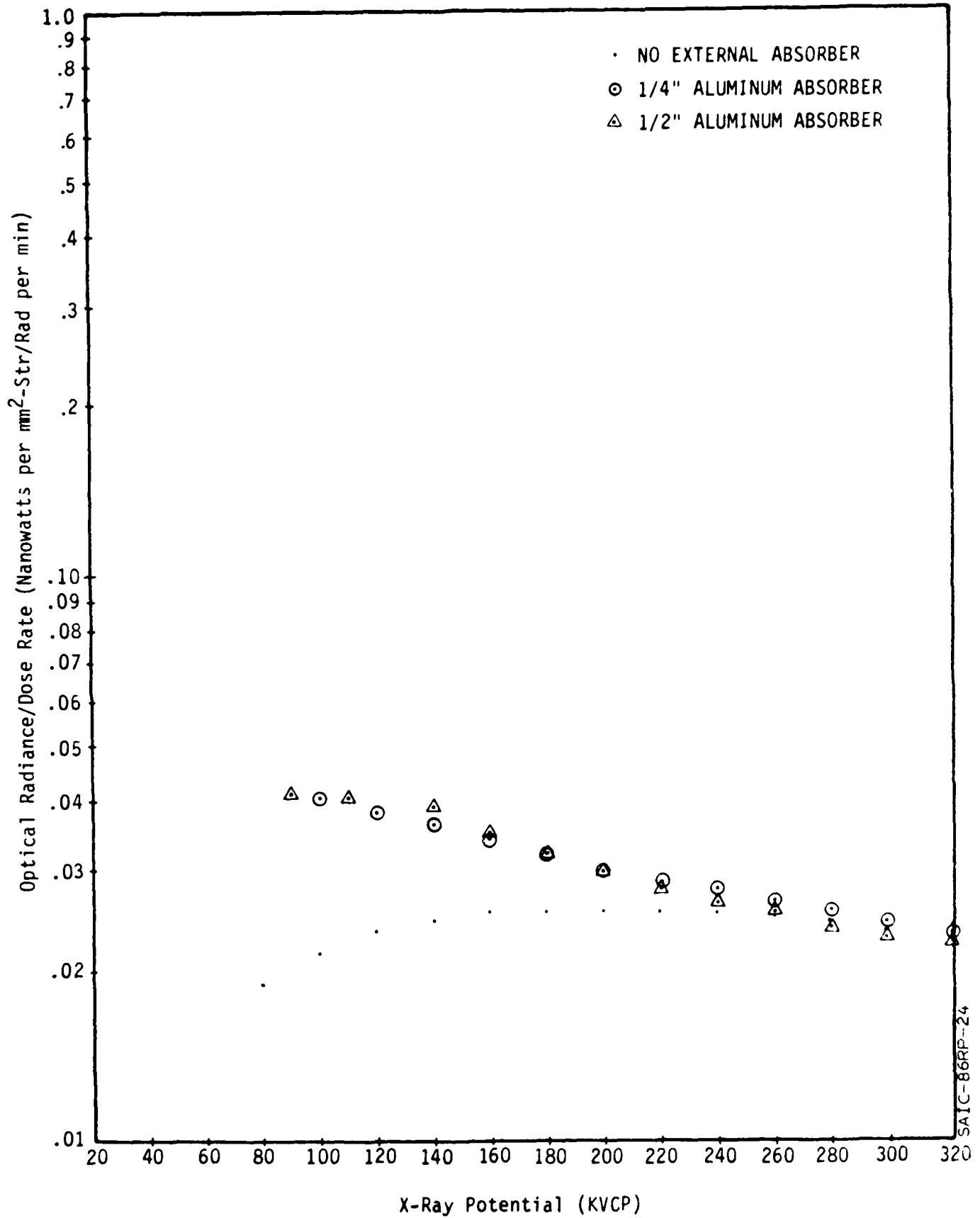
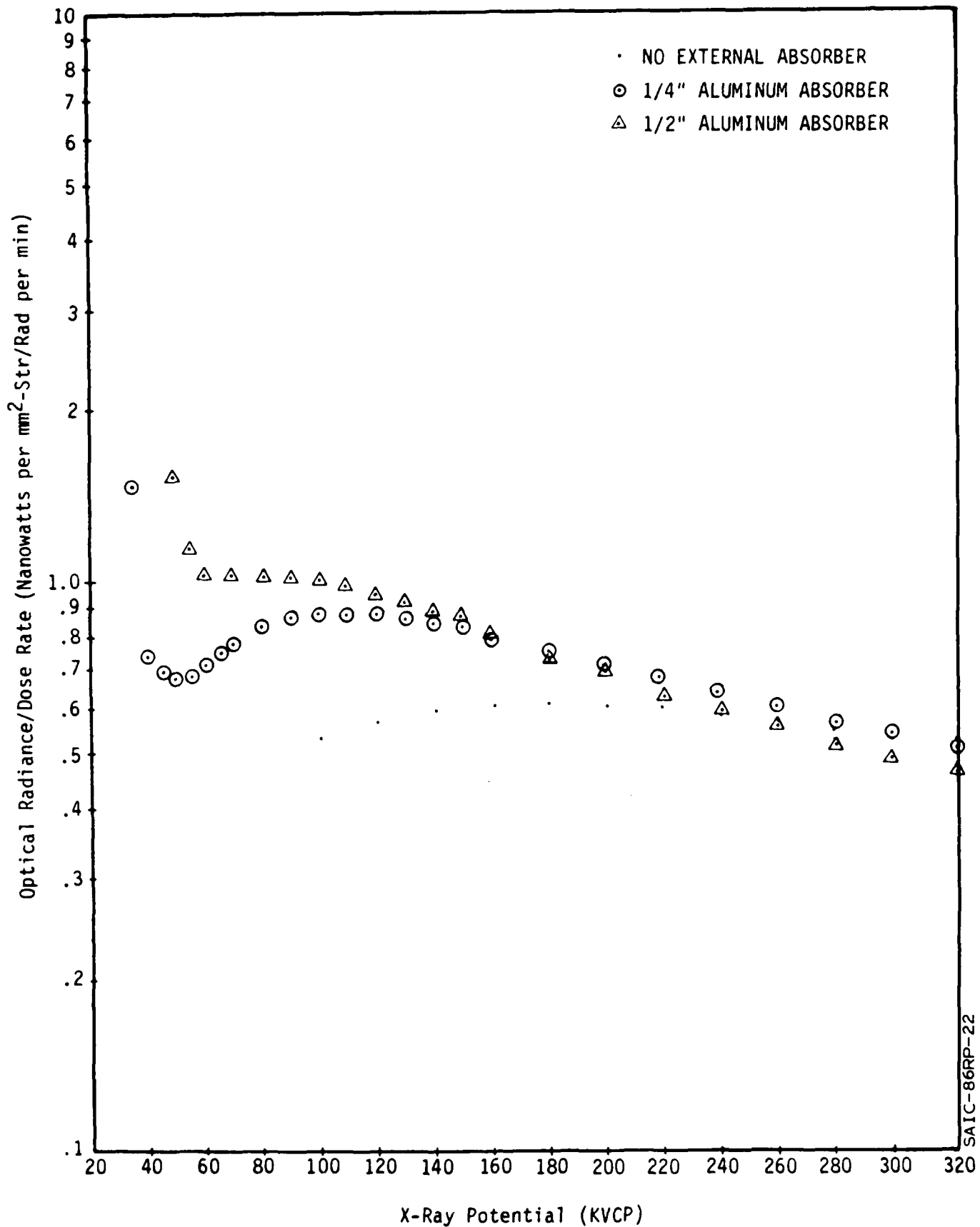


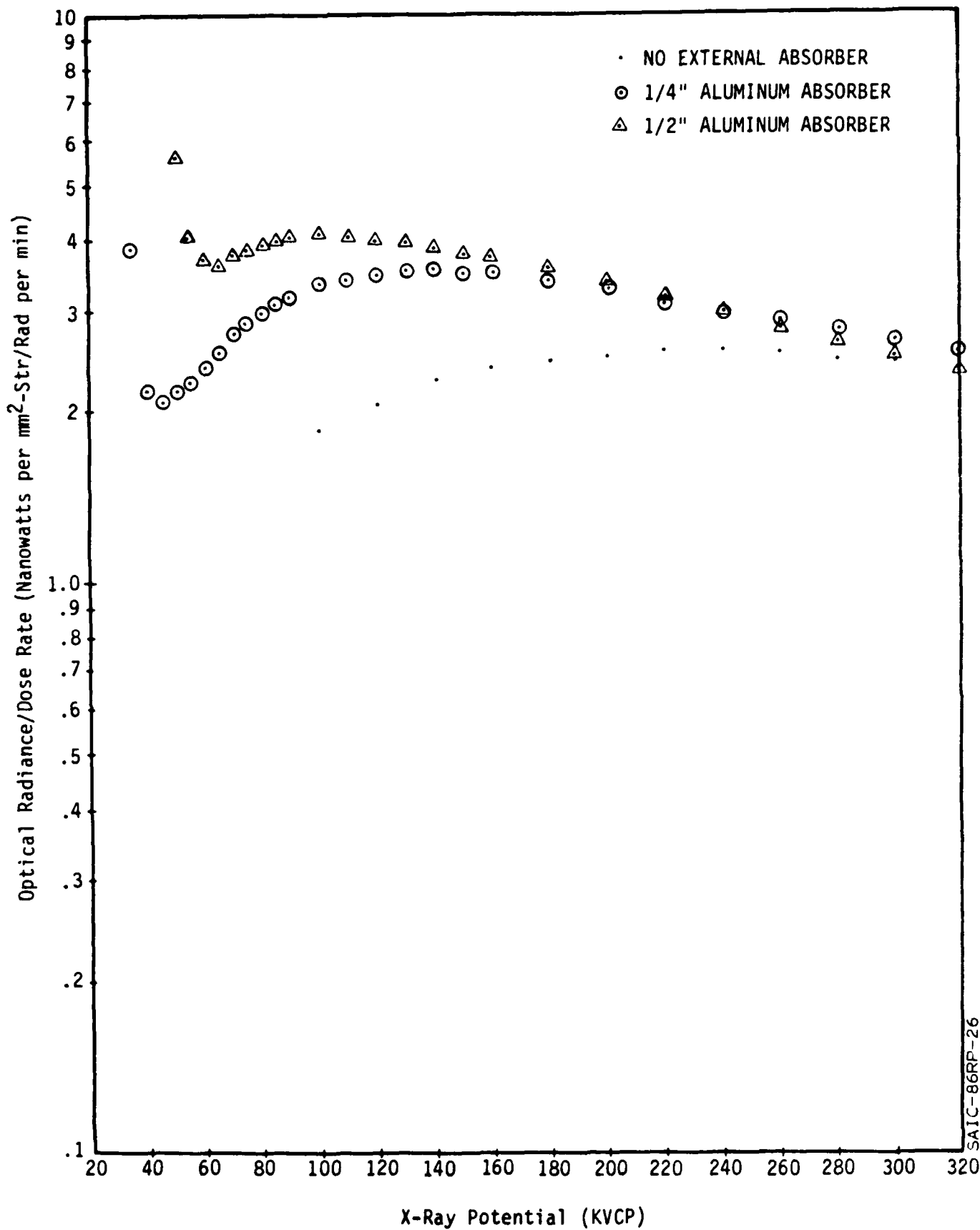
Figure 2.5.5 Radiance/Dose Rate from a 5mm Thick Cerium Doped Glass Fiber Optic Converter Screen.

SAIC-86RP-24



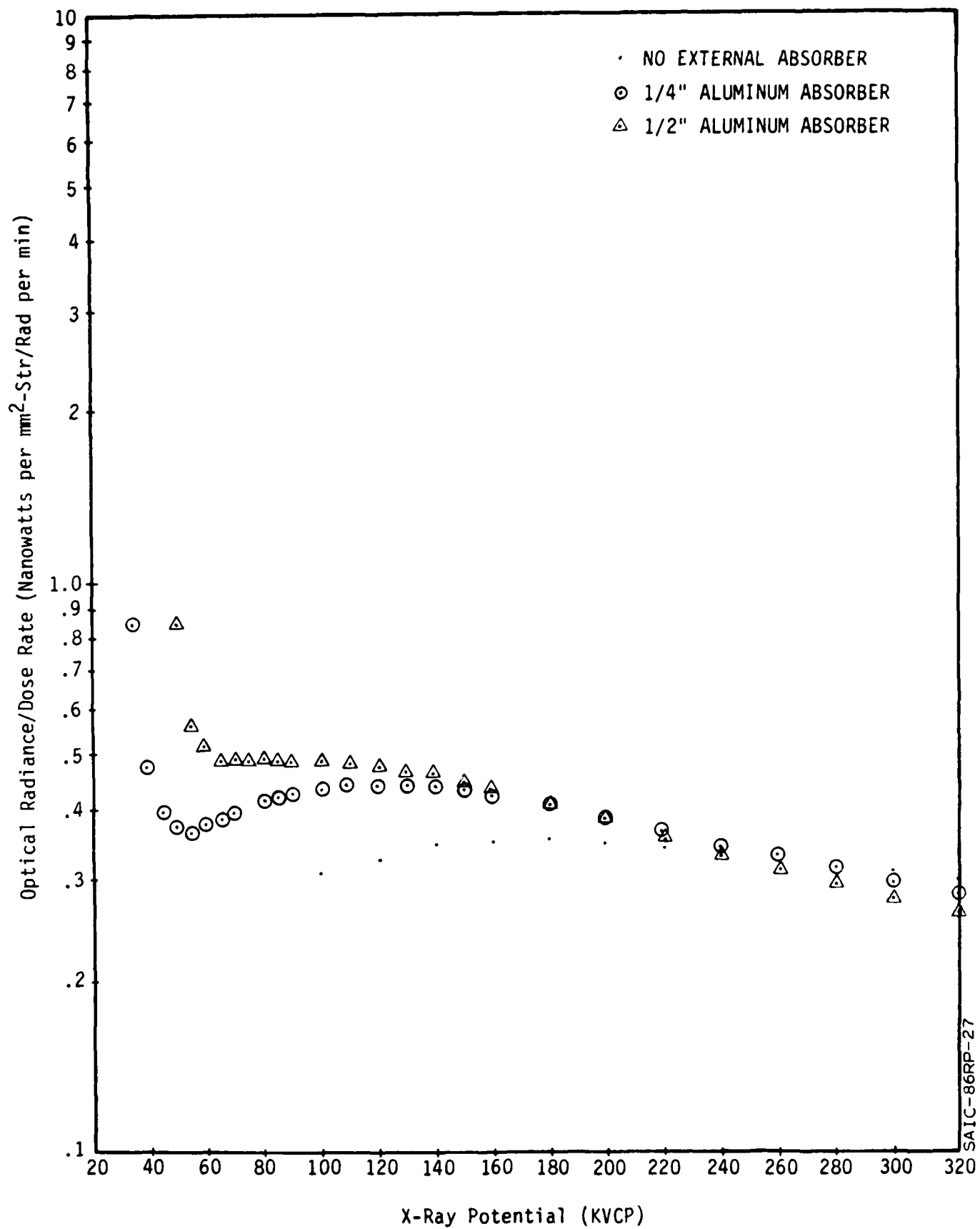
SAIC-86RP-22

Figure 2.5.6 Radiance/Dose Rate from Trimax 2 Converter Screen on na=1 Fiber Optics.



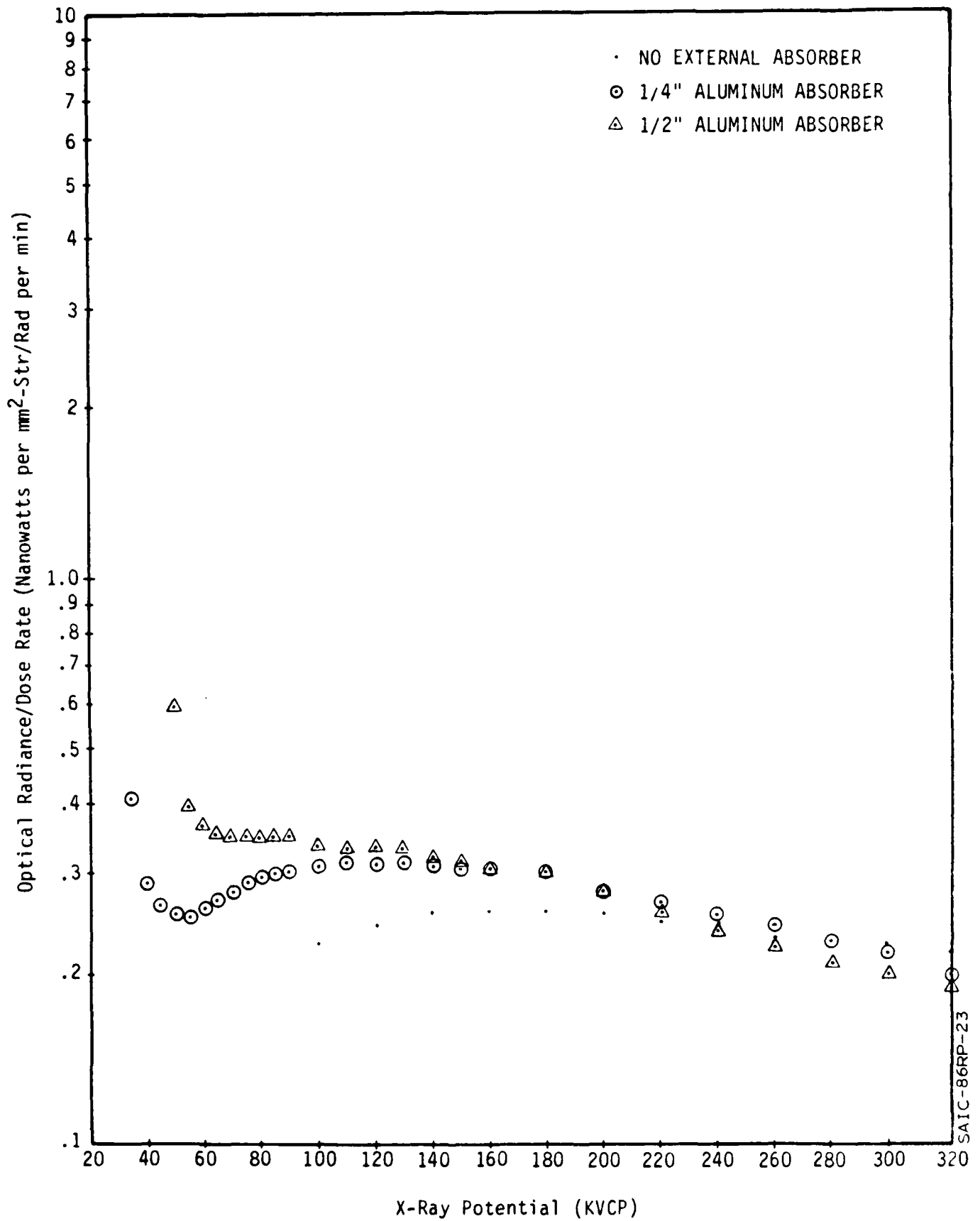
SAIC-86RP-26

Figure 2.5.7 Radiance/Dose Rate from Combination Gd₂O₃S overcoated Terbium Glass Fiber Optic Converter.



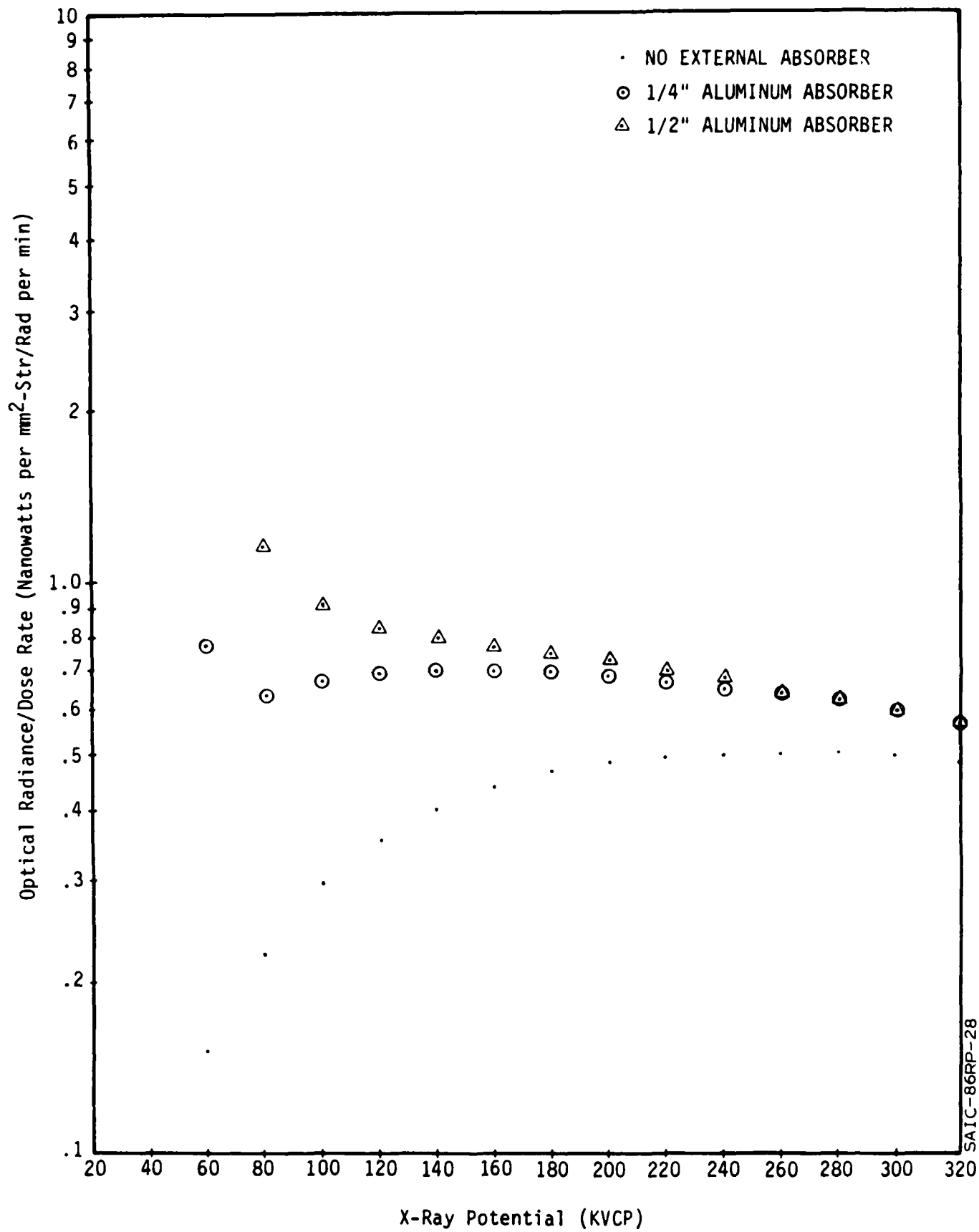
SAIC-86RP-27

Figure 2.5.8 Radiance/Dose Rate from a 0.012-inch deep Intagliated Gd₂O₂S Converter Screen.



SAIC-86RP-23

Figure 2.5.9 Radiance/Dose Rate from a 0.020-inch deep Intaglated Gd₂O₂S Converter Screen.



SAIC-86RP-28

Figure 2.5.10 Radiance/Dose Rate from a 3mm Thick Bismuth Germinate single Crystal Converter Screen.

resulting new spectra when normalized fell completely along the old points supporting this view.

The most innovative conversion screens that were evaluated were those made from scintillating glass formed into fiber optic plates. While it is generally true that such scintillating glasses have lower specific energy to light conversion efficiency, ϵ_s , than the more common salts such as Cds and Gd_2O_2S , the screens are still contenders for a high performance system because of their high resolution and excellent optical coupling efficiency, ϵ_t . Several formulations of scintillating glass have been developed over the last few years, for a variety of neutron and X-ray counting and imaging purposes.

The glass screens evaluated in this study were with one exception, formed from a terbium doped mixture. A small sample of cerium doped material was also obtained and is included for comparison. The terbium doped material represents a very efficient glass formulation and it has relatively little self-absorbtion. The material was supplied in 2-inch x 1/4-inch plates with thicknesses of 2 mm 5 mm and 10 mm. The material has a numerical aperature of approximately 0.6 and has EMA anti-crosstalk coating on the individual fibers. The fiber diameter is 25 microns with about 80% useful packing fraction.

Figures 2.5.2., 2.5.3. and 2.5.4. show the total optical conversion efficiency (OCE) or Radiance/Dose Rate for these three screens as a function of X-ray spectral characteristics. The data are plotted for energies as low as would register on the dosimeter for each absorber. The so-called "no absorber" data does of course have some attenuation both from the tube exit window and the dosimeter itself. This latter data proved to be difficult to match for the two X-ray sources below 100 to 120 KV and so is not included on the plot.

In general, the data shows a nearly similar OCE at lower energies and growing separation as the average beam energy is raised. This reflects the fact that soft X-rays are virtually totally absorbed in all three samples where-as at higher energies, the increasing thickness stop a corresponding larger fraction of the beam. The curves are relatively flat when normalized to dose indicating a good linearity between output and dose over a broad range of energies.

The data from the cerium-doped glass sample is included in Figure 2.5.5. The OCE output is over an order of magnitude lower than that of the terbium glass. This is somewhat mitigated by its better spectral match (lower X_s) for the intensifier used on the linear scanner. None the less, even with this advantage, it still is the lowest sensitivity material tested. Since this material was a scrap sample, it is possible that other formulations of the cerium-doped material could conceivably perform better than the results reported here.

Conventional X-ray screens often have reflective backings to increase the speed. These reflective coatings invariably "spoil" the basic resolution of the converter. Transparent glass screens used with lens coupled systems can of course be made of this scintillating glass. Again, any attempt to use a reflector will further spread the light and degrade spatial resolution. Fiber optic screens have a significant advantage since the light is constrained to move along the individual fibers. The application of a reflective coating on the fibers can, in fact, significantly increase the light output while not affecting resolution. If the coating is closely coupled to the fiber ends, outgoing light will always be reflected back within the same fiber it came from. Tests on the 5mm and 10mm fibers show improvements of 1.42 and 1.52 respective increase when thin aluminum foil was optically bonded to the input side of the plate. These data are shown in Figures 2.5.3 and 2.5.4. This is a significant advantage available to fiber optic systems that cannot be used as effectively on transparent or settled salt screens and should be further exploited.

High resolution "salt" screens were represented in the study with a section of TRIMAX 2 conversion screen bonded to a numerical aperture 1.0 fiber optic plate. Clamping plates put pressure on all but a thin central portion to ensure good contact. Cargill immersion oil was used in this case as a coupling fluid. TRIMAX 2 is a nominally 0.002" thick Gd_2O_2S screen with perhaps some other phosphors added to provide some blue response. Its speed and resolution characteristics are very similar to KODAK'S LANEX FINE or MCI'S RAREX BG FINE. The OCE data for TRIMAX 2 is shown in Figure 2.5.6. The screen is brighter than the Terbium screens at the low energies but falls more rapidly with increasing energy.

Several types of composite screen technology were studied in the program. The simplest and most effective was the use of a 5mm terbium fiber optic plate with a Gd_2O_2S coating on the incident side. The original idea was to improve the low energy response of the terbium with a thin Gd_2O_2S overcoat while using the thick terbium section to strongly influence the high-energy performance. As the data in Figure 2.5.7 shows, the effect was somewhat overdone. The combined screen is typically 5x brighter than the average of all other types tested. The resolution was slightly poorer than expected. This combination of effects is most likely caused by a thicker deposition than the 0.004" originally anticipated. In spite of the thicker than desired coating, the screen performs quite well on the system for several reasons:

- The GOS coating is a very effective reflective coating for the terbium fiber optic increasing its component fraction.
- The low numerical aperture of the terbium fibers restricts the light from the GOS to that which enters at small angles. This reduces the multiply scattered light that might otherwise further reduce resolution.
- The deposition of the GOS directly on the fibers was a better coupling than the fluid coupled TRIMAX 2 screen

This screen or one with a somewhat thinner coating has many of the desirable characteristics of a good general purpose screen. This is evaluated in more detail in section 2.7.

Originally, we proposed a screen, based on fiber like structures filled with a salt scintillator. This concept of intagliation has been studied for use in image tube output screens. Our initial attempts to form such an intagliated screen were not successful. This was due primarily to choosing too small a hole structure and by the need to etch and deposit phosphor evenly. During the course of the program we became aware of hollow glass hole structures similar to that material used in micro-channel plates. These plates were formed and etched prior to being drawn down into finer fibers. Samples of this material having a hole to hole spacing of 60 microns

were obtained and mounted to a commercial fiber optic image plate. The hole structures were ground down and filled with 6-micron mesh Gd_2O_2S by settling. Two plates were fabricated having 0.012" and 0.020" thick layers. The plates were illuminated with X-rays and compared against the terbium glass structure. Visual observations indicated that these intagliated screens were much brighter. Because the plates were unmounted an immediate measurement was not performed. The plates were subsequently mounted into frames similar to the terbium glass samples and tested on the line scanner. The .012" plate was a somewhat uneven deposition but appeared quite bright. The .020" deposition seemed to be much more even, at least on the surface, but not much brighter. The screens were set aside to await a detailed brightness comparison with the other samples. When the screens were tested, they appeared to have lost some of their initial brightness. Examination of the screens indicates a potential lack of good contact between the screen material and the coupling optic as well as some degradation in the material itself. This may be due to humidity or other contaminants. Although the screens are less bright than expected, they still perform well in resolution and only slightly poorer than the 2mm terbium glass. The OCE results from the intagliated screens are shown in Figures 2.5.8 and 2.5.9. Interestingly, the .020" has less brightness than the .012" screen indicating that the light path is disturbed between the front and rear of the screen. This disturbance may be chemical as mentioned above or simply a physical effect caused by vibration or thermal shock. It should be remembered that .020" is an extremely thick screen by phosphor deposition standards and significant surface forces are at work in such a structure. The fact that the screens work and yield resolution compatible with their hole spacing suggest that more work should be carried out in this area.

The OCE data from a 3mm thick bismuth germanate crystal (BGO) is shown in Figure 2.5.10. These data were included since BGO is a well studied material whose spectral and output characteristics are known.

A relative comparison between all the screens is made in Figure 2.5.11. On this figure, data for all screens are plotted together using a similar source spectra (.25" Al absorber). The data show how significantly the different scintillators vary from the cerium glass to the GOS-Terbium combination. Because of the large variations in data, the measurements were

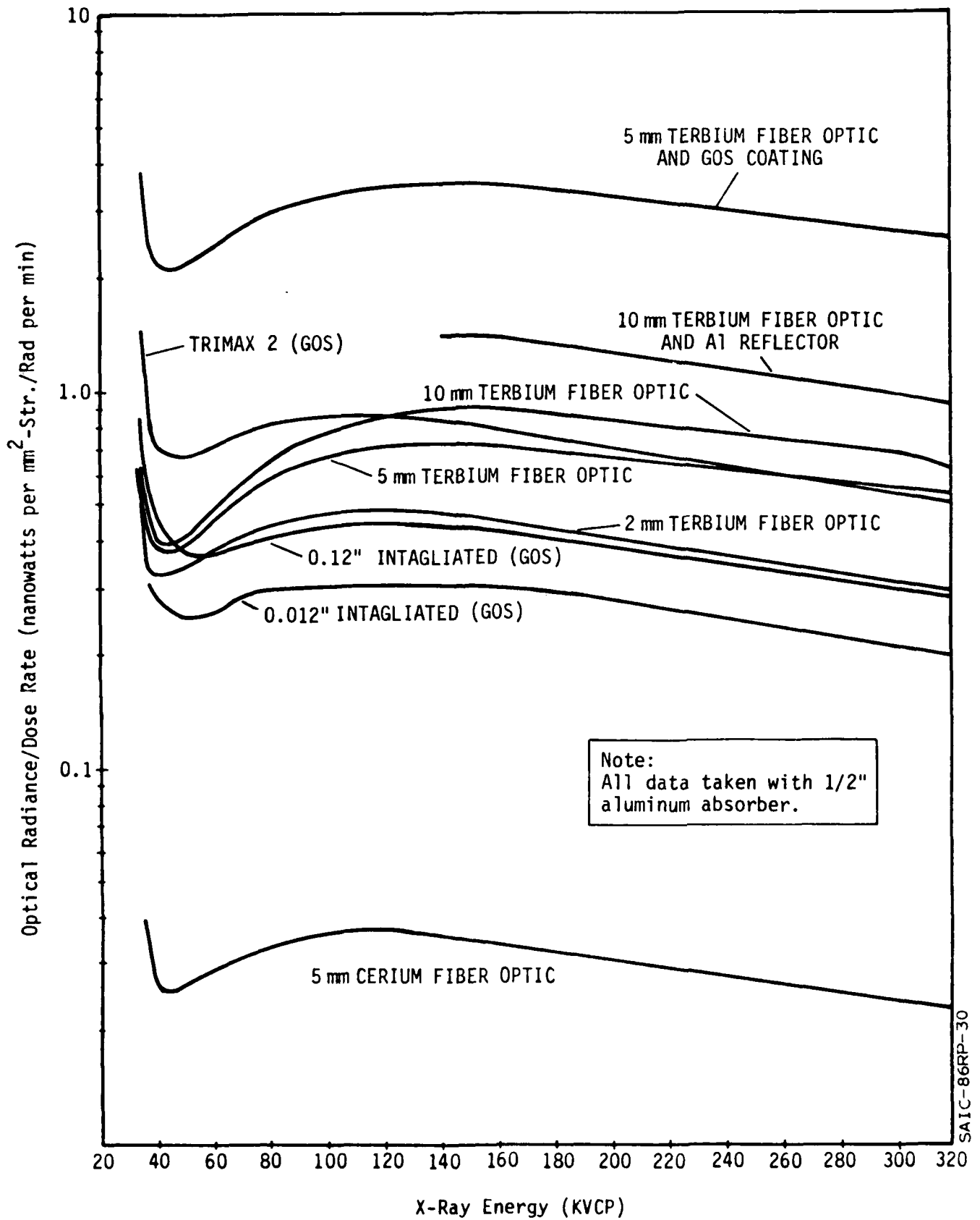


Figure 2.5.11 Relative Comparison of Radiance/Dose Rate for all Screens evaluated in the Study.

repeated about four months after they were initially taken. The results showed very excellent repeatability in some screens with some occasional exception. The Trimax 2 screen has dropped about 35% after extensive use. This loss may well be due to radiation damage on the screen. The remaining screens were reproduced mostly within 10% or better with the occasional deviations always being in the direction of reduction of sensitivity. Since the screens with small numerical aperture showed most of these variability it was assumed that the positioning of the individual samples had varied. When the data was matched over in the 140 to 160 KV region with the old data, good agreement was again obtained. The value of the radiance per unit dose rate at 160 KV is used as a nominal measure of brightness in subsequent sections. This is summarized in Table 2.5.2.

TABLE 2.5.2

Relative Conversion Efficiency for
Screens Tested (160kV)

<u>Converter Screen Type</u>	<u>Optical Conversion Efficiency (160kV)</u>
5mm Terbium + GOS overcoat	3.45
10mm Terbium + Al reflector	1.39
5mm Terbium + Al reflector	1.01
10mm Terbium F.0	.91
Trimax 2	.90
5mm Terbium F.0	.71
2mm Terbium F.0	.45
.012" Intagliated GOS	.42
.020" Intagliated GOS	.30
Cerium F.0.	.034

2.6 QUANTITATIVE EVALUATION METHODOLOGY

2.6.1 Introduction

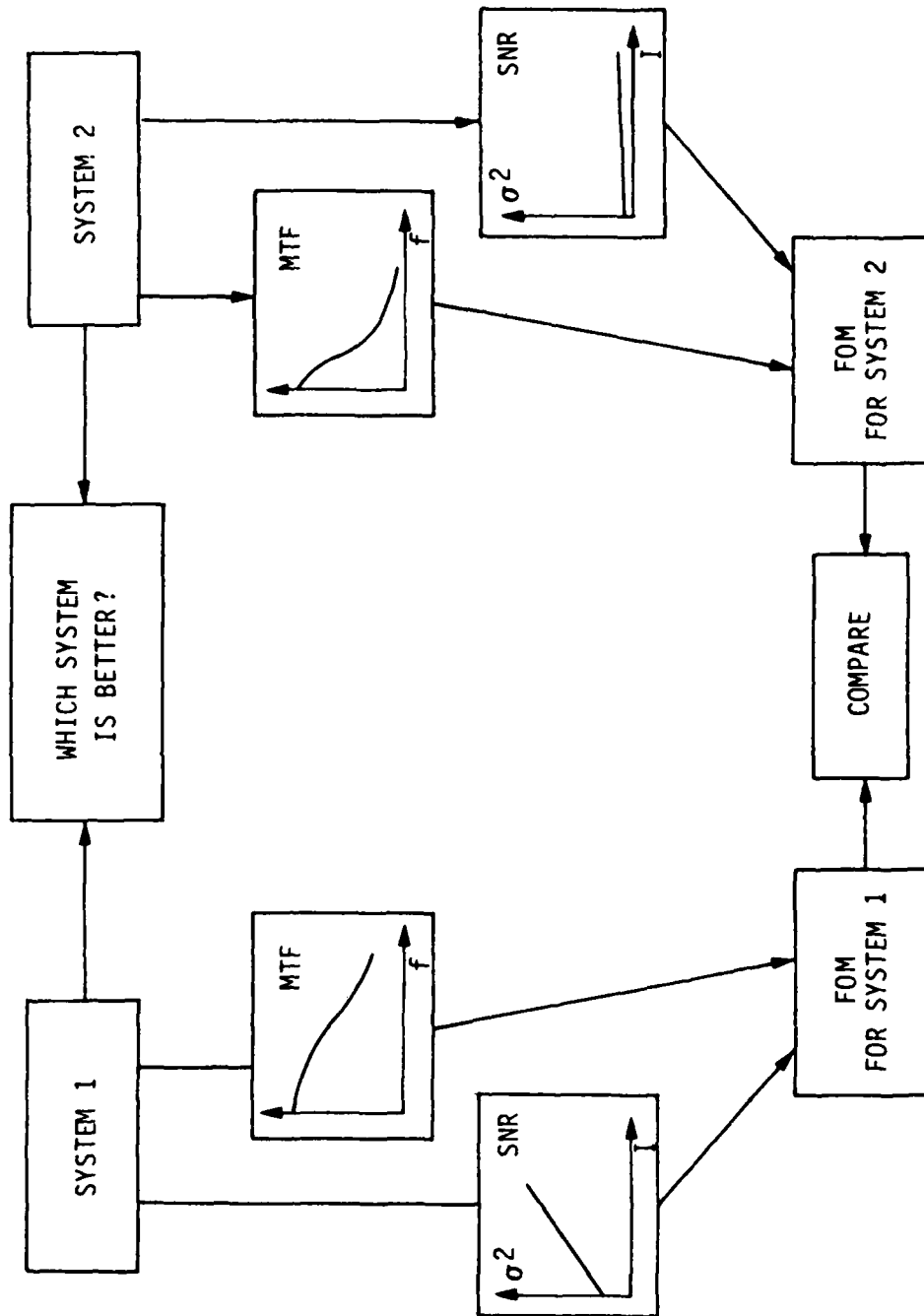
During the early phases of the program a detailed simulation model was developed to predict the effectiveness of any imaging system in revealing a low contrast flaw from a continuous background. The model assumed a digital real time imaging system but was based on simple physical and statistical principals that affect all optical systems. This approach was taken at the suggestion of the Air Force to use some of the concepts to explain target pattern recognition criteria developed by A. Ginsburg, et al.⁵ The development of the methodology in this section is based on the physical properties of the system which can be defined and measured. Other factors of economics or practicality are addressed in the subsequent section on figure of merit.

The methodology that we are looking for should have the following characteristics:

- It should result in a figure of merit which represents the ability of a system to detect small details.
- It must be self-contained, that is no additional instrumentation should be required, other than the data acquisition system of the real time radiography system itself. (In the case of film radiography, additional instrumentation, such as a microdensitometer, would be required.)
- No subjective judgment should be involved.

The factors which can be unequivocally defined and measured are the modulation transfer function and the signal-to-noise ratio. Suppose that we are given two different real time radiographic systems, each characterized by a certain modulation transfer function and by a certain signal to noise ratio. As shown in Figure 2.6.1, one system may have a better modulation transfer function but a worse signal-to-noise ratio than the other. The question is, then, how to decide which system has the best performance in terms of distinguishing small spatial details.

⁵Ginsburg, A. et al, Amer. Jour. Optometry & Physiological Optics, 59
No. 1, Jan. 82.



SAI-84GB-3

Figure 2.6.1 Comparison of Systems Based on Composite Figure of Merit.

It may be objected that modulation transfer function and signal-to-noise ratio are not totally unrelated. If a system has a high noise content, it may be difficult to measure a sharp modulation transfer function. It is, however, possible to conceive of a scheme which will lower the noise without affecting the modulation transfer function, or to devise means for improving or degrading the modulation transfer function without changing the signal-to-noise ratio. The two quantities can, therefore, be thought of as independent.

The proposed methodology consists of three steps. The first step, described in Section 2.6.2, consists of determining the modulation transfer function. The approach used in this study involves the use of a number of fixed spatial frequency standards made with alternate strips of highly absorbing material (Tantalum) and poorly absorbing material (Mylar), and the determination of the area of the characteristic frequency peak in the one-dimensional Fourier transform of the obtained images.

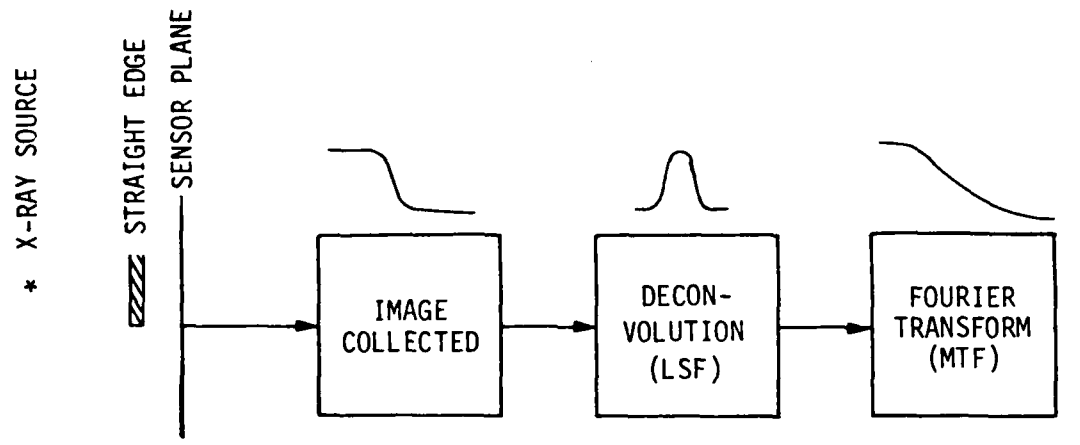
The second step, described in Section 2.6.3, consists of a procedure for obtaining the signal-to-noise ratio from a fit of the variance of the difference of two independent images. The third step, described in Section 2.6.4, is the combination of the information obtained in the two previous steps into a composite figure of merit.

2.6.2 DETERMINATION OF THE MODULATION TRANSFER FUNCTION

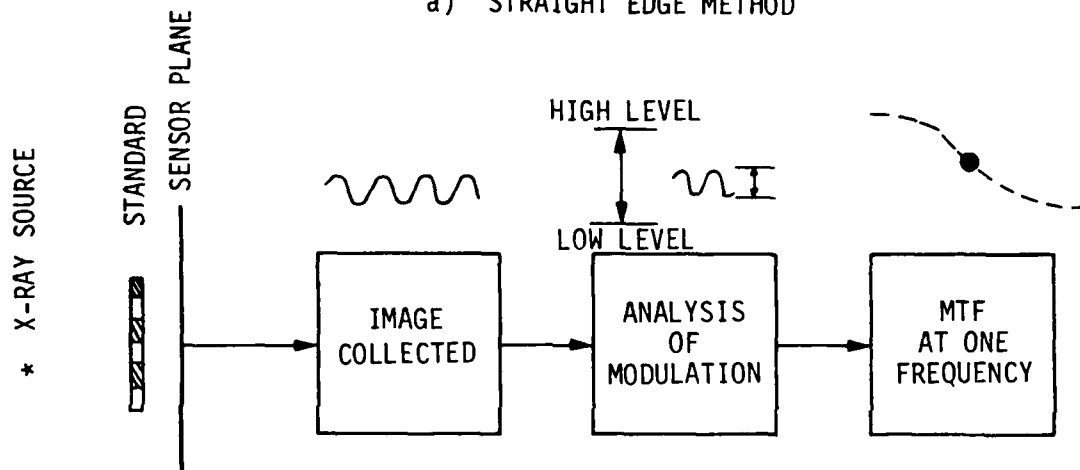
The first step in the methodology is the determination of the Modulation Transfer Function (MTF). The MTF is defined as the ratio of the modulus of the Fourier transform of the input to the modulus of the Fourier transform of the output.

There are three possible approaches for the determination of the MTF. As discussed below, each approach has certain advantages and disadvantages:

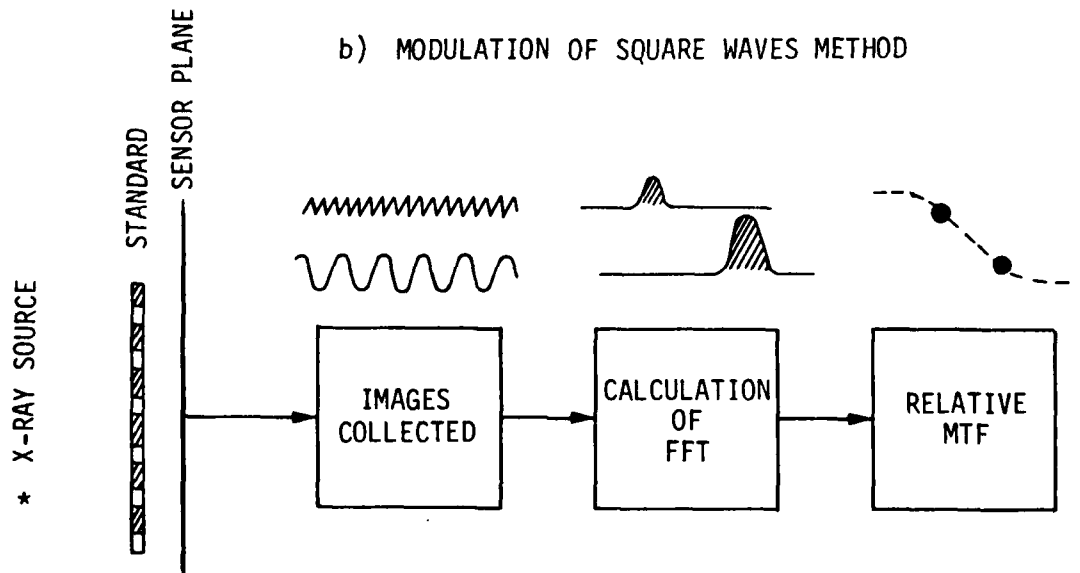
- **STRAIGHT EDGE METHOD:** As illustrated in Figure 2.6.2a, the X-ray radiation impinges on a straight edge and is recorded by the system. Deconvolution of the observed intensity provides the Line Spread Function (LSF) and a Fourier transform of this provides the MTF.



a) STRAIGHT EDGE METHOD



b) MODULATION OF SQUARE WAVES METHOD



c) FOURIER TRANSFORM OF SQUARE WAVE PATTERNS METHOD

Figure 2.6.2 Alternate Approaches for Determination of MTF.

SAI-84RP-7

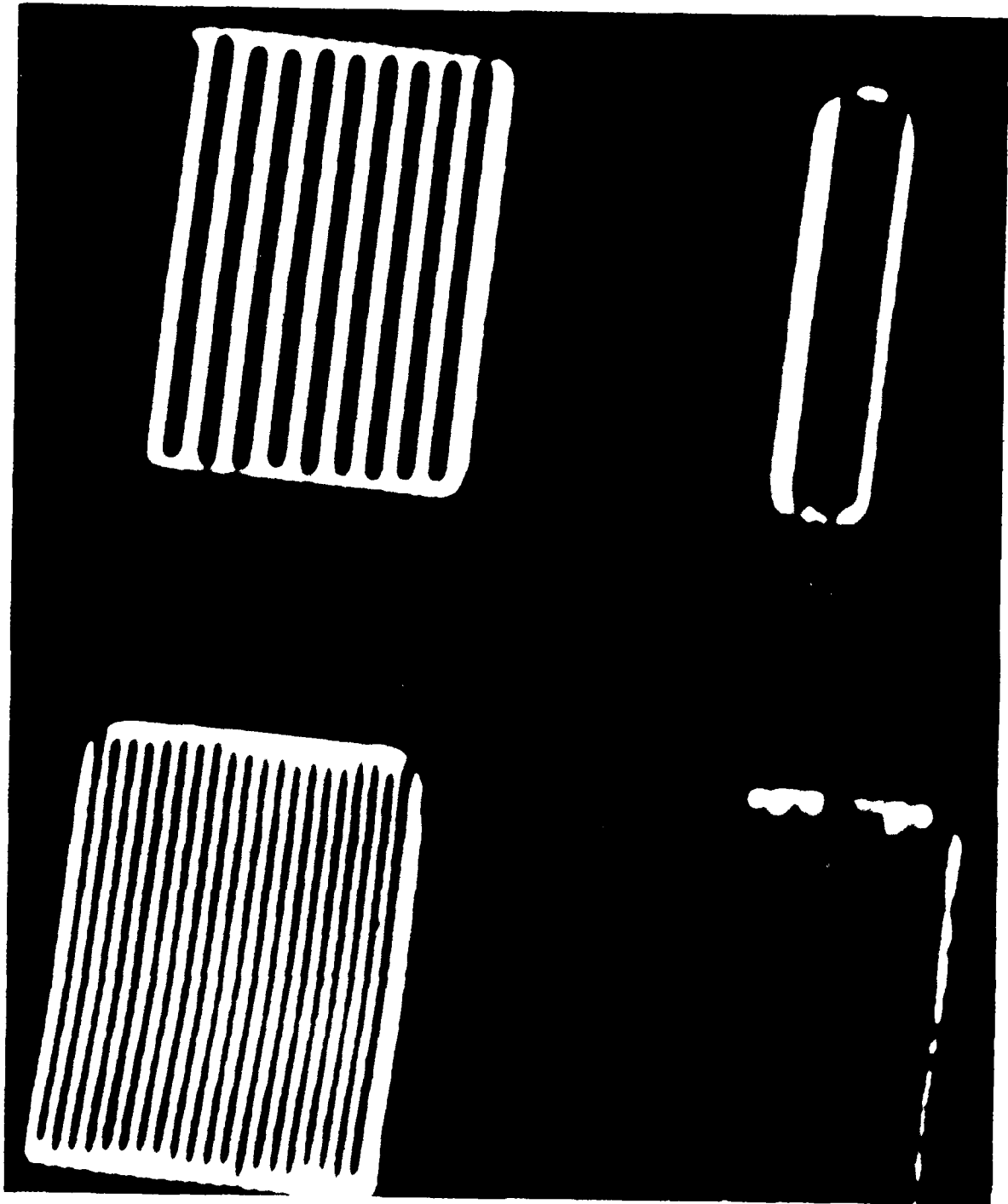


Figure 2.6.3 Low Resolution Radiography of Grid Samples.

The advantage of this method is that it provides the MTF at all frequencies with a single measurement. The disadvantage is that, because the information is usually contained in a small number of points, the derived MTF can be expected to have considerable error.

- MODULATION OF "SQUARE" WAVES METHOD: As illustrated in Figure 2.6.2b, the X-ray radiation impinges on a "square" wave type grating and creates a modulated pattern. The MTF can be derived by measuring the contrast modulation in the pattern. The advantage of this method is that, in conjunction with measurements of the unmodulated response to high and low transmission, it provides a fast determination of the absolute value of the MTF at one frequency. The disadvantage is that at high frequency of the "square" wave and when noise is present, it becomes difficult to decide what the modulation really is. Also, when irregularities in the "square" wave are present (which is practically unavoidable), a computer analysis may be difficult and hand analysis of a limited portion of the data may be required.
- FOURIER TRANSFORM OF "SQUARE" WAVE PATTERN METHOD: As illustrated in Figure 2.6.2c, the data acquisition part of the method is almost the same as in the previous one (the only difference is that a larger sample is needed). The data analysis differs insofar as one computes the Fast Fourier Transform (one-dimensional or two-dimensional) of the image of the grid and assumes as relative value of the MTF the area of the peak in a small range of frequencies about the characteristic frequency of the grid. The advantage of this method is that it uses all the information and that it provides an objective value, obtained in a straightforward way from the measured image. Also, since one integrates over a large area of the grid, the effect of irregularities is washed out. The disadvantage is that in order to obtain enough resolution in frequency space, the method requires a "square" wave pattern that extends over a relatively large number of cycles.

Of the three approaches above, for the purpose of developing the present analysis, the third one was selected. Four grid standards were constructed using alternative strips (2mm high) of Tantalum and Mylar. The thickness of the individual strips in the standards were 20 mils, 10 mils, 5 mils and 2 mils, providing sample frequencies of 1, 2, 4 and 10 lp/mm. An X-ray image of the four standards is shown in Figure 2.6.3.

The purpose of the standards is to provide images which are to be Fourier transformed. The Fast Fourier Transform technique (FFT) is applicable to arrays whose size is a multiple of 2. We have found that a size of 64 is a

good compromise between resolution of the transform function (frequency resolution) and difficulty in construction of the standards. Remember that in a discrete Fourier transform operation:

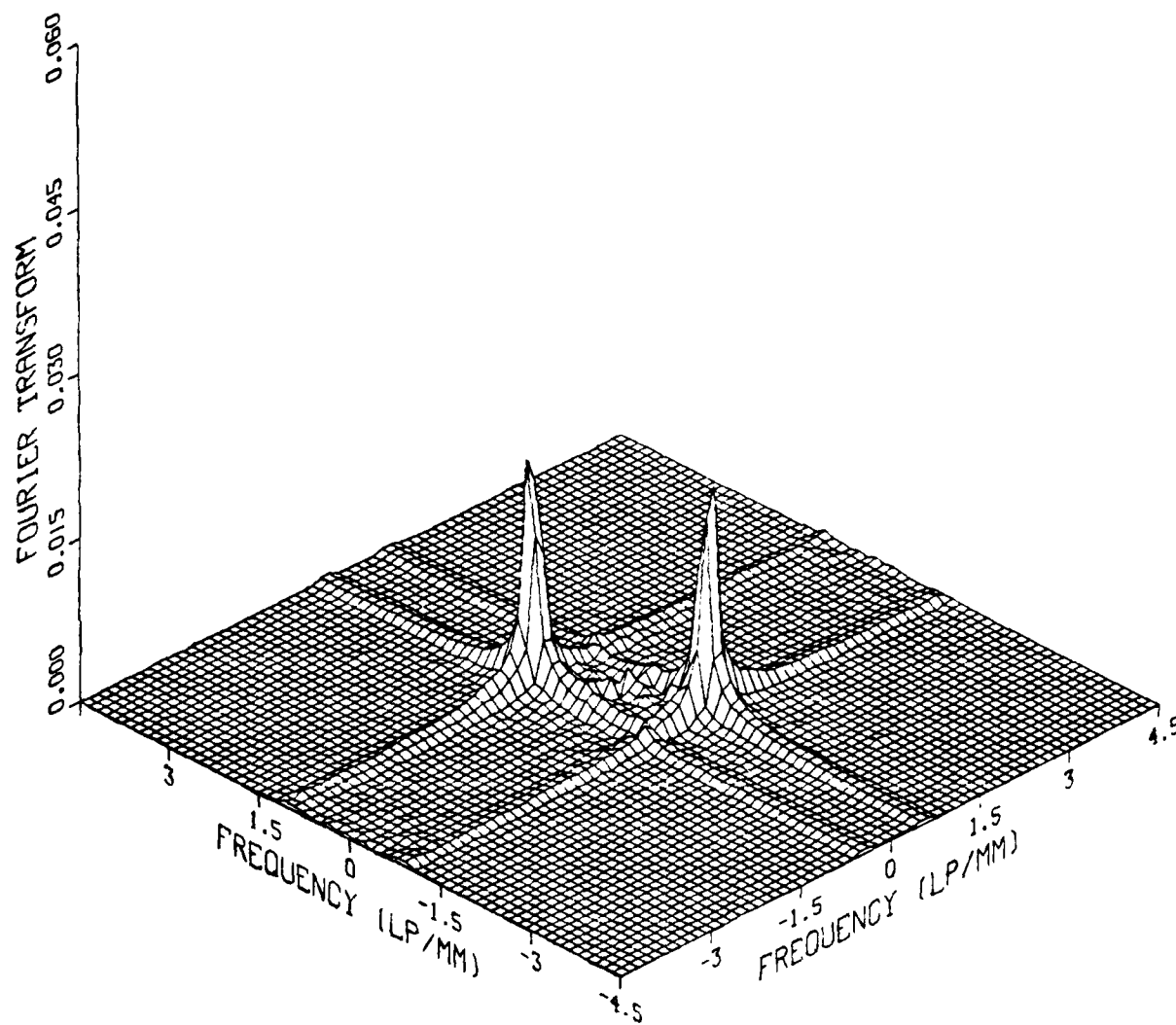
$$\Delta x \Delta f = 1/M \quad (2.6.1)$$

where x is the size of the pixel, f is the frequency interval and M is the number of points in the array being transformed. Therefore, for a certain pixel size, if we want better frequency resolution, we must increase the number of pixels, that is the size of the standard. In Figure 2.6.3 the width of the 10 lp/mm (2-mil strips) standard is smaller than the others because, to provide useful results, it must be used with systems having small pixel size.

It is possible to compute either a two-dimensional or one-dimensional Fourier transform of the grid image. A two-dimensional FFT, such as the one shown in Figure 2.6.4, can provide the MTF for different orientations of the grid. The two-dimensional FFT, however, should be computed off line, not because of computing time limitations, but because of memory limitations. A program for the calculation and analysis of the one-dimensional Fourier transform of selected parts of an image such as the one in Figure 2.6.3 has been written to run on the same PDP 11/23 computer which is used for data taking. The fast Fourier transform routine used is RADIX-4 developed by Morris⁵.

The user inputs the coordinates of the lower left corner of the matrix which one wishes to transform. Each line of the matrix is transformed and the modulus of the transform of each line is averaged recursively. After computing the transform, the area of the peak at the characteristic frequency is calculated. The user inputs an estimate of the range of the peak, from a visual survey of the behaviour of the transform. The program computes the area of the peak by adding the values of the transform function within the range and subtracting the average over intervals of equal width bracketing the peak. When the peak is well defined, the area computed with this procedure is not very sensitive to the choice of the range for the peak.

⁵Morris, Robert L., Time Efficient Radix-4 Fast Fourier Transform, in Programs for Digital Signal Processing, IEEE, 1979, p. 1.8-1).



SAI-84RP-10

Figure 2.6.4 Modulus of Two-Dimensional Fourier Transform of Grid Image.

For low frequencies, only a limited number of cycles is contained in the range of pixels used in the Fourier transform. Chances are that this range will not contain an integer number of cycles, for example an integer number of cycles may take 60 rather than 64 pixels. Since the discrete transform is cyclical, it will be assumed to be periodic with period 64, and a discrepancy, due to edge effects, will arise. In this case it is better to rebin, that is, redistribute (by interpolation) the values of the function in such a way that there will be 64 (smaller) pixels in place of the original 60. Although there is some loss of information and some filtering due to the interpolation, this is usually to be preferred to the edge effects associated with the non-integer number of cycles.

Figure 2.6.5 shows how the method is applied. At the left are parts of the image containing the grids and at the right are the respective Fourier transform moduli, showing the peak areas.

Once two and preferably more peak areas have been computed, the modulation transfer function is obtained by fitting to the data a function of the form:

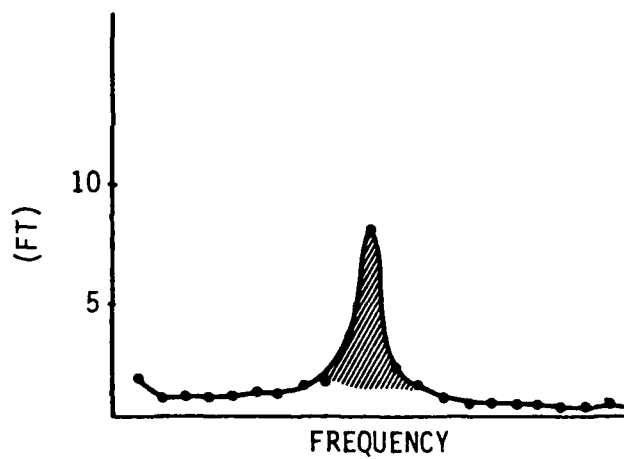
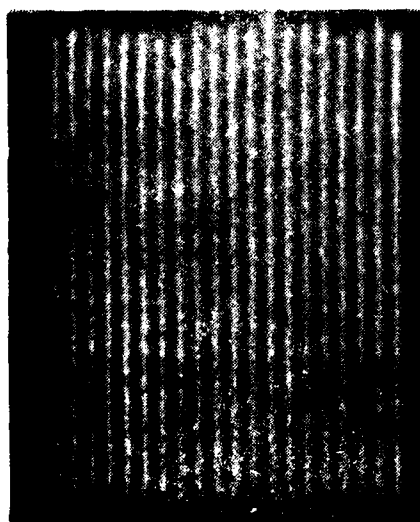
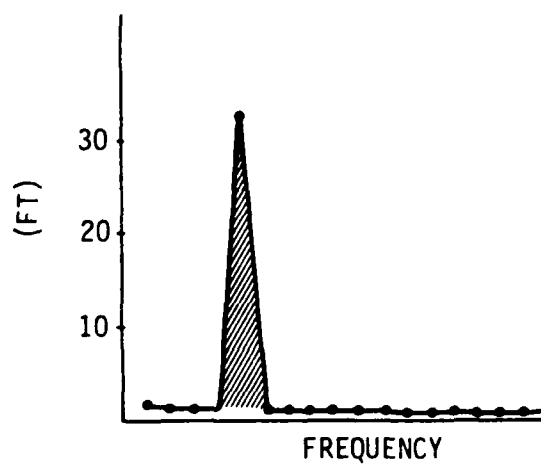
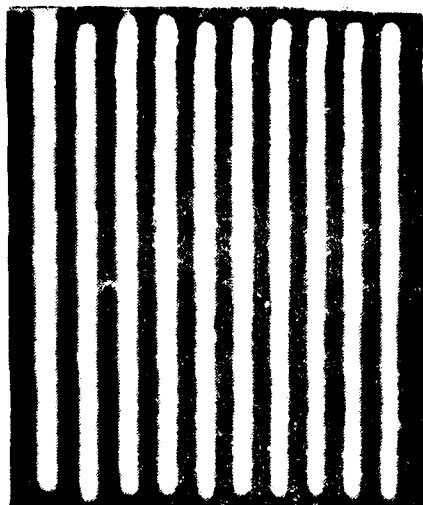
$$\text{MTF} (f) = \text{EXP} - \left(\frac{f}{f_c} \right)^n \quad (2.6.2)$$

where f is the frequency and n and f_c are parameters. An example of such fit from the results of Figure 2.6.5 is given in Figure 2.6.6.

2.6.3 Determination of the Noise Structure

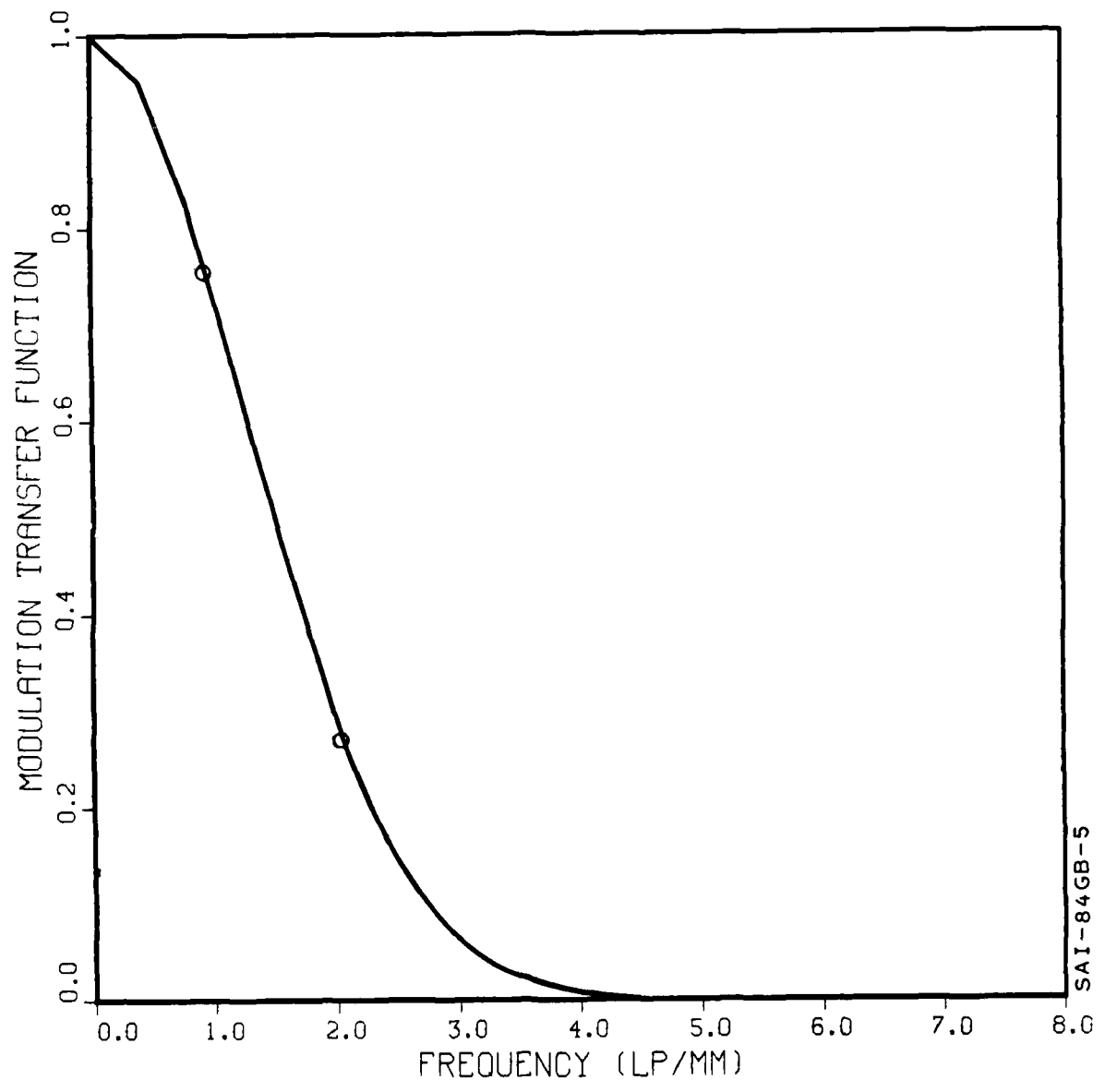
The second step in the methodology is the determination of the dependence of the single pixel noise on the observed intensity level. As it will be shown shortly, this is obtained from an analysis of the variance of the difference of pixel levels in two independently acquired images having similar uniform intensity.

One way of determining experimentally the noise for a single specific pixel would be to follow the variation of the level in this pixel at different times. This would require acquisition and analysis of many independent images.



SAI-84GB-9

Figure 2.6.5 Grid Images and Modulus of Their One-Dimensional Fourier Transforms.



SAI-84GB-5

Figure 2.6.6 Modulation Transfer Function Derived from Data of Fig 2.6.5

Since we are interested in the variance of a generic pixel rather than the variance of a specific pixel, we then would have to average the variance over a group of contiguous pixels.

The same information can be obtained by analyzing the difference of only two independent images, and assuming that, in average, every pixel has the same statistical behaviour. We first collect two independent images which contain areas of different uniform intensity, distributed over the useful dynamic range. Each area should contain at least 20 x 20 pixels to ensure statistical accuracy in the analysis. Figure 2.6.7 shows an example of two such images. The two images should be collected in similar conditions, but there is the possibility that the intensity of the X-ray source may vary from one image to the other.

We now concentrate on the same pixel in a corresponding area of the two images. The level $G_i^{(1)}$ at pixel in image 1 will be:

$$G_i^{(1)} = K_i I^{(1)} + N_{fi} + N_i^{(1)} \quad (2.6.3)$$

where K_i is the gain of pixel i , $I^{(1)}$ is the source intensity, N_{fi} is a fixed pattern noise, and $N_i^{(1)}$ is the intrinsic random noise of pixel i in image 1. Similarly, for image 2:

$$G_i^{(2)} = K_i I^{(2)} + N_{fi} + N_i^{(2)} \quad (2.6.4)$$

We now take the difference of the two images:

$$\Delta_i = K_i (I^{(1)} - I^{(2)}) + N_i^{(1)} - N_i^{(2)} \quad (2.6.5)$$

and calculate the variance over a group of contiguous pixels within the area of uniform intensity:

$$\sigma_{\Delta}^2 = (I^{(1)} - I^{(2)})^2 \sigma_K^2 + \bar{K}^2 (\sigma_{I_1}^2 + \sigma_{I_2}^2) + 2 \sigma_n^2 \quad (2.6.6)$$

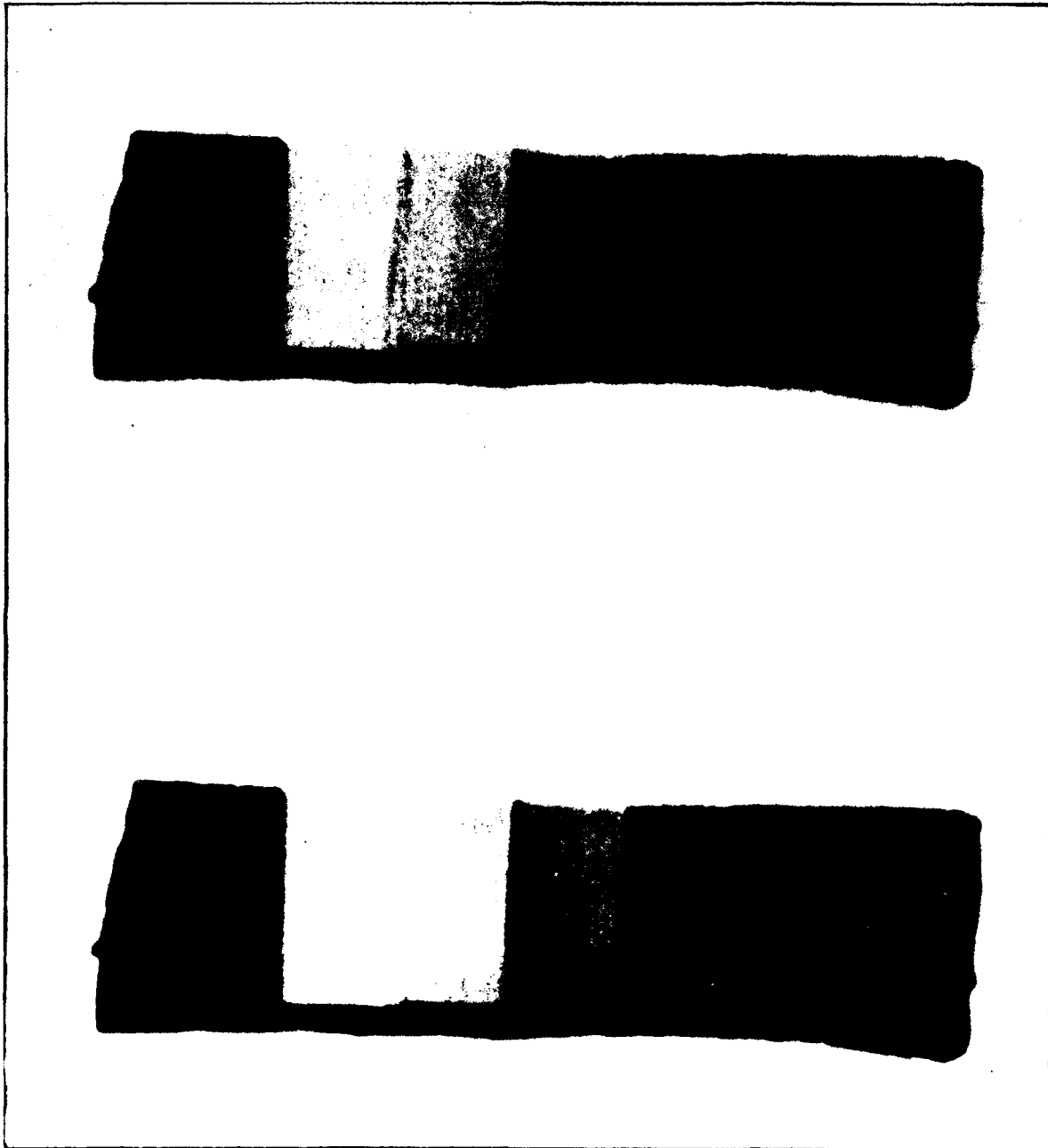


Figure 2.6.7 Example of Two Independent Images for the Analysis of the Noise Structure.

Since the noise due to the radiation is poissonian

$$\sigma_I^2 = K_R I \quad (2.6.7)$$

where K_R is a proportionality constant. If the two source intensities are not equal, then

$$I^{(2)} = C I^{(1)} \quad (2.6.8)$$

When (2.6.7) and (2.6.8) are substituted into (2.6.6) we obtain:

$$\sigma^2 = (1-C)^2 \sigma_K^2 I^2 + (1+C) \bar{K}^2 K_R I + 2 \sigma_N^2 \quad (2.6.9)$$

If the two source intensities are equal ($C = 1$), the variance of the difference is a linear function of the intensity. If the source intensities are not equal, the variance of the difference is a quadratic function of the intensity. Our current experience indicates that a linear analysis of the variance is usually sufficient. However, even if the source intensities are different and a quadratic behavior is apparent, the same analysis applies. In the linear case, we first fit the experimental σ_Δ^2 as follows:

$$\sigma_\Delta^2 = A_1 I + A_0 \quad (2.6.10)$$

and the variance for a single pixel is given by:

$$\sigma^2 = (A_1 I + A_0)/2 \quad (2.6.11)$$

In the quadratic case, we fit the experimental σ^2 as follows:

$$\sigma^2 = A_2 I^2 + A_1 I + A_0 \quad (2.6.12)$$

and the variance for a single pixel is obtained as:

$$\sigma^2 = \frac{A_1}{1+C} I + \frac{A_0}{2} \quad (2.6.13)$$

where the constant C is obtained, as defined by Eq. (2.6.8), as the ratio of the average levels of the areas analyzed.

NO-A100 039

HIGH RESOLUTION PROTOTYPE REAL-TIME RADIOGRAPHY SYSTEM
(U) SCIENCE APPLICATIONS INTERNATIONAL CORP SAN DIEGO
CA R H POLICAR NOV 86 AFMNL-TR-86-4061

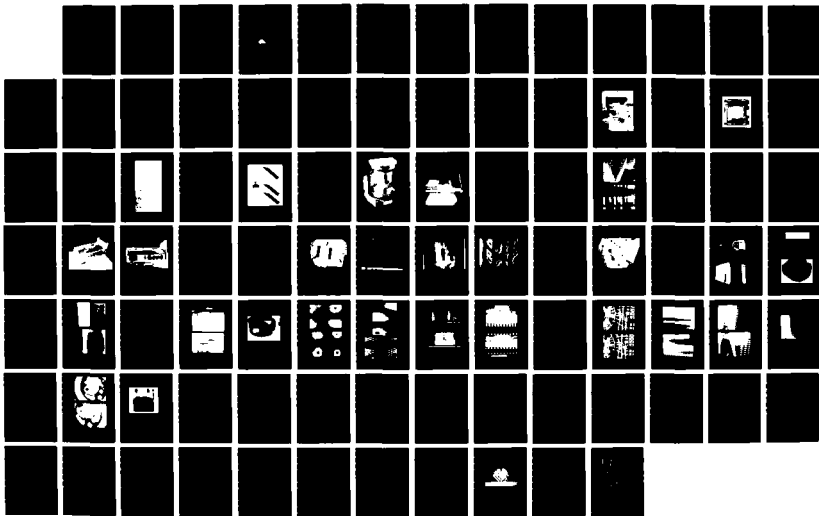
2/2

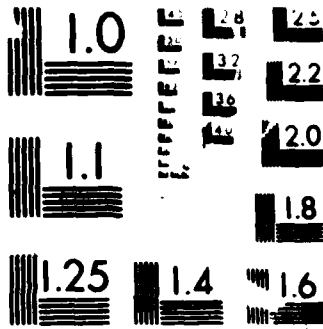
UNCLASSIFIED

F33615-03-C-5010

F/B 14/4

ML





MICROCOPY RESOLUTION TEST CHART

10-1000

Figure 2.6.8 shows an example of linear analysis of experimental values of σ^2 versus I for a Thomson imaging tube and TV system. This analysis provides the signal-to-noise ratio necessary for the calculation of the figure of merit.

2.6.4 Definition of the Figure of Merit

The third step in the methodology is the definition of a technical figure of merit which combines the MTF and the noise structure information to provide an indication of the ease with which one can detect a hole in a penetrometer.

The ability of an observer to detect an abnormality in an image depends both on the signal to noise ratio associated with that abnormality and on the modulation transfer function. Consider an image with uniform intensity of \bar{h} counts per unit surface, containing a disk of diameter D and reduced count density $h - \Delta h$. If the image is not too small (relative to the smearing effect of the MTF), the threshold contrast $\Delta h/\bar{h}$ at which the disk is detected a reasonable number of times by different observers is proportional to $1/\sqrt{\pi D \bar{h}/4}$. This is equivalent to the average signal to noise ratio (inverse of \sqrt{N}/N where N is the total number of counts in the disk) for poissonian statistics.

When the disk diameter becomes small, the MTF has a significant smearing effect and contributes, in addition and separately from the noise effect, to prevent the disk image from being detected. We propose, therefore, to use the following figure of merit:

$$FOM = \frac{D}{p} \frac{I}{\sigma} S(D, MTF) \quad (2.6.14)$$

The ratio I/σ is the signal to noise ratio determined from a fit to experimental data, σ being the standard deviation for a single pixel, and p is the linear dimension of the pixel (D/p is proportional to the square root of the number of pixels in the disk). The factor $S(D, MTF)$ is defined with reference to Figure 2.6.9. Consider first the radially symmetric rectangular function $F_R(r)$, defined as follows:

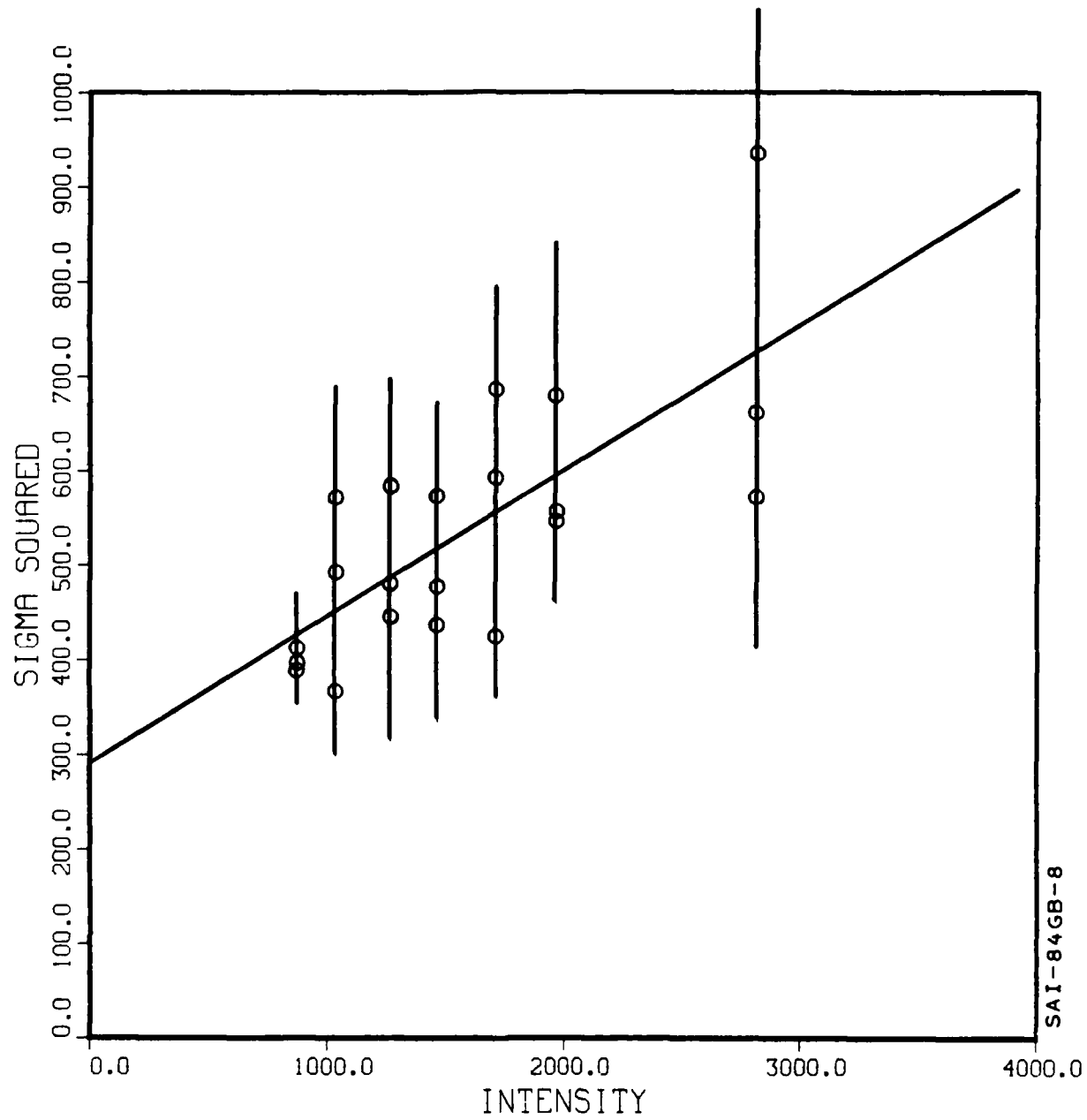
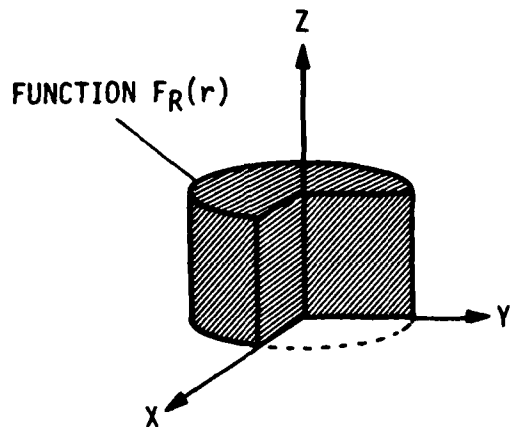
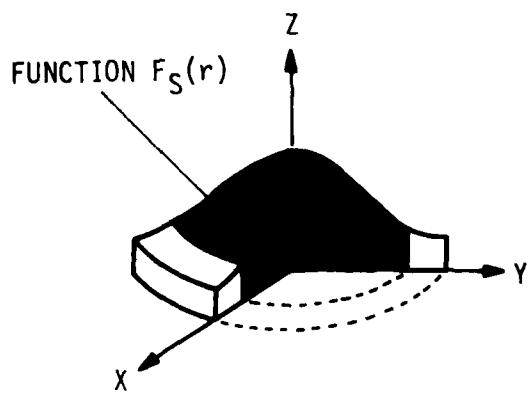


Figure 2.6.8 Analysis of Single Pixel Variance Versus Intensity and Determination of Noise Equivalent.



INTEGRALS

-  S₃
-  S₁
-  S₂



$$S(D, MTF) = \frac{S_1 - S_2}{S_3}$$

SAI-84GB-4

Figure 2.6.9 Definition of the Integral S(D,MTF) used in the Figure of Merit.

$$F_R(r) = \begin{cases} 1 & \text{for } r < D/2 \\ 0 & \text{for } r > D/2 \end{cases} \quad (2.6.15)$$

Consider next the function $F_S(r)$ which results from the effect of the MTF on $F_R(r)$. This function is obtained by the convolution of $F_R(r)$ with the inverse Fourier transform of the MTF. Assuming that the MTF has radial symmetry, $F_S(r)$ also has radial symmetry. Let us now calculate the integral S_1 of $F_S(r)$ over the area of the disk, and integral S_2 over an annular area surrounding the disk and having the same area as the disk. The factor $S(D, \text{MTF})$ in Eq. 2.6.14 is defined as:

$$S(D, \text{MTF}) = \frac{S_1 - S_2}{S_3} \quad (2.6.16)$$

where S_3 , as shown in Figure 2.6.9., is the integral of the unsmeared function $F_R(r)$. It can be seen from the above definition that, when the disk is large enough that the MTF does not have a significant effect, the factor S is close to unity. On the contrary, when the disk is small and is being completely smeared out by the MTF, the factor S tends to zero.

There are two possible ways to compute the integral $S(D, \text{MTF})$. The first way is to first compute the inverse Fourier transform of the MTF, to obtain the line spread function (LSF), then the convolution of the LSF, with the rectangular function, and then the integrals in radial symmetry.

The second way is to compute first the product of a $\sin f/f$ function (this is the Fourier transform of the rectangular function) with the MTF, take the inverse Fourier transform of the result, and then compute the integrals in radial symmetry.

The MTF can be approximated by the analytic form:

$$\text{MTF}(f) = \text{EXP} - \left(\frac{f}{f_c} \right)^n \quad 2.6.17$$

and can therefore be calculated at the points of a fine mesh, both for the calculation of the inverse transform and for the product of transforms method.

Table 2.6-1 shows calculated values of $S(D,MTF)$ for $f_c = 2\text{mm}^{-1}$, $n = 1.5$, and for different values of D , using both calculational schemes. A numerical Fast Fourier Transform (FFT) algorithm using 1024 points was used in the calculation, and the small differences in the values computed with the different methods give an idea of the mesh effect.

It should be stressed that the figure of merit, as defined, assumes that the MTF is radially symmetric. If the MTF in the horizontal direction is significantly different from the MTF in the vertical direction, then an average value should be used to calculate $S(D,MTF)$.

The figure of merit as defined is a function of the intensity I . For the purpose of comparing different systems, one can use its value at the middle of the useful range. Also, to make meaningful comparison, the figure of merit should be computed from data obtained in a similar acquisition mode, for example, single frame, or summing the same number of frames.

A one-dimensional simulation has been carried out to illustrate the effects of the MTF, of the signal to noise ratio, and their combination into a figure of merit. Figures 2.6.10 through 2.6.12 contain three subplots each. The subplot at the top gives the MTF as a function of frequency. The subplot immediately below contains the fractional noise as a function of observed intensity. The subplot at the right contains the simulation of the cross section of the image of a round hole, as modified by noise and MTF. The characteristics of the system and the diameter of the hole are listed on top of this last subplot. For example, in Figure 2.6.10 we see the effect of a rather good MTF on a hole of 1mm diameter, imaged so that the base level (INTENSITY) is at 2500, and the variation (CONTRAST) is 300. Gaussian noise corresponding to the noise subplot has been added in the simulation. The figure of merit, calculated as described in the previous section, is also listed.

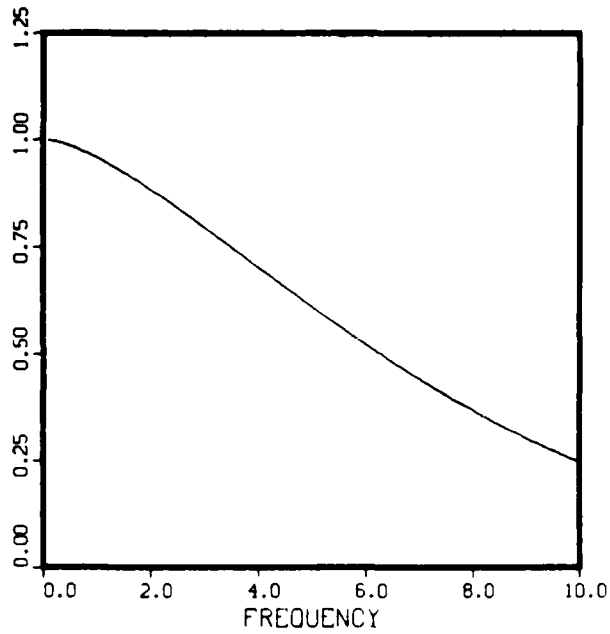
Figure 2.6.11 shows the effect of worsening of the MTF, with unchanged signal to noise ratio. Note that the figure of merit has changed from about 857 to 412. Similarly, Figure 2.6.12 shows the effect of an increase in the noise without varying the MTF, which results in a decrease of the figure of merit to about 115.

TABLE 2.6.1 VALUES OF S(D, MTF) FOR $f_c = 2 \text{ mm}^{-1}$ AND $n = 1.5$.

D (mm)	S (D, MTF)	
	COMPUTED WITH CONVOLUTION METHOD	COMPUTED WITH PRODUCT OF TRANSFORMS METHOD
5.0	.9029	.9034
4.0	.8813	.8812
3.0	.8469	.8456
2.0	.7800	.7788
1.0	.6059	.6108
0.5	.3876	.3979
0.4	.3209	.3298
0.3	.2434	.2480
0.2	.1492	.1446
0.1	.0441	.0343

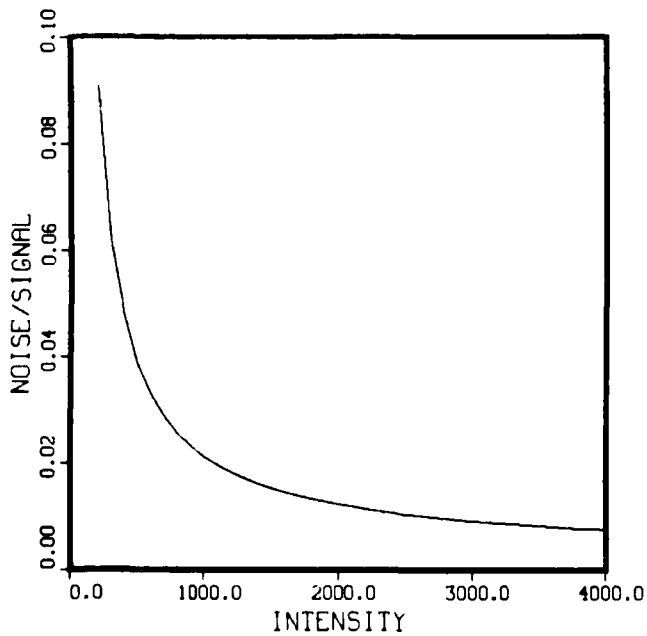
SAI-84GB-11

MTF



MTF EXPONENT - 1.50
CRITICAL FREQUENCY (MM-1) - 8.00
INTENSITY - 2500.00
SIGNAL TO NOISE - 96.23
PIXEL SIZE - 0.10
DIAMETER - 1.00
CONTRAST - 300.00
FIGURE OF MERIT - 857.54

NOISE



SIMULATION

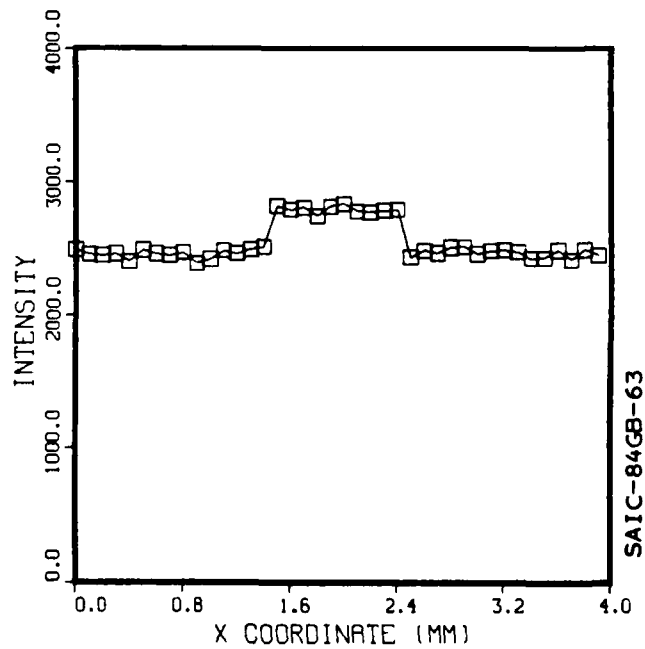
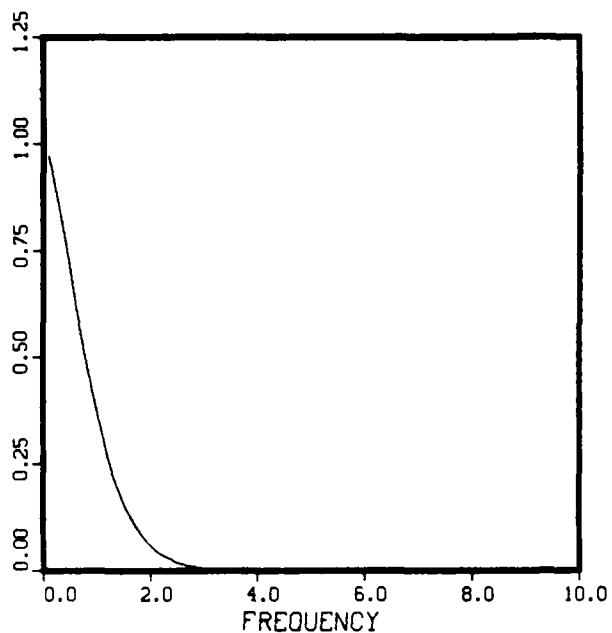


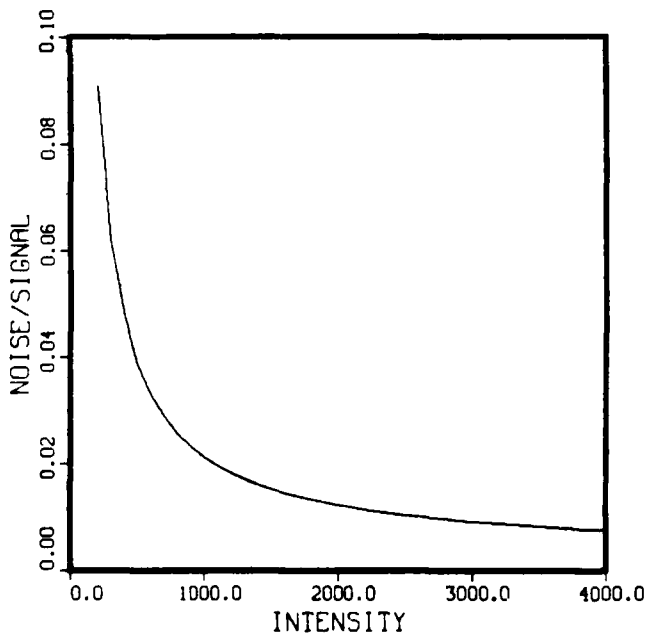
Figure 2.6.10 Simulation of Image of Hole observed with a System characterized by MTF and S/N Ratio.

MTF

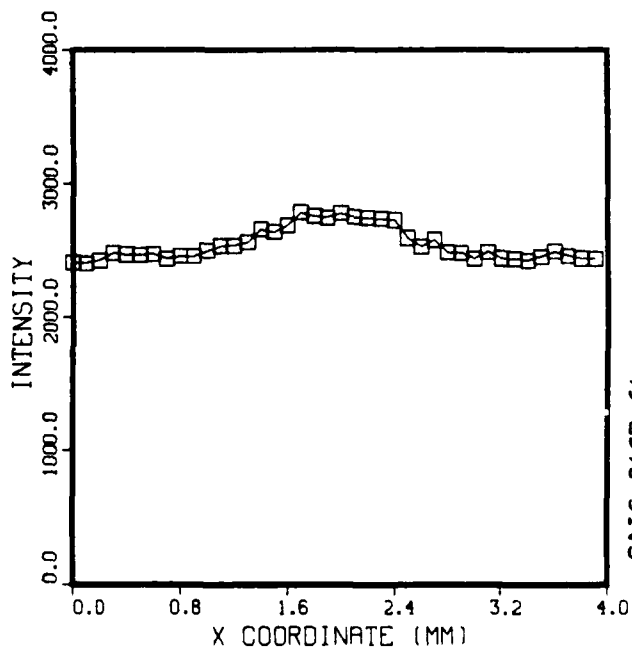


MTF EXPONENT - 1.50
CRITICAL FREQUENCY (MM-1)- 1.00
INTENSITY - 2500.00
SIGNAL TO NOISE - 96.23
PIXEL SIZE - 0.10
DIAMETER - 1.00
CONTRAST - 300.00
FIGURE OF MERIT - 411.89

NOISE

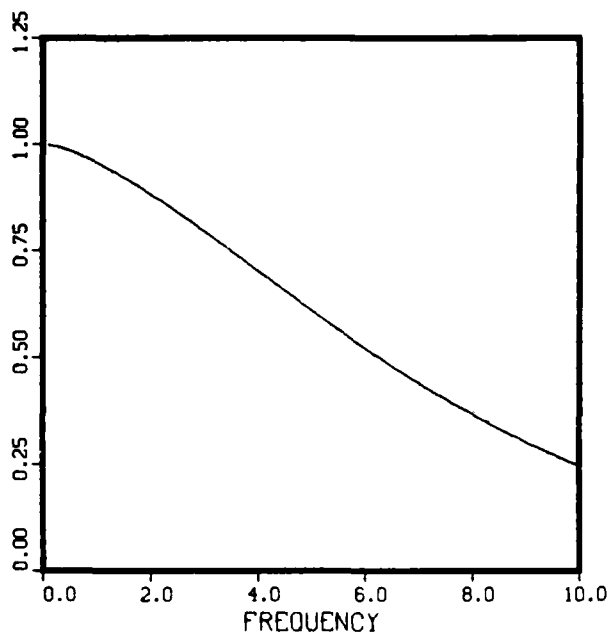


SIMULATION



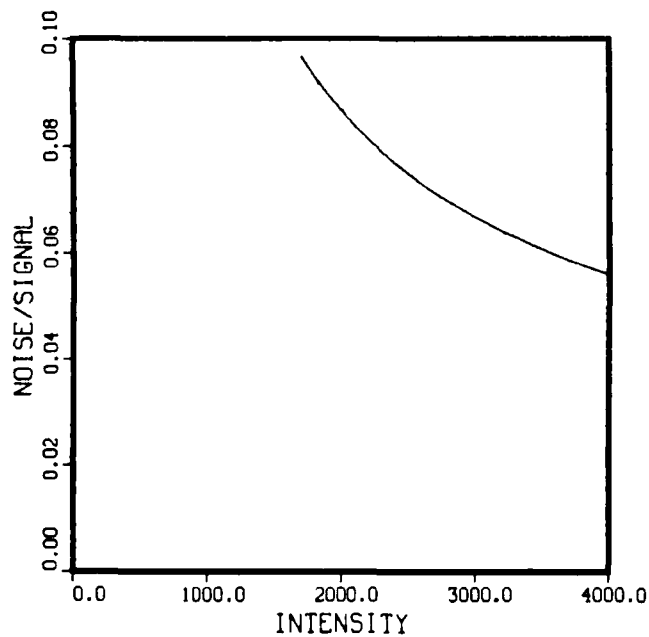
SAIC-84GB-64

Figure 2.6.11 Effect of Worsening of the MTF on the Figure 5.1 Test Case.

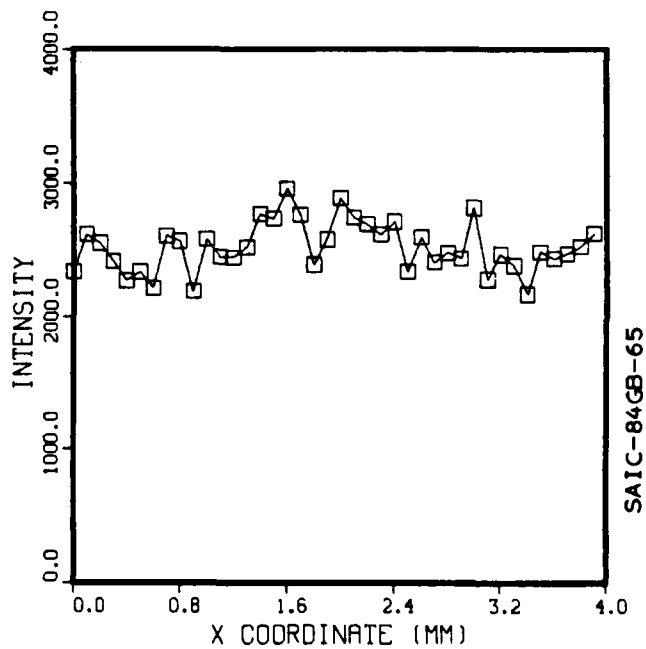


MTF EXPONENT - 1.50
 CRITICAL FREQUENCY (MM-1) - 8.00
 INTENSITY - 2500.00
 SIGNAL TO NOISE - 13.36
 PIXEL SIZE - 0.10
 DIAMETER - 1.00
 CONTRAST - 300.00
 FIGURE OF MERIT - 115.23

NOISE



SIMULATION



SAIC-84GB-65

Figure 2.6.12 Effect of Worsening of the S/N Ratio on the Figure 5.1 Test Case.

2.7 DEVELOPMENT OF A PRACTICAL FIGURE OF MERIT RANKING CONVERSION SCREENS

In the preceding section, a model is developed for the Figure of Merit as a measure of the ability of a system to sense a low contrast defect against a noisy background. The model has many appealing features in that it realistically describes both the effects of MTF and noise on the recognition criteria for varying size defects. The integral, $S(D,MTF)$, properly takes into account the reduction in apparent contrast due to the reduction of the image inside the actual object diameter as well as the increase in the "background" outside the object diameter due to the effects of the point spread function. While the model is valid and physically intuitive it has some significant drawbacks.

- It is difficult to calculate without analytical forms of the MTF.
- It is truly only valid for circular defects.
- It uses signal-to-noise ratios that can be easily measured on an electronic system but are not well defined for single components like the converter screen.

To simplify the model and make it more applicable to screen analysis and ranking, several approximations can be made.

The original model used the form for Figure of Merit

$$FOM = \frac{D}{p} \left(\frac{I}{\sigma} \right) S(D,MTF)$$

where: I/σ is the pixel signal to noise ratio
 $(D/p)^2$ is proportional to the number of pixels covering the defect.

$S(D,MTF)$ is the overlap integral that determines the effect of MTF on reducing the signal from D and on increasing the background in the immediate area.

To apply the model to a simple passive converter screen one can make a similar argument using screen brightness and defect areas. Since the signal coming out from a given area of the screen is proportional to the radiance and

the area in question and its variance is proportional to the square root of I, the first two terms in the above equation can be replaced by

$$\frac{D}{p} \left(\frac{I}{\sigma} \right) \Rightarrow D \sqrt{R/d} \quad \begin{array}{l} \text{where } D \text{ is the defect diameter} \\ R/d \text{ is the radiance/dose rate} \\ \text{and is proportional to } I \end{array}$$

The integral $S(D, MTF)$ is more complicated since it is the averaged difference between the convolution of the defect and MTF inside and outside the actual defect diameter. Although it is not exactly correct, the simple MTF curve itself represents a good approximation to the behavior of $S(D, MTF)$. This can be seen in Figure 2.7.1, where the S integral and a curve proportional to the MTF for the example given in the previous section are used. (Actually the curve is 90% of the original MTF) The effective frequency has been taken as the fundamental spacial frequency describing the effective defect diameter. Assuming a circular defect of diameter D , one can show that the effective diameter along a single axis is $8/3 D$ or about $.85D$. Since the fundamental spatial frequency for an object of dimension D_e is:

$$f = \frac{1}{2 D_{\text{eff}}} = \frac{1}{16/3\pi D} \cong \frac{1}{1.7 D}$$

for a circular defect

Thus an effective figure of merit that can be used to predict screen performance for varying sized defects is

$$FOM = D \sqrt{R/d} \quad MTF \left(\frac{1}{1.7 D} \right)$$

NOTE: To be more accurate, the spectral overlap X_s should also be included, but since it is very nearly constant for the screens of interest it is omitted.

The use of the MTF rather than the true S will slightly weigh the FOM toward the mid resolution performance which may in fact be desirable. In any case, since the FOM is plotted as a function of D , one can always compare relative performance at the resolution level of interest. The figures of merit

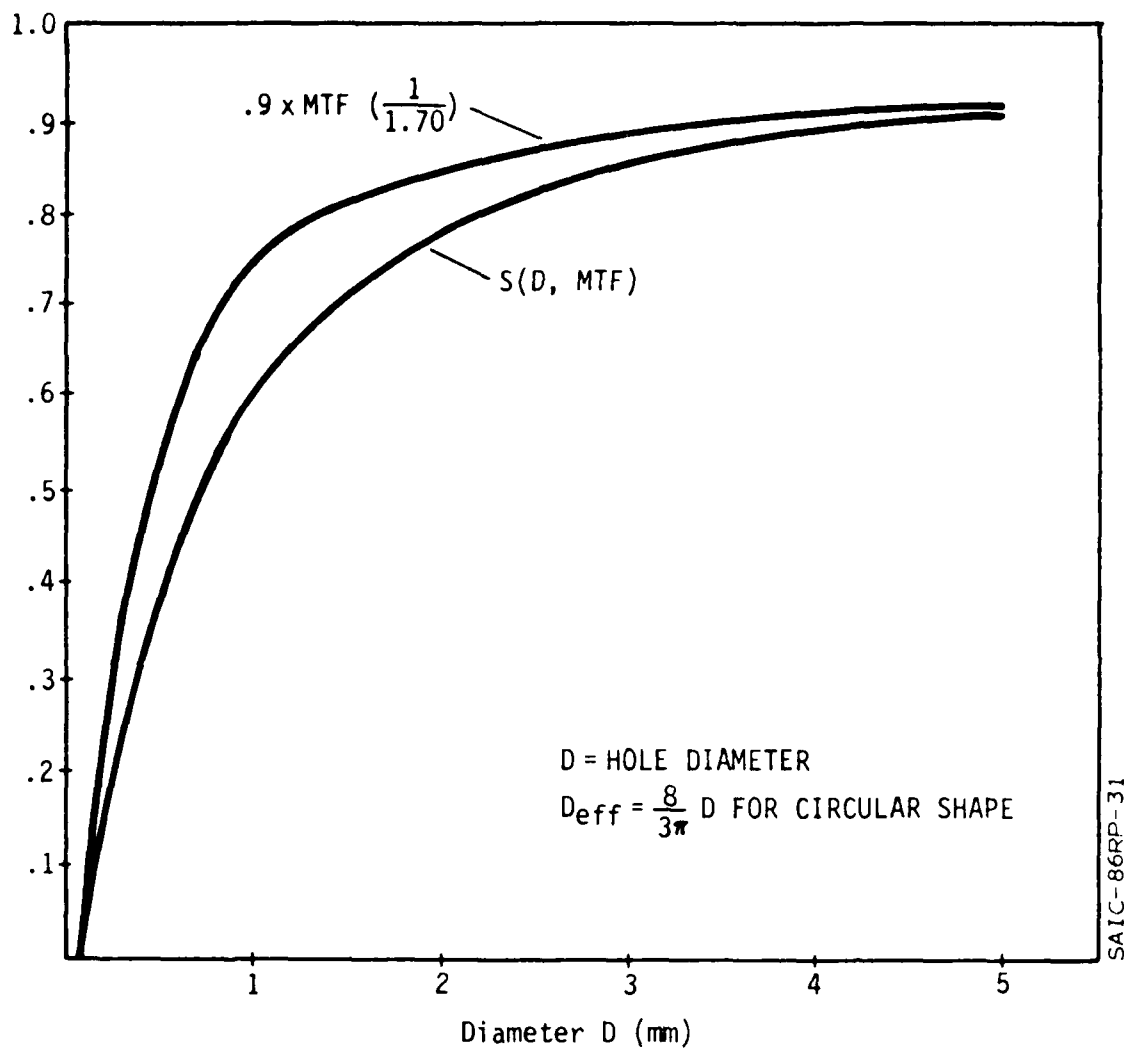


Figure 2.7.1 Comparison of $S(D, \text{MTF})$ Integral Developed for FOM Model and the Corresponding MTF Curve for $F_{\text{eff}} = D \frac{1}{2 D_{\text{eff}}}$.

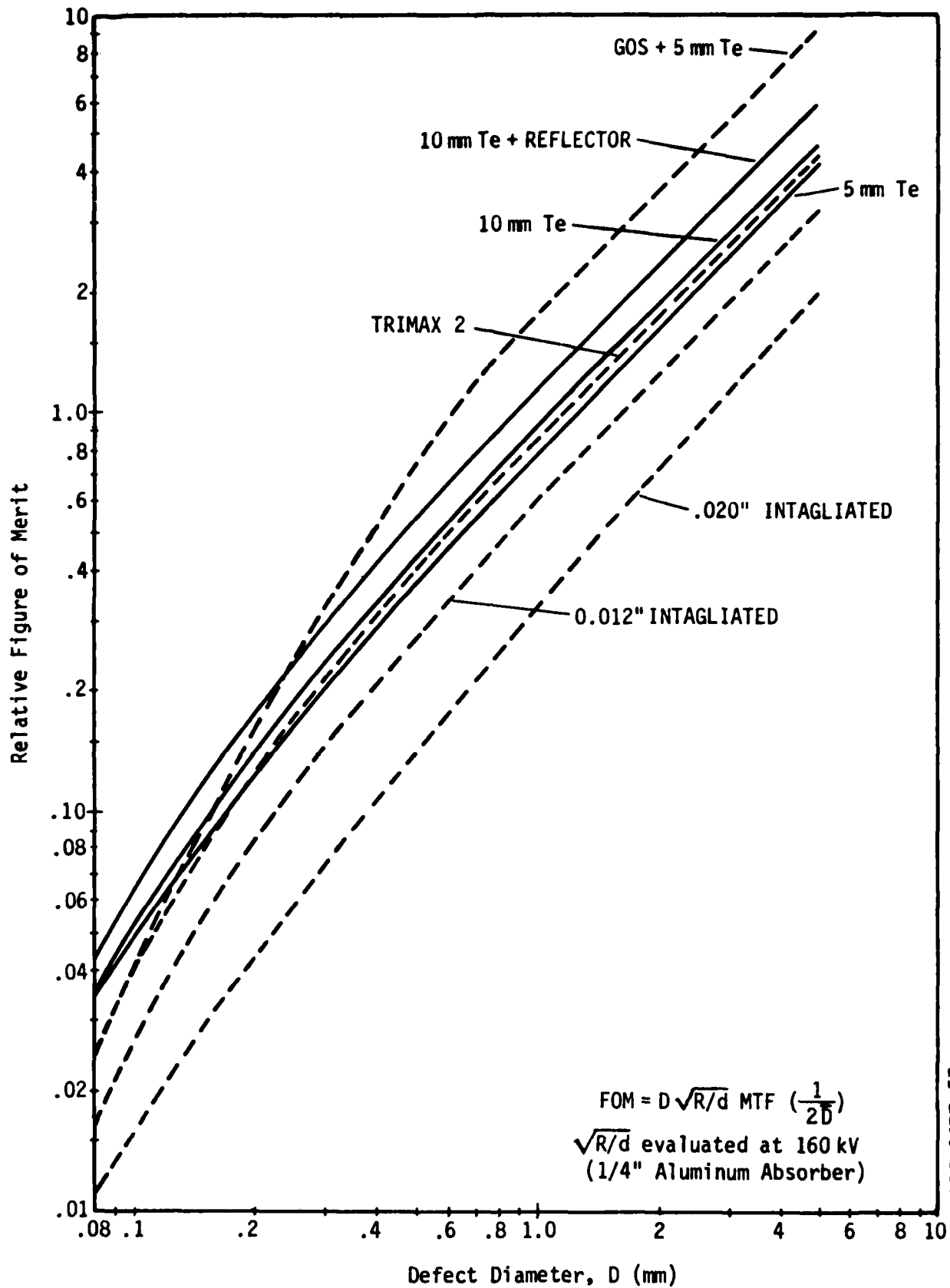


Figure 2.7.2 Figure of Merit for Conversion Screens Based on Recognition of Circular Defect of Diameter, D.(mm).

for all screen measured are shown in the log-log plot of Figure 2.7.2 for an X-ray potential of 160KV and 1/4" Aluminum absorber. This curve will look somewhat different at every low energies where the GOS screens show up as brighter. The plot shows that certain screens may excel in one region yet be quite average in another. The GOS overcoated terbium fiber optic screen is such an example. Its overwhelming brightness makes it the clear standout in the mid to low resolution areas but it drops off at the higher resolution (small D) areas.

Figure of merit as defined here is a reasonable predictor of performance. Other factors may influence the decision on which screen to choose. The intensities used in the FOM calculation are taken from the 160kV values of Radiance/Dose Rate or Optical Conversion Efficiency. Operating at a much higher or lower energy might change the relative weights. In the experiments carried on with the line scanner, three screens were used most often and their selection depended on the subject and required energy range. These included

GOS + 5mm Terbium:	General Purpose-mid Energy Ranges
10mm Terbium + Reflector:	High Energies, good scatter rejection
TRIMAX 2:	Very soft X-rays - useful down to 13KV

Interestingly enough, the measurements made on the line scanner showed the TRIMAX 2 screen to be the brightest. This was somewhat puzzling at first but can be understood when the measurement process of Section 2.5 is compared to the scanner itself.

The optical conversion efficiency was measured on all screens using a calibrated 1:1 lens. This provided an exact measure of area and solid angle. For the lens used, the half angle of acceptance was about 14.0° . All the screens except the TRIMAX used a $na = .6$ fiber bundle which produce a half angle of emission of 36° . Thus the lens sampled the peak portion of the beam with no loss. The TRIMAX screen was mounted on a $na = 1.0$ plate and its emission could be expected to follow a lambertian distribution out to nearly 90° . Since the input to the linear scanner is also a $na = 1$ system, virtually all the light from the TRIMAX screen is collected in the system. This could

lead to 2x to 2.5x higher efficiency for the TRIMAX 2 system than for the other screens which was consistent with our linear scanner measurements. The examples shown in Section 3.4 use these three screens and demonstrate the effectiveness of each. In particular, the TRIMAX 2 screen is extremely effective on composites using very soft X-rays and the 10mm terbium is equally effective at looking into thick steel parts such as ordinance which are normally extremely difficult to inspect in real time.

The fact that the FOM's for the different screens are all quite close truly reflects the fact that there already has been a significant preselection in converter screen types. A similar analysis comparing a typical real time image amplifier system and any of the better screens coupled to a linear scanner would show a dramatic difference in performance.

3.0 LINEAR SCANNER TECHNOLOGY

3.1 BASIC PRINCIPLES OF OPERATION

The present work on conversion devices has emphasized those scintillation screens that would work with a fiber optically coupled line scanner. Although the analysis has been quite general, it has limited the screens to either fiber optic materials that were direct converters or to those screens that can be proximity coupled to fiber optic systems. The data obtained on the screens is useful for both area and line scan devices and with lens or fiber optic coupling. Nevertheless a limitation was imposed on the types of materials surveyed, and in this section we shall explore the design criteria that justified that specialization in outlook.

The distinction between a conventional area sensor scanned by a video camera and a line scanner is somewhat arbitrary. The video scan does indeed dissect the area into a number of discreet lines which are displayed sequentially on the video monitor. The line scanner produces the complete image by physically moving an object past a single line sensor and storing the result in a video memory. From the point of view of the display, both pictures are complete two-dimensional images formed of discreet video lines of data, differing only in the rate at which that data is collected. The area imager is typically collected at a 30Hz frame rate while it may take several seconds to produce a line scan image making the area imager more nearly "real time" than the line scanner.

For X-ray sensors, this difference in scan technology has additional implications in the actual quality of the image. Radiographs are in fact shadows or skiagrams of the variations in sample density and atomic number. If the only process involved were X-ray absorption, these shadow images would represent idealized measures of the material distribution. Unfortunately for most medium-to-low atomic numbered materials and for all but the lowest energies, X-ray images are strongly affected by the non-local effects of Compton scattering. Since this scattering is typically isotropic or at least broadly spread in a forward direction, its effect is to reduce the effective contrast of the incident X-ray distribution. The effect of scattering is

analogous to having someone turn on a light while watching a movie in that generally the darker parts of the image are most affected. X-ray line scanners permit the use of a radial fan beam which is collimated before it reaches the sample. Since beam line and the scanner slit are matched, the total detected scatter is reduced. This reduction occurs because both just a single narrow line of the part is illuminated with radiation, as well as because only a small fraction of the scatter from that reduced area overlaps with the line detector. Factors of 100x to 1000x reduction in the effects of scatter are realized on well collimated systems. Another special characteristic of line scan technology is the removal of parallax from one axis. Thus subjects like honeycomb panels which typically have only a 2 to 3 inch useful field of view can be scanned without limit along one axis.

The second property of the present approach is the use of fiber optic coupling throughout the system. The decision to use fiber optics rather than lenses to couple the light is based primarily on the enhanced efficiency of direct fiber optical coupling. This is made more practical using the line scanner since it is much simpler to deal with a single line than with a large area when using fiber optic materials. Typically Ω , the solid angle subtended by a lens viewing a converter screen can be expressed as a function of the magnification (less than unity in our case) and the aperture of the lens (f stop).

$$\text{where } \Omega = \frac{\pi}{4f^2} \frac{M^2}{(1+M)^2} \quad (3.1.1)$$

and the included conical angle α is given by:

$$\sin^2 \alpha = \frac{1}{(\pi/\Omega)+1} \quad \text{for small } \alpha \quad (3.1.2)$$

since $\sin \alpha$ is the same quantity that describes the numerical aperture of a fiber optic bundle, this is a relatively good way to compare lens and fiber coupled systems. Generally, the relative fraction of capture in the forward half sphere is expressed as

$$\frac{\Omega}{2\pi} = \frac{1/2 \sin^2 \alpha}{1 - \sin^2 \alpha} = \frac{M^2}{8f^2 (1+M)^2} \quad (3.1.3)$$

One can use this relationship to compare what fraction of the light is collected in an optical system as a function of the components used. The above equations fail in the limit of very large aperture because the effective lens area is no longer expressed correctly by the f number.

Without fully analyzing the system at this point it can be seen that for an f 1.0 lens and unity magnification, the relative light collection with a single lens is 1/32 while with a n.a. = 1 fiber optic all the light is collected. Both calculations are based only on solid angle and neglect self absorption in the media itself. The difference between the efficiency of collection of a lens and fiber optic system becomes an order of magnitude greater in practical imager designs and is the principal driver in this design decision.

The last compelling factor that strongly suggested a fiber optically coupled line scanner was the resolution requirements. To practically achieve the resolutions of 10 lp/mm on field of view from 8 to 10 inches on a side requires a 16 Megapixel array. This far exceeds the performance of any area imaging device yet developed. The most obvious way to cope with this information gathering requirement is to develop some approach to segmenting the problem into a number of smaller ones. Some suggestions have included mosaic detector arrays and successive views with small area sensors which form the final image in small tiles. The approach of the line scanner is also a similar segmentation. Since the detectors are linear, they can be stacked physically along a single axis to form longer (and higher resolution) arrays. Because only one line is recorded at a time, the complexity of the processing is reduced to only one line repeated rather than an entire image at once. It is much easier to reach the very high pixel densities on linear imagers than with area devices. It is also much easier for a line scanner to use non-equal resolution elements along the two axis to provide a visually sharp picture with relaxed data acquisition specifications.

These advantages of the linear scanner must be weighed against several potential disadvantages including:

- Greater flux requirements,
- Complexity of solid state detector readout system,
- The necessity of Physical coupling of the converter screen to sensor,
- Longer required exposure time.

These problems are addressed at two levels. The first is a clear separation of what problems are caused by the resolution requirement independent of the imager technology. The second is how a practical prototype design can overcome potential disadvantages to produce a high-performance real-time imaging system.

3.2 FLUX REQUIREMENTS AND RESOLUTION

It has been mentioned several times in this report that the line scanner is X-ray flux intensive. In that sense it is important to emphasize the relationship between flux, contrast sensitivity and resolution. The ability to distinguish one pixel from its neighbor is set by the internal noise within the system and the statistical fluctuations of the quanta detected within the pixel area. Careful design and cooling can reduce the internal electronic noise to any desired level but the fundamental limitations set by detection statistics cannot be circumvented. If a beam of X-rays of flux, ϕ falls on a sensor, each detector element of area A, efficiency E records a certain number of counts N, in time Δt . Where

$$N = \phi \left(\frac{\text{Photons}}{\text{cm}^2 \text{ sec}} \right) \cdot A (\text{cm}^2) \cdot E \cdot \Delta t(\text{sec}) \quad (3.2.1)$$

The dose rate from an average X-ray tube operating at 100KV at 10ma and passing through a typical thin part might be approximately 200 R/hr. This corresponds to a flux of about 1.7×10^9 photons/cm²-sec at the detector. From Poisson statistics, one knows that the standard deviation of a number of events N is given by $1/\sqrt{N}$. To separate one pixel reliably from another we might require at least 2σ difference such that, if one pixel differs from its neighbor by a given fraction F, this should be greater than 2σ .

For a square pixel of dimensions, r , the 2σ requirement becomes:

$$F > \frac{2}{\sqrt{\phi \cdot \epsilon \cdot \Delta t \cdot r^2}} \quad (3.2.2)$$

In the example of our 100Kv, 10ma X-ray (E typically = .5) one might ask what resolution could be achieved at a given contrast ratio, F .

$$r > \frac{2}{F \sqrt{\phi \cdot \epsilon \cdot \Delta t}} \quad \text{at } 2\sigma \quad (3.2.3)$$

for television where t is 1/30 sec/frame, in one frame time at a contrast difference per pixel of F :

$F = 5\%$	$r = .12 \text{ mm}$	or	4.2 lp/mm
$F = 2\%$	$r = .19 \text{ mm}$		2.6 lp/mm
$F = 1\%$	$r = .38 \text{ mm}$		1.33 lp/mm

This clearly doesn't come close to the needs of this project which indicates that either a more intensive source must be sought or integration employed (or both). Working backward, one sees that to achieve a 1% contrast sensitivity and a resolution of 10 lp/mm, the flux time product (or fluence) is

$$\begin{aligned} \phi \Delta t &> \frac{4}{r^2 F^2 \epsilon} \\ &> 3.2 \times 10^9 \frac{\text{photons}}{\text{cm}^2} \quad (\text{at } 2\sigma) \quad (3.2.4) \end{aligned}$$

With a flux of 1.6×10^9 photons/cm²-sec, t must be at least 2 seconds or 60 frame times in standard video. Clearly these numbers can be reduced somewhat with larger sources and higher efficiencies, but the basic fact that with conventional sources, some significant integration is required to produce a 1% contrast sensitivity. This time is more a function of statistical physics than small changes in system design. This can be appreciated most clearly when one considers the fact that the typical 9 inch image amplifier digitized to 512 pixel resolution has approximately 10 times large pixels and hence requires 1/100 the fluence to achieve a 1% pixel to pixel contrast sensitivity. High resolution extracts its price both in device complexity as well as in increased inspection time.

3.3 DEVELOPMENT OF BREADBOARD SCANNER

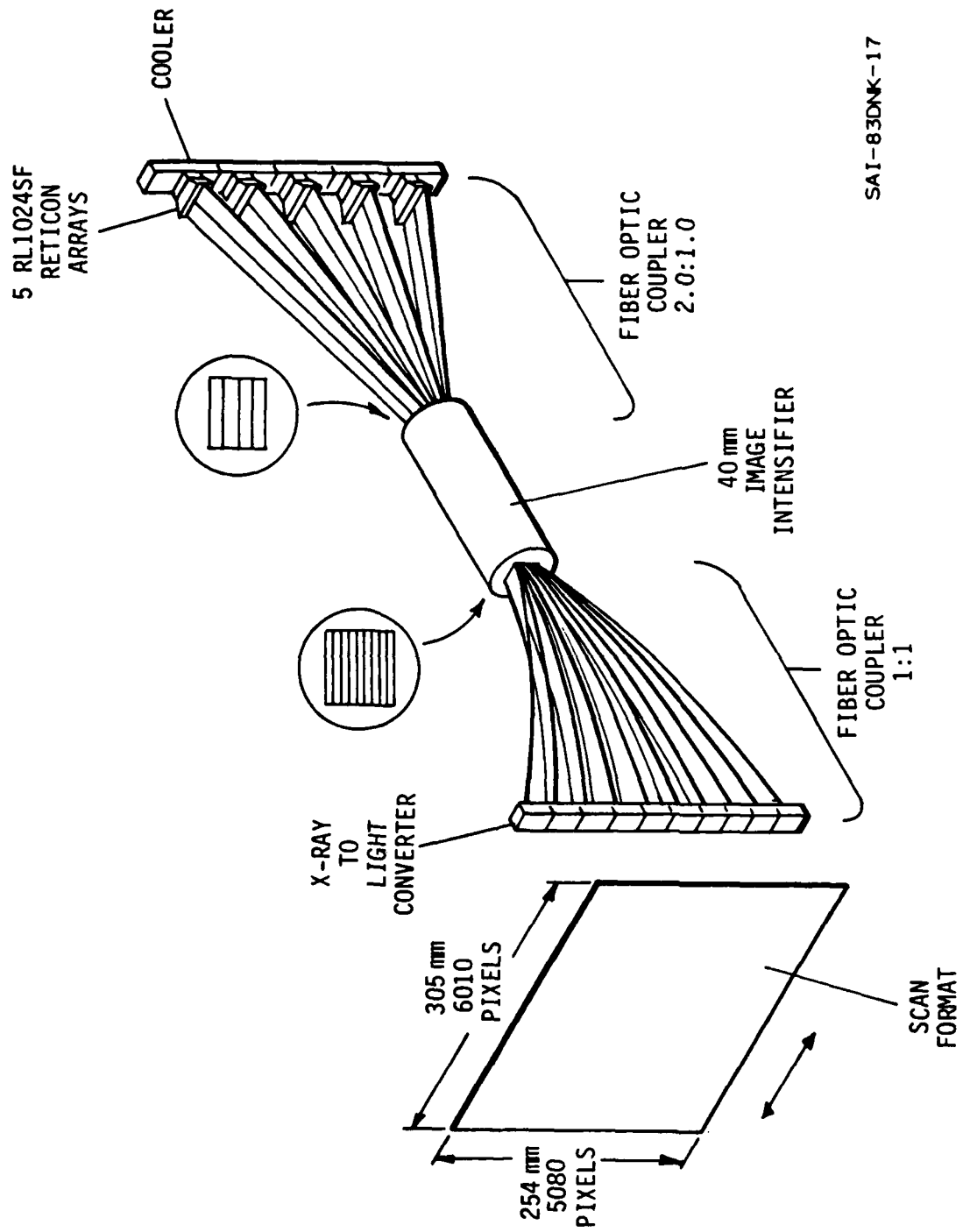
The linear scanner design suggested in our original proposal included several important features. As shown schematically in Figure 3.3.1, it included a long X-ray to light converter, segmented by a series of fiber optic ribbons to a common intensification stage and then broken out into several solid-state photo diode arrays by a second set of image ribbons. While the original design called out five 2-inch sections on a 10-inch screen, we suggested that a more practicable and manageable system would involve only four 1024 element sensors with either 2.0" sections to form an 8-inch field of view. This would permit a 512 pixel/inch detector pitch which just exceeded a limiting resolution of 10 lp/mm. It was also pointed out that even if some of the components exceeded this performance, the composite system would undoubtedly show a measured resolution somewhat less than the 10 lp/mm goal because of the effects of aliasing at the Nyquist frequency limit of the digitization.

The major features that dominated the design, i.e.

- Fiber optic coupling,
- Segmentation to multiple arrays,
- Common Intensifier stage to improve signal-to-noise ratio,
- Self-scanned photo diode for simple readout

have remained constant throughout this work although we have experimented with a number of variations to seek a more effective approach.

Before the program began, experiments had been in progress in our laboratory with a simple scanner system. This system had used a lens coupled screen and a two-stage intensifier to provide sensitivity sufficient to record images. The scanner shown in Figure 3.3.2 demonstrated about 4-5 lp/mm resolution and 2 to 3% contrast sensitivity. By comparing the effects of screen brightness and contrast sensitivity it was verified that a fiber optically coupled system and single stage intensifier should provide the best match for a high performance system.



SAI-83DNK-17

Figure 3.3.1 Linear Scanner Detector Configuration.



Figure 3.3.2 View of Breadboard X-Ray Linear Scanner.

We initially planned to use the breadboard scanner to make measurements and to support other independent measurements. For this reason several modifications to the existing sensor and readout system were started soon after the program's initiation.

The first of these modifications involved the design of an improved preamplifier and driver for the Reticon S array. The detector unit shown in Figure 3.3.3 was built using a number of design improvements to reduce clock noise and generally improve performance. The shielded box also provided a means of attaching the Reticon self-scanned diode array to the system and maintain a light but even pressure on the fiber optic coupling.

The choice of an S series Reticon photodiode array was made because of its high-density linear spacing and large charge well capacity. The array elements are on a 25-micron center to center spacing yet have a 2500 micron width. The wide detector makes the task of alignment much easier and provides a very deep full-scale charge well. This deep well means that much more light can be integrated before saturation occurs reducing the intrinsic statistical fluctuations inherent in charge collection process. This is a significant improvement over CCD devices which use the charge transport element also as the charge storage device. We suggest one important reason why early attempts to use CCD cameras for radiography have not been successful. The photodiode array uses a separate diode storage element which can be made as large as desired to increase charge capacity upper limit. The linear structure of the array simplifies the readout through two MOS switching matrices that successively couple alternate cells to the video line. Since the 1024 array is read out through alternate odd and even video amplifiers, one can easily reduce the resolution and increase the signal by summing the two alternate signals. The type S array is available with a built in fiber optic coupler that provides good contact to the silicon device and the input source. The arrays chip does have a significant dead space on either side of the active line but the use of individual coupling fiber ribbons permits virtually contiguous joining of units. The intrinsic modulation transfer of the S array is excellent since it provides virtually no dead spaces between pixels. In fact, modulation transfer is nearly 50% at the Nyquist limit which can be seen in the graph in Figure

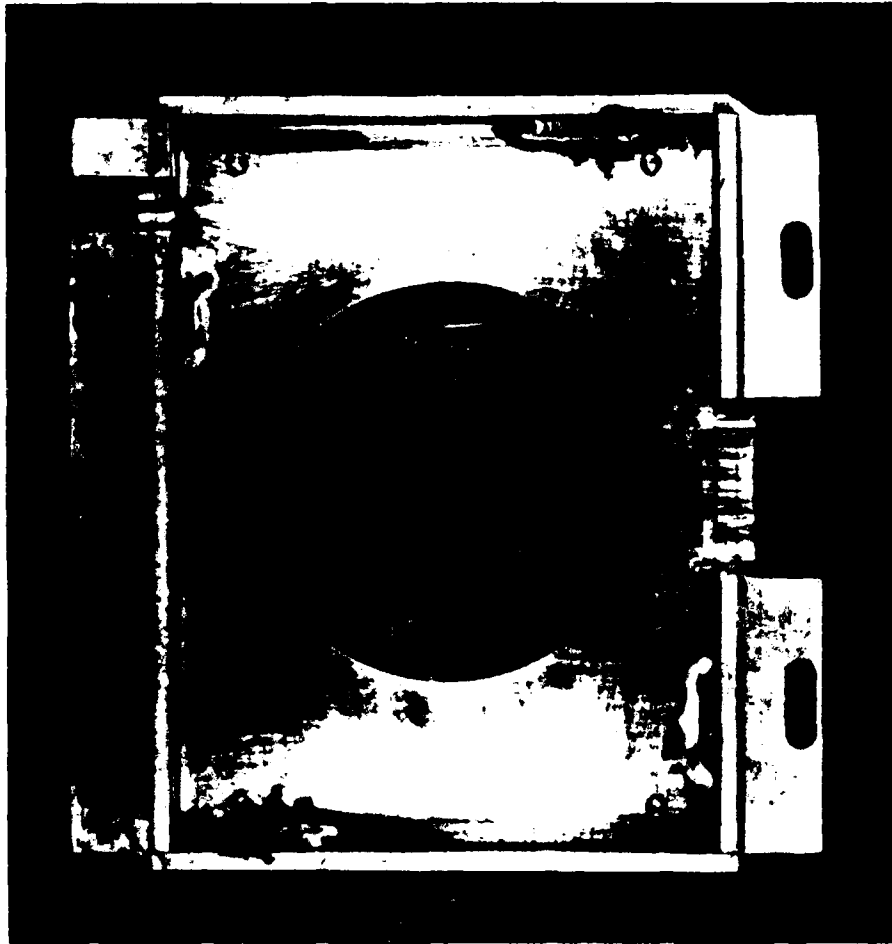


Figure 3.3.3 Mounting of the Linear Diode Array and Preamplifier.

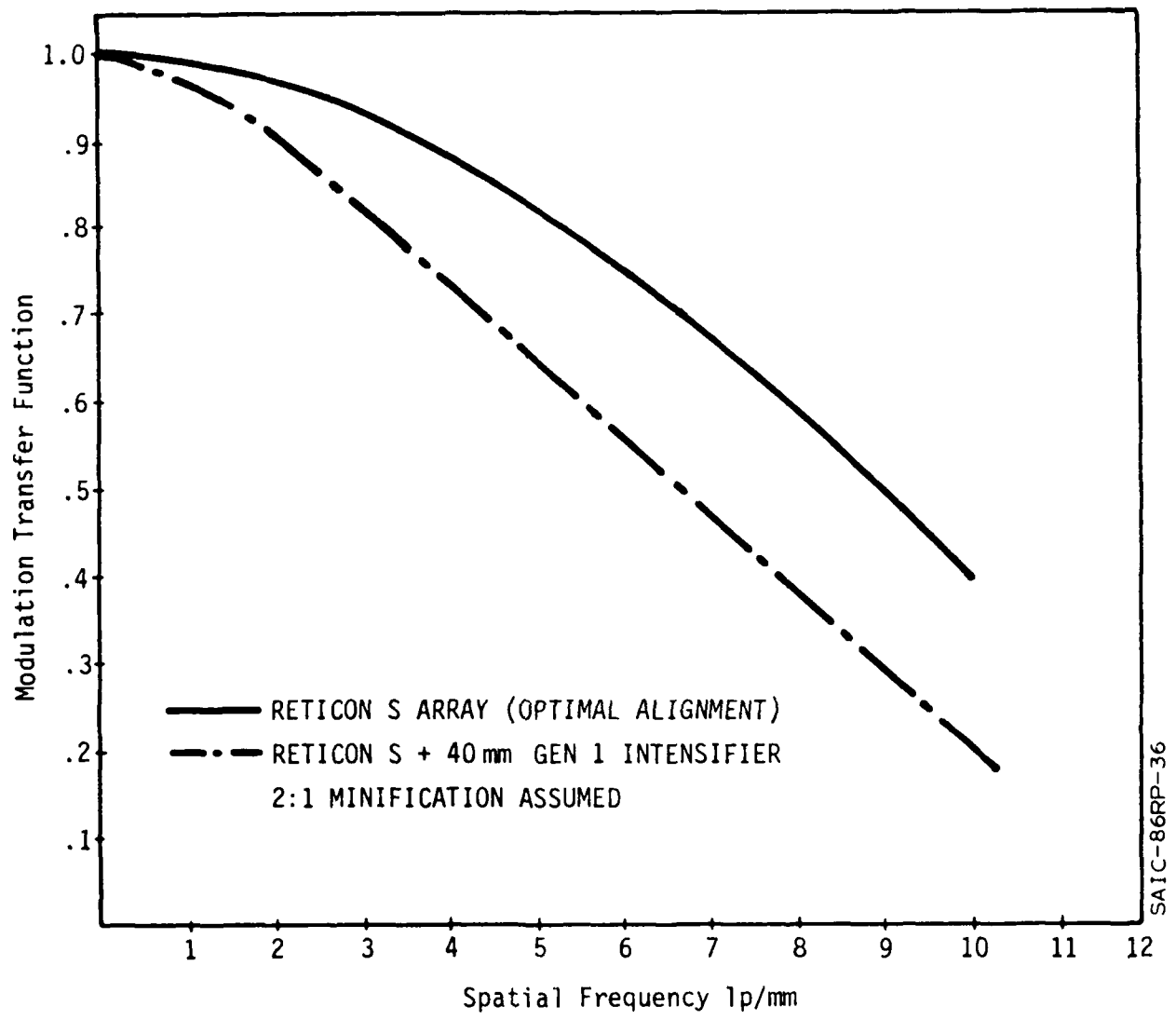


Figure 3.3.4 M.T.F. of Linear Scanner.

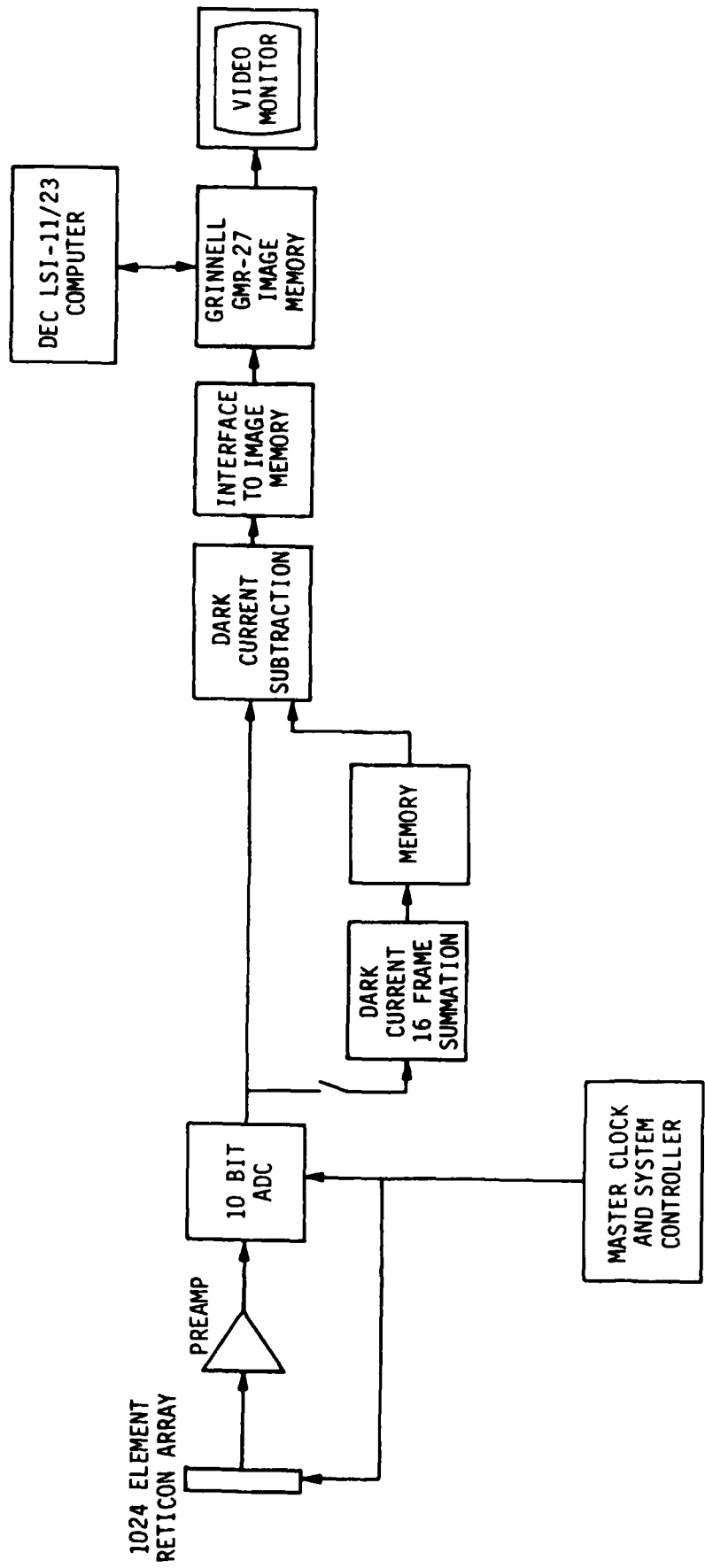
SAIC-86RP-36

3.3.4. Because of the digital nature of the system, the readout does not cause significant degradation of this performance.

The electronics system was rebuilt to permit expansion of functions. Many of the same cards were reused, but several important improvements were installed. The most important improvement in performance provided a locked synchronization so that the scanner frequency was always a multiple of the 60 Hz power lines. The early scanners required the use a special ultra stable X-ray source to remove all ripple from the flux since this ripple put line to line brightness variations in the image. When both the scanner and display are locked to a multiple of the line frequency, any ripple induced on the X-ray affects each line in approximately the same way. With this modification any conventional source from a self rectified portable to a 3-phase high current generator can be used successfully with the scanner.

The second improvement that was installed was a dark current subtractor which permits pixel by pixel subtraction of the individual average dark current. A separate memory holds a 16 line average of this background. A more important correction for pixel to pixel gain variations was attempted but not completed on the breadboard. This correction currently must be done using software after the image is acquired. A hardware version of this process was designed and tested and described in section 3.5.

The electronics readout was coupled to a 512- x 512- x 12-bit Grinnel image memory (GMR-27) and the entire system supervised by an LSI 11/23 computer. The system can display the entire array at a 5 lp/mm limiting pixel resolution or any section of 512 contiguous pixels out of the full 1024 with a 10 lp/mm limiting resolution. The system has several disk drives that permit data to be transferred to other systems for subsequent analysis. The data is maintained to a 10-bit accuracy which can be upgraded to 12 bits with an improved analog to digital converter. A block diagram of the readout system is shown in Figure 3.3.5 and a photograph of the breadboard electronics is shown in Figure 3.3.6.



SAI-84GB-21

Figure 3.3.5 Block Diagram of Linear Scanner Data Processing System.



Figure 3.3.6 Front Panel of the Control Box for the Linear Diode Array.

The major engineering effort on the breadboard system centered on the input coupling to the converter screen and the subsequent down sizing (minification) and intensification. It was here that one could appreciate the greater complexity and difficulty in combining fiber optic components over their lens counterparts. The original conceptual design had called for a complicated ribbon minifier. When this task was posed to several fiber optics vendors, they all recommended alternative approaches to which they felt would be more producible. One alternative would have been to simply double the resolution and use no minification. This is clearly the highest performance alternative since it would provide 1024 pixels/inch or 20 lp/mm resolution. The complexity of dealing with an 8000 pixel array or finding some recognizable sample to show on a 1/2-inch wide field of view discouraged us toward this approach. Moreover, any savings in the front end optical components would be overshadowed by the increase in complexity and cost of the readout. Other alternatives involved using a drawn cylindrical taper, using straight ribbon cut on a slant and using electro-optical minification in the focusing characteristics of the image intensifier stage. All of these last alternatives were explored with varying levels of success.

The slant cut ribbon minifier was the most attractive option initially since it appeared to offer reasonable light transmission and great simplicity in construction. Moreover, it offered a straight forward method of stacking segments onto a large converter screen with minimal dead space. The process involved taking ribbons 1-inch wide and cutting and polishing an end 30° off the fiber axis. This produced an entrance 2-inches wide with a 60° entrance angle. Initial samples seemed quite promising since they appeared to transmit a surprisingly large fraction of what was an asymmetric acceptance cone. Calculations modeled on a simple numerical aperture concept of acceptance indicated that more than 50% of the light would be captured. The results obtained subsequently were all quite disappointing since they ranged from no coherent transmission (too low a numerical aperture.) to asymmetric line shapes and 20% or less transmission in the best case. It appeared that the use of EMA coating to reduce crosstalk was absorbing most of the light. The first test samples did not have this coating which may have explained their performance. A group of some of the "ribbon minifiers" is shown in Figure 3.3.7.

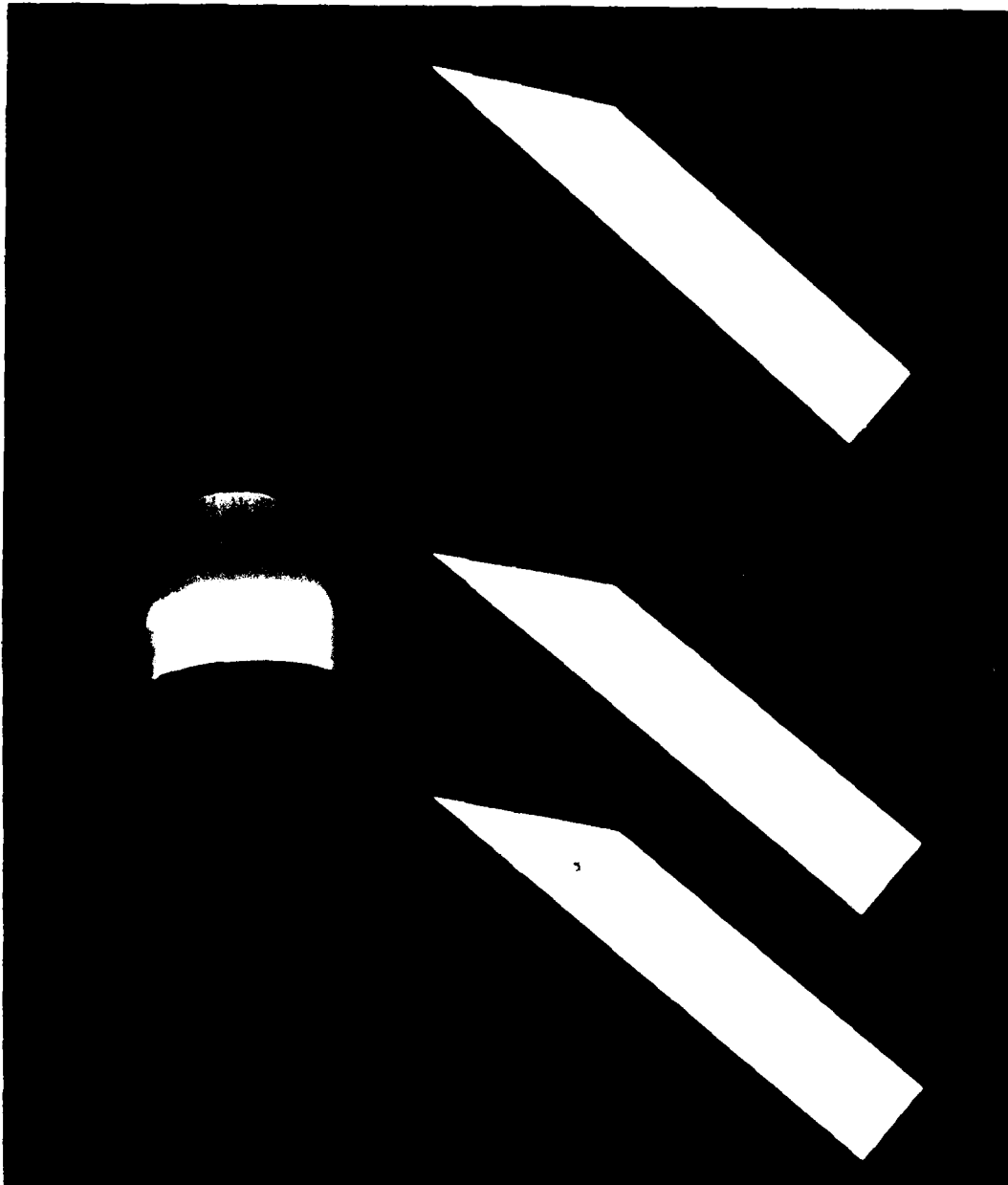


Figure 3.3.7 Fiber Optic Minifiers: Slant Cut and Drawn Type.

The second approach evaluated the use of a minifying image intensifier. This approach should yield the best results for both resolution and transmission. It also involves the fewest number of interfaces between optical components. An engineering sample of a Westinghouse 40mm - 25mm diode-type image amplifier was obtained. To run the photocathode at ground potential, it was necessary to elevate the output anode screen to +15000 volts. A housing was designed that held the intensifier and clamped the Reticon array and preamp to the output fiber optic. Initial tests made in the laboratory indicated that all standoffs were adequate to hold the potential although the system did show an increase in noise with the intensifier operating. During the first tests in the X-ray cell the system began to spark under the effect of the ionizing radiation. Unfortunately before it could be shut off, an arc discharge broke through to the array catastrophically damaging it. The system was rebuilt with a 1-inch-long fiber optic coupler to increase the separation. The coupler was cemented to the rear of the intensifier and the entire end potted. A conductive overcoating was then applied and connected to ground potentials. After replacing the S array the system performed quite well and no further problems were encountered. The intensifier and mounting to connect the screens under test is shown in Figure 3.3.8.

The intensifier and array were mounted into an aluminum box that also contained the high voltage power supply, clock electronics, and preamp. Individual converter screens mounted on standard frames were coupled to the intensifier input using Cargill immersion oil and clamped with moderate pressure with two screws mounted along the screen center line. A set of preset lead collimating slits were mounted so that they made a snug fit over each test screen frame. The jaws were set using brass shims and locked into position so that the slit size remained constant for each test. The entire breadboard scanner is shown in Figure 3.3.9. The X-ray source was located on a moving table in front of the slit. The table was moved back and forth to optimize the beam alignment and then additional precollimating shielding was installed. Parts are moved on a small linear motion table powered by a slow speed universal gear motor.

The breadboard system was supposed to use a full 2-inch field of view. Since the 40- 25-mm intensifier was a diode type tube, it could not be zoomed

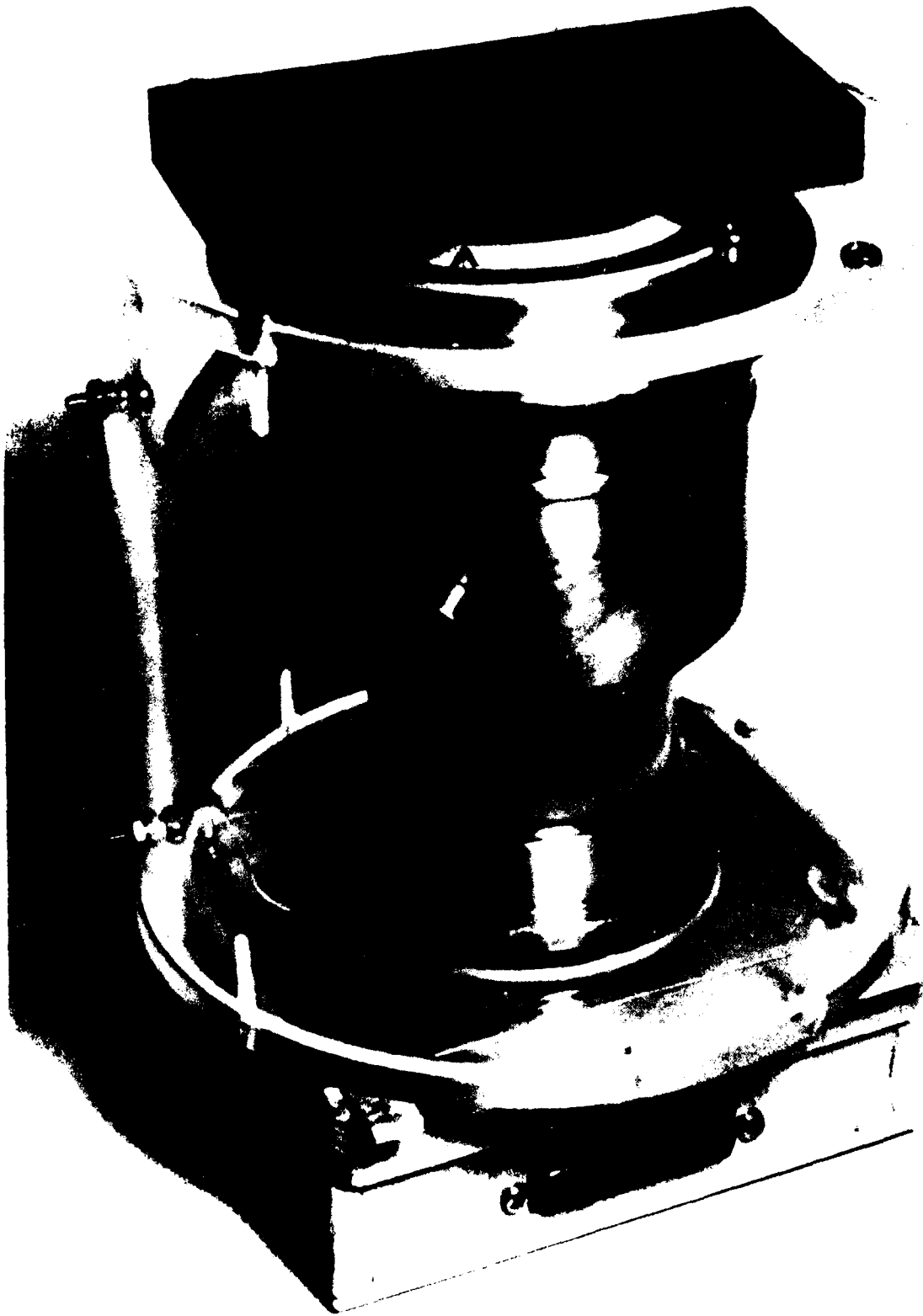


Figure 3.3.8 Test Screen Mounted to Westinghouse
40- 25-mm Intensifier and Reticon Preamplifier.

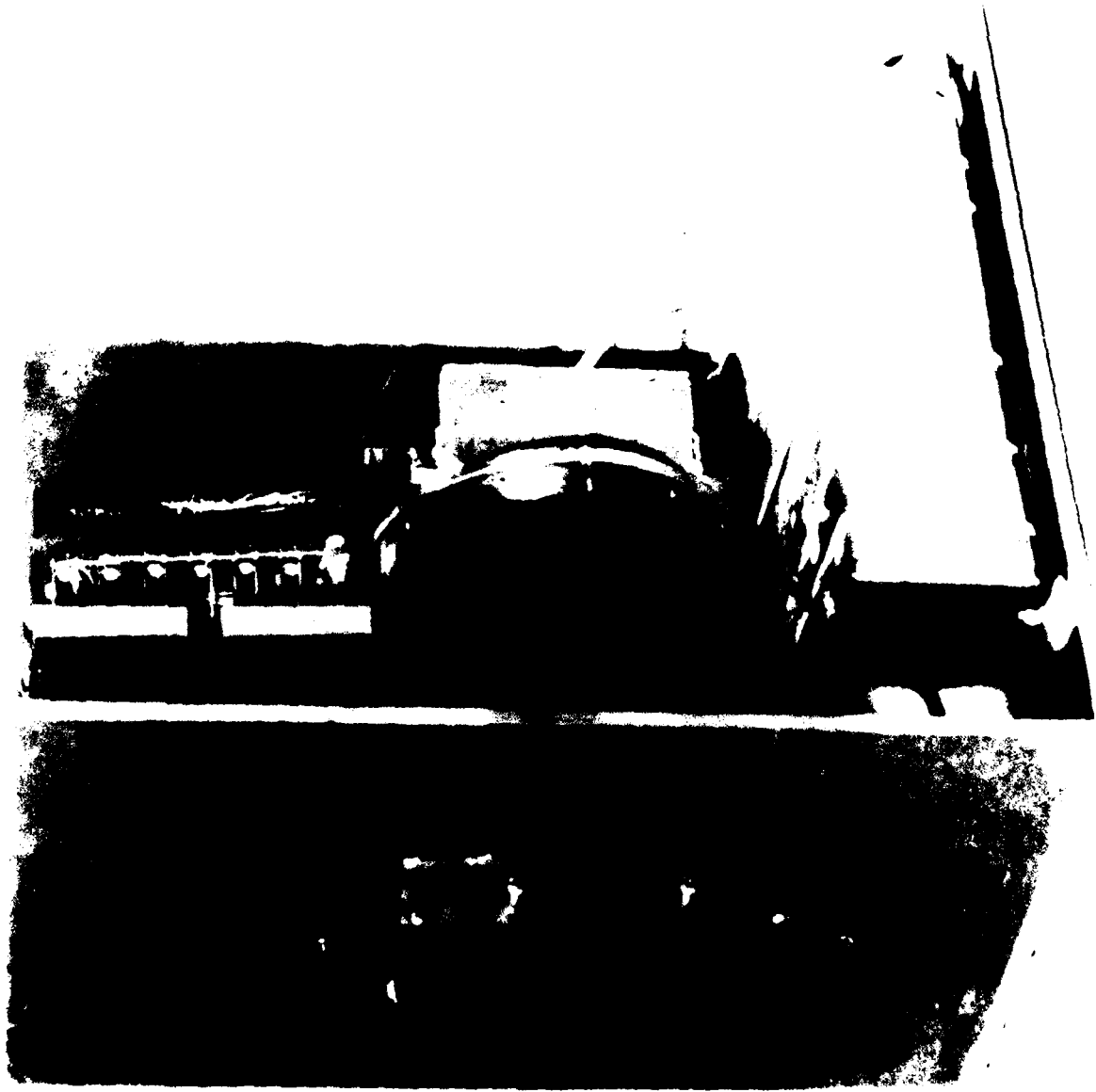


Figure 3.3.9 2-inch Field Breadboard Linear X-Ray Scanner with Lead Defining Slits.

to change magnification. During the course of experiments, it became clear that the engineering sample was not operating at its full specifications. Optical measurement indicated both resolution and gain were significantly below the manufacturer's specification. In particular, we measured a total green light gain of 25 for the intensifier which should have measured in excess of 100. Although we did not have facilities to measure optical MTF of the intensifier, it was noted that for 1.6-inch active field of view, the resolution with our best converter screens was limited to about 8 lp/mm. This result occurred even with screens that had independently been measured as having resolutions much greater than 10 lp/mm.

To resolve these questions a third system was constructed using a cylindrical taper fiber optic minifier and standard 40 mm VARO single-stage intensifier. This arrangement yielded a gain of approximately 40 and significantly improved resolution even on the larger 2-inch field of view. This arrangement is not ideal since it had more interfaces and placed the fiber optic minifier before the intensifier (not ideal for optimum resolution). Even with these handicaps, this system consistently performed at 9 lp/mm or more with most of the converter screens. It was mounted in a fixture that permitted it to be interchanged with the original intensifier combination. All results on typical aerospace components and in the evaluation of total system performance were taken with this system.

3.4 REVIEW OF BREADBOARD SYSTEM PERFORMANCE

The 2-inch field-of-view breadboard scanner was evaluated with several of the converter screens that had better figure of merits. The three screens that were used all produced limiting resolutions of between 8 to 9 line pair/mm when used on the scanner and were each used to accent their particular strengths. These screens included:

- 10mm Terbium f.o. with an Aluminum Reflector: Best resolution and high energy contrast sensitivity,
- Gd_2O_3S overcoated Terbium f.o. good general overall performance and high output,
- TRIMAX 2 excellent soft X-ray performance, high output and good resolution.

The system was operated with a variety of standard X-ray sources including:

0 - 30 kV	High current source for composite material inspection
20 - 160kV	General purpose source for highest resolution (0.4mm focal spot)
50 - 320kV	High energy source

The system could be operated over approximately a 10x gain range with additional sensitivity available in a 1-to-4x increase in integration times. Typical results were obtained from 60 lines/sec down to 20 lines/sec scan rates for the above sources.

A typical resolution response observed on the Funk star pattern taken at the 1024 pixel/inch resolution mode is shown in Figure 3.4.1. This figure shows the resolution along both the electronically scanned and mechanically scanned axis. The pattern taken along the electronically scanned axis measures the response of the converter screen and readout and easily shows 9 lp/mm or greater resolution. The resolution along the mechanical scan direction shows blur at 4 lp/mm and then a phase reversal. This is characteristic of the sinc behavior of scanning a rectangular slit of width δ . In this case, the first zero of the sinc function corresponds to a slit width of 0.005". The apparent

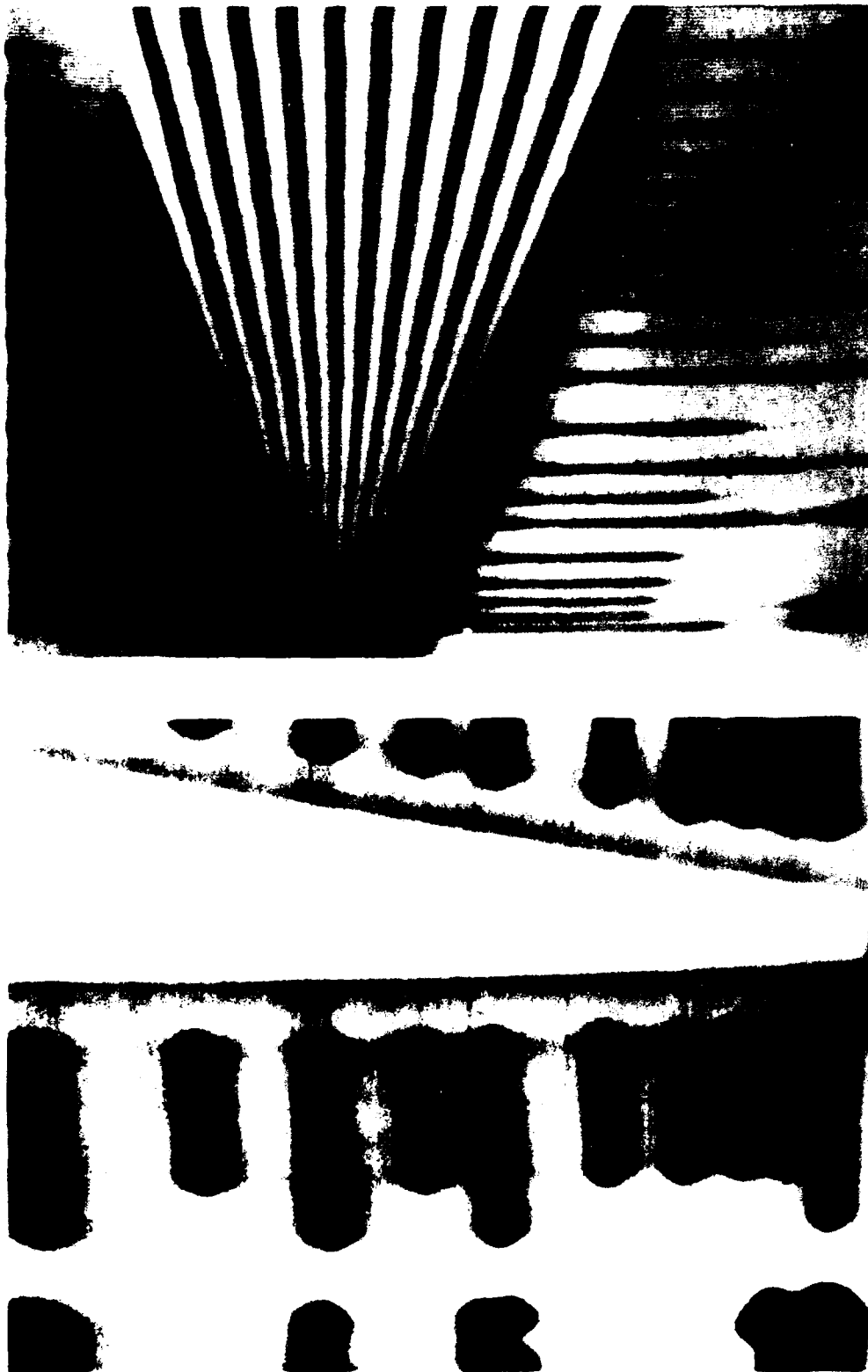
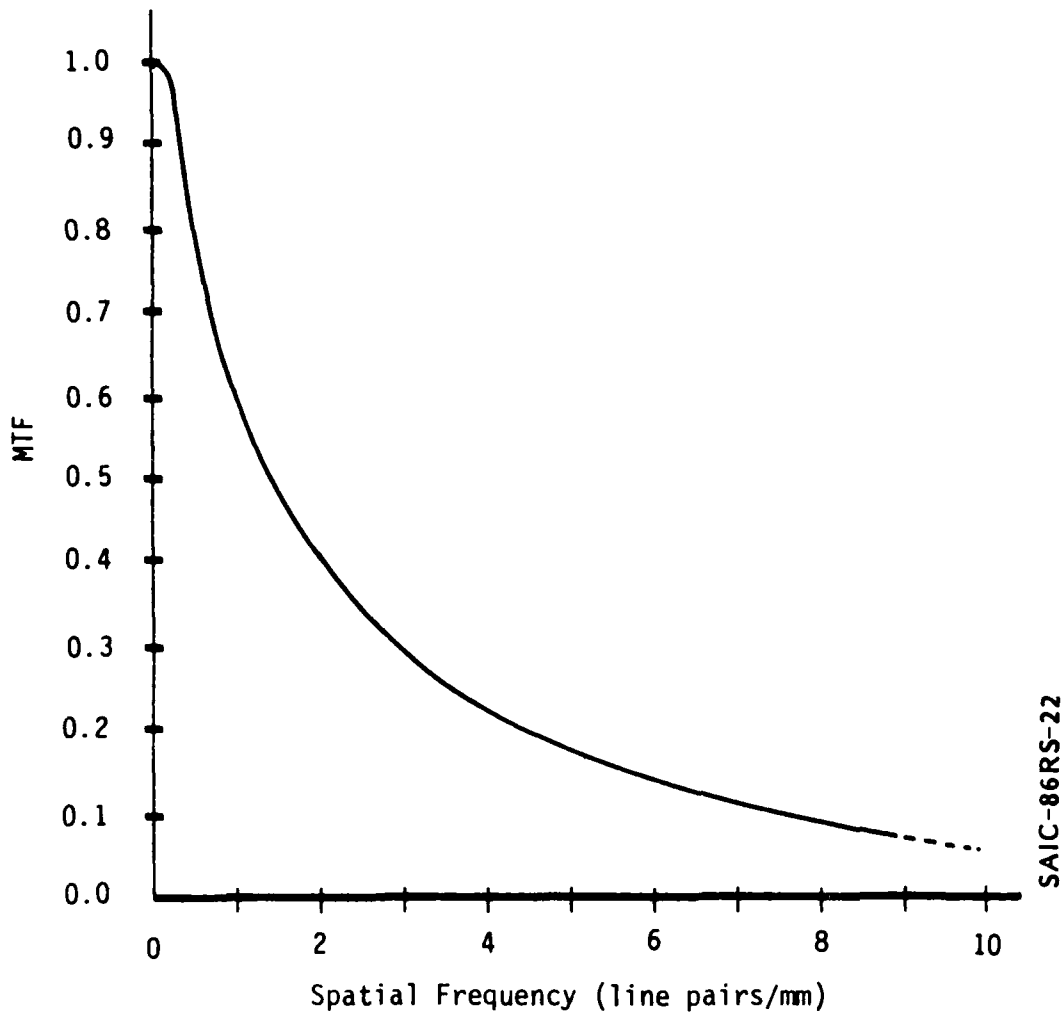


Figure 3.4.1 Funk Star Radiographs recorded on the 2-inch Breadboard Scanner, a.) along the Electronic Scan Direction and b.) along the Mechanical Scan Direction. (Notice Aliasing in b at Frequencies above 4 lp/mm.)

resolution above this limit is due to interference or aliasing of the test grid with the slit and is not useable resolution. Measurements of burst patterns were also recorded and yielded composite MTF's along the electronic scan such as shown in Figure 3.4.2. When operated in its half resolution mode (512 pixel/2 inch), the system predictably produced 5 lp/mm with all screens and provided a full 2-inch field of view. The choice of mechanical scanner speed affected the resolution in the conjugate axis and this was adjusted to match where possible. For some scan rates, it was not possible and sometimes not desired to produce square pixels. This distortion is apparent in some examples but is not an inherent limitation in the system.

A scanner drive employing a stepper motor or d.c. servo with velocity feed back would provide the wide range of scan speeds required. Occasionally it is desirable to compress the motion and purposely distort the display. This is particularly true if all the potential features are one dimensional and one wishes to record more of the sample in a single view. Examples of this type of inspection are in such cases as monitoring fiber spacing on long rolls of composite material or other calendared stock. (e.g. reinforced rubber sheeting for tires or similar materials). Examples of typical radiographs made with the breadboard scanner are discussed in Section 4.



SAIC-86RS-22

Figure 3.4.2 Compounded Modulation Transfer Function of Line Scan Inspection System Utilizing a Trimax 2 Screen in Contact with a Fiber Optic Coupler.

3.5 OPERATIONAL EXPERIENCE WITH AN 8-INCH PROTOTYPE SCANNER

During the course of carrying out this program, the opportunity arose to build a full scale prototype linear X-ray scanner system. The requirements and delivery schedule did not permit transferring all of the technology under development but did permit trying out many of the concepts on a production type system. The scanner used the same basic design that was outlined in our original proposal to provide an 8-inch active field of view. A schematic drawing of the system concept is shown in Figure 3.5.1. The screen was a removable GOS type converter in contact with a fiber optic coupler. Flexible coherent fiber ribbons segmented the image into four sections which were then minified, intensified and recoupled to four discrete 1024 pixel photodiode arrays.

The prototype system was designed and built for the Northrop Co. to inspect composite panels. It was optimized for inspection of thin parts requiring from 15 to 80 KV X-ray energy. It has been successfully operated over the entire range. It has a measured resolution along the detector of about 5 lp/mm limited primarily by the screen used and the 2-stage intensifier arrangement. The readout is fully capable of supporting a full 10 lp/mm Nyquist resolution limit.

The scanner uses flexible fiber bundles to couple the light from the screen to the intensifier and from the intensifier to the Reticon arrays. These bundles can be clearly seen in the view of the interior detail shown in Figure 3.5.2. The entire scanner box weighs about 30 pounds and is moved on a stepper driven table to provide a controlled velocity as the part is scanned. This can be seen in figure 3.5.3. Adjustable tungsten collimators provide a fixed slit width for the scan. Several collimators are mounted on interchangeable frames so that the preset widths can be interchanged in a highly reproducible manner. The entire box is shielded with lead to protect the intensifiers, arrays and readout electronics from the incident radiation. A number of life tests have been carried out which indicate no significant browning or degradation of the input conversion screen and fiber optic coupler with typical radiation fluxes. The system operates with a Phillips MG104 high current X-ray source which provides currents up to 80 ma with low inherent ripple.

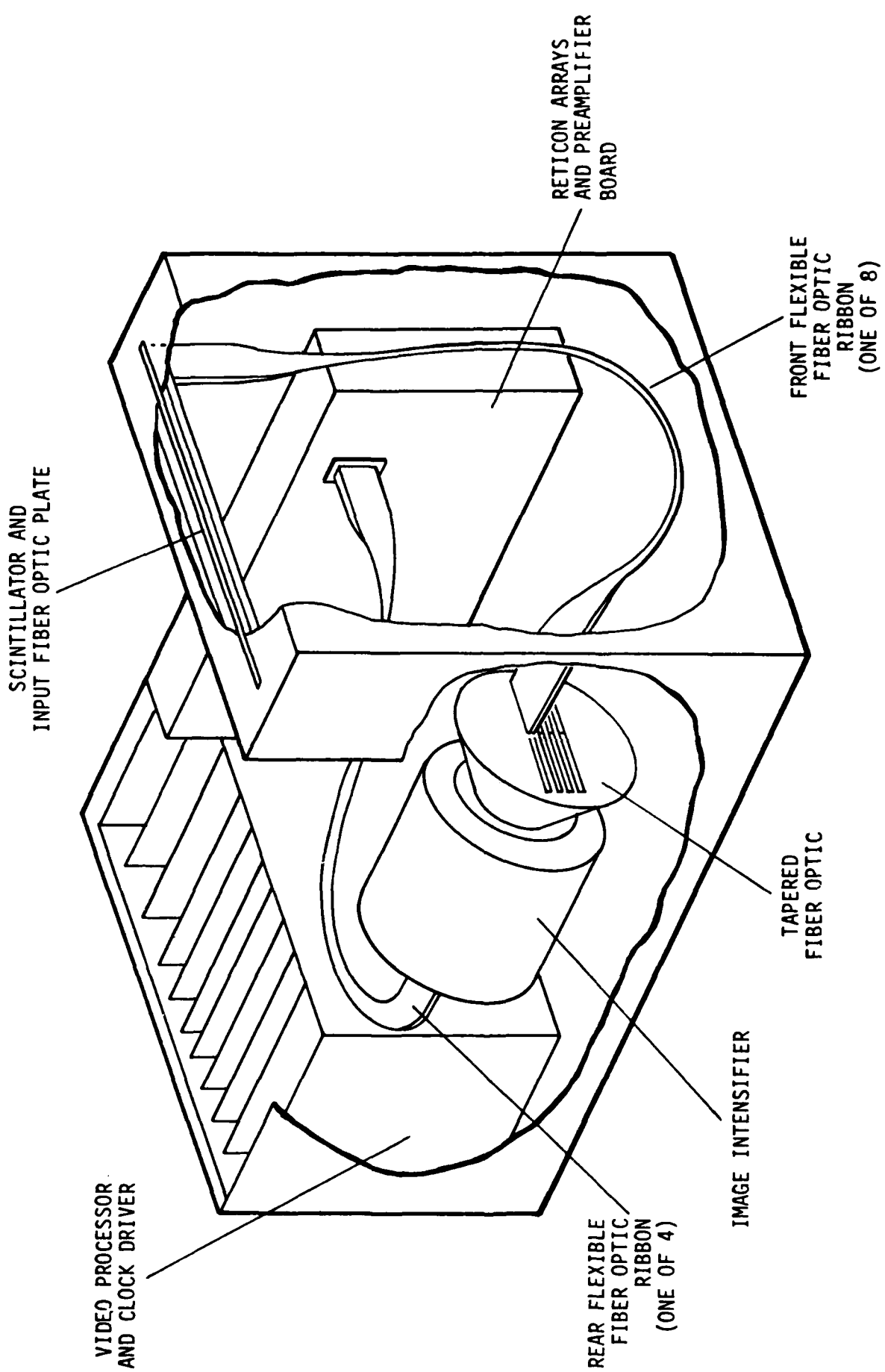


Figure 3.5.1 Arrangement of Major Components in Linear Scanner.

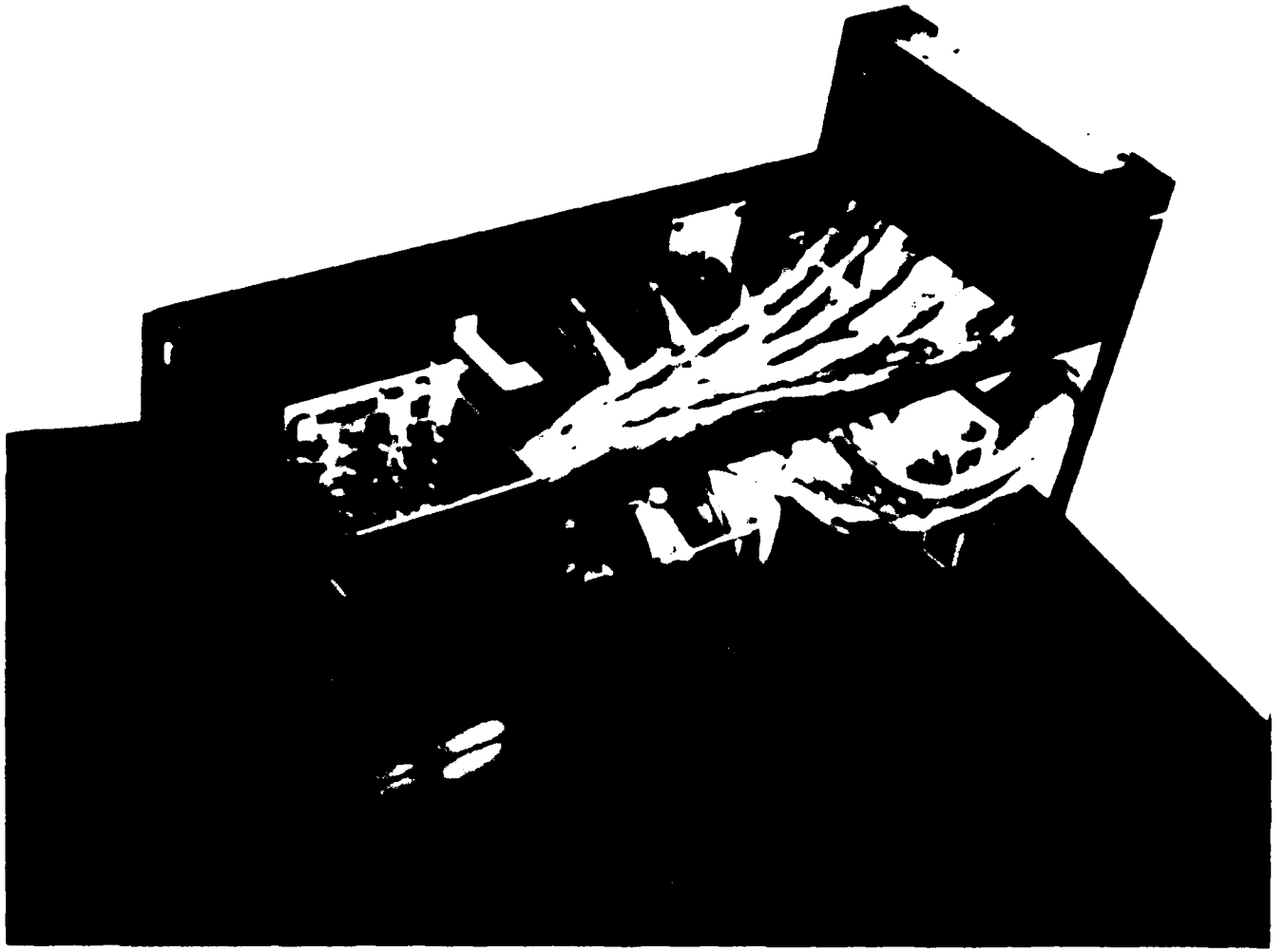


Figure 3.5.2 SAIC Linear X-Ray Scanner for High-Resolution Radiographic Inspection of Aircraft Composites.



Figure 3.5.3 SAIC Prototype 8-inch Linear Scanner
Shown with Scanning Table Assembly.

The electronics system used to gather and process data as well as control the scan process is shown schematically in Figure 3.5.4. The system consists of three major building blocks indicated in the diagram as linear image detector, system controller, and motor controller. These three major subsystems are all directly operated by the control computer. The display used is a commercial 1024 x 1024 image memory, the Recognition Concepts Trapix System. The computer is a Digital Equipment Corporation PDP 11 Series machine operating under the RSX11M+ operating system.

The system has met virtually all of its performance goals. It scans a full 8-inch section in approximately 30 seconds and achieves a 2-T sensitivity on most parts. Several typical images are shown in Figure 3.5.5 through 3.5.7. These represent typical skin and honeycomb sections as well as more complex structures such as a speed brake panel. All the views shown here are taken of the 1024 x 1024 display which displays the compressed data set in real time. Since the system can be operated at two increased magnification (2x and 4x) it is possible to see the scan from a 4-inch segment at the 1024 pixel resolution. An example of this is shown in Figure 3.5.8.

One flaw in the performance has been the matching between detector segments. This is exacerbated by the fact that the scanner is operated as a moving slit in reference to a fixed source. The controller hardware is capable of correcting significant variations in sensitivity over the field of view. These however remain correct only if the system response is constant. Because of some instrumental problems in the fiber optic ribbon and intensifier there are significant corrections in some portions of the image and the change in overall illumination caused by the changing source position causes some discontinuities to be visible at the interfaces. A hardware circuit permits removing offending pixels but this will lead to missing segments if over used.

A software solution to the problem was developed which permitted the image to be smoothed and joined with no visible interfaces. The system used a two pass approach and a computer fit to match the segments. This level of sophistication was only necessary on very low contrast parts and future improvements in the design of the ribbon segments should make it unnecessary.

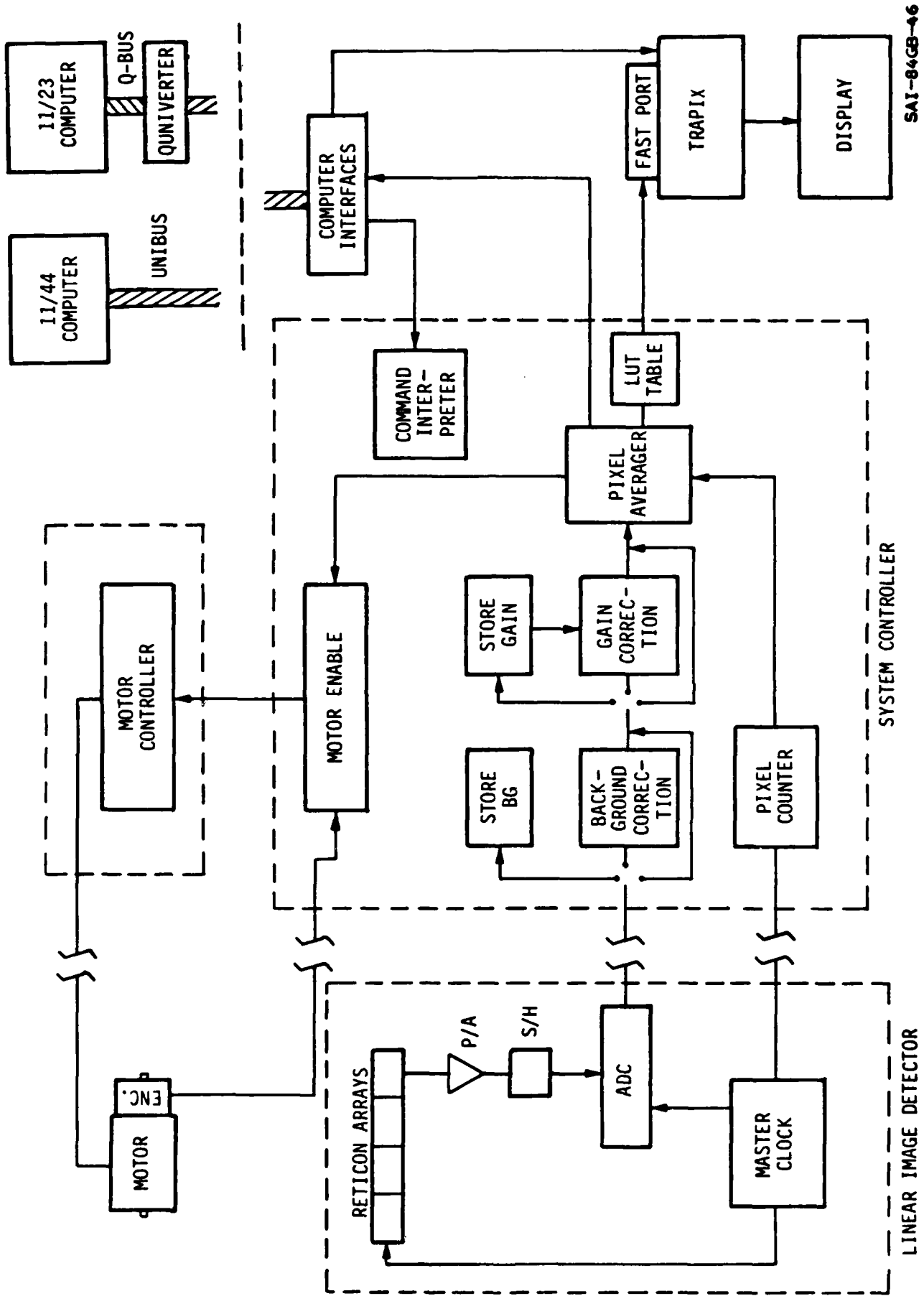


Figure 3.5.4 Simplified Block Diagram of the System Electronics.

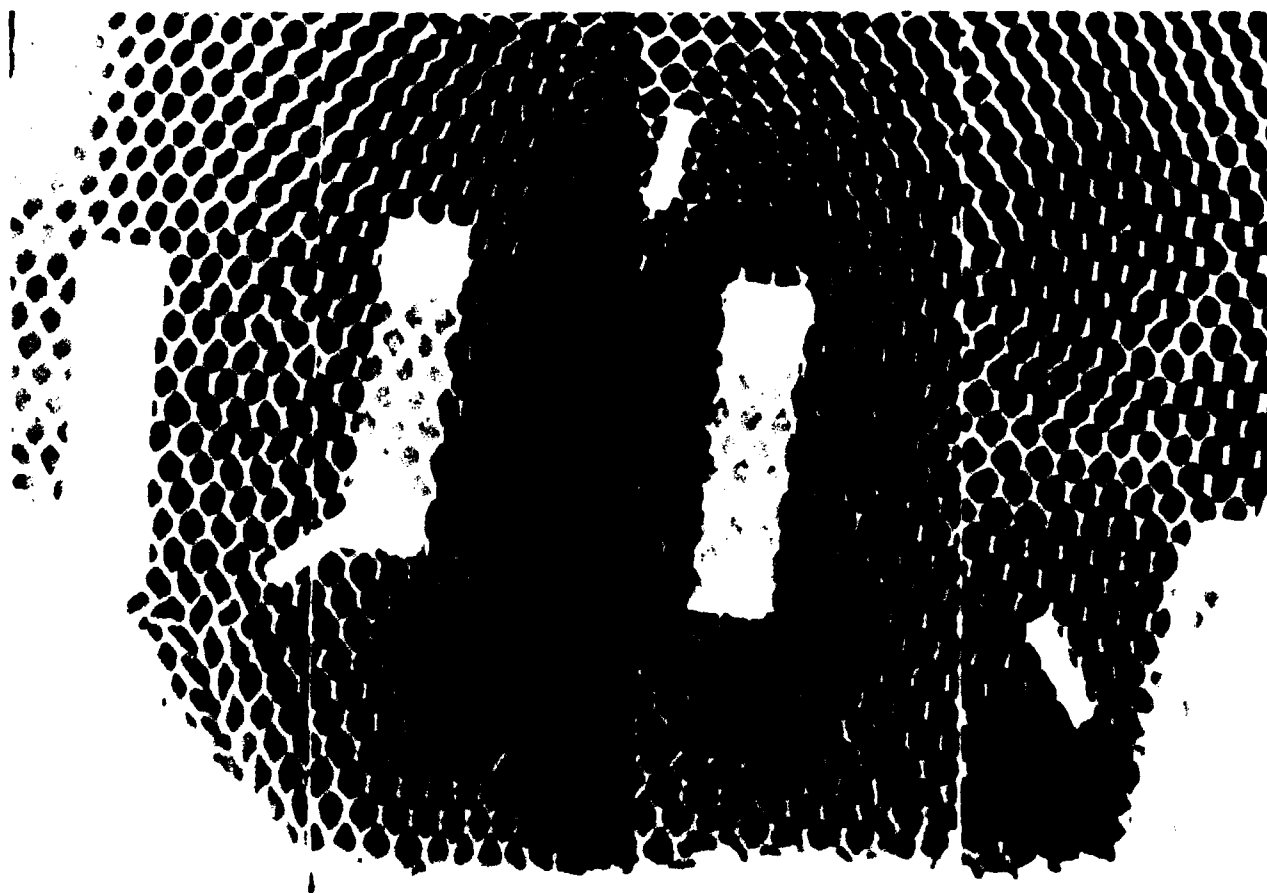


Figure 3.5.5 Leading Edge Section (Northrop) Image
with 8-inch Prototype Scanner.

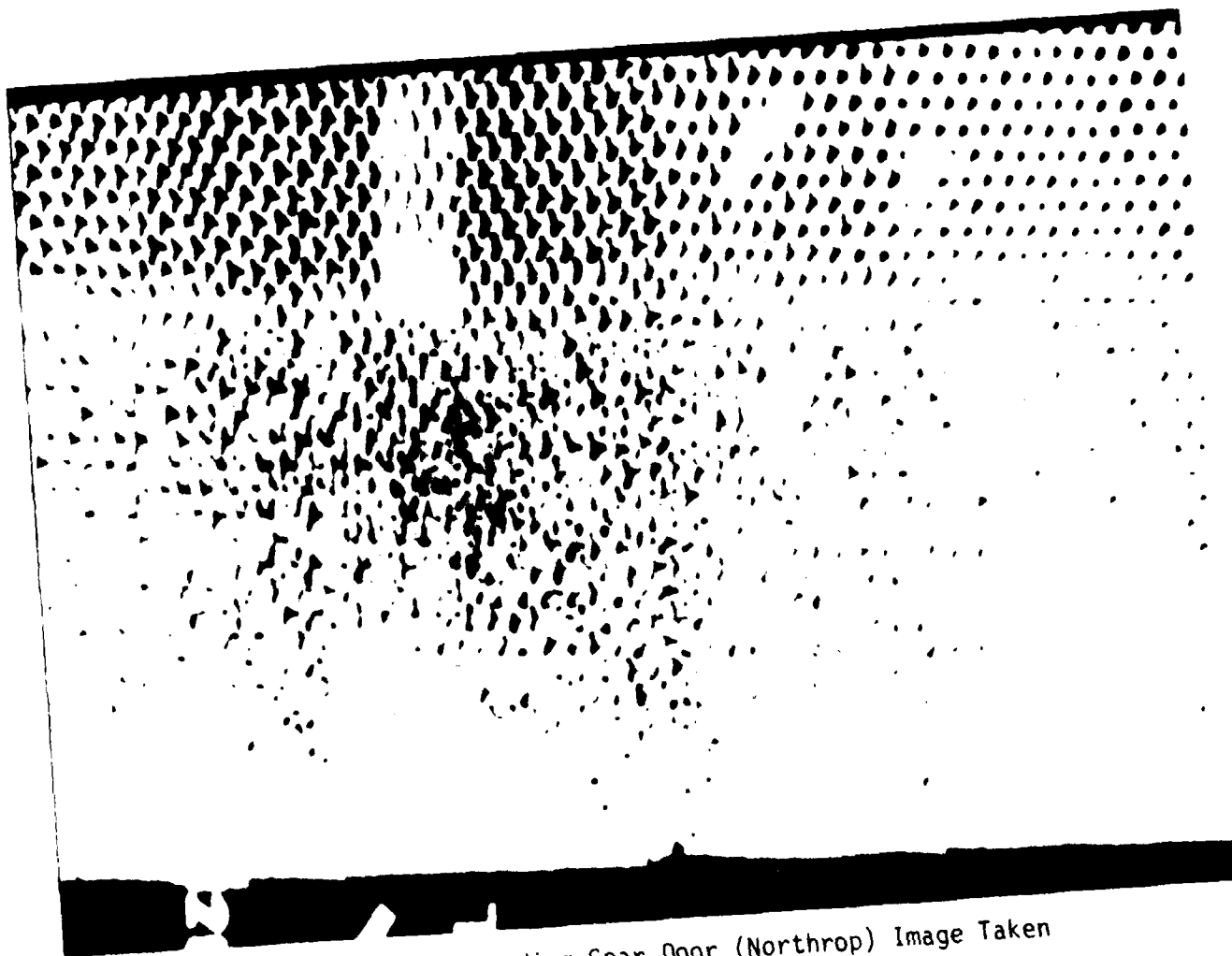


Figure 3.5.6. Landing Gear Door (Northrop) Image Taken with 8-inch Prototype Linear Scanner.

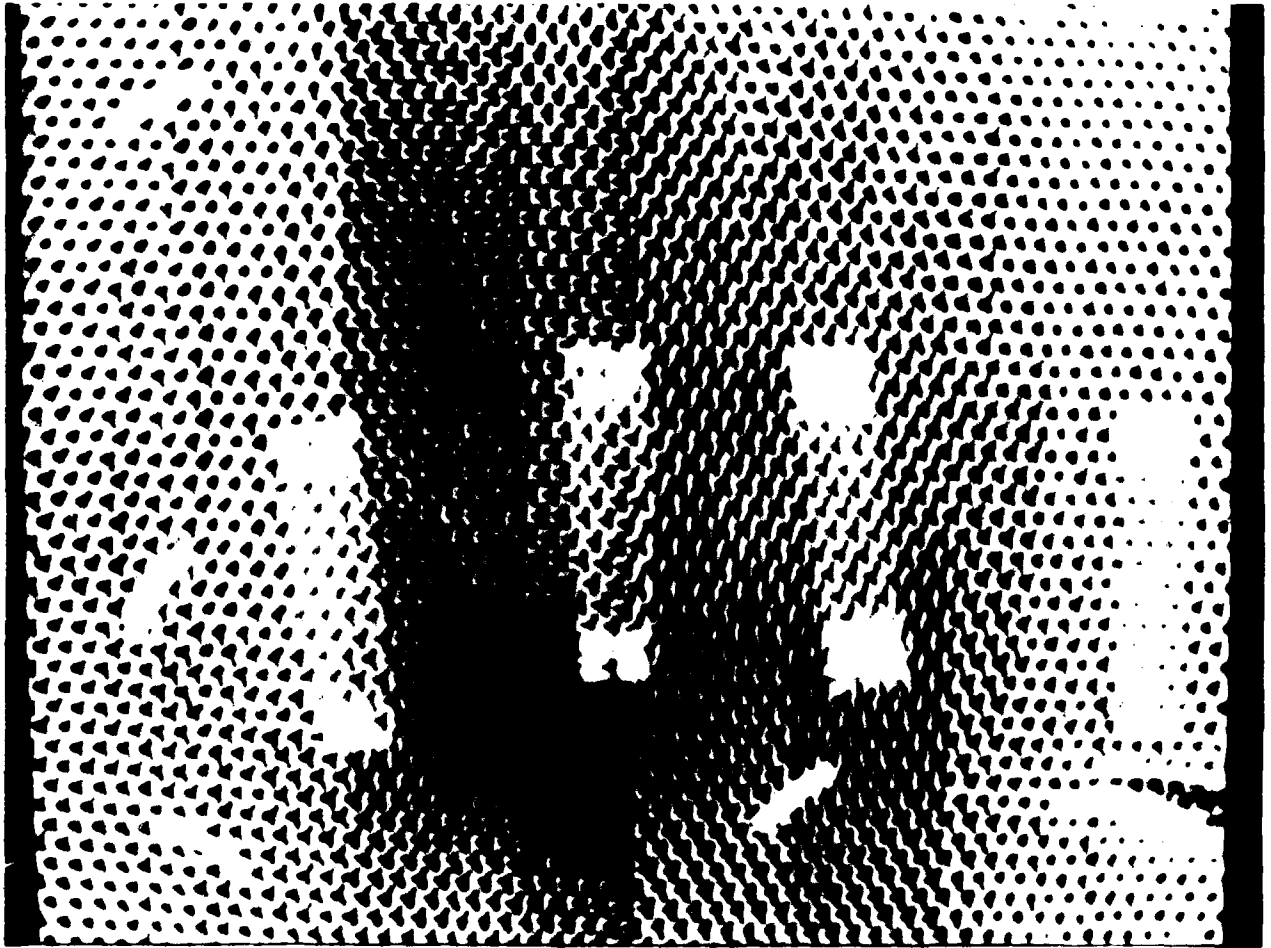


Figure 3.5.7. Landing Gear Door Honeycomb (Northrop)
Image using 8-inch Prototype.

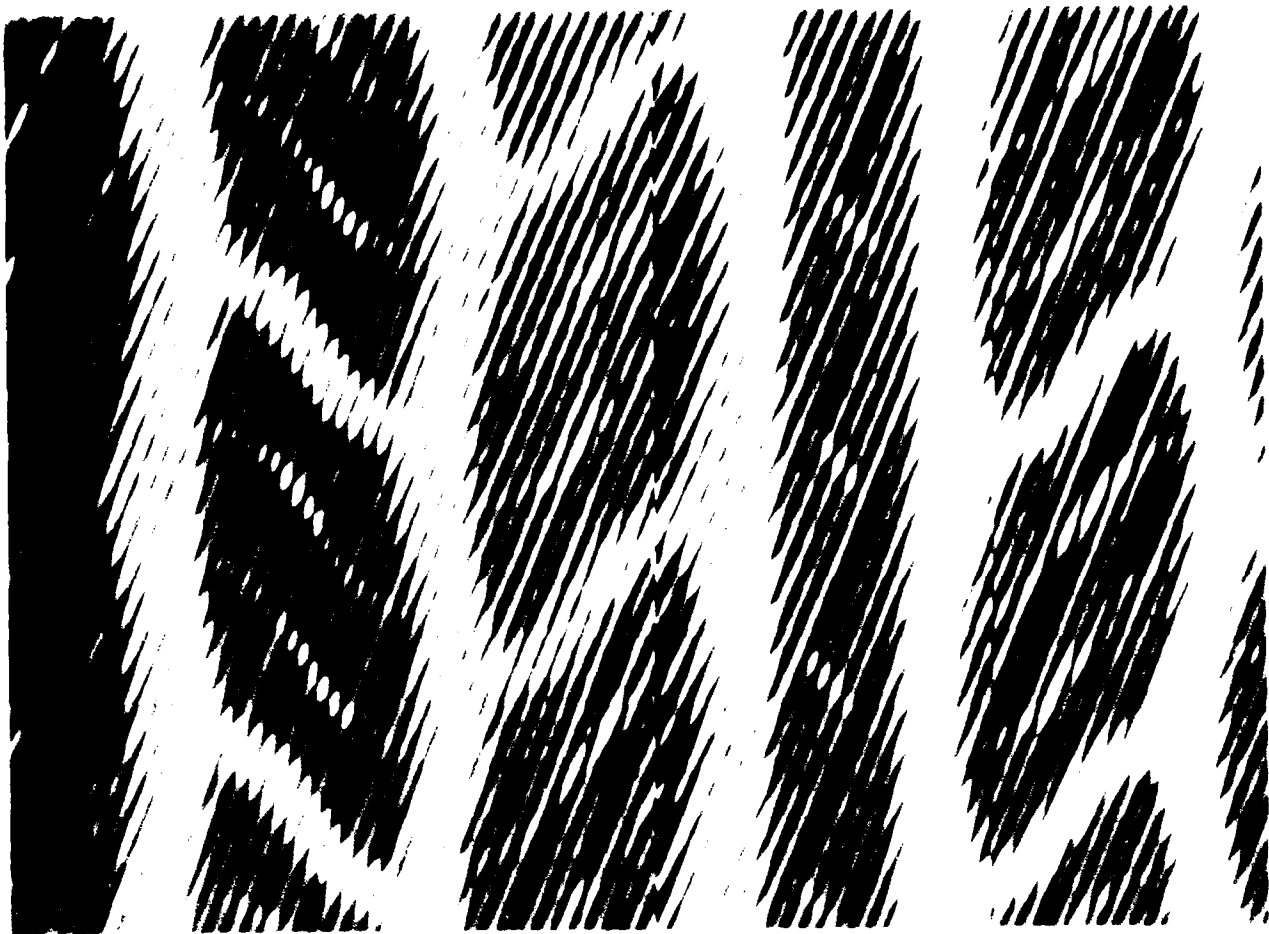


Figure 3.5.8 Radiograph of Tire Tread using 4-inch
high Resolution Mode of Prototype Linear Scanner.

A photo of the results of the software matching as shown in Figure 3.5.9. This clearly shows the smooth joining of all segments to form an electronic analog to a film image.

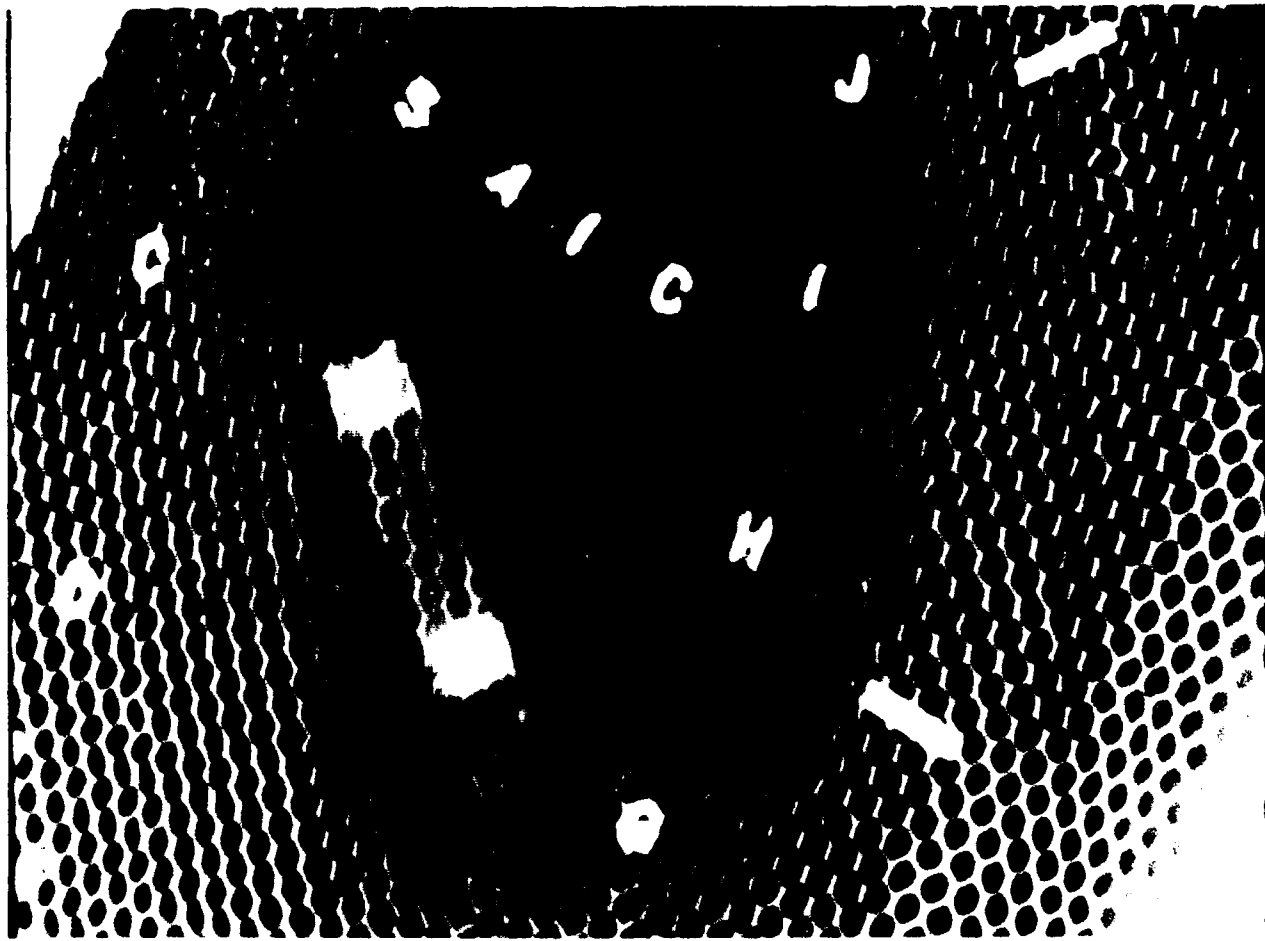


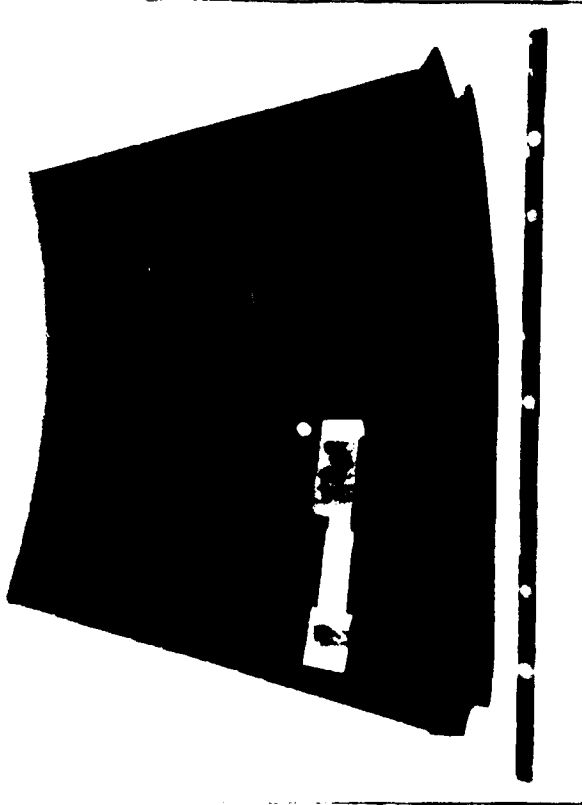
Figure 3.5.9 Software Matched Image of Honeycomb on 8-inch Prototype Scanner.

4.0 BREADBOARD SYSTEM RADIOGRAPHY OF TYPICAL AIRCRAFT PARTS

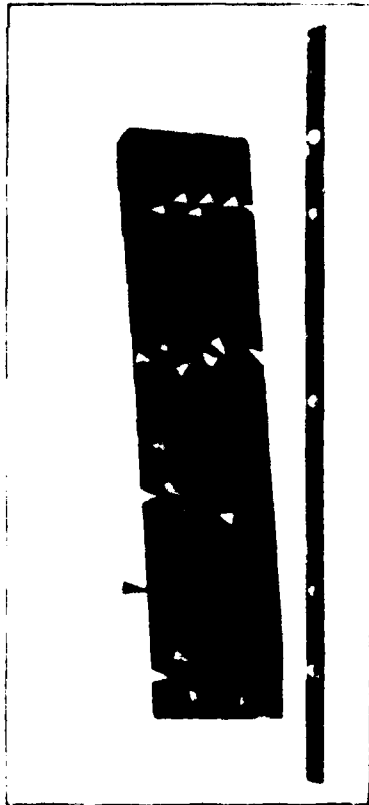
Part of the original program plan including an evaluation of the breadboard linear scanner on a group of typical aircraft parts. We have sought out a number of examples from various sources within the aircraft community which fall broadly into the groupings of composite materials, thin metal structures, electronics, small castings and complex mechanisms. These are the general groupings of components that were suggested to the Air Force early in the program. The difficulty has been finding objects that have interesting and performance revealing structure that would be accommodated in a one or two inch field of view. In some cases, data were recorded for both fields of view to show the ultimate resolution. On other examples only a single view is shown since it best portrays the characteristic being described. In all cases companion images were recorded with a high performance RTR system operating on a 4-1/2 inch field of view. This comparison is somewhat of an understatement of system performance since the resolution of the linear scanner is constant as more segments are cascaded while the area imager's resolution falls off with linear size. A more "typical" comparison would have been made using the 9-inch image amplifier field of view but the more conservative comparison still clearly shows the distinct advantages of the breadboard scanner. All scanner images shown have a software pixel to pixel gain correction applied before the display was photographed.

The first four objects studied are shown in Figure 4.1. The first object in Figure 4.1a is a bulkhead section of carbon epoxy with a number of manufactured defects built in. The part as well as the hat section shown in Figure 4.1b were provided by General Dynamics, Fort Worth Division. The step wedge shown in Figure 4.1c is a sensitivity indicator which has a number of calibrated nylon and metal fibers running across the wedges and was supplied by McDonnell Douglas Corporation. The last picture shown in Figure 4.1c is an aluminum honeycomb section with corrosion damage around the boltholes. This piece was supplied by Sacramento Air Logistics Center at McClellan Air Force Base and has been removed from an operational aircraft.

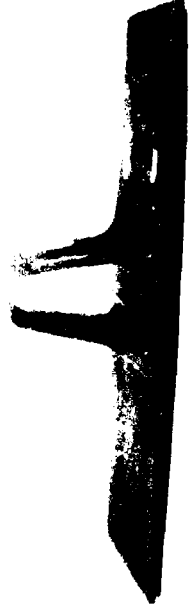
The two images shown in Figure 4.2 represent a small cut patch placed inside the bulkhead section. The data in Figure 4.2a is taken with the linear



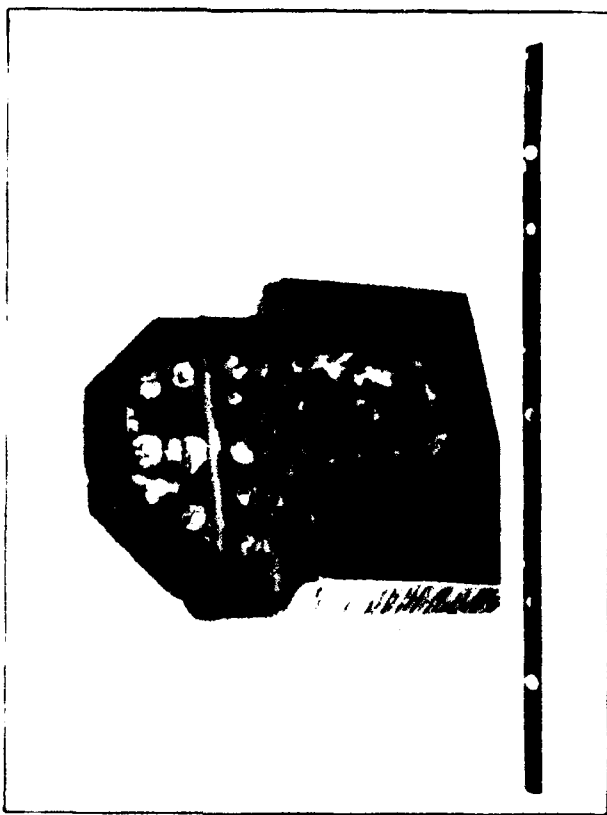
(c). Carbon Epoxy bulkhead (General Dynamics F.W.D.)



(c). Carbon Epoxy Test Wedge (McDonald Douglas)



(b). Flat stiffener section (General Dynamics F.W.D.)

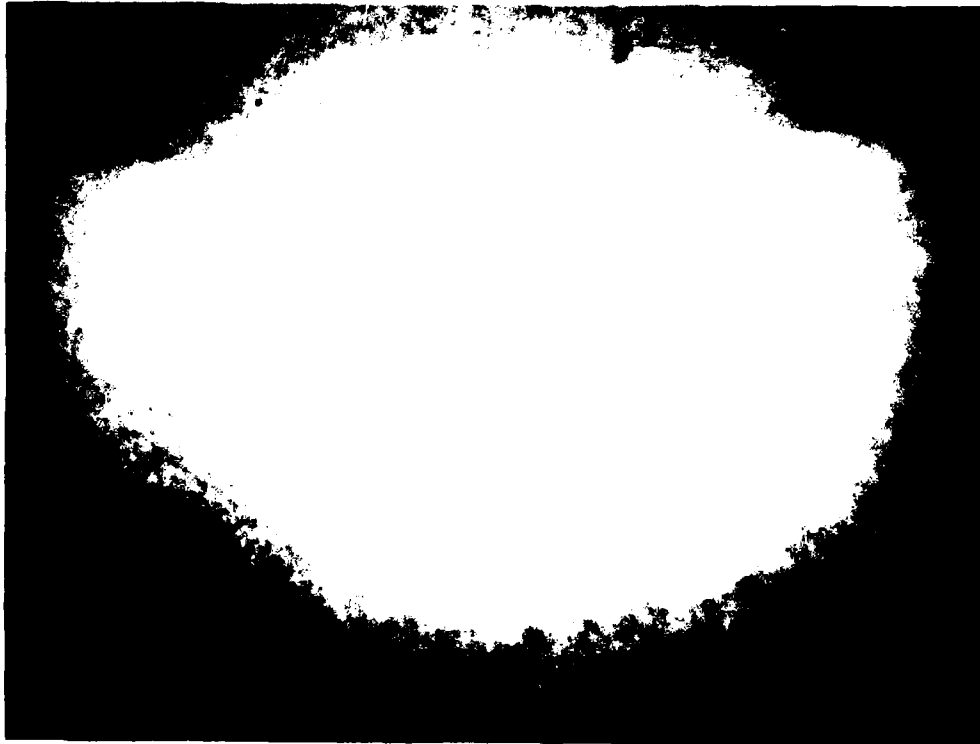


(d). Aluminum Honeycomb with Corrosion (SALC, McClellan AFB).

Figure 4.1 Typical Aircraft Components used to show Performance of Breadboard Scanner.



a.



b.

Figure 4.2 Simulated Cut Patch Inside General Dynamics Carbon Epoxy Bulkhead Test Piece. a.) Linear Scanner View with 2 inch Field and b.) Image Amplifier RTR Image.

scanner operating at a 2-inch field of view. The picture is compressed somewhat in the horizontal axis due to too fast a scan velocity. The picture has been expanded on the monitor to better represent the correct aspect ratio. The exposure was at 16kV at 35 ma. The corresponding picture in Figure 4.2b is taken with a conventional image amplifier. Due to its thicker entrance window, the exposure had to be made at 23kV. The increased clarity of the edges of the patch and penetrameter are clearly visible in the line scan image. Moreover, the picture shows the striking increase in contrast sensitivity with the very thin entrance window of the line scanner converter screen which permits soft X-ray energy operation. Other low contrast defects in this same sample are equally well revealed with the line scanner operated at this low energy. A 1-T hole is easily visible on a 0.125" aluminum penetrameter.

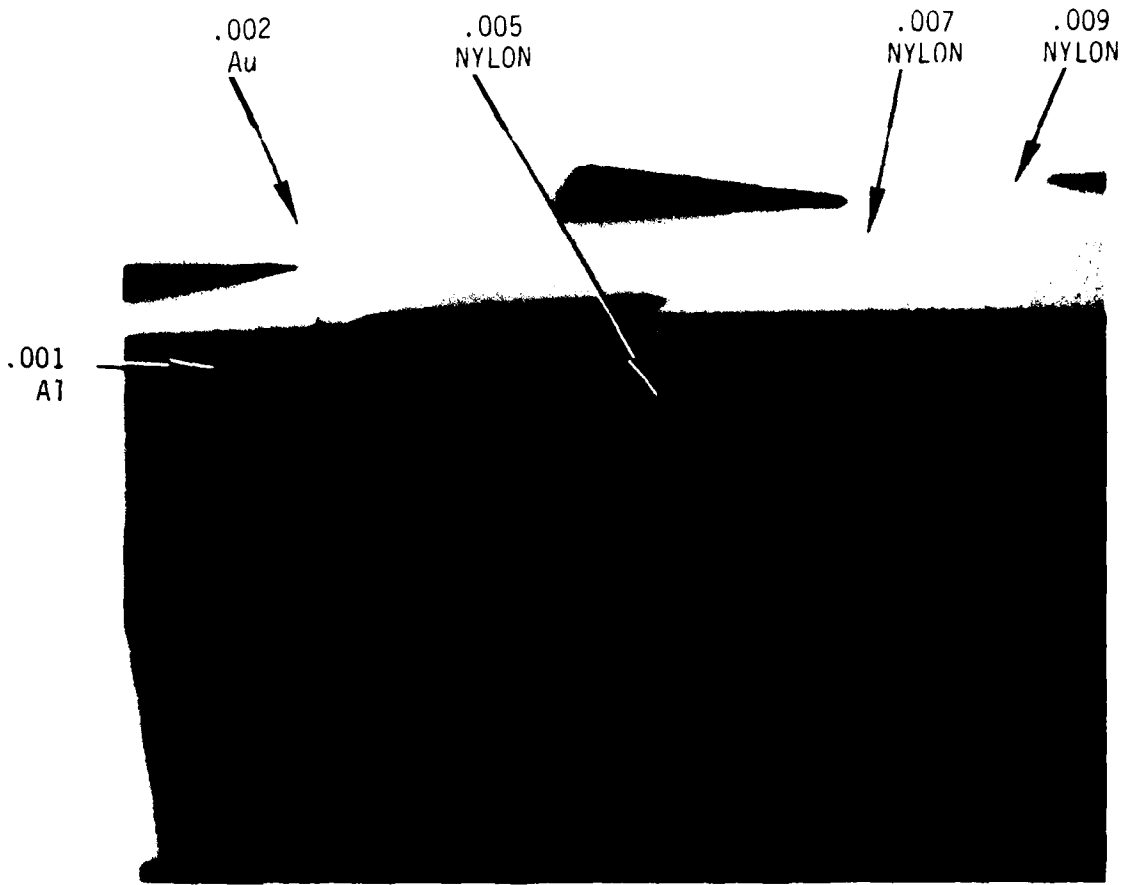
The hat stiffener section test object shown in Figure 4.1b was imaged straight down from the top. The upper section of the stiffener had two small holes drilled in the wall (about 3 inches away from the base). The base section had two fine (0.020" and 0.010") holes drilled inward from the edge. The image shown in Figure 4.3a is again a linear scanner image with some compression along the mechanical scan axis (horizontally). The two holes from the side as well as one of the two holes in the hat top are all clearly visible (the other hole is not in this view). Although the digital image "wraps around" causing an apparent dark overload region, the active region of the picture is unaffected. Unlike blooming which smears the edges near an overload region, this data is completely recoverable by including the next significant digit in the image processor. (In this case, the most significant 8 bits out of the 10 bit data are shown). The fine mesh pattern observed on the part is reproduced also in the film radiography and is due to the fabric layer on the surface. Figure 4.3b shows the same image viewed on an image amplifier. The lead mask sets the visible image to 2"x2" and the unmasked image area must be limited to prevent blooming. One on axis hole in the top section is visible but the two holes drilled from the sides can barely be seen and then only if the location is known in advance.

The McDonnell Douglas Test wedge was designed to test the sensitivity of real time systems. It is composed of carbon epoxy in a series of steps starting with 0.040", 0.060", 0.90" and 0.120" as the first four. Taped under

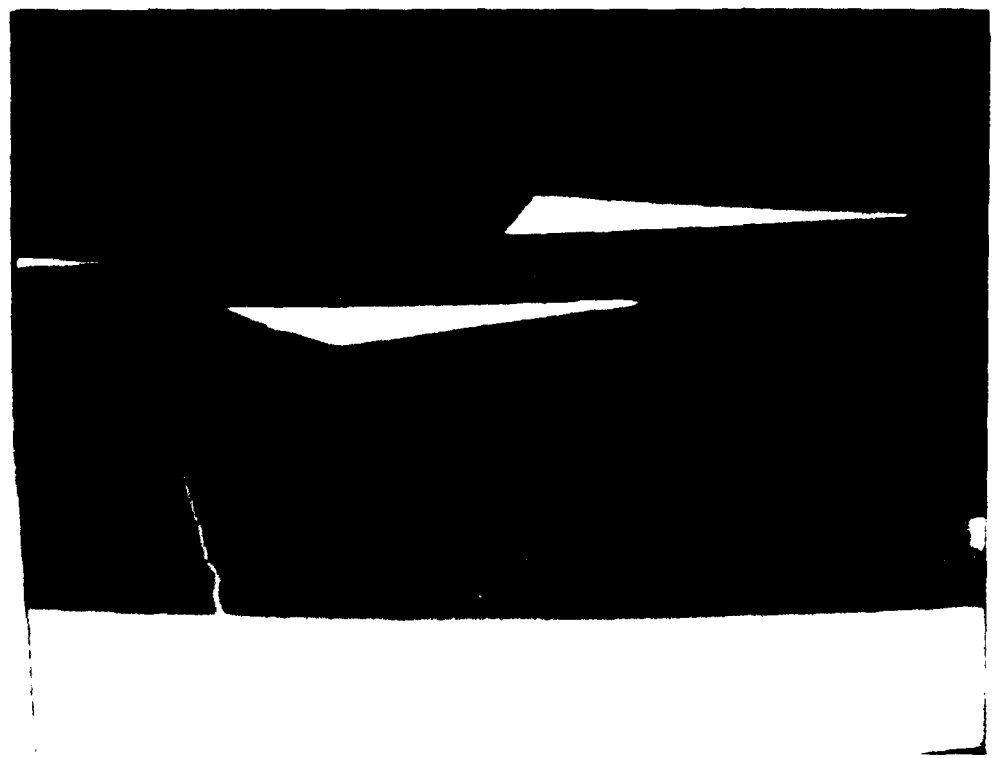
the sample are: a 0.001" aluminum wire, 0.002" gold wire and several nylon fibers with the thinnest being 0.005", 0.007" and 0.009". In 2-inch wide field of view shown in Figure 4.4a, taken at 13 kV and 48 ma, all wires are clearly visible through four layers of the step wedge although limitations in the monitor make it difficult to see all steps simultaneously. The data in Figure 4.4b shows the 1-inch wide field of view in reverse video with a logarithmic grey scale similar to a film image. In both images, the scan is purposely compressed by a factor of 2 to permit all four steps to be visible on the same picture. The image amplifier image in 4.4c shows the 0.002" gold wire and some of the 0.009" nylon wire but all finer details are generally lost even on the thinnest two steps.

The sample of honeycomb with corrosion around the bolt holes is a good subject for comparison. The image in Figure 4.5a is a 2-inch wide linear scanner view taken at 48kV. Some fine damage is visible in the honeycomb adjacent to the bolt holes. This detail is totally lost on the standard RTR image in Figure 4.5b. The reversed polarity of the linear scanner image brings out even more detail in Figure 4.5c and the enlarged high resolution view in Figure 4.5d shows even higher detail although the effects of statistical noise are beginning to become evident. One important feature in all these images is the relatively constant angle of parallax. With a 2-inch imager, one could, in principle go on for an indefinite distance along the scan direction keeping the honeycomb axis aligned with the X-ray beam.

Some of the other types of components used as test objects are shown in Figure 4.6. These components include electronics, turbine blades and pieces from munitions. One of the most striking demonstrations of X-ray resolution can be found when attempting to image electronic components. The component imaged in Figure 4.7 is one half of a LSI microcomputer chip. The image shown in Figure 4.7a is a 1-inch wide line scan of the part. The corresponding image is an enlarged view taken of the 4 1/2" image amplifier based RTR system. The scan lines are quite visible because of the considerable enlargement required to make the two images a similar size. The line scan images were taken with the combined Gd_2O_3S + Terbium Fiber Optic converter screen at 110kV at 5 ma while the image amplifier used approximately 90kV at 2 ma.



a.



b.

Figure 4.4 Real-Time X-Ray Images of First Four Steps of McDonnell Douglas Test Wedge, a.) 2-inch Line Scan Image and b). 1-inch Line Scan Image, (High Resolution) 13 kV, 40 mA in Reverse Video and Logarithmic Grey Scale similar to Film.

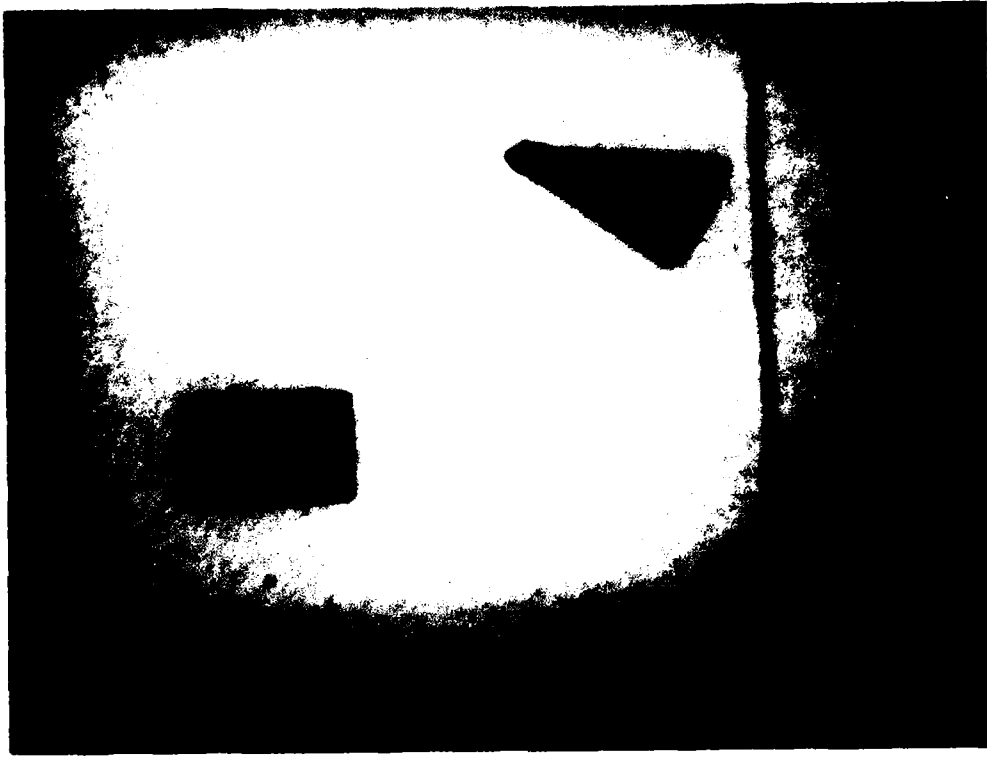


Figure 4.4 c. Conventional RTR Image of McDonnell Douglas Carbon Epoxy Test Wedge. (steps 1, 2, and 3)
(Compare with Figure 4.4 a.)

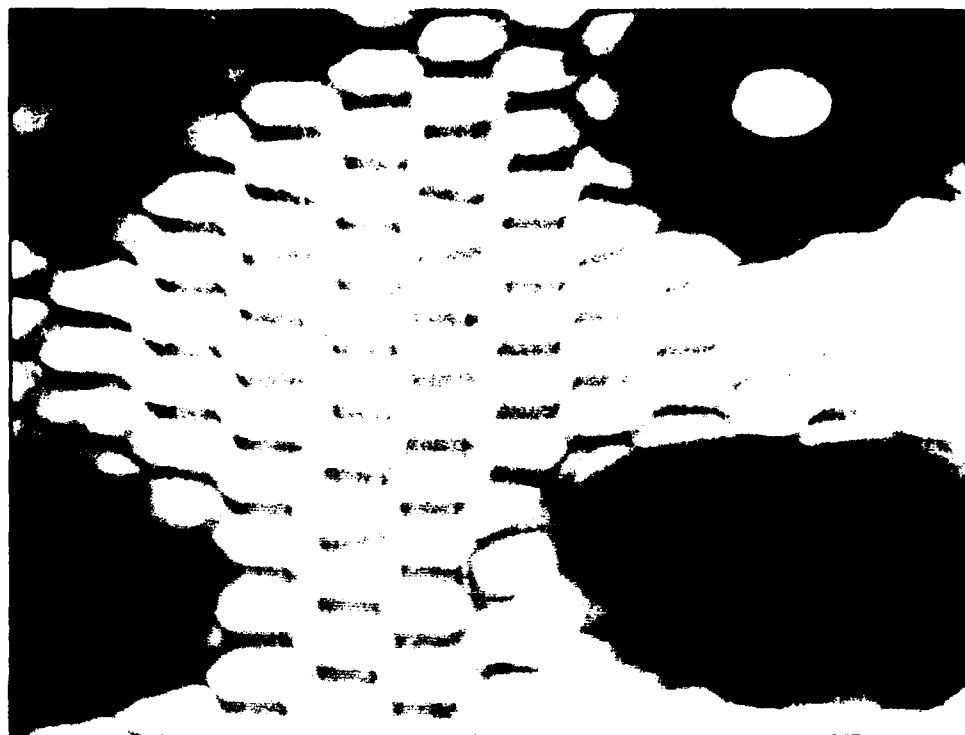
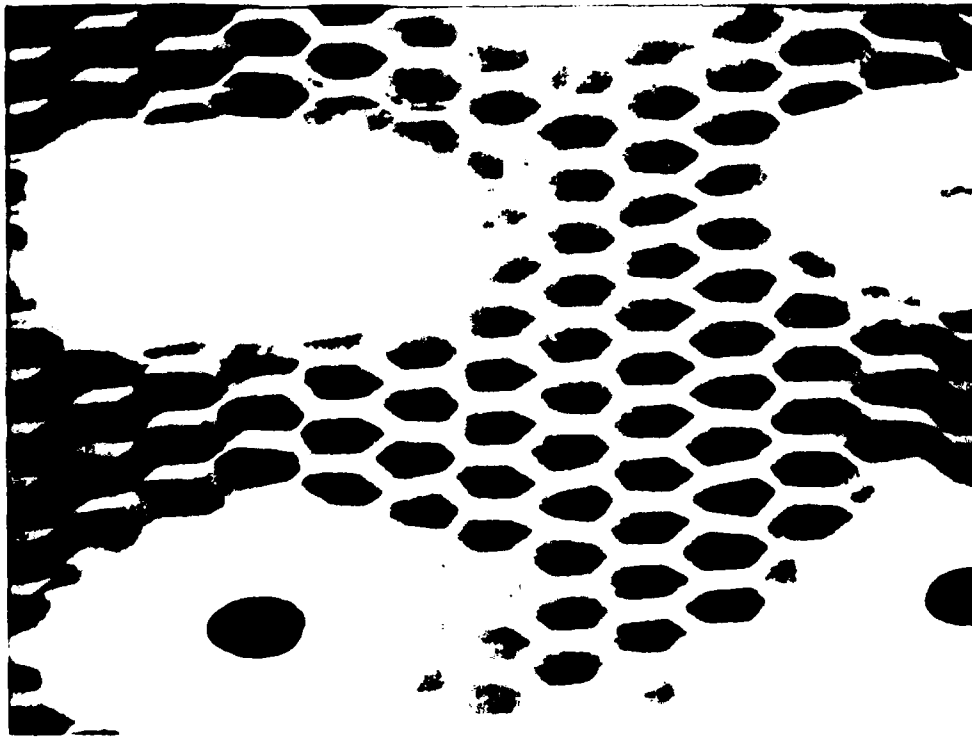


Figure 4.5 Aluminum Honeycomb Section Removed from Service showing Evidence of Corrosion a.) 2-inch Linear Scanner Image and b.) Similar Image on Conventional Image Amplifier RTR System.

c.



d.

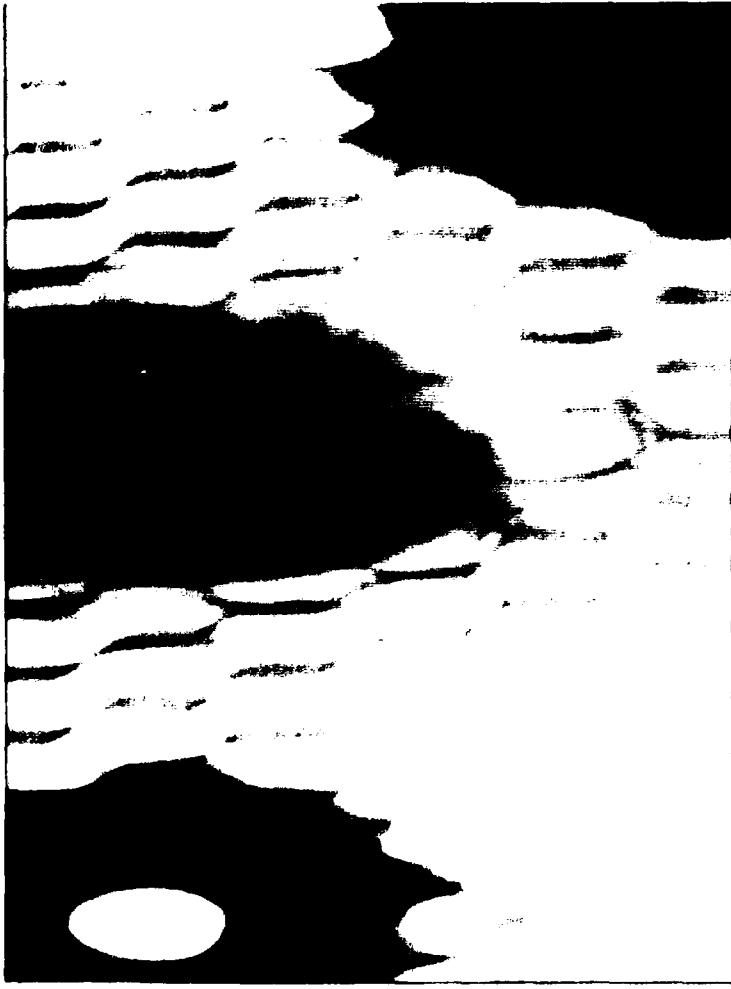


Figure 4.5. Aluminum Honeycomb Section Removed from Service showing Evidence of Corrosion (McClellan AFB) c.) Reversed 2" Image (film type gray scale) and d.) High Resolution 1" Field Linear Scanner Images.

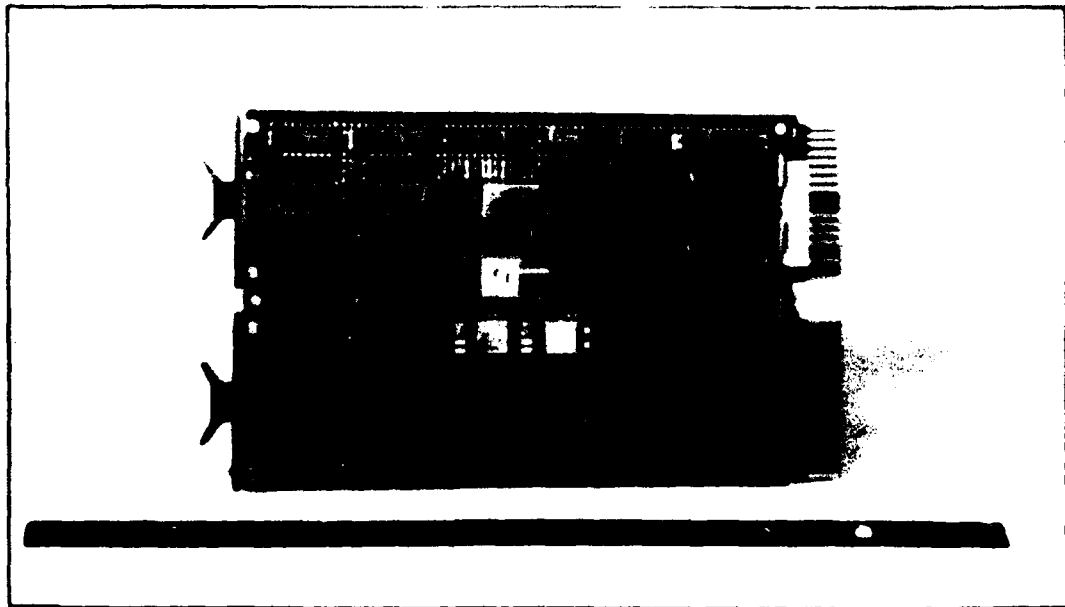
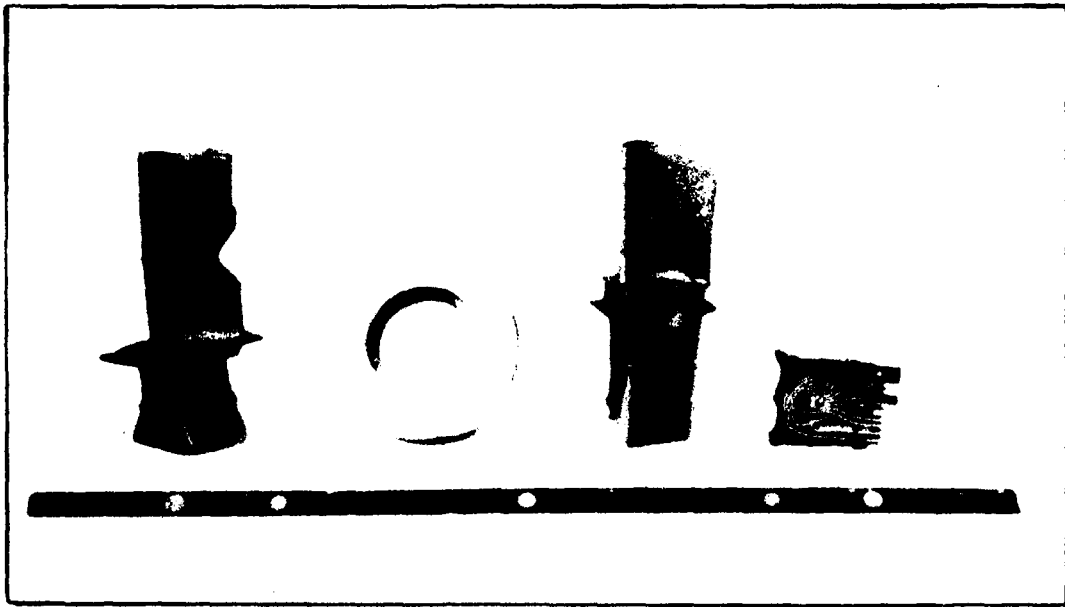
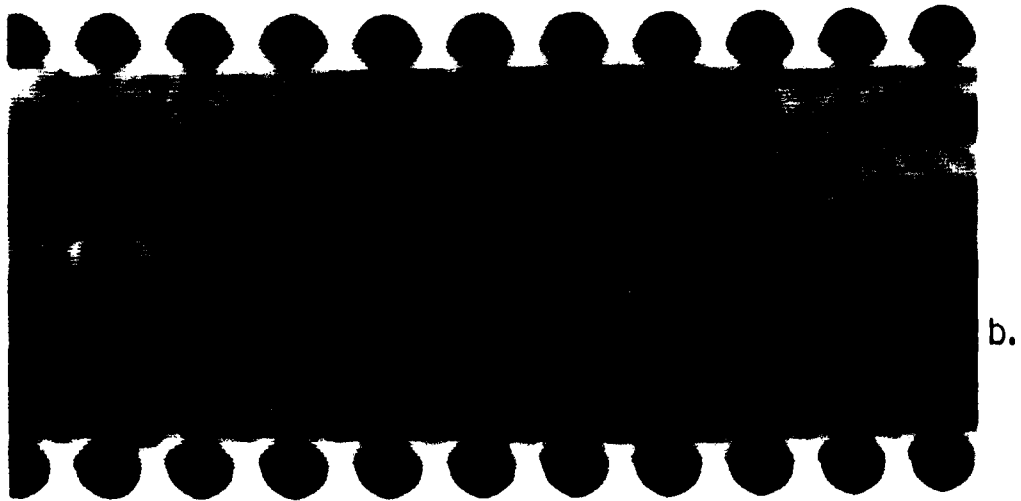


Figure 4.6 Examples of Test Objects used to Evaluate Breadboard System at Higher Energies. Includes Turbine Blades, Printed Circuit Switch, Fuse Safe/Arm Mechanism and LSI Micro Circuit Chips.



d.



b.

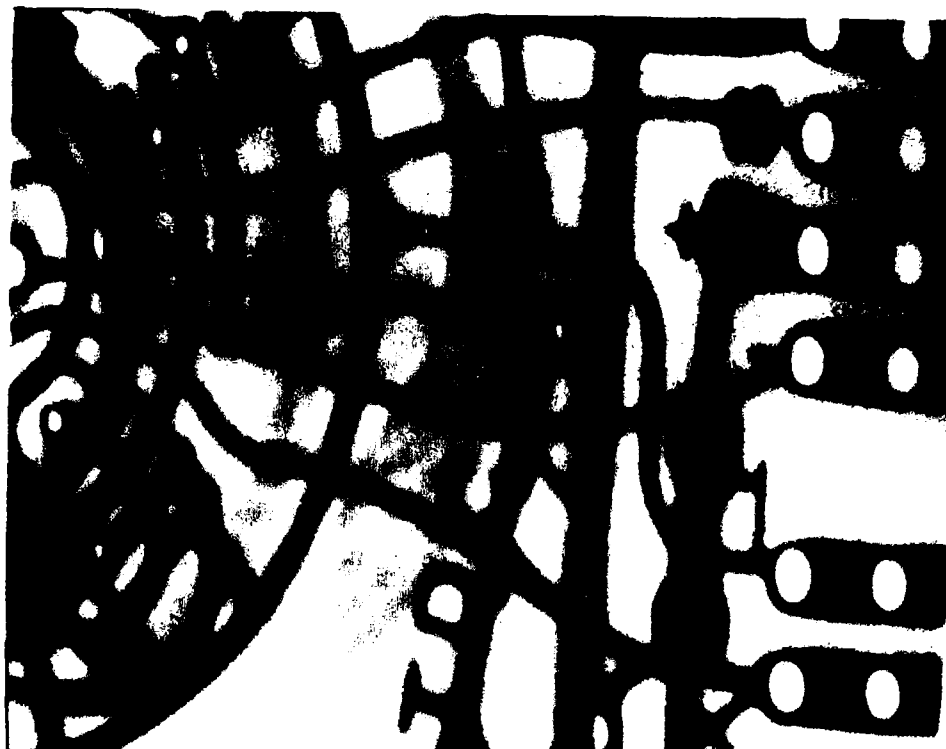


Figure 4.7 LSI 11/23 Microcomputer Chip taken with
a.) 1-inch high Resolution Linear Scanner and
b.) Conventional Image Amplifier RTR System.

A similar comparison in system resolution can be observed in Figure 4.8 which compares a 1-inch line-scan view of a printed circuit thumbwheel switch with the image taken on the conventional RTR system. Although nothing in particular requires the high resolution in this part, it is clear from comparing the sharpness of the images that small cracks or flaws in the traces would be relatively easy to detect in the line scan image.

Probably one of the most important applications of high-resolution line scanners to aircraft component is the imaging of turbine blades. These blades generally require high energy to penetrate, are filled with complex passages and often present complex coherent scattering patterns that obscure the interpretation. The linear scanner addresses all of these technical difficulties in an effective manner. The one inch wide image of the tip of a complex blade in Figure 4.9a reveals fine passage ways and several irregularities on the tip region. At 100kV at 14 ma some overload is evident for which the monitor is unable to accommodate. The line-scan image however shows much more internal structure than the corresponding RTR image in Figure 4.9b. A thicker blade is shown in a 2-inch line scan image in Figure 4.10a. All internal structure is clearly visible even in this half resolution image right out to the edge of the part. (The lines in the cut out region are due to digital wrap around in the image processor and are not significant). The full resolution image shown in Figure 4.10b brings out even more structure in the central region of the blade. The RTR image shown in Figure 4.10c is totally overloaded and cannot keep the entire surface region of the blade within the operating range of the system. This is a very typical result on the image amplifier and usually requires careful masking of the differing regions of the blade to make them individually visible.

The last two samples are shown to illustrate the high energy response of the converter screen and linear scanner. In both cases, the subjects are related to ordinance rather than aircraft components but are chosen as examples of either complex mechanism or strongly scattering subjects that would provide recognizable images within the small format available. The 10 mm Terbium-doped fiber-optic screen was used in these examples to further reduce the effects of scatter.

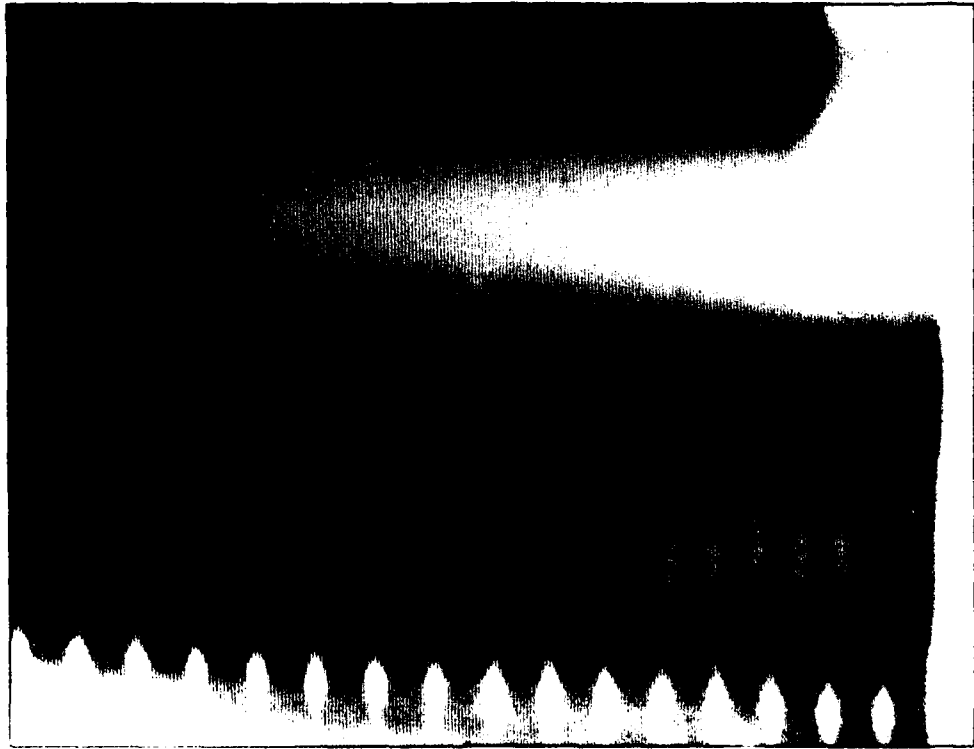


d.

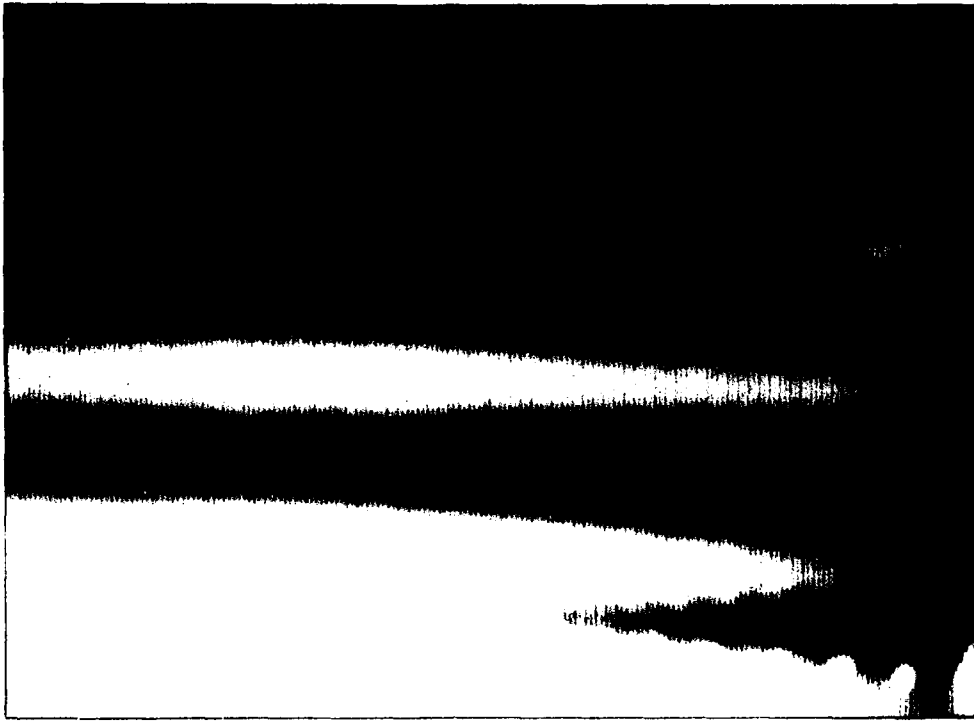


b.

Figure 4.8 Printed Circuit Board Thumbwheel Switch taken with a.) 1-inch High Resolution Linear Scanner and b.) Image Amplifier RTR System.

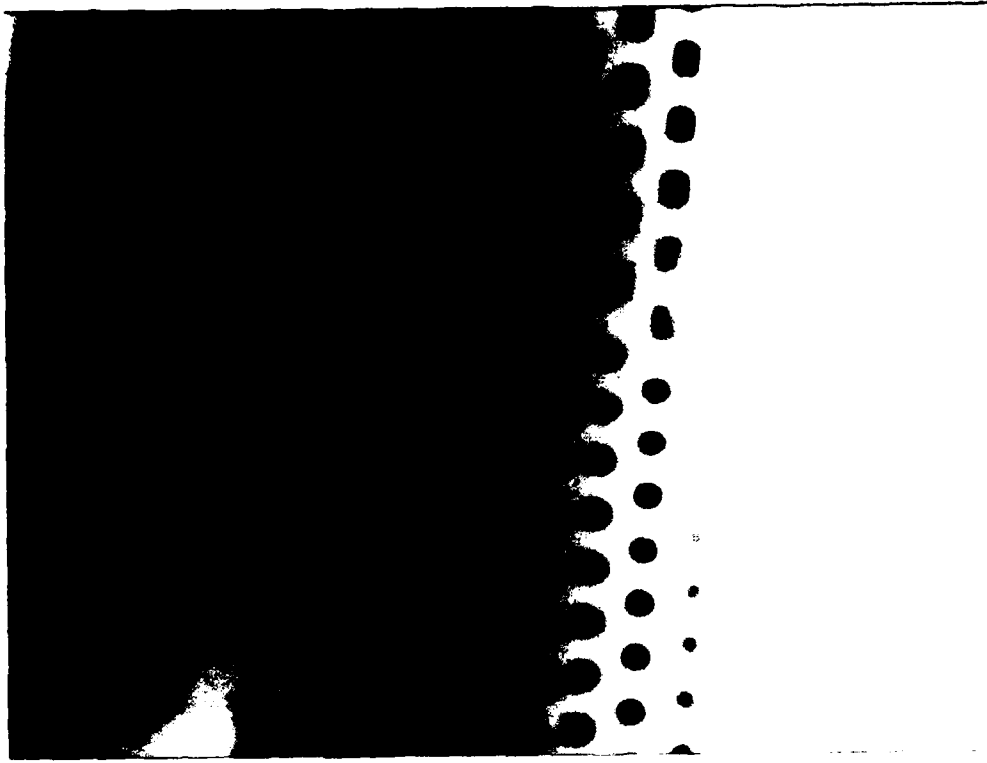


a.



b.

Figure 4.9 View of Aircraft Turbine Blade taken with
a.) 1-inch wide High-Resolution Line Scanner and,
b.) Conventional Image Amplifier RTR System.

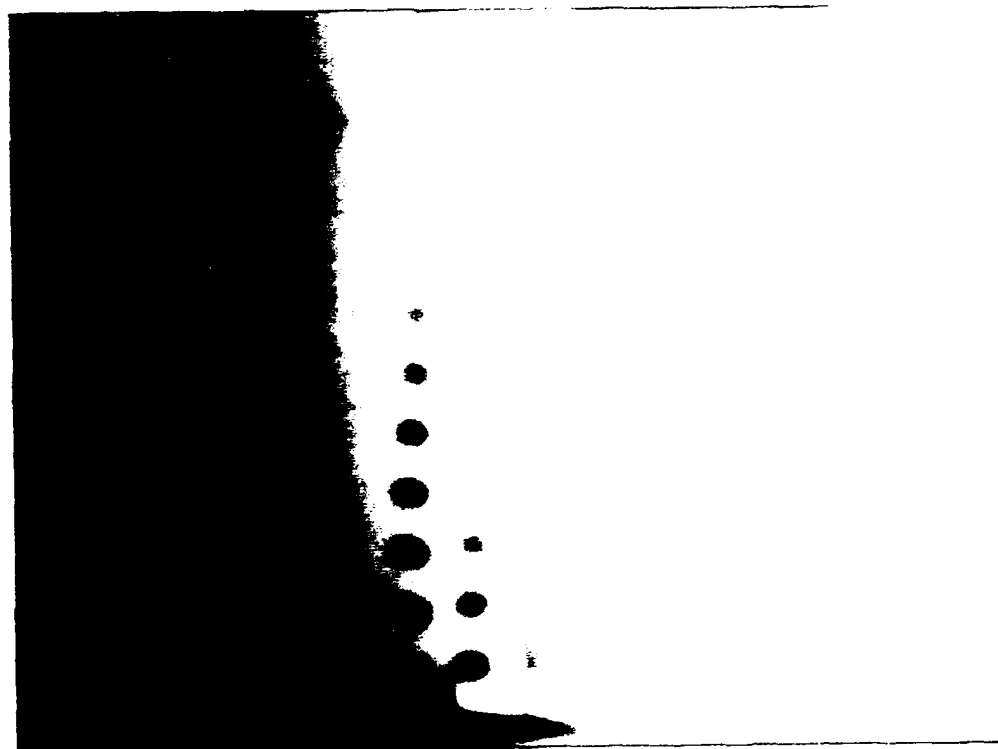


a.



b.

Figure 4.10 Real-Time Radiograph of Complex Turbine Blade showing internal passages, a.) 2-inch Line-Scan View, b.) 1-inch Line-Scan View.

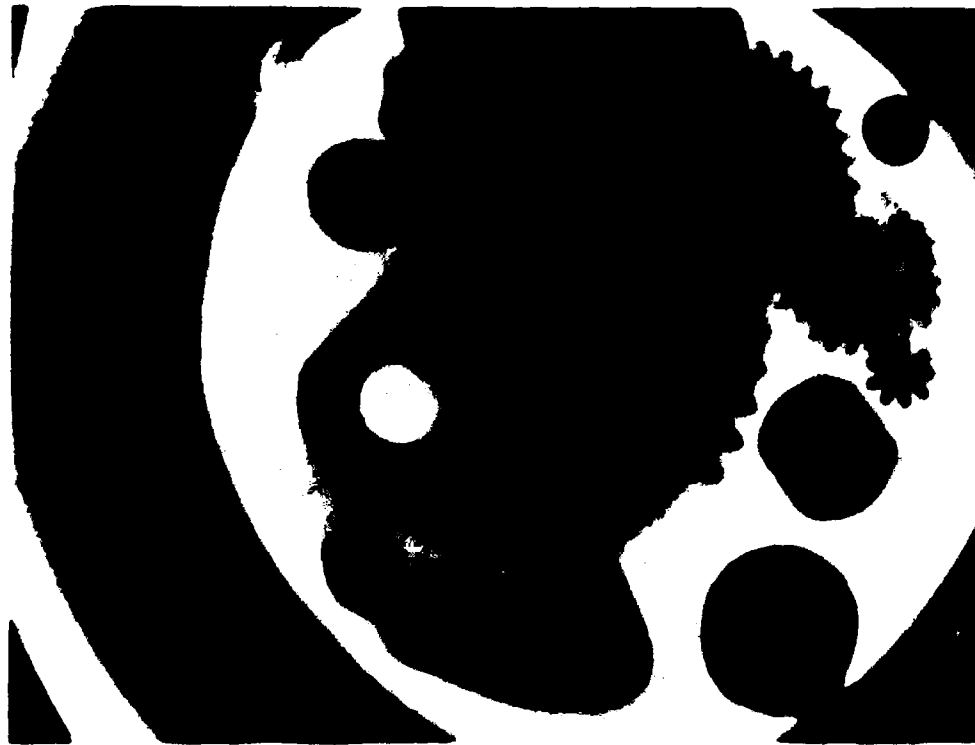


C.

Figure 4.10c Real-Time Radiograph of Complex Turbine Blade showing internal passages, c.) Conventional Real-Time Image Amplifier System.

Figure 4.11a shows a 2-inch wide line scan of the safe and arming mechanism of a time delayed fuse. This is mounted in a thick aluminum holder that is at least 2-inches thick around the rim. The scanned image was made at 156kV at 4 ma axially through the holder with the mechanism mounted inside. Notice how clearly the position of all components can be determined. Figure 4.11b was the final result of a standard RTR measurement. This measurement required careful masking to reduce blooming and keep the overload under control. The image was shot at a somewhat lower kV and hence looks more contrasty but the resolution is definitely poorer than the line scanned image.

The image in Figure 4.12 is a 1-inch line scan of the explosive/base interface at the aft end of an 81 mm mortar. This region is a critical area and one needs to detect base separation, voids and porosity. The inert test sample easily shows porosity and the presence of a good bond on the nearly hemispherical bottom of the base. This image demonstrates not only the good resolution of the line scanner but its dramatic reduction in scatter from the steel shell body and explosive internal mass. This may well represent one of the most effective applications for line scan technology in approaching or surpassing film radiographic performance.



a.



b.

Figure 4. (a) *Salvia* stem showing sclerenchyma (dark) in the cortex. (b) *Salvia* stem showing sclerenchyma (dark) in the cortex and in the vascular bundle.



Figure 4.12 Rear Portion of Inert 81mm Mortar Shell showing Details of Aft Steel-Explosive Simulant Interface. Taken at 280kV using 2 inch Field Linear Scanner. (Note This Photographic Reproduction does not Show all of the Detail Available from the Monitor. Porosity Should be Easily Visible Throughout the Simulant.)

5.0 PROPOSED-FULL SCALE DESIGN

Using the experience gained during the testing and evaluation of converter screens, the building of the 2-inch breadboard scanner and the prototype 8-inch scanner we have evolved a design that takes advantage of the best of each system. It is predicated on a design that can be built out of existing or readily fabricated components and which can be read out on commercially available image memories and displays.

The proposed system would incorporate a fiber optically coupled line scanner using variants of the screens described in this report. It is aimed at applications requiring the highest level of performance and not necessarily the field level type of inspection. In the final section of this report other alternatives are discussed which use major parts of the technology to produce an electronic radiography system that is more serviceable for portable use and still retains substantial improvements over existing RTR system capabilities.

5.1 PROPOSED SYSTEM SPECIFICATIONS

The proposed scanner would have a 4096 pixel readout resolution as this represents the largest line width of currently available digital image memories. This will provide a 10 lp/mm Nyquist limiting resolution for an 8 inch wide scanner or an 8 lp/mm limit for a 10-inch scanner. In any case the screen chosen will be adequate to maintain the system resolution when measured by standard MTF techniques.

The resolution along the mechanical scan direction of the proposed system would be variable. Several Tungsten slits would be provided to permit calibrated slit widths from 0.002" to 0.020". This would correspond to resolutions from 1 to 10 lp/mm along this axis. The mechanical part scanner will permit a corresponding range of speeds to either match or purposely over or underscan the mechanical axis to best suit the inspection needs. This would also permit a virtually unlimited scan length limited only by the mechanical drive itself. This would permit looking at very large parts in continuous 8-inch-wide views which could be scrolled in either direction across the display monitor.

The system will include both a pixel by pixel dark current and gain correction that can be independently controlled. With only slight cooling of detectors, the system will be able to double the current sensitivity range while maintaining or improving its signal to noise performance. The digitization will be done to 1 part in 4095 with an active black level clamp that will permit expansion of particular grey levels or stable logarithmic grey scales for particular applications.

The readout will use rigid fiber optic bundles to transmit and split the image into four 1024 pixel imagers. The fused glass optics have demonstrated a 2.5x improvement in transmission over the flexible optics and can be fabricated with less than a 50-micron gap between sections. The use of these ribbons and of a more advanced minifier-intensifier will permit only a single gain stage to be required which will improve resolution and overload performance.

The system will permit the use of several advanced screens so that the operator can optimize performance for soft X-ray, general purpose applications and highly scattering or thick components. This change will be simple and self calibrating. Screens employing Gd_2O_2S deposited directly on fiber optics or on terbium doped fiber scintillators will be employed on the system. A special calibration screen with metalized grids will be provided to test the electro optics using a back-lit optical source to permit adjustment without using X-rays.

The system will be supplied with the most advanced low-angle anode X-ray sources. These X-ray tubes permit significant increases in tube power using smaller projected focal spots. They achieve this performance by restricting the X-ray cone size on one axis. This is clearly an advantage for a line scanner since it only uses a very small angle along the mechanical scan axis. Pre-collimators restrict the beam to a narrow fan that just illuminates the detector further reducing scatter and hence shielding requirements for such a system.

The entire system is controlled from a small computer which permits the operator to set up the image memory, calculate and load in all in process

correction terms and start the scan. Data from the scanner can be stored on magnetic or optical media since its resolution is far too great to use analog storage. Display will be on a 1024 x 1024 monitor, with 2048 x 2048 capability built into the system. The entire package will be human engineered to permit a radiographer with little specialized training to learn to use the system effectively.

5.2 SCANNER HEAD DESIGN

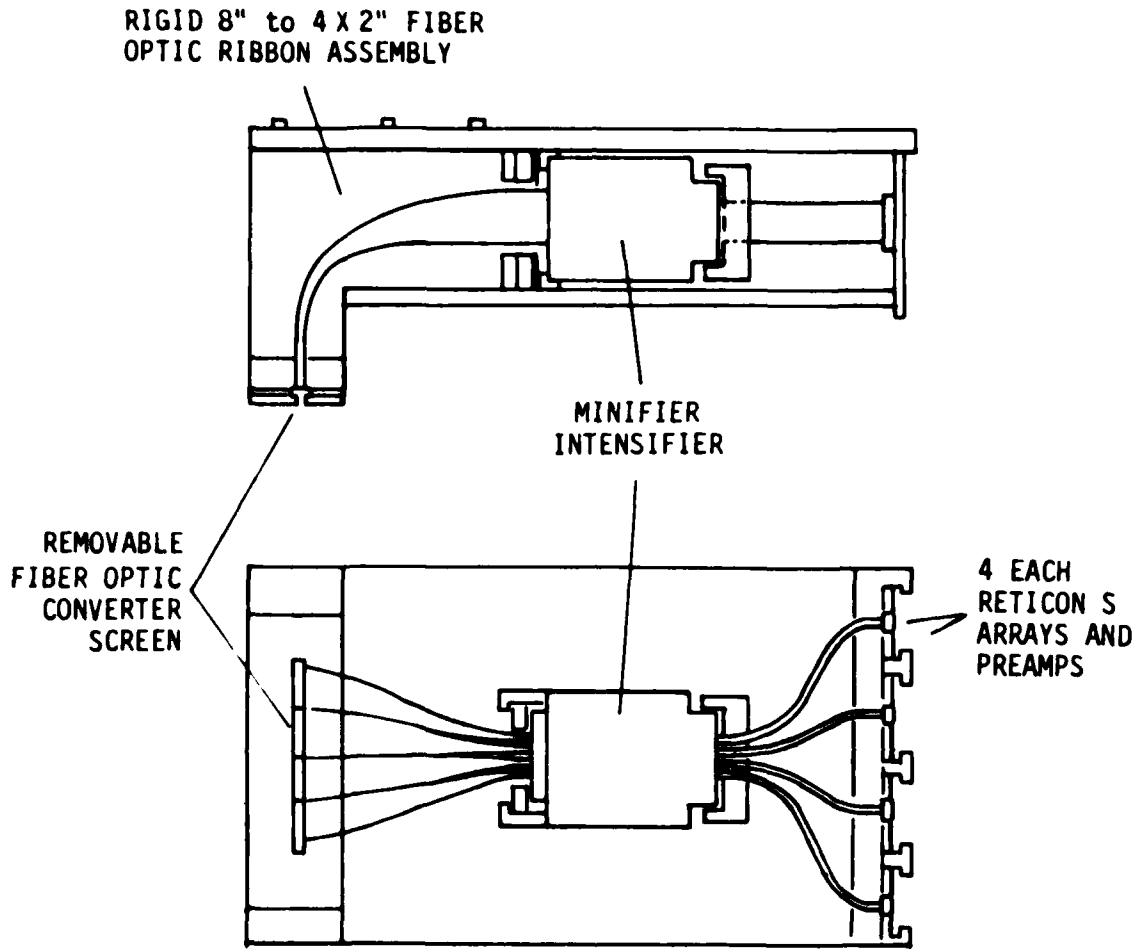
The scanner head design is shown in Figure 5.2.1. It couples the removable fiber-optic screen to a fused fiber ribbon to transmit the light away from the radiation area and break the image into four contiguous segments. The light, now broken into four lines passes through a minifier-intensifier assembly which provides a minimum of 150x green light gain with an output spectrum that matches the self-scanned silicon arrays. The light from the anode screen of the intensifier is individually piped to the four arrays and preamps. Adjustable stops permit precise alignment of the components both on the intensifier output as well as at the silicon array. This ensures that no information is lost. Unused pixels on the array can be skipped in readout so that there will not be a visible seam between sections of the screen. The box holding the scanner is shielded and held fixed in relationship with the source for optimal alignment. Failure to maintain alignment at these performance levels will produce visible irregularities in the picture that are not tolerable.

The part is moved on a two axis manipulator (up/down and along the scan axis). The control for the scan speed is derived from the clock rate of the readout so that perfect synchronism is always maintained. The use of a precision motion table and encoder stabilized stepper drive provide smooth and reproducible motion for parts of any reasonable length.

5.3 SYSTEM ELECTRONICS AND CONTROL

System Overview

The basic block diagram proposed is similar to that developed for the 8 inch prototype system (see Figure 5.3.1). It differs primarily in its use of



SAIC-86RP-32

Figure 5.2.1 Design of Fiber-Optic Scanner Head for Prototype Scanner.

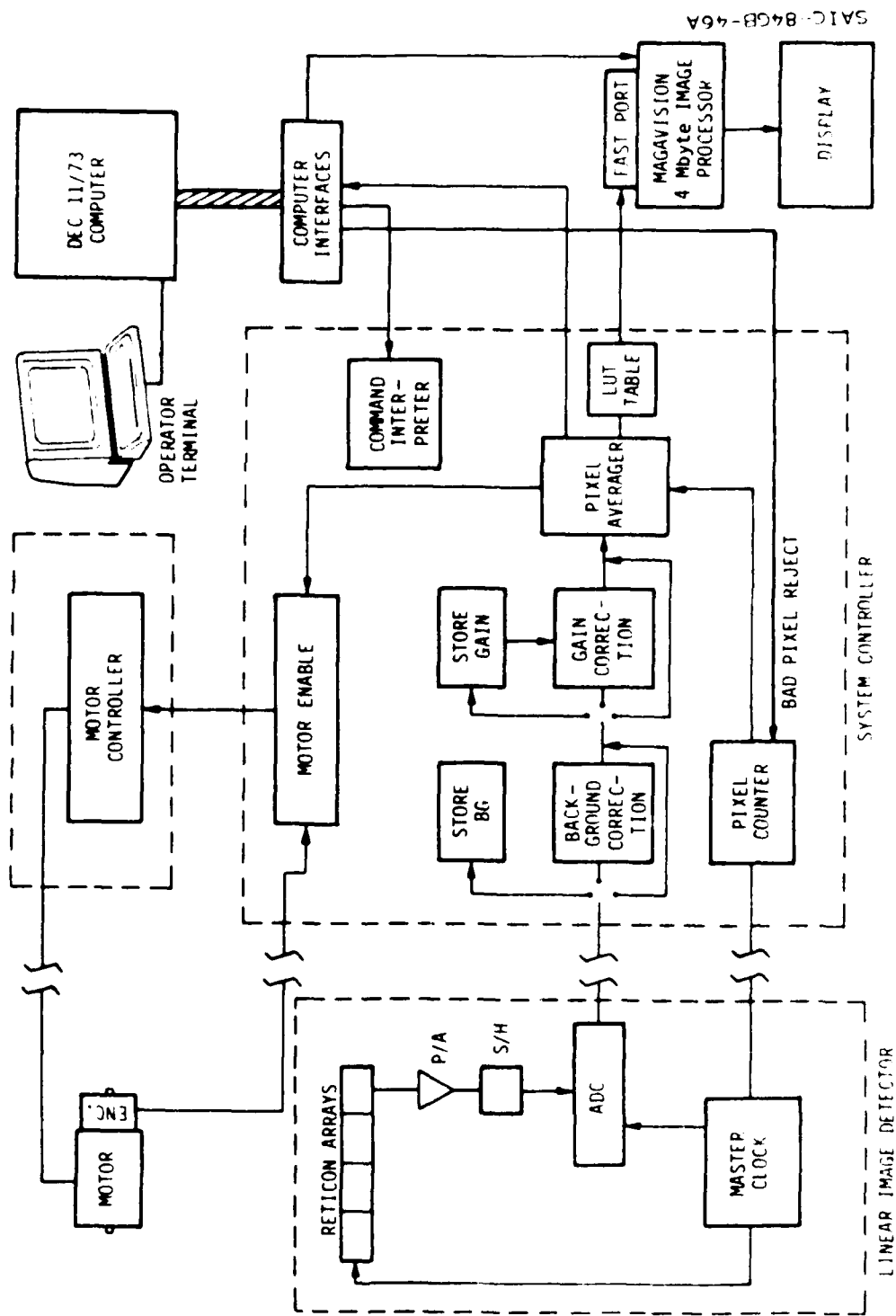


Figure 5.3.1. Simplified Block Diagram of the System Electronics.

a 40-MHz clock rate image processor capable of storing a 4096 x 4096 image. Its ECL (emitter coupled logic) permits the system to process and display data at a true 1024 x 1024 rate and be expanded to 2048 resolution in the future. The computer used is a LSI 11/73 microprocessor which puts a great deal of processing power together in a small and easily integrated package.

The Electronics System is broken down into the analog electronics, the digital clocks, digitizer and correction circuits, the control for the stepper motor and the storage and display system. The following discussion centers on those portions of the system that require custom design and engineering.

Analog Electronics

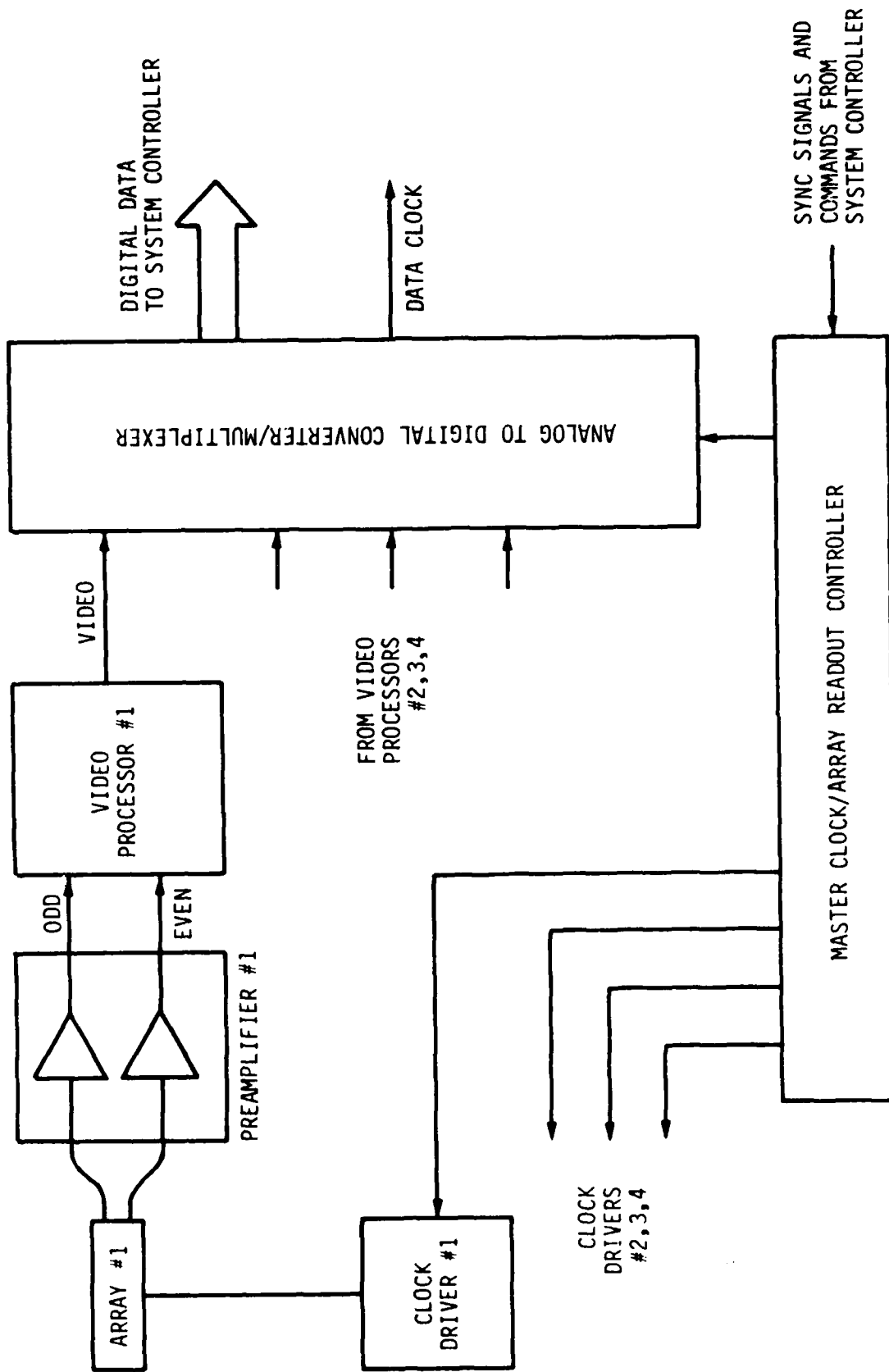
The linear scanner analog electronics includes four linear photodiode arrays (Reticon 1024SF), each with its own dedicated preamplifier, clock driver, and video processor, plus an analog-to-digital converter/multiplexer and a master clock which are common to the four arrays. A simplified block diagram showing the arrangement and interconnection of these components is shown in Figure 5.3.3.

The individual photodiodes (pixels) are read out sequentially from 1 through 4096. The maximum data rate corresponds to approximately 8 microseconds/pixel, yielding a total line (four arrays) scan time of 33.3 milliseconds. This is the normal integration time. Two longer integration times (X2 and X4) are included and are selectable by software.

The data from the arrays is digitized in the analog processing unit so that only digital data, along with a synchronizing data clock, are transmitted back to the control/computer room. The reason for this is to prevent the possible pickup of noise on long analog lines.

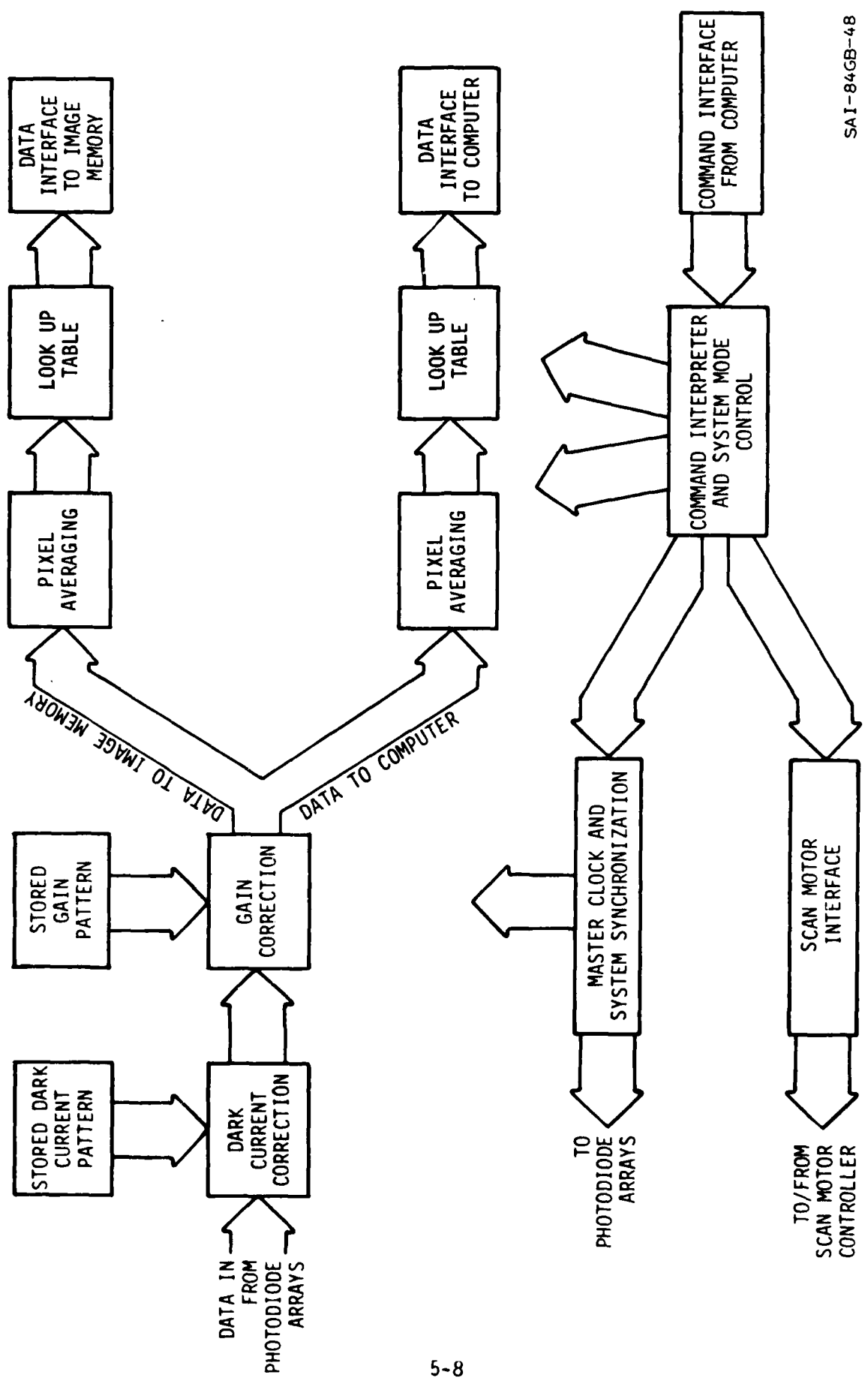
Physically, all the analog electronics except the preamplifiers reside on plug-in cards in a card cage. Interconnections between the card cage and the preamplifiers is by means of four individual cable assemblies.

Each preamplifier consists of two identical low-noise amplifying circuits. The reason for this dual channel is that the output from the arrays



SAI-84GB-47

Figure 5.3.2. Simplified Block Diagram of Analog Electronics.



SAI-84GB-48

Figure 5.3.3. High Resolution X-Ray System Unit Digital Data Processing and System Control.

is in the form of even pixels and odd pixels which are amplified separately. The basic preamplifier consists of three stages: high input impedance, low-noise differential FET, differential running stage (to remove fixed pattern noise), and output-gain stage.

Each clock driver provides the clocking signals required to readout the photodiode array. The clocking signals, which are generated on the array readout controller board, must have their level modified and independently adjusted for optimum performance of each array. This is one reason for separate clock drivers.

Each video processor has the function of recombining the separately read odd and even pixels. This is accomplished through a double sample and hold circuitry, and a double sample correlation technique which reduces frequency related noise.

The master clock/array readout controller has the purpose of providing a uniform clock which is routed to the clock drivers, video processors, and analog to digital converter.

The analog-to-digital converter/multiplexer switches between video channels 1 through 4, and each channel is digitized pixel by pixel. The A/D will always digitize 4096 pixels contiguously, so that the selected integration time will not change if one decides (through processing of the data in a following stage) to observe or record data from one array only. The A/D digitizes each pixel to 12-bit precision. Its output is transmitted in serial format along with appropriate status signals which allow for its deserialization in the system controller.

System Controller

The system controller electronics perform three types of functions. These include: (1) operations performed on the digital data received from the linear scanner and the interfacing of these data to the computer and to the display memory, (2) synchronization of the data acquisition with the motion of the linear detector during the scanning, and (3) interpretation of commands received from the computer.

An operational block diagram of the system controller is shown in Figure 5.3.3 with data flow across the top and control functions on the bottom.

Digital data from the analog-to-digital converter enter the system unit at the upper left of the block diagram. First, a correction is made for the signal due to the background, or dark-current of the photodiodes. Each photodiode has a small leakage current, or dark-current, independent of the light level, which is summed to the signal produced by the illumination. The system controller stores this dark current pattern in 4K of RAM memory and subtracts the correct value of dark current signal from each pixel as the data arrives from the detector unit. Options available to the operator for this correction include: (1) All data are corrected for dark-current, the normal mode of data acquisition. (2) The data can bypass the correction, a feature that will be used during system diagnostics. (3) The dark current correction can be read from the RAM memory to the computer. (4) A dark-current pattern can be entered from the computer into the RAM memory. (5) A dark-current pattern can be stored into the RAM memory directly from the array. To reduce the effect of random fluctuations, the system controller automatically averages 16 scans of dark current for this mode of entry. The details of the dark-current corrections are shown in Figure 5.3.4.

A multiplicative correction is then applied to the data to compensate for variations in sensitivity along the 8-inch length of the entrance slit. The multiplicative gain-correction is performed by adding the logarithms of the input data and of the gain correction ratio. The incoming data is converted to its equivalent logarithmic value in a ROM look-up table. The correction ratio for each pixel is stored as a logarithm in the gain-correction RAM. As the data from each pixel arrives, it is converted to the log value and is added to the corresponding log of the correction ratio from RAM. The sum, which is the log of the gain-corrected signal, is converted back to its linear value by an anti-log ROM look-up table. This system avoids the critical timing associated with multiplier IC chips, and simplifies the calculation of the gain-correction data.

The details of the gain correction are illustrated in Figure 5.3.5. The same five options exist for the gain correction as for the dark current

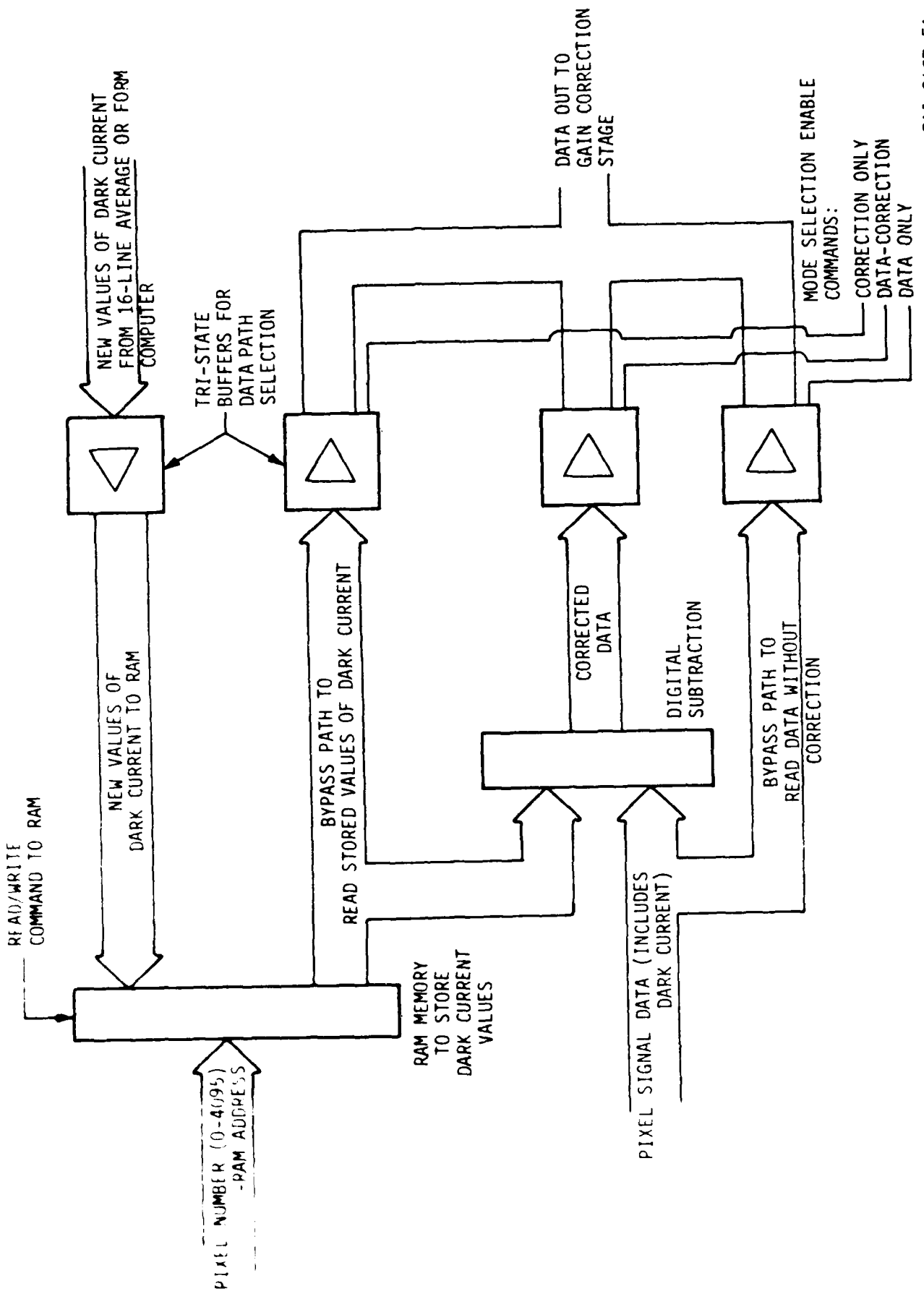
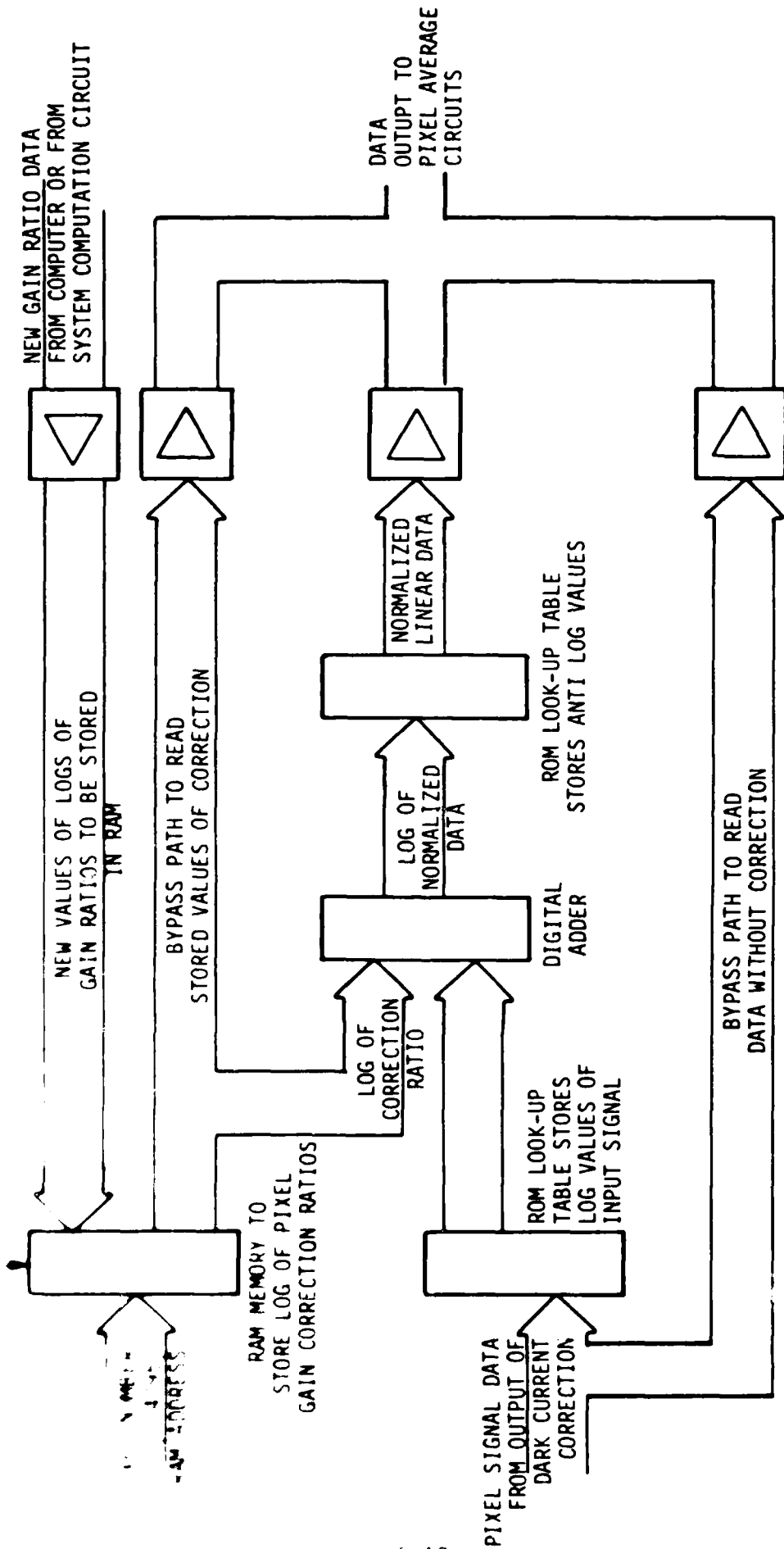


Figure 5.3.4. Detail of Dark Current Correction.

RAM ADDRESS



SAI-84GB-50

Figure 5.3.5. Detail of Gain Correction Circuit.

correction; except that, when the correction pattern is to be entered directly from the array, one must ensure that a uniform radiation field falls over the input slit.

Following the gain correction, two data paths exist. One path is for the data to be transferred to the computer and the other one is for transfer of the data to the RCI TRAPIX image processor. The same functions can be applied separately to the two paths.

The first function is pixel averaging. To reduce the resolution, pixels can be averaged horizontally (along the 8-inch scan line) and/or vertically (in the direction of scanner motion). Pixels can be averaged in groups of 2, 4, 8, or 16.

The second function is modification of the pixels intensity by passing the data through a RAM stored look-up table. This table is loaded from the computer and can be used, for example, to correct for the intrinsically nonlinear nature of X-ray absorption, to expand or compress ranges of intensity in the image, or to reverse the polarity of the video image. Lastly, the data are transmitted to the 11/73 computer through a DEC DR11 interface card. The data to be displayed are sent to the image processor through the Megavision Image Processor "fast data port."

Operational mode commands are input from the computer to the system controller where they are stored and interpreted. These commands may affect the operation of the system controller (parameter setting) or may be forwarded to the detection unit or motor controller, as appropriate.

The system controller provides the master clock synchronization for the various units in the system. The data readout scan of the photodiode arrays begins in the detector unit on receipt of a start-of-line pulse from the system controller. Also, the pulses to the stepping motor are triggered by pulses from the system controller and are synchronized with the data acquisition rate.

Scan Drive Control

The scan drive is a stepper servo system whose clock rate is derived from the imager scan rate. The system provides constant velocity motion from specific point-to-point operation. An independent encoder keeps track of absolute motion and provides a positive indication of proper motion. The table will be designed to scan at least 2x the width of the scanner (about 16 inches) and take objects up to 50 lbs. in weight. A separate drive will permit moving the table up and down to allow different portions of the part to be inspected. Operation of the scanner drive is controlled from the computer and simple controls permit jogging or resetting the position back to a given fiducial to home point.

6.0 PROGRAM SUMMARY AND RECOMMENDATIONS FOR FURTHER STUDY

During the course of the program, all major tasks detailed in the statements of work have been accomplished. These have included:

- Testing and evaluation of a number of converter screens
- Development of a practical, non-subjective figure of merit
- Collection of a number of representative aircraft related samples
- Design and construction of a breadboard X-ray imager system
- Evaluation of the breadboard instrument on typical aircraft samples
- Conceptual design and specification for a full sized prototype imager

The results of the program have confirmed the fact that converter screens exist which can support 10 lp/mm on practical X-ray imaging systems. Although this study limited itself to analysis of only fiber optic components, the screens evaluated could be equally well used on a lens coupled system. The three major types of screens all performed quite well.

The scintillating glass fiber-optic materials, especially the terbium-doped glass, performed very well. Since the beginning of this program, a new formulation of this glass has become available and shows an even higher output with equally good resolution. The differences in MTFs of the fiber-optics screen are almost entirely determined by the fiber size and packing fraction. The thicker fibers provide a higher relative efficiency for high energy radiation when compared to thin screens and hence reduce the effect of internally scattered (low energy) radiation on thick or extended objects.

The use of deposited "salt" screens on fiber optics proved to be very effective. The inherently high energy to light conversion of the Gd_2O_2S converter is a strong influence on total light output. The use of a thin screen on large numerical aperture fiber optics was particularly effective for soft X-ray imaging of composite materials. Its high sensitivity at the lowest energy with rapid fall off at higher energies emphasized the energy region with

the most information content. The use of thicker coatings of Gd_2O_2S on lower numerical aperture fibers such as the combination Gd_2O_2S + Terbium screen showed that the fiber optic can act as a light collimator and provide a much higher resolution than might be expected from direct contact with such a thick screen.

The intagliated screens were fabricated without much prior development and in fact did not rank as highly as the other types of screens. This probably reflects a poor optical coupling of the microcrystals within each column. This decoupling or lack of contact may have occurred after settling either from thermal or mechanical shock or some chemical interaction such as absorbing moisture.

This is one area that would certainly benefit from more study. The intagliation process should provide one of the brightest and most efficient screens and the materials used are much less expensive to obtain compared with finished fiber optics. This process would lend itself to construction of either a linear or an area screen. The results from the current experiments certainly show that the screens, even if imperfectly constructed, still work quite well and show a great potential for very high performance with additional development.

The figure of merit developed in the study is an easily calculable quantity either for a component such as the converter screen or for a total system. More importantly, it is based on a defect recognition model that realistically deals with the effects of both the MTF and signal to noise ratio on the resulting image. The use of a simplified model that does not require any complex convolution integrals makes the procedure easy to implement either as a built in function on a computer based image processor or even by hand if the basic data is known. More work is needed to develop test objects that can effectively measure MTF over a wide range of X-ray energies. The standard developed in this study, while effective, proved to be complicated to make and required precise alignment with the beam. The standard should be usable both with film and on real-time systems to permit easy validation.

The aircraft components collected during the program came from a number of sources in the industry and represented both in service components as well as manufactured test pieces. They represented a broad range of X ray density and material composition to fully test the performance of the breadboard system. In practice, images were taken as low as 13kV for the thin composites to above 280kV for the mortar sample. The problem encountered in the thicker samples was finding objects that contained interesting detail that could be shown in a 1 or 2-inch wide field of view. The ordinance components displayed material (steel and explosive simulant) which demonstrated both sensitivity and dynamic range.

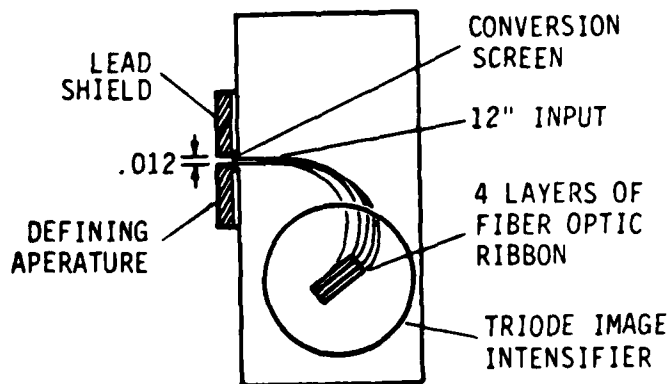
The breadboard scanner went through several iterations during the program. The final configuration was still not an optimal one but clearly reached the design goals of the r.f.p. in that it approached 10 lp/mm for the best screens and had a useful signal range of 1024 grey levels and was tolerant of significant overload without blooming. The scanner was used both in its full resolution (1" f.o.v.) and half resolution (2" f.o.v.) mode. It was necessary to do this because the in-house image processor was only capable of displaying 512 x 512 pixels. The system worked well enough to illustrate many of the advantages of line scanning and some of the disadvantages. The pictures and test object all showed a reproducible resolution and general freedom from blooming that is quite unique in real-time systems. The data taken at very soft X-ray energies showed the very low effective entrance window absorption and a system sensitivity to low-energy radiation which is an absolute prerequisite for sensitive imaging in carbon composites. The experience with the 8- inch prototype system also illustrated the feasibility and problems associated in expanding a two 2-system by fourfold stacking of identical elements. Parallel developments in custom fiber optic engineering also indicate more effective designs for subsequent systems.

The major advantage of the linear scanner design, as conceived here, is just this expandability with no loss in resolution or contrast sensitivity. The fact that the breadboard system achieved the major design goals using advanced converter screens and that the 8-inch prototype successfully integrated what are essentially four 2-inch segments handling the problems of

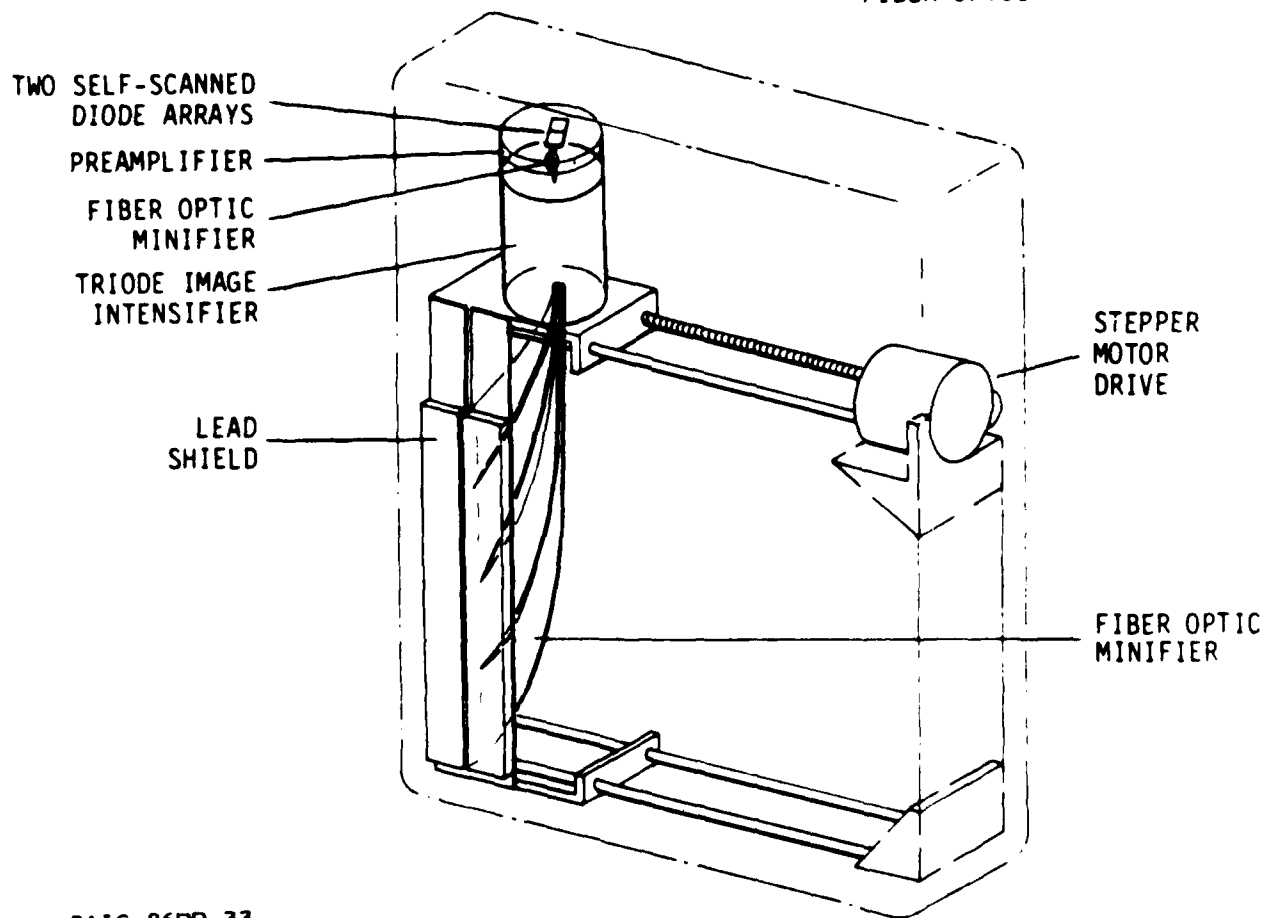
noncontiguous pixels, gain variations and other scaling problems fully demonstrates the viability of this approach.

In summary, this work has shown the feasibility of X-ray converter screens and imaging systems capable of achieving very high radiographic resolution. The question of what type of system is best suited for particular application is relevant in the light of the current experience. Real-Time Radiography systems whose performance exceeds current technology would bring significant savings and increased effectiveness to all areas of radiography in the aircraft industry. The ultra high resolution and contrast sensitivity sought in this program bring special requirements of source strength and integration time. These resources may well be available in a test laboratory or in a dedicated manufacturing facility but hard to achieve on the flight line with portable sources and difficult field conditions. Designs for a portable line scanner are certainly possible as evidenced with the concept shown in Figure 6.1. However, it appears to us that a more reasonable approach to the task is to use area scanners where flux and time are important and line scanners where ultimate performance are more important. Fortunately, many of the converter screens developed in this and similar studies can be used in both types of systems.

The major remaining problem for the area scanners will be to find a solid state analog to the sensors used for the linear scanner and which can fully match the performance of the commonly used Image ISOCON. The ISOCON, while providing many desirable performance features is fragile and bulky and totally unsuited for field applications. It is also true that totally fiber-optic systems (i.e., no lens) are not practical for large areas although some small systems have been constructed. The most practical solution seems to be with one of the new 800 - 1000 TV line solid state imaging arrays and a properly designed intensified optical system. Some chips are appearing now, at least at the development level, that are specifically designed for high-resolution radiographic or scientific imaging. An example of a 1024 x 1024 imager of this type is shown in Figure 6.2. Such chips have a number of features in their operation that makes them better suited for this application than devices designed for the commercial television market. It would seem that



TOP VIEW OF CONVOLUTED FIBER OPTIC RIBBONS



SAIC-86RP-33

SCHEMATIC OF STEPPER DRIVE SCANNER ASSEMBLY

Figure 6.1 X-Ray Linear Scanner Concept for a Field Portable System.

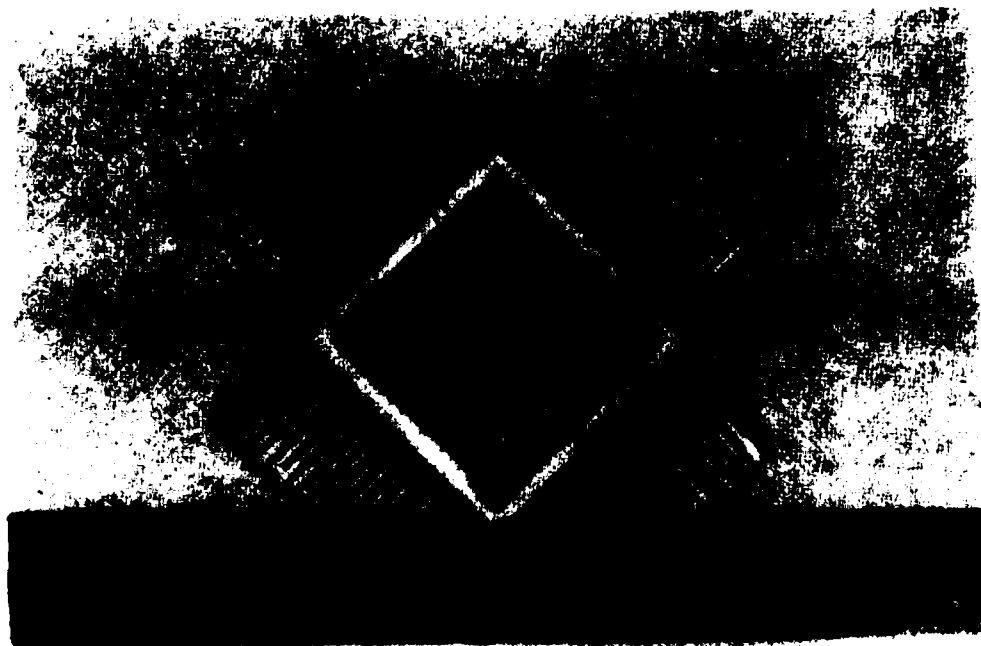


Figure 6.2 SAIC 1024 X 1024 Pixel Solid State Imager.

the rapid development of this technology could make a 1000 line portable real-time X-ray imager a reality in a relatively short time and that such a device would provide a useful and valid alternative to the ultra high performance systems sought in this program.

END

DATE

FILMED

FEB.

1988